

STELLINGEN

behorend bij het proefschrift

Modelling of the Kinetics of Suspension Crystallizers

R Ó MEADHRA

1. For well soluble compounds, the models described in van der Heijden et al. (*J. Crystal Growth* **118**, 14-26,1992) cannot be used to model the dynamic and steady-state growth behaviour of secondary nuclei without first combining them with expressions for diffusion limited growth.
2. The 22 L crystallizer can be used just as effectively as the 970 L crystallizer, to determine the CSD start-up and steady-state CSD behaviour, and to improve the design of crystallizers.
3. The typical S-shaped curve of the attrition function (chapter 5, this thesis) is linked to the probability of a crystal colliding with the impeller, and the probability that such a collision will result in the formation of an attrition fragment.
4. The results of small contact nucleation experiments, where a crystal surface is contacted with a falling steel rod, (see for example Garside and Jancic, *AIChE J.* **25** (6): 948-958, 1979, and Clontz and McCabe, *Chem. Eng. Progr. Symp. Ser.* **67** (110):6, 1971), show that secondary nuclei grow with a constant crystal growth behaviour. This mechanism does not describe the growth behaviour of secondary nuclei produced in a crystallizer.
5. The limitation in the number of measurable variables in a crystallizer, such as flow / supersaturation profiles, spatial crystal size distributions, compared to the complexity of the kinetic and physical processes occurring, causes a so-called over parameterisation of the crystallizer model.
6. European community financing of research is misplaced if its' main objective is to improve communications to promote pan-European integration.
7. The often underestimated principal product of research projects in a university environment is the personnel who have the experience and ability to put the knowledge gained into commercial practice.

8. With the availability of faster computing power on the market, the principles of efficient and compact programming are being neglected.
9. Similar to secondary nuclei in a crystallizer, students entering their last year project phase at the TU Delft exhibit a growth rate dispersion, whereby some need extra encouragement to grow to the required product specification in the allotted residence time.
10. "*Beter Holland dan heimwee*" is te prefereren boven de oude zeemannspreuk "*Beter heimwee dan Holland*".

**Modelling of the Kinetics of
Suspension Crystallizers**

A new Model for Secondary Nucleation

Dit proefschrift is goedgekeurd door de promotor:
Prof.dr.ir. G. M. van Rosmalen

Toegevoegd promotor:
Dr.ir. H.J.M. Kramer

Samenstelling promotiecommissie:

Rector Magnificus, voorzitter
Prof.dr.ir. G.M. van Rosmalen, Technische Universiteit Delft, promotor
Dr.ir. H.J.M. Kramer, Technische Universiteit Delft, co-promotor
Prof. B. Scarlett M.Sc., Technische Universiteit Delft
Prof.ir. H. van den Berg, Dow Chemicals (Benelux)
Prof. K. Roberts, University of Edinburgh, Schotland
Dr. M. Noonan, Cork Regional Technical College, Ierland
Dr. C.W. Sink PE, Eastman Chemical Company, Tennessee, USA
Prof.ir. J. Grievink, Technische Universiteit Delft, reservelid

Cover illustration : Detail of Ammonium Sulphate crystal face

CIP-DATA KONINKLIJKE BIBLIOTHEEK, DEN HAAG

Ó Meadhra, Ruairí

Modelling of the kinetics of suspension crystallizers, A new model for
secondary nucleation / Ruairí Ó Meadhra. - Delft : Delft University Press. - Ill.
Thesis Delft University of Technology. - With ref. - With summary in Dutch
ISBN 90-407-1190-9

NUGI 813

Subject headings: industrial crystallization / kinetics modelling / secondary
nucleation

Copyright © 1995 by R. Ó Meadhra

All rights reserved

No part of the material protected by this copyright notice may be reproduced or
utilized in any form or by any means, electronic or mechanical, including
photocopying, recording or by any information storage and retrieval system,
without permission from the publisher: Delft University Press, Stevinweg 1,
2628 CN Delft, The Netherlands

Printed in The Netherlands

Do Mum agus Dad

Preface

This thesis is a result of four years of work carried out within the framework of the UNIAK II crystallization research project at the Laboratory for Process Equipment at the Delft University of Technology.

The results, simulations and ideas contained within this thesis could not have been achieved without the assistance of a large number of people, with whom I have had the good fortune to work with, and learn from over the last four years.

Firstly, I would like to thank my supervisors Gerda van Rosmalen and Herman Kramer for the stimulating discussions, excellent guidance, support and freedom they gave me while working towards my thesis.

My gratitude to the project leader Brian Scarlett for taking a risk four years ago with an Irish engineer from Cork RTC looking for a challenge, and for the encouragement and discussions..

My UNIAK colleagues Rob Eek, Hans Gerla and Camiel Heffels, thanks for your friendship, and for making my task easier, varied and much more interesting. Andreas, Joost and Seán, good luck with the UNIAK III phase.

The many enjoyable hours spent with undergraduate students wrestling with temperamental crystallizers, brainstorming over wild hypotheses and devouring pizzas remain some of the highlights. I wish Murk Peutz, Wopke Talsma, Albert Mukidjam (waar zit je eigenlijk ?), William Jackman, Dirk Martens, Erwin Nederkoorn, Rein-Jan Koolwijk, Roger Blokland, Preeti Singh, Martin Payne, Marit Skotheim every success in the future with their chosen careers.

Further, I would like to acknowledge Antoine van der Heijden, Rob Geertman and Kevin Roberts for their valuable contributions, and my predecessor Peter Daudey for suggestions and the clear starting point he left for further work on secondary nucleation, and all the staff and students (including the Kentuckians) at the Laboratory for Process Equipment for their participation.

Finally I would like to thank my new employers at Eastman Chemical Company in Den Haag and Kingsport for allowing me the time to finish work on my thesis.

I also acknowledge the support of a number of concerns for their financial support of the UNIAK project - The Dutch Foundation of Technology (STW), Akzo Nobel, Dow Benelux, DSM, E.I. du Pont de Nemours, ICI, Eastman Chemical Company.

Summary

The modelling of the crystal size distribution (CSD) from industrial suspension crystallizers is still proving to be a problem. Inadequate modelling of the product quality stems from the fact that the combinations of kinetic processes leading to the production of the CSD have not been properly identified, and secondly, there is lack of reliable mechanistic models which can be applied to a wide variety of materials, to simulate the CSD in a well-mixed crystallizer.

In this thesis, the above problems are addressed. The main requirement is to produce mechanistic models for the kinetic processes of crystal growth, attrition and secondary nucleation with which it is possible to describe the CSD oscillatory behaviour in the product stream of crystallizers.

The first step is to apply a first principles method to the modelling of a crystallizer system. A series of mass and energy balances together with a crystal population balance are used to define the changes in the fluid phase concentration and the change in the state of the CSD. The population balance provides the framework with which the influence of the kinetic processes of crystal growth, attrition and secondary nucleation change the CSD. A numerical solution technique to solve the population balance is introduced.

With this simulation framework, a number of existing models from literature are tested. It is shown that the empirical power law for secondary nucleation, which has often been used in literature to predict steady-state nucleation rates of a known system, cannot be used to simulate the start-up oscillatory behaviour of the CSD. A modified version of the power law, where target efficiencies are used to identify the crystals which collide with the impeller to produce attrition fragments, is shown to perform much better in simulating the start-up phase.

A closer look at the growth of secondary nuclei is taken in chapter 4. From literature, many references can be found which report a growth rate dispersion (GRD) mechanism of growth for several materials. In a suspension crystallizer, a GRD type of growth and a size dependent growth (SDG) mechanism cannot be distinguished from each other. This is also not possible from a mathematical point of view. For this reason and as a SDG correlation is easier to handle in the population balance, a SDG mechanism function is determined for ammonium sulphate. This is done on-line by

measuring the growth rate of a suspension of sub- 250 μm crystals isolated into a 2 L growth cell using a Malvern forward light scattering instrument. The results showed that the growth rate of ammonium sulphate can be described using a SDG rate which shows that average crystal growth rate of ammonium sulphate increase up to a size of 250 μm . In the same chapter, recent models which claim that crystal internal strain leads to a GRD/SDG mechanism are tested. The same type of crystals are analysed using a Laue diffraction technique, and the results show that a SDG/GRD mechanism for ammonium sulphate is to be expected up to sizes of 300 μm agreeing with the results of the 2 L growth cell experiments.

In chapter 5, a new secondary nucleation model is developed. A three step model is used. The first step is the formation of attrition fragments. This is described by an empirical attrition function which describes an increasing attrition rate with increasing crystal size, with which it is possible to calculate the formation rate of attrition fragments. The second step, removal of attrition fragments describes the probability that an attrition fragment on a crystal surface is removed into the suspension. For most materials, the value of this factor is unity. The last step is the survival and outgrowth of attrition fragments. From the results of the mosaic spread measurements in chapter 4, it was shown that sub- 60 μm crystals contain a high degree of strain which may prevent crystals from growing out unless they experience a higher supersaturation. For this reason, a supersaturation dependent survival efficiency is defined. The model is validated on a set of data from the 970 L crystallizer. Three types of experiments are used for validation, constant operating condition start-up experiments, semi-batch start-up experiments and continuous steady-state identification experiments.

In chapters 6 and 7 the models developed in chapters 2, 4 and 5 are tested on the crystallization of three materials on a 22 L scale in continuous evaporative mode. The materials were ammonium sulphate, and pentaerythritol and adipic acid, the last two materials having a much lower solubility than ammonium sulphate. The results of the ammonium sulphate experiments reveal that the start-up behaviour did not differ greatly from that observed for ammonium sulphate crystallization in the 970 L crystallizer and could be described using the same model with practically the same kinetic parameters.

The models was also shown to be applicable to the crystallization of the other two materials. It was also shown that the inclusion of a SDG rate and a supersaturation dependent survival efficiency was vital for the accurate simulation of the start-up behaviour.

Contents

CHAPTER 1	1
INTRODUCTION.....	1
1.1 INTRODUCTION.....	1
1.2 CRYSTALLIZATION KINETICS	2
1.3 DETERMINATION OF KINETICS.....	5
1.4 PROBLEM FORMULATION.....	6
1.5 OBJECTIVES AND APPROACH	9
1.6 STRUCTURE OF THE THESIS	11
CHAPTER 2	13
SIMULATION FRAMEWORK AND KINETIC MODEL REVIEW	13
2.1 INTRODUCTION.....	14
2.2 GENERAL MODEL FOR A CRYSTALLIZER	14
2.2.1 <i>System description</i>	14
2.2.2 <i>Population balance</i>	16
2.2.3 <i>Kinetic Parameters</i>	17
2.2.4 <i>Class I and II systems</i>	21
2.2.5 <i>Mass and energy balances</i>	21
2.3 SIMULATIONS.....	22
2.3.1 <i>Numerical methods and stability</i>	22
2.3.2 <i>Moments of the distribution</i>	23
2.3.3 <i>Steady-State solution of the population balance</i>	24
2.3.4 <i>Summary and interrelation of kinetics</i>	25
2.4 SIMULATIONS OF THE DYNAMIC BEHAVIOUR	26
2.4.1 <i>Experiments</i>	27
2.4.2 <i>Kinetic parameter values</i>	27
2.4.3 <i>Simulation results</i>	28
2.4.4 <i>Simulations of the steady State Distributions</i>	30
2.5 DISCUSSION	31
2.6 CONCLUSIONS.....	33

CHAPTER 3	35
-----------------	----

EQUIPMENT/ SENSING DEVICES/ MODEL MATERIALS.....35

3.1 INTRODUCTION	36
3.2 CRYSTALLIZERS	36
3.3 CRYSTALLIZER DESCRIPTIONS.....	37
3.3.1 970 L Crystallizer	37
3.3.2 22 L Crystallizer	39
3.3.3 2L Growth Cell	42
3.3.5 Product removal	43
3.3.6 Fines removal	46
3.4 SENSING EQUIPMENT.....	47
3.4.1 LIGHT SCATTERING DEVICES.....	47
3.4.1.1 Forward light scattering.....	47
3.4.1.2 Back light scattering.....	50
3.4.2 Camera Observations.....	50
3.4.3 Synchrotron Radiation Source	51
3.5 MODEL MATERIALS	54

CHAPTER 4	59
-----------------	----

GROWTH OF AMMONIUM SULPHATE CRYSTALS IN A CRYSTALLIZER59

4.0 INTRODUCTION	60
4.1 BACKGROUND	60
4.2 SOURCES OF GROWTH RATE DISPERSION	64
4.3 MECHANISMS OF GRD	65
4.4 STRAIN MECHANISMS	67
4.5 IDENTIFYING THE STRAIN MECHANISM	68
4.6 EXPERIMENTAL STRATEGY	70
4.7 2 L GROWTH CELL EXPERIMENTS	71
4.7.1 Operation.....	71
4.7.2 Modelling of the 2 L growth cell CSD results	72
4.7.3 Simulation.....	75
4.7.4 Results and Discussion.....	75
4.7.5 Conclusions : 2 L Growth Cell Experiments	82
4.8 MOSAIC SPREAD MEASUREMENTS.....	82
4.8.1 Experimental.....	82
4.8.2 Analysis.....	84
4.8.3 Results and discussion.....	85
4.8.4 Conclusions	88

CHAPTER 5	91
-----------------	----

**A MODEL FOR SECONDARY NUCLEATION IN A SUSPENSION
CRYSTALLIZER.....91**

5.1 INTRODUCTION	92
5.2 THEORY OF SECONDARY NUCLEATION MODELS	93
5.2.1 <i>The empirical power law</i>	93
5.2.2 <i>Mechanistic models</i>	95
5.3 NEW MODEL	97
5.4 EXPERIMENTAL	100
5.4.1 <i>Effect of attrition on the start-up behaviour</i>	100
5.4.2 <i>Semi-batch Start-ups</i>	102
5.4.3 <i>Continuous identification experiments</i>	102
5.5 RESULTS AND DISCUSSION	104
5.5.1 <i>Attrition experiments</i>	104
5.5.1.1 <i>Bench Scale</i>	104
5.5.1.2 <i>Pilot Scale experiments</i>	105
5.5.2 <i>Batch Start-ups</i>	113
5.5.3 <i>Continuous identification experiments</i>	114
5.6 CONCLUSIONS	117

CHAPTER 6	119
-----------------	-----

KINETICS AND THE SCALE OF CRYSTALLIZERS 119

6.1 INTRODUCTION.....	120
6.2 SCALE-UP REVIEW	121
6.3 EXPERIMENTAL	125
6.3.1 <i>Equipment</i>	125
6.3.2 <i>Experiments</i>	126
6.4 RESULTS AND DISCUSSION	128
6.5 MODEL SIMULATIONS	136
6.6 CONCLUSIONS	140

CHAPTER 7	143
-----------------	-----

CRYSTALLIZATION OF PENTAERYTHRITOL AND ADIPIC ACID 143

7.1 INTRODUCTION.....	144
7.2 LITERATURE	144
7.3 KINETIC RELATIONS	146
7.4 EQUIPMENT AND SENSORS.....	146
7.5 RESULTS AND DISCUSSION	147

7.5.1 <i>Crystallization of Pentaerythritol</i>	147
7.5.2 <i>Crystallization of Adipic acid</i>	151
7.6 MODEL CHOICE EFFECT ON SIMULATION	157
7.7 CONCLUDING COMMENTS	159
CHAPTER 8	161
CONCLUSIONS AND SUGGESTIONS FOR FUTURE WORK	161
8.1 CONCLUSIONS	161
8.1 SUGGESTIONS FOR FUTURE WORK	164
APPENDIX A	167
MASS AND ENERGY BALANCES	167
APPENDIX B	175
MATERIAL PHYSICAL PROPERTIES	175
APPENDIX C	177
SIMPLE CLASSIFICATION MODEL	177
APPENDIX D	181
IMPELLER STEP CHANGE RESPONSE IN A NON-IDEALLY MIXED CRYSTALLIZER	181
REFERENCES	185
LIST OF SYMBOLS	195
SAMENVATTING	201
PUBLICATIONS	205
CURRICULUM VITAE	207

Chapter 1

Introduction

1.1 Introduction

Crystallization is a well known and commonly used process in the chemical industries, whereby advantage is taken of the solubility characteristics of certain materials in a particular solvent to produce crystalline particles of a very high purity. The importance of crystallization is evident from the vast amounts of saleable product and intermediates produced via this unit operation e.g. annual production rates of sodium chloride, sodium and ammonium sulphates and sucrose each exceed 100 million metric tons per year (Kirk-Othmer). Crystallization is only second in importance to distillation as a separation and purifying technique. Unlike distillation however, the mechanisms describing the various physical and kinetic processes occurring in the crystallizer are very poorly understood and for this reason, crystallization has received little attention from other fields of research such as equipment design, process modelling and control, in efforts to try and improve the product quality from the crystallizers.

Four types of solution crystallization processes are found in industry and can be differentiated by the way in which the supersaturation is generated. This can be done via evaporation, cooling, precipitation/reaction and by salting/drowning out for these cases. By making use of one of these crystallization techniques, a solid crystalline product possessing a characteristic crystal size distribution (CSD) is produced from a crystallizer.

Irrespective of the mode of crystallization applied, similar criteria are set on the product of all crystallizers in terms of quality and quantity. The product quality is determined by the efficiency of the solid/liquid separation in downstream processes such as the filterability of the product. A slurry with a large number of fine crystals will require a higher filter pressure and a larger surface area to attain the required separation, thus involving higher capital and maintenance costs. A product which contains large numbers of inclusions could result in caking problems as the liquor seeps out of the crystals during transport. The most important quality constraint is however, the CSD for which users of the product will pay a premium for an 'in specification' product. The most important considerations in determining the CSD in a crystallizer are those associated with the crystallization kinetics.

1.2 Crystallization kinetics

It is generally accepted (Garside, 1985, Dirksen & Ring, 1991) that given a supersaturation in a crystallizer and a well-mixed crystal slurry, a number of kinetic processes are induced, those being - crystal growth, attrition, agglomeration and primary and secondary nucleation.

Attrition is defined as the process by which the size of a particle (or crystal as in this case), is reduced due to it being subjected to some mechanical action. The rate of attrition is dependent on a number of factors both internal and external to the crystal. Crystalline material properties such as brittleness and yield strength as well as purity and the numbers of inclusions are all internal parameters. Further, the crystal shape and surface structure also have a bearing on the attrition rate as a rougher crystal surface will provide more potential sites for attrition. External parameters refer to vessel size, vessel and stirrer geometry and hydrodynamics. The supersaturation as external parameter, also has a crucial role to play, as it determines surface roughness and it is a controlling factor in the healing process of a site damaged by attrition when the crystal is located in a supersaturated environment.

In general, crystals located in a supersaturated solution will **grow**. The linear *growth rate* (m/s) of a crystal can be related to the supersaturation by a simple correlation used by most workers :

$$G = k(\Delta c)^n \quad (1.1)$$

where $n = 1$ for diffusion limited growth and $n > 1$ for surface reaction limited growth. This equality expresses a simplification of much more complicated theories on growth where a two step growth mechanism is envisaged, that of diffusion of a

growth unit, molecule or ion through the surface laminar layer surrounding a crystal in solution and secondly, the resistance to incorporation of the growth unit/ion/molecule into the crystal itself. The controlling growth mechanism in a particular crystallizer is determined by a number of factors, most importantly the level of supersaturation, the size of the crystal, the hydrodynamics and the level of impurities.

Fragments produced by an attrition mechanism have been shown to exhibit a wide variety of growth rates. The two groups of attrition fragments produced in the experiments of Garside and Jancic (1979) and Rusli et al. (1980) as mentioned above, were shown to exhibit two types of growers. The 1-4 μm particles were shown to exhibit a growth rate which was up to a factor 20 times slower than the larger fragments which had sizes up to 70 μm . More recent experiments (Kitamura and Endo, 1990) have shown similar results, where sub 20-30 μm secondary nuclei were shown to grow a factor 2 times slower than larger crystals above 40 μm .

Other experiments (Ristic et al., 1988), have shown that the slow growth of attrition fragments produced by a contact mechanism can be directly correlated to the levels of internal stress present in a crystal as measured by a Laue diffraction technique. This stress enters the crystal, as very often, during the attrition step in the crystallizer, high energy collisions lead to a plastic deformation in the newly formed attrition fragments. This increases the chemical potential of the solid phase, thus lowering the chemical potential difference between solid and liquid phases, which is the driving force for growth. This is equivalent to lowering the supersaturation which is 'felt' by the crystals. If the stress is so high that the crystals 'feel' no supersaturation or even a negative supersaturation, they may dissolve. A physical model for the growth of stressed crystals developed by Van der Heijden et al. (1992) and applied to the data of Ristic et al. (1988) showed that internal stress in a crystal present in the form of grain boundary dislocations is most likely responsible for the observations of size dependent growth (SDG) where the growth rate of a crystal increases with the crystal length, and growth rate dispersion (GRD) where all secondary nuclei measured at a particular size exhibit a distribution of growth rates.

Secondary nucleation, is the most important of all the kinetic processes occurring in the crystallizer. Secondary nucleation is defined as the process by which new crystals are formed due to the presence of already existing parent crystals. Several ways of breeding secondary nuclei have been identified- initial, dendritic, contact and fluid shear breeding. A full definition of each type is given in (Hurle, 1994). Only contact breeding will be considered here because nuclei which are bred by contact nucleation result from collisions between two crystals or a crystal and the crystallizer

(impeller, walls). During the early stages of research into contact secondary nucleation, and judging from the amount of literature available, there was much debate as to the exact source of secondary nuclei. From the experimentally verified work of Ottens et al. (1973) and Botsaris (1976), it was shown that the rate of secondary nucleation was dependent upon a number of factors expressed as a power law equality, namely, a term describing the state of the fluid phase in the crystallizer such as the supersaturation (σ), (related to the growth rate (G)), a moment of the distribution or the total mass of solids in the slurry (M_p), and a term for the impeller speed (N) or power input via the impeller (ϵ),

$$B \sim \sigma^b N^h M_p^j \sim G^i \epsilon^k M_p^j. \quad (1.2)$$

Having identified these dependencies, it was still not clear where the nuclei originated from and for a long time, a theory persisted which identified a pre-ordered layer of molecules on the crystal surface as the source of these nuclei. This pre-ordered layer or solute clusters as called by Powers (1963) could then act as a source of nuclei (Lal et al., 1969, Clontz & McCabe, 1971). The solute clusters were thought to be of the order of the critical nucleus size. It was thought that the dependence on supersaturation arose because the thickness of the layer increased or decreased in direct proportion to the prevailing supersaturation. This theory was eventually discarded in the light of evidence from the experiments of Garside and Larson (1978), who showed that by contacting a crystal surface directly with a steel rod, attrition fragments possessing a CSD were chipped off. Since then, other workers (Garside et al., 1979, Wissing et al., 1986, Van der Heijden et al., 1989) have obtained similar results, supporting the notion that nuclei are formed by attrition of a crystal surface.

Based on the above observations, Daudey et al. (1990) proposed a model framework for contact nucleation. They suggested that the two types of attrition fragments found by Garside and Larson and Rusli et al. originated from different sources i.e. that the larger fragments were produced by chipping off of growth entities on the crystal surface such as macrosteps, while the other smaller fragments were produced by the removal of other material from the crystal surface not previously recognisable as potential nuclei. The difference in size could be explained by assuming that between each macrostep layer on the crystal surface, the presence of impurities would provide a weak plane along which a portion of the macrostep could be prised loose by a strong enough collision. Three steps to the production of a viable secondary nucleus were defined. The first step is the *formation* step where a potential nucleus is formed on a parent crystal surface. In the case of surface breeding, the nucleus is already visible on the parent crystal surface as a macrostep or other growth entity, which is not the case for mechanical breeding. Next, a *removal* efficiency is

defined describing the efficiency with which formed attrition fragments are removed from the parent crystal surface, and finally, an efficiency is defined describing the fraction of fragments *surviving* and *growing out* in the solution. Table 1.1 sums up the two types of nucleation breeding and the three mechanistic steps.

Table 1.1 : *General modelling framework for secondary nucleation divided into two nuclei sources and three steps.*

<i>Mechanism</i>	<i>Formation</i>	<i>Removal</i>	<i>Survival/Outgrowth</i>
Surface breeding	$\sim f(G)A$	$\sim \eta_r f(G)A$	$\sim \eta_s \eta_r f(G)A$
Mechanical breeding	$\sim h(L, N)$	$\sim \eta_r h(L, N)$	$\sim \eta_s \eta_r h(L, N)$

In 1992, Van der Heijden in his thesis, gave proper quantifiable forms to all of these terms for both crystal/crystal and crystal/crystallizer impacts. In his work, he combines elements used by Mermann et al. (1988) to determine the attrition volume produced by a single collision (Hertz-Huber theory, Landau and Lifshitz, 1986). He also takes account of the types of growth formations commonly found on crystal surfaces and he refers to the work of Levich (1962), who estimated the linear speed of particles in a draft-tube as a function of particle size and impeller speed to determine the energy of collisions. He compared his results to those obtained by Mersmann et al. (1988) and Pohlisch and Mersmann (1988) using their mechanistic approach. The results showed good agreement in terms of the powers predicted for the three parameters i.e. supersaturation, impeller speed/ power input and distribution moment.

1.3 Determination of Kinetics

The phenomena of attrition of the larger crystals and SDG/GRD can be illustrated by examining the steady-state CSD of a suspension crystallizer. Several deviations are observed from the ideal MSMPR straight line and intercept notion. Below a certain size, a strong upward curvature is observed. If SDG and GRD are taken into account, this upward curvature can be understood as a reduced growth rate below this size which will lead to an accumulation of crystals in these size ranges. In the upper crystal size ranges, above about 600 μm , a downward curvature in the population density plot is caused by the size dependency of the attrition rate. The combination of these two effects along with secondary nucleation leads to the observed deviation from the ideal MSMPR line. Clearly, these kinetic effects must be quantified to be able to accurately model the overall crystallizer behaviour.

A lot of work has been put into measuring, identifying and modelling these phenomena in the past. The approach used has nearly always been to isolate a particular phenomena by designing a suitable experiment, to simulate the same effect as is found in an industrial crystallizer. These experiments can be divided up into several types, characterised by the phenomenon of interest.

The results of a large number of small scale experiments are available, which are mainly focused on the problem of identifying the factors affecting the production of secondary nuclei, by a contact mechanism. Typical examples are the work of Clontz & Mc Cabe (1971), Wissing et al. (1986) and Van der Heijden et al. (1990). These studies have mostly been concerned with the effect of supersaturation, crystal surface relief and contact energy on the numbers, type and CSD of secondary nuclei produced. Other experiments on this scale have been concerned with following the growth rates of individual secondary nuclei, of which Garside and Ristic (1983), Berglund et al. (1983) are good examples.

The separate examination of the attrition rate of large parent crystals in a well mixed vessel, have also formed the basis of a large volume of work.. This work is concerned with the identification of the attrition mechanisms leading to the characteristic downward curvature in the steady-state CSD at larger sizes, found in industrial crystallizers. Typical examples of attrition experiments are those found in Chianese et al. (1986), and Mazzarotta (1992), where crystal fractions with initial sizes between 500 and nearly 1200 μm were suspended in a saturated solution and subjected to attrition.

The third type of experiments are those concerned with using real data from industrial or semi-industrial crystallizers. A feature of these studies was the use of the population balance approach combined with some empirical models for nucleation (Zumstein and Rousseau, 1987), and a size dependent growth rate (Jones et al., 1986).

Dynamic modelling of crystallizers also falls into this category where attrition, nucleation and growth kinetics are combined with mass and energy balances to simulate the effects of process conditions on the crystallizer behaviour (Eek et al, 1995).

1.4 Problem formulation

Based on the above experimental results, it is at this time possible, with some certainty, to give a complete mechanistic description of the factors affecting the kinetics of crystal growth and attrition and secondary nucleation. Problems still exist however when trying to interpret the kinetics of the same materials for the case of a large scale suspension crystallizer. This arises, as the conditions in a crystallizer can

never be as accurately controlled or monitored as in a small growth cell suitable for use with a microscope. In such small scale experiments, the state of the fluid phase (supersaturation, impurity level, hydrodynamics) and the solid phase (crystal size, shape, surface structure) are fixed by the operator. In an industrial crystallizer however, only the global operating conditions such as residence time and heat input can be fixed while local differences in supersaturation, particle concentration and crystal size distribution in the crystallizer can affect the CSD and the quality of the crystals in the product stream.

Ideally seen, true mechanistic models are required where the effects of all possible process circumstances on the kinetics are taken into account. With such models, it would then be possible to model the kinetics on another scale as a function of the changed global and local conditions. In their absence, the most that can be done is to use simplified mechanistic models for the kinetics, which are a function of easily measurable or obtainable process parameters.

The traditional way of analysing the kinetics in a crystallizer, is by doing a steady-state analysis of the crystallizer population density function. In doing this analysis, conceptual difficulties are encountered as many of the assumptions made, are not valid in a non-ideal crystallizer. Assumptions such as, zero attrition rate, perfectly mixed suspension, constant linear growth rates of crystals and nucleation at zero length via a non-specific nucleation source, have led to badly conditioned models and are inaccurate in simulating the measured population density function. A much greater problem lies in the fact that long before a steady-state is reached in the crystallizer, the CSD passes through a dynamic phase which yields an unpredictable product CSD, causing operational problems in further downstream unit operations.

Several attempts have been made to model the crystallizer dynamic simulations by improving models resulting from steady-state experiments for growth, attrition and secondary nucleation. However, several obvious and fundamental problems are encountered with these models.

Attrition models describing the downward curvature in the $\ln(n)$ vs. L plot, have been estimated by some workers doing so called 'inert' experiments. The problems with the models yielded from these experiments are,

- The contribution of surface bred attrition fragments present in an industrial crystallizer cannot be determined from so called 'inert experiments', as any surface relief originally present on the growing crystal, will disappear when the crystal is removed from this environment and treated before reuse in an attrition experiment.

- The 'hurt' areas of a crystal are 'healed' in a crystallizer due to regrowth on the crystal surface. Thus, the regenerated areas are able to contribute to the attrition rate in a crystallizer but this effect is missed in an 'inert' situation.
- The effect of the properties of a different suspending fluid, may also have a significant effect on the attrition rate of the particle, and may also affect the CSD of the attrition fragments produced.

With respect to secondary nucleation, models resembling equation (1.2) have not been very successful for several reasons,

- Simple empirical correlations for secondary nucleation, predict an effective nucleation rate i.e. the numbers of crystals which nucleate and grow out to larger sizes, as opposed to the actual nucleation rate which accounts for all nuclei born which will or will not grow out.
- No direct link is made between the source of attrition fragments and the secondary nucleation rate.
- In the presence of SDG/GRD effects, the effective nucleation rates will be much lower than the real nucleation rates. With a SDG in some systems exhibited up to sizes of 300 μm , this discrepancy will create a significant difference between the actual and modelled product CSD.
- An inaccurate empirical model for secondary nucleation based on small scale experiments cannot be used as a scale-up criterion, as no account is taken of changing geometry and hydrodynamics conditions.

Several attempts to overcome these problems, and to use a more mechanistic approach to secondary nucleation modelling (Pohlisch and Mersmann, 1988, Ploß and Mersmann, 1989) were not successful as the amount of unknown parameters in the eventual useable forms of the mechanistic models, were far in excess of the amount of information available on the various hydrodynamic and kinetic processes. This often resulted in a lumping of the unknown parameters together, to again be estimated by empirical means.

Conversely to the second point above, inaccurate modelling of the SDG/GRD phenomenon has consequences for the successful modelling of the growth of the secondary nuclei, and thus the entire crystallizer dynamics, as the correct nucleation rate model, combined with a bad description of their growth behaviour, will also lead to an unacceptable modelling of the entire crystallization behaviour.

Current models for the growth behaviour of small crystals in suspension are very arbitrary. They are mostly based on the observations of the growth of only a few crystals, and are almost exclusively functions of crystal length and the supersaturation. Attempts have been made to relate the growth rate of crystals to some property of the crystal such as the number of dislocations or internal stress level. The experimental findings are contradictory, with some workers finding that within a certain defined size class, a distribution of growth rates exists, while other workers find that each class has a unique growth rate. Instead of generating more data regarding crystal growth, more effort should be directed towards finding the underlying cause of SDG rates and GRD mechanisms and then it will be possible to compare the results of different experiments on the same basis.

True modelling of the growth mechanism of secondary nuclei requires three components which are currently not available, those being -

- Knowledge of the source and the size of the secondary nuclei is necessary, as according to the microscopic contact experiments discussed above, differently bred nuclei (surface and mechanically bred) will exhibit different growth behaviours fragments. Evidence also suggests that differently bred fragments may have different sizes.
- The level of damage present in the form of internal crystal strain in the secondary nuclei is necessary as the level of this strain is, along with the supersaturation, the controlling factor in the regrowth process.
- An on-line knowledge of the supersaturation is required to be able to determine overall growth rates.

Before any physical model for crystal growth can be validated, these three criteria will have to be satisfied.

1.5 Objectives and Approach

Clearly, an abundance of information exists on the various kinetic processes occurring in a crystallizer. The first step in the approach is therefore to review a lot of this information to determine how much is relevant to the problem of suspension crystallization, and to weigh up the complexity of the models against the information available on the suspension crystallizer. By doing this, it is possible to identify what extra information is necessary to improve the kinetic description of the crystallizer behaviour.

In this approach, interest will be directed more towards mechanistic and physical models of the kinetics than empirical models. This is done as a validated mechanistic framework can be applied to all suspension crystallizers while empirical models are valid for only a specific system.

Mechanical and physical models which cannot be directly measured on-line due to measurement difficulties will be measured off-line as in the case of crystal internal strain or will be simulated via the system mass, energy and population balances as for the case of the supersaturation.

In summary, the objectives of this thesis can be split up into a number of sub-objectives.

- Development of an overall method to modelling of the dynamic crystallization behaviour based on a population balance approach with the inclusion of the important kinetic processes of crystal growth, attrition and secondary nucleation.
- Development of general mechanistic models for crystal growth, attrition and secondary nucleation must be found or constructed, which are consistent with literature observations of their effect on crystallizer steady-state and dynamic behaviours.
- Verification of models subject to dynamic start-up and steady-state process condition step changes.
- Extension of the models to a general form which can be applied to the crystallization of different materials and different scales of operation.

With regard to the separate kinetic processes, the following approach will be taken.

Attrition

Other functions besides those introduced by Jager et al. and Pohlisch will be tested will be done to examine the effect of a different shaped attrition function on the dynamic and steady-state CSD behaviour, and experiments will be done to show that 'inert' background experiments are invalid when trying to determine an attrition function for a system where crystals are growing

Secondary nucleation

With regard to secondary nucleation, the mechanistic approach outlined in table 1.1 forms a good starting point for the building of a useable mechanistic model for secondary nucleation. The accuracy with which the various terms for formation, removal and survival/outgrowth can be estimated must be determined, and further if it is possible to make a distinction between mechanical and surface breeding.

Crystal Growth

Of the three criteria listed in section 1.4 for crystal growth for the validation of a physical model i.e., crystal origin (mechanical or surface bred), level of strain and supersaturation, only the last is at best measurable on-line at this moment. The origin of the crystals, is practically impossible to determine. It has been shown that even under controlled laboratory conditions, and single contact experiments, this is very difficult, but in a crystallizer, this is simply not feasible. The second requirement, strain level, can at the current time be measured off-line, using a Laue diffraction technique.

The approach taken to modelling growth rate will consist of two parts. The first will concentrate on examining the effect of different process conditions on the growth behaviour of the viable secondary nuclei, by isolating large numbers of fine (<250 μm) crystals from the crystallizer into a separate batch crystallizer.

The second approach will examine the cause of reduced growth rate effects by analysing the strain present in crystals removed from the crystallizer and correlating the findings via a physical model to the observed growth rates.

1.6 Structure of the thesis

In **chapter 2**, a mass, energy and population balance are introduced which completely define all streams entering and leaving a DTB crystallizer. The mass and energy balances are solved to yield an expression for the supersaturation. A numerical solution method for the population balance is introduced.

A review of empirical growth, attrition and secondary nucleation models is given which have been used by other workers to model crystal kinetics. These models are used together with the population balance to simulate the crystallizer CSD behaviour. The results are compared to a set of measured data from a 970 L crystallizer and recommendations are made for the improvement of these models.

In **chapter 3**, the equipment used for experimentation and the manner of operation of the equipment are described. Differences between normal crystallizer design and the designs used here are highlighted as well as any important modifications to improve operation or data acquisition. The on- and off-line instruments used in the analyses of the CSD and fluid phases are also described and the problems encountered in sampling of the suspension.

In **chapter 4**, experiments to measure the growth rate of ammonium sulphate crystals are described. The measured data are modelled using both empirical SDG and GRD correlations. An attempt to confirm that the mechanism behind the observed lower growth rates of smaller crystals is caused by the presence of internal stress is made, by measuring the levels of stress in different crystal size fractions, using the synchrotron radiation source, located at Daresbury in England. There is also a discussion of the large body of evidence contained in the literature supporting a constant crystal growth (CCG) mechanism. Finally, a recommendation is made as to which model should be further used in the modelling procedure.

In **chapter 5**, a new model for secondary nucleation is presented and tested on a series of start-up and continuous data from a crystallizer. The effects of various operating conditions on the crystallizer product CSD are examined. The effect of other process inputs such as the effect of internal and classification is modelled and also the effect of an increased level of attrition on the CSD.

In **chapter 6**, the modelling procedure developed in the previous chapter is tested on the crystallization of ammonium sulphate on a smaller scale, to examine if the established procedure is also capable of extension to other scales. An assessment of its' ability to do so is made and special attention is paid to the changes in the kinetic parameters on changing the scale of operation.

Chapter 7 extends the model to the crystallization of other materials on the 22 L scale, namely, pentaerythritol and adipic acid which are substantially different to ammonium sulphate in terms of solubility, morphology and introduce some new operational difficulties.

Finally, **chapter 8** completes the thesis with a number of conclusions and suggestions for further work.

Chapter 2

Simulation framework and kinetic model review

Summary - In this chapter, the modelling framework which will be used throughout the thesis to model the kinetics of suspension crystallization is presented. A crystallizer system is defined and a number of simplifying assumptions are made to reduce the mass and energy balances to an equation for the supersaturation. The framework used is based on the population balance approach which is the standard tool used when relating the kinetics of growth, attrition and secondary nucleation and the operating conditions, to the CSD in a well mixed crystallizer. Simple kinetic equations commonly used in the literature for crystal growth, attrition and secondary nucleation are tested on a set of experimental data to evaluate their validity in simulating the observed oscillatory behaviour of the CSD. From the performance of the complete model, the shortcomings in the currently available kinetic relations are highlighted and recommendations are made for the improvement of the relations.

2.1 Introduction

Like most unit operations, a set of mass and energy balances can be defined for a crystallizer which relate material and system properties to the operating conditions. For a crystallizer, a population balance is also required which describes the movement of crystals from one size class to another due to kinetic processes such as crystal growth, attrition, agglomeration, birth and death.

A framework based on these balances is built and is tested on a set of experimental data from a 970 L crystallizer. The kinetics of growth, attrition and secondary nucleation are modelled using simple kinetic relations commonly used in literature.

In this chapter, it is not the intention to give an in-depth discussion of the merits of these kinetic relations on a mechanistic basis, but rather, to note their performance and refer to their qualitative properties as a basis for a description of more mechanistic models in the following chapters. A further purpose is to assess how complicated the overall model must be to accurately simulate the entire crystallization process.

2.2 General model for a crystallizer

2.2.1 System description

In this section, the mass, energy and population balances around a crystallizer are set-up and solved under a number of general assumptions relating to the operating conditions of a crystallizer. The initial forms of the balances are set-up in appendix A for the system defined below in figure 2.1, which represents a draft-tube-baffled crystallizer. The original derivation of this approach was developed by de Wolf (1990). The following general assumptions are made.

Crystallizer Assumptions

- 1 The crystallizer is ideally mixed and constant in time with respect to the liquid and solid phases.
- 2 Temperature variations during operation are minimal and have a negligible influence on either the mass in the system or the crystal size distribution :

$$\frac{dT(t)}{dt} = 0. \quad (2.1)$$

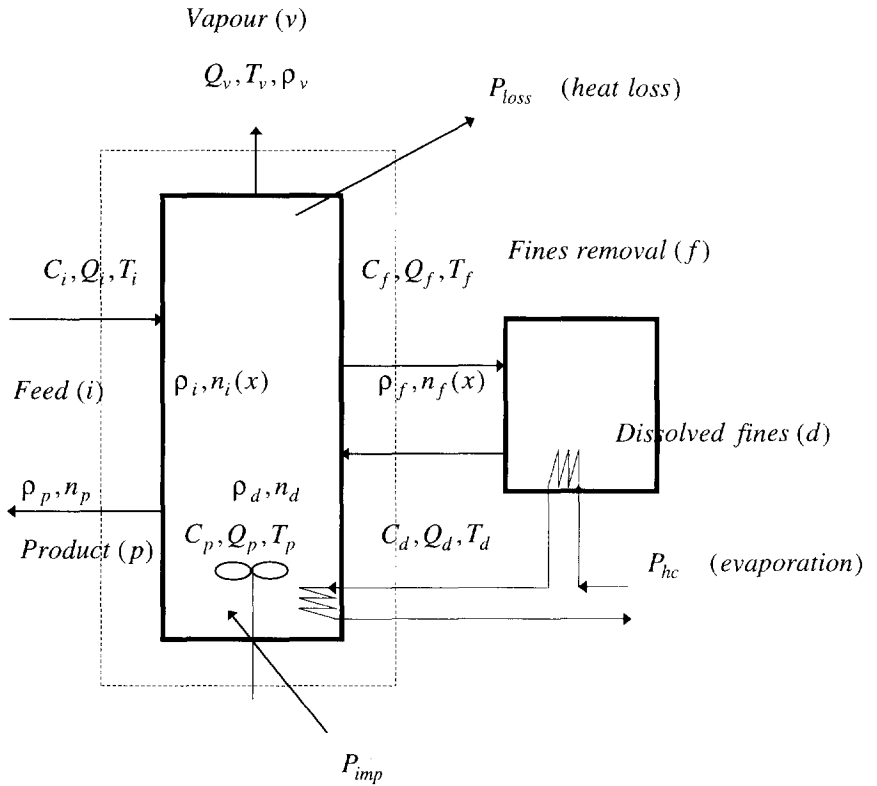


Figure 2.1 : Schematic representation of the crystallizer and fines vessel input and output streams.

- 3 A non-classified isokinetic product ($n(x, t)$) is removed from the crystallizer.
- 4 A crystal free feed enters the crystallizer at the same temperature as the contents of the crystallizer.
- 5 The fines loop is defined as a separate system. The fines are removed from the crystallizer according to a classification function ($h_f(x)$) where,

$$n_f(x, t) = h_f(x)n(x, t). \quad (2.2)$$

- 6 The fines are completely dissolved in the fines dissolution vessel and the solution is returned to the crystallizer.
- 7 The vapour flow is at the same temperature as the contents of the vessel and contains no solute or crystals.

- 8 The energy input via the mechanical action of the impeller to the system is equal to the energy loss due to the inefficiency of the insulation (the validity of this assumption was borne out by the results of later measurements).
- 9 The impeller speed is also constant in time.

All the in- and out-going streams are marked in figure 2.1. In total there are three inputs (feed (i), dissolved fines (d) and heat input (P_{hc})), and three output streams (product (p), fines stream (f) and the vapour flow (v)). The system boundary is given by the hatched line which includes the crystallizer and cuts the lines to and from the fines dissolution vessel as well as the heat input lines.

Four balances, together with kinetic relations for crystal growth, attrition and secondary nucleation in the population balance completely define the system. The balances are the population balance, the crystal mass balance, the salt in solution balance and a total mass balance around the crystallizer, which are listed in appendix A. After making a number of simplifications, the balances are reduced to a system of three equations with three unknowns, the feed flow (Q_i), the vapour flow (Q_v) and the growth rate (G). By rearrangement and substitution for the unknowns, three equations are derived which can be readily solved if the operating conditions, system constants such as the crystallizer volume and material constants are known (section 2.2.5).

2.2.2 Population balance

The population balance method of relating the product CSD to the crystallization kinetics was first derived by Randolph and Larson (1964) and Randolph and Larson (1988). The balance is given below, subject to several assumptions, i.e. a crystal free feed is entering the crystallizer and the crystallizer volume is constant. The balance contains a number of terms describing the movement of crystals into and out of a particular crystal size class, by a number of different processes, such as the effective crystal growth rate (G_{eff}); product (Q_p) and fines (Q_f) removal rates; crystal birth ($B(x)$) and death ($D(x)$) rate functions caused by secondary nucleation (only the birth function is used for this case), crystal breakage and agglomeration. The accumulation term ($\partial n / \partial t$) describes the cumulative effect of these processes on the CSD with time :

$$\frac{\partial n(x,t)V}{\partial t} + V \frac{\partial G_{eff}(x,t)n(x,t)}{\partial x} + Q_p n(x,t) + Q_f h_f(x)n(x,t) = B(x)V - D(x)V. \quad (2.3)$$

V represents the volume of the suspension in the crystallizer with dimensions of m^3 . The population density ($n(x,t)$) has units of ($\#/m^4s$) and if plotted as a cumulative function is defined by :

$$N_{cumulative}(x,t) = \int_{class=1}^x n(x,t)dx . \quad (2.4)$$

The effective growth rate of crystals is given by $G_{eff}(x,t)$ which contains a length dependency, for the case that size dependent growth due to attrition or kinetic growth is to be modelled.

The secondary nucleation rate function ($B(x)$) can be eliminated from equation (2.3) by defining it as a boundary condition (B_o). The relation between these two terms is

$$B_o = \int_{class=1}^x B(x)dx . \quad (2.5)$$

2.2.3 Kinetic Parameters

The rate of **secondary nucleation** when used as a boundary condition (B_o) is commonly estimated by using a power law correlation of the form :

$$B_o \propto \sigma^b N^h M_p^j , \quad (1.2)$$

(see also section 1.2).

Values for the model parameters for the specific case of ammonium sulphate crystallization were obtained from literature values for experiments carried out in continuous mode, with the driving force for growth provided either by cooling of the suspension (Chambliss, 1966, Larson and Mullin, 1973, Larson and Klekar, 1973, Bourne and Faubel, 1982), or evaporation (Daudey et al, 1990, Jager et al., 1990). The results for the exponents in the **secondary nucleation** correlation vary over a narrow range according to

$$B_o = k_n G^{1.03 \rightarrow 2.1} m_3^{1 \rightarrow 1.3} . \quad (2.6)$$

A variation of this equation was successfully used by Eek et al. (1995) to model the same crystallizer (970 L DTBE) under study in this work. In their equation, account is taken of the observation that only large particles are subjected to collisions which are capable of producing attrition particles. These attrition fragments can then subsequently act as secondary nuclei. For this reason, a minimum parent crystal size (X_{\min}) is chosen below which no secondary nuclei are generated :

$$B_o = k_n \int_{X_{\min}}^{X_{\max}} m_3 . \quad (2.7)$$

A precedence for this equation is found in the original formulation of Ottens et al. (1972) of a mechanistic model for secondary nucleation, who used a step target efficiency function instead of an underlimit for the integration, which is in effect the same as the approach used by Eek et al. (1995). Similar target efficiency functions can be identified from formulations of mechanistic models for secondary nucleation by other authors. In the work of Ploß et al. (1985), they defined a target efficiency function which was a modified Stokes number and in the work of Van der Heijden et al. (1994), they took the target efficiency as simply proportional to the crystal length times the impeller speed. These functions do not define a step function but a continuous function which express an increasing probability of attrition fragment production with increasing parent crystal size.

In reality, the moments evaluated in a secondary nucleation correlation (equation (2.6)) should not be the entire moments of the distribution but only the part of the distribution which is affected by a collision as defined by the target efficiency $\eta_t(x)$. Assuming that crystal/impeller interactions are dominant and that the impeller speed is constant, the nucleation rate can be evaluated according to (Ploß et al., 1985) :

$$B_o = \frac{\eta_{survival}}{\tau_{circ}} \int_0^x \eta_t(x) N_{attr}(x) n(x) dx . \quad (2.8)$$

τ_{cicr} is the recirculation time of the slurry around the draft-tube or the time it takes for a crystal to pass through the impeller area. Substitution for the number of attrition particles produced per collision term (N_{attr}) (Ottens et al, 1972) by the kinetic energy mv_m^2 ($m \propto x^3$), and $v_m \propto N$ yields:

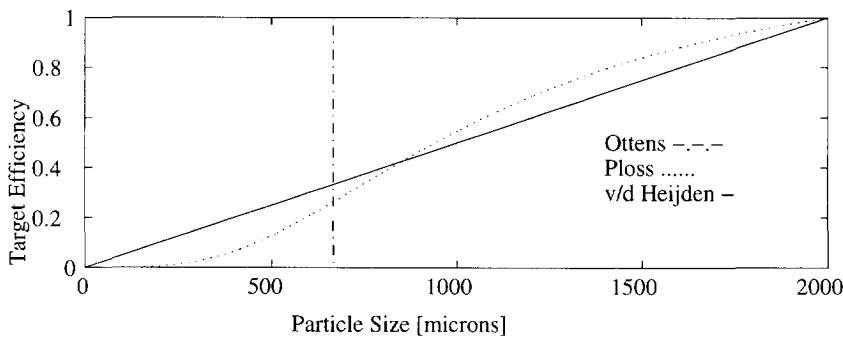


Figure 2.2 : Target functions as given by equations (2.10) (Ottens), (2.11) (Ploß) and (2.12) (v/d Heijden).

$$B_o \sim \frac{\eta_{survival} N^2 \rho_c \pi}{8\tau_{circ}} \int_0^x \eta_t(x) x^3 n(x) dx,$$

$$B_o = C \int_0^x \eta_t(x) x^3 n(x) dx, \quad (2.9)$$

where C is a constant for a system where the volume and impeller speeds are kept constant. $\eta_{survival}$ is the survival efficiency and expresses the probability that an attrition fragment survives and begins to grow. The target efficiency term can be substituted by equations (2.10) to (2.12), and are plotted in figure 2.2.

$$\begin{aligned} \eta_t(x) &= 0 \quad \forall x < x_{min} \\ \eta_t(x) &= 1 \quad \forall x > x_{min} \end{aligned} \quad \text{Ottens et al.} \quad (2.10)$$

$$\eta_t(x) = k1 \left(\frac{x^2}{k2 + x^2} \right)^{2.1} \quad \text{Ploß et al.} \quad (2.11)$$

$$\eta_t(x) = k3 x \quad \text{V/d Heijden et al.} \quad (2.12)$$

In most of the experiments reported in literature, the **growth rate** is calculated using mass and energy balance considerations from which the supersaturation is calculated and is then related to the growth rate by the correlation :

$$G_{kin} = k_{kin} \sigma^n. \quad (2.13)$$

For the case of ammonium sulphate crystallization, values for the exponent of the growth rate/ supersaturation correlation vary from 1 (Daudey, 1987) to 1.5 (Mullin et

al., 1970). The value of the kinetic growth constant was reported by Daudey as being approximately 5.10^{-6} m/s or,

$$G = 5.10^{-6} \cdot \sigma^{1 \rightarrow 1.5} \quad (2.14)$$

Three recent examples of equations used to describe **attrition** by Pohlisch et al. (1988), Jager et al. (1990) and Eek et al. (1995) are,

$$G_{attr}(x) = k_{attr} x^m, \quad (2.15)$$

$$\begin{aligned} G_{attr}(x) &= k_{attr} (x - x_{attr})^b & x > x_{attr}, \\ G_{attr}(x) &= 0 & x \leq x_{attr}, \end{aligned} \quad (2.16)$$

$$G_{attr}(x) = k_{attr} \frac{x^p (x_e^p + x_a^p)}{x_e^p (x^p + x_a^p)}. \quad (2.17)$$

All of these relations are functions of crystal size only and describe an increasing function with crystal size. The function used by Jager et al. is a discontinuous function based on the observation that (Bauer et al., 1974, Ramshaw, 1974, Daudey, 1987) secondary nuclei are produced in a crystallizer only if the size of the parent crystals exceeds a certain minimum size. Equation (2.17) (Eek et al., 1995) is an S-shaped curve with x_a as the point of inflection and x_e as the maximum simulated crystal size. The sharpness of the curve is dependent on the value of the exponent p .

Little information on the values of the parameters in these equations is available. For ammonium sulphate, Jager et al. and Eek et al. report the attrition rate as being of the same order as the growth rate for crystals above sizes of about $800 \mu\text{m}$.

The attrition rate is combined into the population balance by visualising it as a negative growth rate which is opposing the positive growth rate caused by diffusion or integration limited growth. This was first suggested by Juzaszek and Kawecki (1973) and later adopted by Jager et al. (1990). The result is that the net growth rate is a summation of two separate functions :

$$G_{eff}(\sigma, x) = G_{kin}(\sigma) - G_{attr}(x). \quad (2.18)$$

2.2.4 Class I and II systems

The growth rate is calculated by an alternative of two methods (appendix A), depending on the type of material which is being crystallized. Randolph and Larson (1988), classified materials into two types, calling them class I and II systems. A class I system, they defined as a system in which the supersaturation decay occurs very slowly during the start-up of the crystallizer or when a disturbance enters the system, while a class II system is a system in which the decay in supersaturation occurs much faster. The rate of supersaturation decay is set by the value of the kinetic growth constant (k_{kin}) in equation (2.13). A low value will give a slow decay rate of the supersaturation and a high value will have the opposite effect. In appendix A, the mass and energy balances are solved for both cases of class I and II systems. As the decay rate of the supersaturation for a class II system occurs quickly, the variation in fluid phase concentration will be only minimal. For this reason, the concentration variation expression with time is set equal to zero ($dC/dt = 0$). In the case of a class II system where the variation in liquid phase concentration is minimal, the growth rate is used in the secondary nucleation correlation (equation (2.6)) instead of the liquid phase concentration, which has been the general trend adopted for well soluble materials in the literature (Ploß et al., 1985, Kuijvenhoven, 1983).

For ammonium sulphate, a class I system will be used. This is done as according to Eek et al. (1995), materials which have kinetic growth coefficients greater than $2 \cdot 10^{-6}$ m/s show significant differences if modelled by using a class I instead of a class II system.

2.2.5 Mass and energy balances

The mass and energy balances for the system shown in figure 2.1 are described in full in appendix A. For a class I system, A22, A23 and A24 can be backsubstituted into A14 to eliminate the vapour flow rate (Q_v) and the feed flow rate (Q_i), to yield an expression for the change of the fluid phase concentration with time,

$$\frac{dC(t+1)}{dt} = \frac{1}{\varepsilon(t)V} \left[((Q_p + Q_f)k_1 + Q_d k_2 + P_{nc} k_3)C(t) + Q_d C_d k_4 - (\rho_c - C(t))3k_v V \int_0^\infty G_{kin} n x^2 dx \right]. \quad (2.19)$$

k_1 , k_2 , k_3 and k_4 remain constant as long as material properties such as the densities and heat capacities also remain constant. The kinetic growth rate can be calculated by converting the concentration to supersaturation ($\sigma(t) = (C(t) - C_{eq})/C_{eq}$) and substituting equation (2.19) into equation (2.13).

From the scheme in figure 2.3, it can be seen that besides the information needed for the mass and energy balances, only relations for crystal growth, attrition and nucleation are required to be able to carry out a simulation.

2.3 Simulations

2.3.1 Numerical methods and stability

The population balance equation (equation (2.3)) forms a hyperbolic partial differentiation equation for which there is no analytical solution. This necessitates the use of a numerical solution technique, to simulate the changing population numbers with time. A complete review of the numerical techniques used to solve the population balance in the past are given in de Wolf (1990), and Jager (1990). They identified four possible techniques from published literature which have commonly been used to solve the population balance equation. For the kinetic modelling of crystal populations, they recommended the use of the so-called "method of lines" technique whereby the second term in the population balance is transformed into a set of ordinary differential equations by substitution of the partial derivative with respect to length ($\partial/\partial x$) by a set of central difference schemes and a forward and back difference scheme at the left and right boundaries respectively. In his thesis, de Wolf (1990) considered two types of solution methods for the ODE's, the Adams-Moulton method and the Runge-Kutta method. He also considered 1st, 2nd and 4th order difference schemes for each of these methods. His findings showed that a second order Runge-Kutta gave the best results in terms of solution stability and required calculation times.

In applying the technique to equation (2.3), it must be first rearranged to :

$$\frac{\partial n}{\partial t} = -\frac{\partial}{\partial x}(Gn) - \left(\frac{Q_p}{V} + \frac{Q_f h_f}{V}\right)n + B. \quad (2.20)$$

With a central difference scheme, the first term on the right hand side is approximated by a set of central differences equal to the number of grid points chosen to discretise the length grid, and an equation at the left (2.21) and right (2.23) boundary (Vermuri and Karplus, 1981), denoted class k ,

$$\left(\frac{\partial}{\partial x}(Gn)\right)_{x=x_1} = \frac{1}{2\Delta x}(-3(Gn)_1 + 4(Gn)_2 - 1(Gn)_3) + 0(\Delta x^2) \quad (2.21)$$

$$\left(\frac{\partial}{\partial x}(Gn)\right)_{x=x_i} = \frac{1}{2\Delta x}(-(Gn)_{i-1} + (Gn)_{i+1}) + 0(\Delta x^2) \quad (2.22)$$

As can be seen from the mass and energy balances in appendix A, it is necessary to calculate the moments of the distributions after each time interval. The moments are given by the following formula for a given moment, j ,

$$m_j = \sum_{i=1}^k n(x, t) x^j dx \quad \left[\frac{m^{j+1}}{m^4} \right]. \quad (2.27)$$

The attrition moment ($m_2 G_{attr}$) and growth moment ($m_2 G_{kin}$) are given by :

$$m_2 G_{attr} = \sum_{i=1}^k G_{attr}(x) n(x, t) x^2 dx \quad \left[\frac{m^4}{m^4 s} \right], \quad (2.28)$$

$$m_2 G_{kin} = \sum_{i=1}^k G_{kin}(x) n(x, t) x^2 dx \quad \left[\frac{m^4}{m^4 s} \right]. \quad (2.29)$$

2.3.3 Steady-State solution of the population balance

In the case when the crystallizer is in a steady-state situation i.e. all the kinetic processes are in equilibrium and constant, and the operating conditions are fixed. The partial derivative of the population balance with respect to time can be set to zero. If agglomeration and breakage of crystals are not considered, equation (2.3) reduces to,

$$\frac{d(G_{eff}(x)n(x))}{dx} = B(x) - \frac{Q_p + Q_f h_f(x)}{V} n(x). \quad (2.30)$$

The birth rate function $B(x)$ ($\#/m^4 s$) represents the birth of secondary nuclei and can be used as a boundary condition B_o ($\#/m^3 s$) given by,

$$B_o = \left. \frac{dN_{cumulative}}{dt} \right|_{x \rightarrow 0} = \left[\left(\frac{dx}{dt} \right) \left(\frac{dN}{dx} \right) \right]_{x \rightarrow 0} = n_o G_o. \quad (2.31)$$

The equation is simplified and can be partially solved for the case of a length dependent growth rate ($G_{eff}(x)$) yielding the following :

$$n(x) = \frac{G_0 n_0}{G_{eff}(x)} \exp \left[\int_0^x \frac{Q_p + Q_f h_f(x)}{VG_{eff}(x)} dx \right]. \quad (2.32)$$

Depending on the complexity of the growth function used, an analytical solution for this equation may be possible. In most cases however, the combination of the SDG function and the fines classification function do not allow this.

Under the simplifying assumption that there is no fines removal and that the growth rate is independent of size, equation (2.32) reduces to the well known MSMR form :

$$n(x) = n_0 \exp \left[-\frac{xQ_p}{G_{eff}V} \right]. \quad (2.33)$$

2.3.4 Summary and interrelation of kinetics

In this section, an outline is given of the way in which the operating conditions, system physical properties and the kinetics of the system interact.

Given a set of process and crystallizer operating conditions and the conditions in the crystallizer at time 't', the mass and energy balances will predict the supersaturation increase or decrease in the fluid phase after a time increment 'dt'. Given a kinetic growth co-efficient, the growth rate can be calculated. The rate of attrition is, in this first approach, taken to be a function of the crystal length only as given for example by any one of the equations (2.15), (2.16) and (2.17). This attrition rate is combined with the kinetic growth rate to yield an effective growth rate. A correlation for the nucleation rate is chosen such as equation (2.6) or (2.9). So, having calculated these three rates, the population balance equation is employed to give the change in the population density when subjected to these kinetic processes. From the calculated CSD at time 't + dt', the moments are calculated and this information is passed back to the mass and energy balances as well as the secondary nucleation correlation to again calculate the rates of the kinetic processes for the following step.

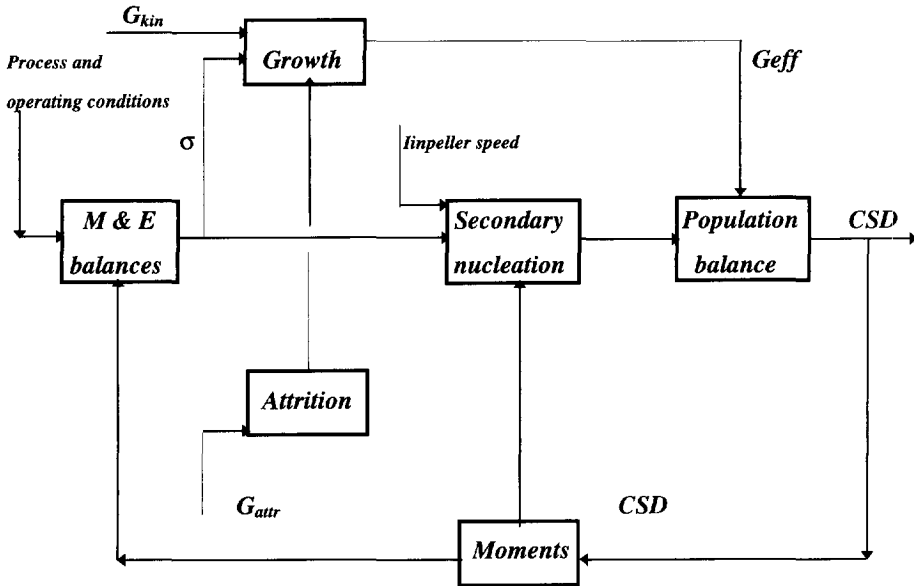


Figure 2.3 : Flow sheet of the interactions between crystallizer kinetics, operating conditions and the CSD

2.4 Simulations of the dynamic behaviour

In this section, the validity of the kinetic equations is tested and will be compared to a given set of experimental data from a 970 L crystallizer with ammonium sulphate as the model material for crystallization. The simulation framework and the kinetic models for growth, attrition and secondary nucleation will be tested to see whether they give a sufficiently accurate prediction of the dynamic and steady-state behaviours of the CSD.

The structure of the simulation program is the same as the flow scheme shown in figure 2.3. The simulations are carried out in such a way that the eventual steady-state median size and distribution spread are approximately the same as the value measured for the crystallizer CSD. The simulated dynamic behaviour of the CSD, and the eventual steady-state CSD can be compared with the measured values to identify where the deviations between measurement and simulation are the strongest. The kinetic equations used in the simulation compared to the quality of fit, should indicate how the kinetics effect the dynamic behaviour and steady-state situation of the CSD, and where improvements in the kinetic equations are necessary to improve the quality of fit.

2.4.1 Experiments

A series of start-up experiments in the 970 L crystallizer from a crystal free solution were carried out to examine the effect of the operating conditions on the dynamic and steady-state behaviour of the CSD. Three operating conditions were varied (the residence time, the heat input and the fines flow removal rate). For each experiment, the operating conditions were held constant. The results of the entire series of experiments is reported in Eek (1995). In this section, the results of one of these experiments was chosen for model framework validation. In chapter 3, the layout of the plant and the measurement systems used to obtain the results are explained. The model material used for crystallization was ammonium sulphate $(\text{NH}_4)_2\text{SO}_4$. The conditions for the experiment are given below in table 2.1. An on-line Malvern 2600C and a slurry dilution unit was used to measure the change in the CSD with time.

Table 2.1 : *Operating conditions and process constants for the sample experiment carried out in the 970 L crystallizer.*

<i>Property</i>	<i>Volume</i>	<i>Temperature</i>	<i>Residence Time</i>	<i>Heat Input</i>	<i>Fines Flow</i>	<i>Impeller Speed</i>
<i>Units</i>	L	°C	mins	kW/m^3	L/s	RPM
<i>Value</i>	970	50	75	120	1	315

From the scheme in figure 2.3, it can be seen that besides the information needed for the mass and energy balances, only relations for crystal growth, attrition and nucleation are required to be able to carry out a simulation.

2.4.2 Kinetic parameter values

Table 2.2 shows the combinations of kinetic equations and relations used in the simulations shown in figures 2.4, 2.5 and 2.6. Most of the values were taken from literature describing ammonium sulphate crystallization experiments, as mentioned in section 2.2.3.

Equation (2.13) combined with equation (2.16) were used to calculate the effective growth rate. For the secondary nucleation correlation, equations (2.6) and (2.9) were used. The growth rate in equation (2.6) was replaced by the supersaturation

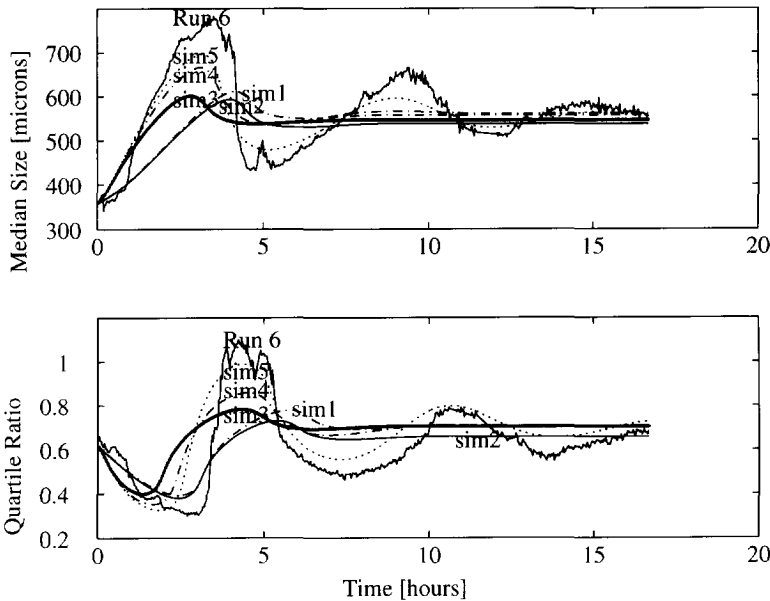


Figure 2.4 : Measured and simulated start-up trend in the 970 L crystallizer for the condition given in table 2.1. Kinetic relations used for the simulations are given in table 2.2. Upper diagram shows the simulated and measured median sizes and the lower plot shows the quartile ratio ($\log(x_{75}/x_{25})$)

which increases the range of the exponent to between 1 and 3 (see equation (2.14)). In the test simulations an average value of 2 was taken for this exponent.

The initial distribution ($n(x, t_0)$) was found to be best fitted with a combination of two log-normal distributions. The initial concentration of the fluid phase was measured to be equal to a relative supersaturation of 1.6 % in the liquid phase. The initial concentration of the solid phase was obtained by measuring the solids content of the suspension at the point of nucleation, and assuming that the increase in suspension density beyond this point was due to growth of the original primary nuclei distribution.

2.4.3 Simulation results

A number of simulations (sim1 to sim5) were carried out to test the model framework described above. The kinetic relations used in each simulation are listed in table 2.2. The simulation was programmed with the same set of operating conditions as was used for the experiment. The results of the simulations on the experimental data are given in figures 2.4 and 2.5. Figure 2.4 shows the median size trend and the

quartile ratio ($\log(x_{75}/x_{25})$) while figure 2.5 shows the third moment and the growth rate.

To obtain the proper phase of the median and quartile ratio in sim1 and sim2, the simulation boundary condition had to be altered to increase the initial population mass fourfold from a measured third moment value of 0.1 up to 0.4. By adhering to the measured boundary condition, the CSD median size and quartile ratio oscillate in anti-phase to the measured trend. Clearly, the fact that the boundary condition had to be changed to obtain the correct phase is already an indication that the power law model for secondary is not valid.

Compared to the reference simulation (sim1), the three simulations (sim3 to sim5) give a much better dynamic response. The model of Ottens (1972) (sim5) gives the best fit, being able to follow the median size trend up to the end of the simulated period. No value for the under limit in the integration function with respect to crystal size was reported by Ottens (1972). A value of 650 μm was chosen here as this gave a

Table 2.2 : Kinetic equations used in the simulations in figure 2.4 and 2.5. Growth rate is given by equation (2.13) and (2.19). The attrition function as defined by Jager (2.16) is used. The target efficiencies as shown in figure 2.2 are tested.

Tag	Sim1	Sim2	Sim3	Sim4	Sim5
Growth	(2.13)	(2.13)	(2.13)	(2.13)	(2.13)
	$k_{kin} = 5e^{-6} m \setminus s$	$k_{kin} = 5e^{-6} m \setminus s$	$k_{kin} = 5e^{-6} m \setminus s$	$k_{kin} = 5e^{-6} m \setminus s$	$k_{kin} = 5e^{-6} m \setminus s$
	$n = 1$	$n = 1$	$n = 1$	$n = 1$	$n = 1$
Attrition	-	Jager (2.16)	-	-	-
		$k_{attr} = 3e^{-8} m \setminus s$			
		$x_{attr} = 500 \mu\text{m}$			
		$b = 1$			
Target Efficiency η_t	-	-	Ploß (2.11)	v/d Heijden (2.12)	Ottens (2.10)
			$k1 = 1.23$	$k3 = 5000 m^{-1}$	$X_{min} = 650 \mu\text{m}$
			$k2 = 4e^{-9} m^2$		
Nucleation	(2.6)	(2.6)	(2.9)	(2.9)	(2.9)
	$\sim m3\sigma^2$	$\sim m3\sigma^2$	$\sim m3(\eta_t)$	$\sim m3(\eta_t)$	$\sim m3(\eta_t)$

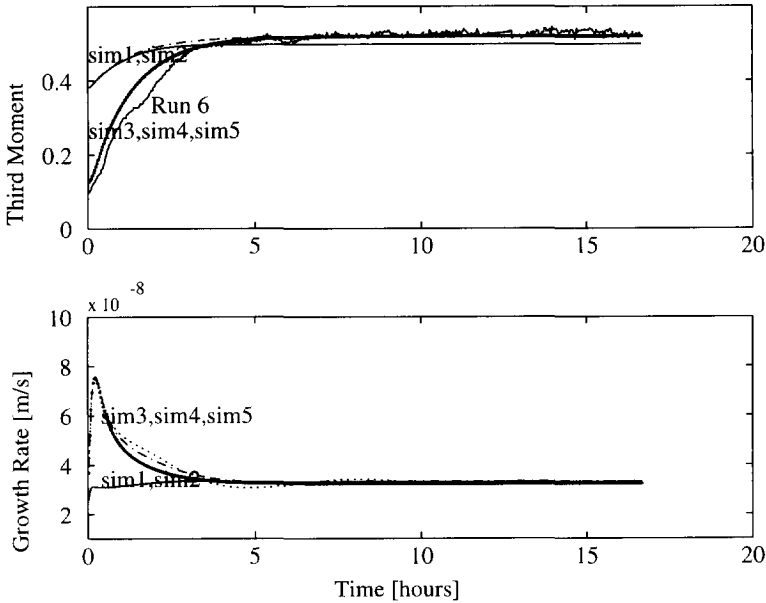


Figure 2.5 : Measured and simulated start-up response in the 970 L crystallizer in terms of the third moment (upper) and the growth rate (lower) for the experimental conditions in table 2.1.

good fit to the data and the nucleation constant is chosen so that the median size at steady-state corresponds to the measured value. The other two functions were a lot less flexible as the values of the exponents and the inflexion points were already fixed. By changing the exponent in equation (2.11), the same result can be achieved as to that of Ottens. Figure 2.5 shows that the third moment trend where the target efficiencies are used, are much more realistic when compared to the measured third moments, than the simulations for sim1. The significant difference between the two methods (sim1, 2 versus sim3 ,4 ,5) in estimating the nucleation rate is that in the reference experiment (sim1), the nucleation rate is correlated to the entire third moment of the CSD while for the experiments where a target efficiency is used, the nucleation rate is effectively correlated to only a part of the distribution, i.e. to the larger crystals.

2.4.4 Simulations of the steady State Distributions

Figure 2.6 shows a plot of a number of steady-state distributions plotted as the log of the number density versus crystal length. Also included is the experimentally

measured steady-state distribution. The increasing curvature in the sub 200 μm size range is caused by the removal of fines crystals, and also by a decreasing effective growth rate of the smaller crystals. A decreasing growth rate towards the smaller sizes will cause the crystals to have a longer residence time in the smaller size classes, thus leading to an accumulation of crystals in these classes. The deviation between simulated and measured CSD's in this range occurs, as no account is taken of the possible changing growth behaviours.

In the larger size classes, there is a difference in the behaviours of the five simulations. Simulation sim2 shows a downward curvature caused by the inclusion of an attrition function while the other simulations follow a straight line in this size range.

2.5 Discussion

From the examples given in the previous section, it is clear that 'traditional' secondary nucleation functions are not capable of describing the dynamic behaviour of the CSD in a semi-industrial crystallizer. The models are able to predict a nucleation rate at steady-state, but a closer look at the size distribution reveals that there are deviations between measured and simulated data in the small and large crystal size classes. The nucleation rates predicted by the nucleation models are actually effective nucleation rates and without the inclusion of a model to describe the upward curvature in the small particle size ranges, it is not possible to calculate the actual nucleation rate. The deviation in the large particle size ranges can be modelled by including an attrition function which models a decreasing growth rate of the large crystals. This in combination with the positive kinetic growth rate, yields an effective growth rate of the crystals. This leads to a better prediction of the shape of the steady-state distribution (sim5), but it doesn't lead to any improvement in the simulation of the dynamic response. The only effect it does have on the dynamic behaviour is to create an offset in the simulation with respect to the median size by reducing the numbers of large crystals in the crystallizer. This can be seen in figure 2.4 when the CSD has reached a steady-state. However, if so wished, this can be corrected for by decreasing the constant in the nucleation rate which will return the median size back to the measured value.

In summarising the nucleation models presented in the literature, some authors have had a tendency to oversimplify the approaches taken in order to produce a simple correlation for the secondary nucleation rate and also to present the models in a way which enabled comparison with the empirically determined power law dependencies

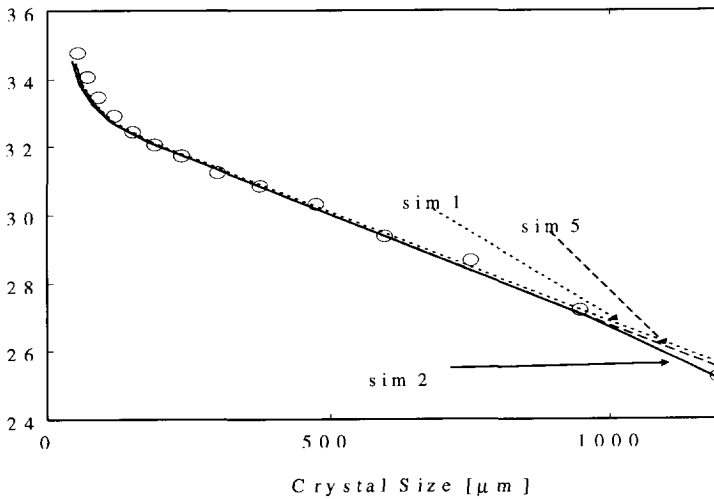


Figure 2.6 : Steady-state plots using the relations in table 2.2. Plot shows the effect of including an attrition rate function into the calculation of an effective growth rate by the presence of a downward curvature in the large particle size ranges.

and exponents. Very often, in doing so, some of the more important conceptual aspects of the models have been neglected. This point is demonstrated in figure 2.2 where target efficiencies defined by the different workers are extracted from their modelling procedures and used to model secondary nucleation for the case of a crystal/impeller collision dominated systems. The notion of these target efficiencies is related to the fact that only crystals above a certain size will contribute to the nucleation rate. By using the step function defined by Ottens et al. (1972), a very accurate description of the dynamic trend of the CSD is obtained. It suffers from the same failing at steady-state as the power law secondary nucleation model, in that it predicts an effective and not an actual nucleation rate.

Inclusion of an attrition function will further improve the steady-state simulation in the large crystal size ranges.

If the requirement of the model is only to predict the median size and spread of the distribution at steady-state, it is sufficient to use only such secondary nucleation correlations. The big advantage of using such a model, is that it is only necessary to estimate two parameters, the nucleation constant and the length parameter which defines the under limit for which the third moment is calculated (k_n and X_{\min} in equation (2.7)), to simulate the product CSD position and spread. This model can even

be improved by using the physical model for the target efficiency of Ploß et al. (1985), as an empirical correlation, and allowing the two parameters to be optimised with the experimental data.

From the results presented here, it seems that crystal/impeller collisions are dominant in determining the secondary nucleation rate in the crystallizer. This is indicated by the success of using the target efficiency functions instead of the approximations given by equation (1.2).

2.6 Conclusions

Current secondary nucleation models of the type in equation (1.2), whether derived via a consideration of the mechanics of secondary nucleation, or are based on the results of experimental measurements as a power law relation, are able to predict the steady-state position of the CSD in a crystallizer, provided that the correct proportionality constant is chosen. They are not able to predict the dynamic behaviour of the CSD during the start-up phase of a crystallizer, and will also not be able to predict the response of the system to a disturbance in one of the operating conditions at steady-state. The fit obtained by correlating the nucleation rate to a part of the third moment of the CSD, as defined by the target efficiencies, hints at the importance of considering only the part of the CSD from which attrition particles are produced, in evaluating the secondary nucleation rate. This notion will be further built upon in chapter 5.

To simulate the correct form of the steady-state CSD, account must be taken of the process of attrition of large crystals in the crystallizer, to correctly predict the deviation from the ideal MSMR situation in the large particle size ranges. Account must also be taken of processes occurring the small particle size ranges which may cause an exaggerated upward curvature in this area. This effect is reported in the literature as being caused by a growth rate dispersion (GRD) effect or a size dependent growth (SDG) effect.

Correct modelling of these processes will also lead to a better prediction of the actual nucleation rate as opposed to an effective, which is what is modelled by the current secondary nucleation relations. Inclusion of a GRD/SDG function for example, models the slow growth of secondary nuclei, and raises the numbers of nuclei in the small crystal size range. The phenomena of GRD/SDG will be further examined in chapter 4, to try and estimate a model for the upward curvature in the small size ranges and to get some insight into the causes of GRD/SDG.

The framework demonstrated to account for process operating conditions, material properties, and for the inclusion of kinetic models has proven to be very

effective as a framework for kinetic models describing crystal growth, attrition and secondary nucleation.

Chapter 3

Equipment/ Sensing devices/ Model materials

Summary - In this chapter the tools used to obtain experimental results are described. Three draft tube baffled (DTB) crystallizers having volumes of 970, 22 and a 2 L growth cell were used to crystallize various materials. The larger two crystallizers were operated in evaporative mode while the 2 L cell was operated in a batch cooling mode. An on-line Malvern 2600 C forward light scattering device was used to measure the CSD in the crystallizers and an on-line CCD camera was used for particle shape and solids concentration monitoring. Three materials were crystallized, ammonium sulphate (970, 22 and 2 L), pentaerythritol (22 L) and adipic acid (22 L).

3.1 Introduction

In this chapter, three topics are covered. The first topic concerns the experimental equipment used, the second concerns the sensing instruments employed to measure the CSD and the product density. Also the instruments used for off-line studies are described e.g. the scanning electron and optical microscopes. The processing of the sensing instruments results, from the raw data stage to its' final useable form is described. Finally, a summary of the model materials used in the experiments is given.

3.2 Crystallizers

Three crystallizers were used to obtain the results presented in this thesis. Two of the crystallizers (970 L and 22 L Draft-Tube-Baffled Crystallizers) were inherited from the previous phase of the project (UNIAK I), and a much smaller, 2 L crystallizer was constructed, to study the outgrowth of crystal samples isolated from the larger crystallizers. The core design and basic construction of the two larger crystallizers have remained the same since they were originally commissioned, but a lot of the ancillary equipment has been modernised to improve the operation, to facilitate on-line measurement systems and to improve the quality of the data.

Together with a forced circulation and fluidised bed crystallizer, the DTB crystallizer is one of the most commonly used types of crystallizers in industry. The types of materials crystallized by all three is similar, being mostly well soluble salts such as NaCl, KCl and $(\text{NH}_4)_2\text{SO}_4$. As the objective of the UNIAK II project was the control of crystallizers and not a study into crystallizer hydrodynamics, a crystallizer was required which came as close as possible to the MSMPR ideal with respect to the liquid and solid phases. The DTB crystallizers were used as they satisfied these criteria.

The availability of a second smaller scale (22 L) was useful as the scale up factor between both crystallizers resembled the difference in scale between the large 970 L crystallizer and an industrial crystallizer. Normal industrial crystallizer sizes can vary between a few hundred litres up to 100 m^3 . The large crystallizer generates enough crystals to allow a fines and product classification system to be implemented.

The design of the crystallizers was originally done so as to reduce the operator demand to a minimum. This meant keeping the number of moving parts, such as impellers and pumps as low as possible, to reduce the areas where problems could arise. The number of operational degrees of freedom was made as high as possible.

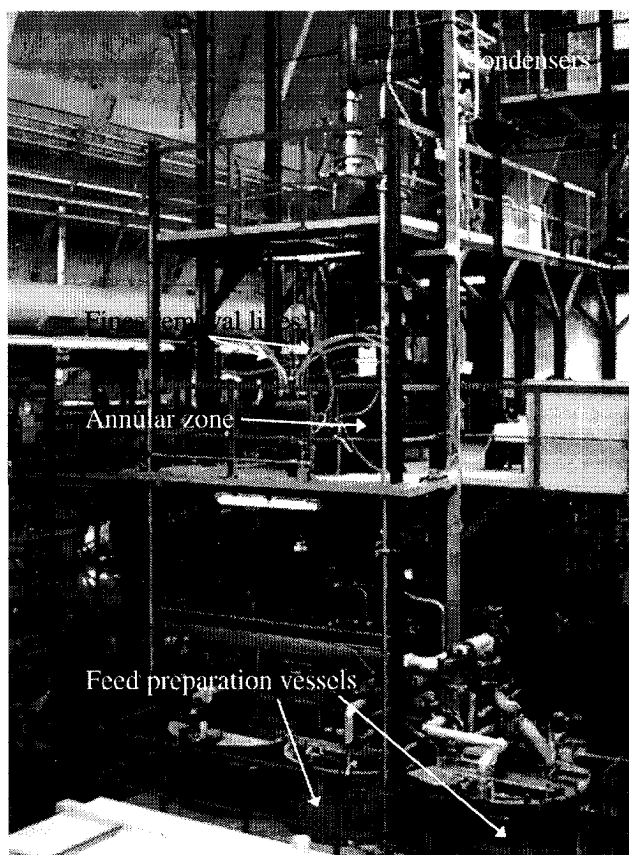


Figure 3.1 : 970 L Draft-tube baffled crystallizer located at the Laboratory for process equipment (TU Delft)

Three operational conditions can be varied, those being, residence time (product removal rate), power input (for evaporation), and fines removal rate.

3.3 Crystallizer descriptions

3.3.1 970 L Crystallizer

Figure 3.1 shows a photograph of the 970 L crystallizer and figure 3.2 shows a simplified process scheme of the 970 L crystallizer.

The plant is made up of two separate areas, the first is the crystallizer itself and the second is the area containing the ancillary vessels for feed preparation, solution storage and the hot water vessels.

Construction

A primary feed and product dissolution vessel, is split into two areas, an inner zone inside a conical surround and an outer zone where the product stream is returned from the crystallizer for dissolution. From the conical inner zone, a crystal free liquor leaves via an overflow line into a secondary feed vessel. From this vessel, the feed enters the crystallizer. A separate feed is also removed from the secondary feed vessel to dilute the product stream to enable a measurement to be done with the CSD measuring device. Other vessels in this area include a buffer tank for storage of the crystallizer contents between experiments. A hot water vessel is held at 95°C, which is circulated through the crystallizer internal heat exchanger, to effect evaporation of the solution at 50°C at a pressure of 80 mbars.

The crystallizer itself, is constructed from stainless steel. The crystallizer is equipped with a draft-tube, constructed for almost half its' length as a shell and tube heat exchanger. The heat exchanger is used to evaporate the solvent, (water in this case) with hot water held at 95°C providing the driving force. The vapour is condensed in two condensers located at the top of the crystallizer, and the condensate can be pumped back to the primary feed vessel to aid the dissolution of product crystals. The suspension in the crystallizer is pumped around the draft-tube, through the tubes of the heat exchanger by a rubber coated 485 mm marine impeller. Around the central part of the crystallizer is an annular zone. A fines pump located on the ground floor is used to remove a stream of particles from this zone. Crystals are classified according to their size and physical properties and the flow rate of the fines removal stream. The fine crystals are subsequently dissolved in an external plate heat exchanger, by heating the stream from 50°C, which is the crystallizer operating temperature, up to 60°C, after which it is returned to the crystallizer. Product is removed at the base of the outside of the draft-tube and depending on whether the crystallizer is operating in batch or continuous mode, it is either returned to the crystallizer after measurement of the CSD or pumped to the primary feed vessel. A side stream is removed from the product line and the slurry sample is mixed with crystal free solution to enable a CSD measurement to be made. An Endress-Hausen M-point density meter is also located in the product line which continuously measures the density of the entire suspension.

Process Control

An IBM/Compaq computer using DMACS software is used to control the crystallizer. There are five main control loops. The first is aimed at regulating the residence time in the crystallizer. This is done by keeping the product flow constant.

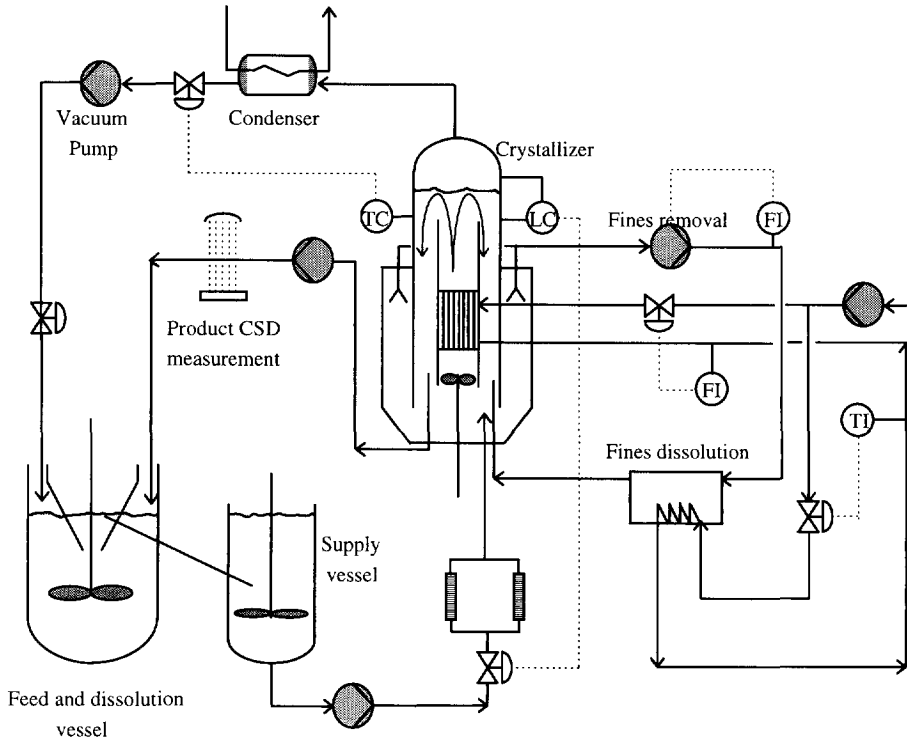


Figure 3.2 : Schematic drawing of the 970 L crystallizer and ancillary equipment

The second is to hold the level in the crystallizer constant. This is done using an automatic valve situated in the feed line. The third is to hold the temperature in the crystallizer constant. This is achieved by regulating the pressure in the crystallizer via two vapour valves situated just before the condensers. If the temperature is too high, the valves open and if it is too low, the valves will close thus allowing less vapour to escape. The fourth is used to maintain a constant power input to the crystallizer. A valve in the hot water line to the internal heat exchanger regulates the amount of hot water passing through the heat exchanger and by controlling the position of this valve, the power input can be held constant. The fifth and last control loop controls the speed of the fines pump according to an operator value for the setpoint.

3.3.2 22 L Crystallizer

The 22 L crystallizer is similar in many respects to the 970 L crystallizers. It contains many of the same elements and control loops, but because the scale is much

smaller, it has been possible to use a few simplifications. Figure 3.3 gives a schematic diagram of the most important elements of the crystallizer and figure 3.4 shows a photograph of the 22 L crystallizer.

Once again, the process is split up into two separate areas, a feed preparation/product dissolution and classification area and the crystallizer itself.

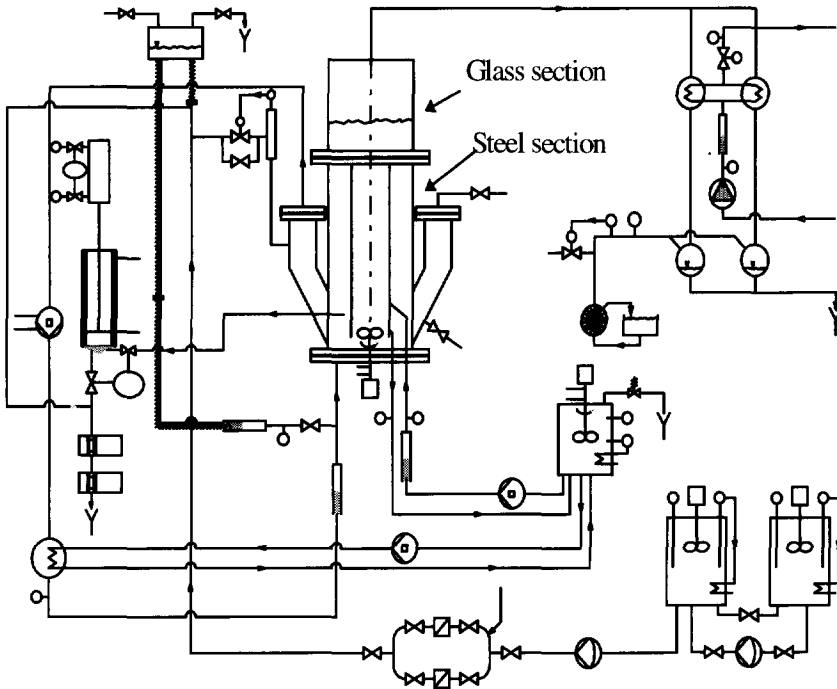


Figure 3.3 : Shows schematic diagram of the most important elements of the 22 L crystallizer and the feed vessels. Measuring instruments are situated in the product stream below the product cylinder

Construction

The crystallizer has a nominal volume of 22 L. The upper section is made of glass and the lower section is constructed of stainless steel. All feed, product, hot water and fines recirculation lines leave and enter the lower section of the crystallizer, so for this reason, it was constructed of the more flexible steel which could be easily manipulated if another line had to be constructed. The upper half was made of glass primarily for observation purposes of the suspension and boiling zone. A hollow draft-tube, around which the suspension is pumped also acts as a heat exchanger through

which hot water is pumped providing heat of evaporation for the water. The slurry is pumped upwards through the draft tube to the boiling zone. Evaporated water is condensed by two glass coils through which water is circulating. The condensate is collected in two large collection bulbs having a combined volume of 50 L. The crystallizer is also equipped with a fines removal system from which fine particles can be removed, redissolved and returned to the crystallizer as saturated feed. A variable speed marine type propeller is used to mix the suspension.

Process line

This crystallizer was first designed in 1982 by P.J. Daudey. It has been revised several times since then during UNIAK I and again during UNIAK II. The major alterations during this time have been to install fines removal arms on either side of the crystallizer and also to install a closed circuit saturated solution line which has three functions, those being, (a), provide feed to the crystallizer, (b) act as a pick-up liquid for the product which is removed with a cylinder from the crystallizer at regular time intervals, and (c) dilute the product stream to the proper

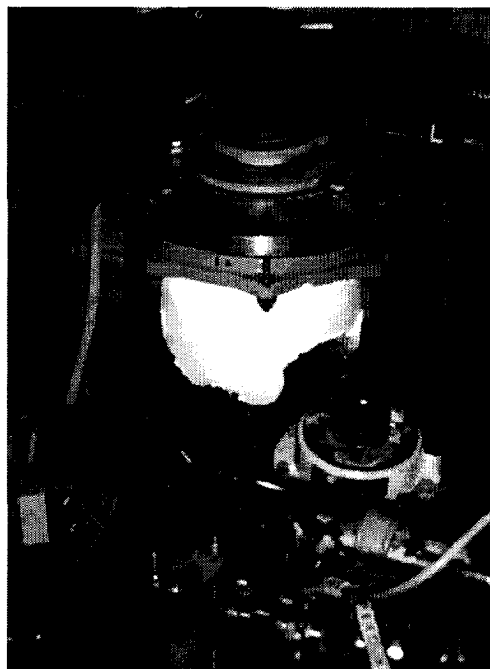


Figure 3.4 : *Top glass section of the 22 L crystallizer*

concentration to enable a measurement of the CSD to be made in the Malvern. The product is transported back to the product dissolution vessel where the crystals remain while saturated liquid flows into a separate feed vessel. The feed is held at the same constant temperature as the operating temperature of the crystallizer and the level is held constant by adding water.

3.3.3 2L Growth Cell

The third crystallizer used for experimentation in this work, is a 2 L plastic growth cell. It was built to study the growth behaviour of small sub 300 μm crystals

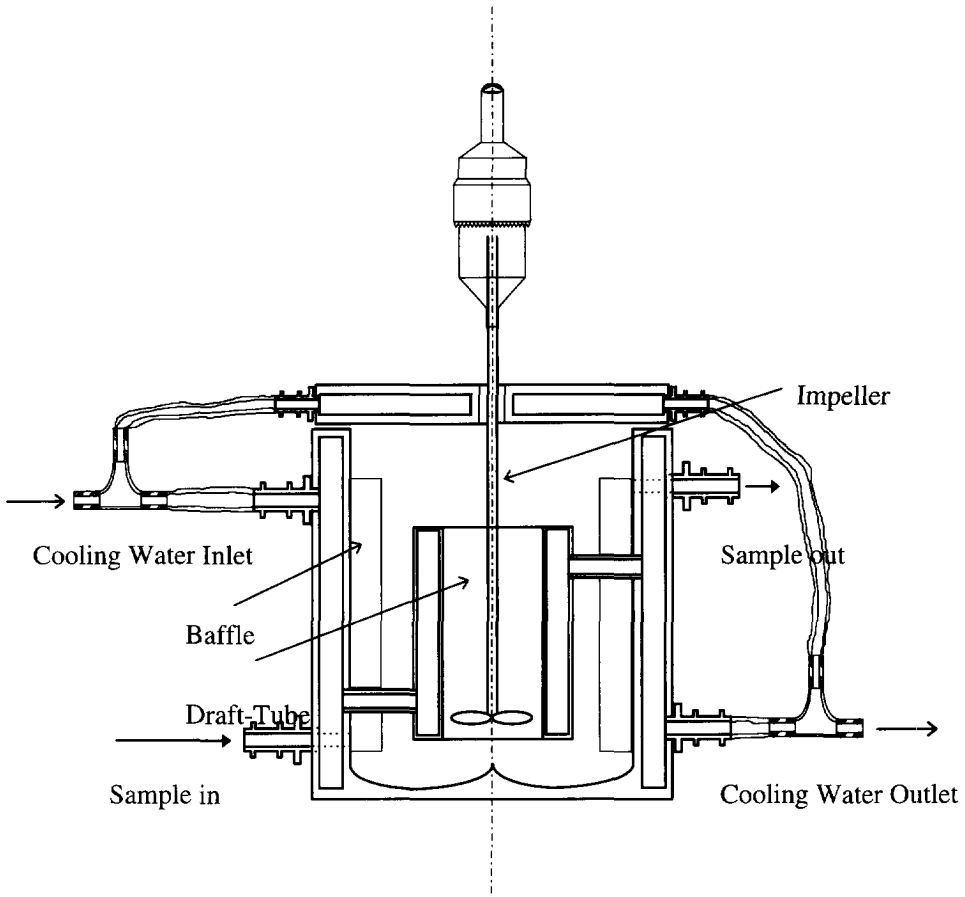


Figure 3.5 : *Diagram of the 2 L growth cell*

isolated from the fines line of either the 970 or 22 L crystallizers. The growth cell was built similar to the large crystallizers as a draft-tube-baffled crystallizer with every surface which comes into contact with the crystal suspension acting as a cooling or heating surface depending on whether the crystals were to be grown or dissolved respectively. Figure 3.5 gives a detail of the growth cell design. The cell is equipped with a plastic marine type impeller and it pumps the suspension around the draft-tube to maintain the crystals in suspension. A Malvern was placed next to the cell and from two extra inlets, it was possible to recirculate a continuous sample from the cell

through the Malvern. A typical result of these measurements is shown in section 3.4.1.1. The rate at which the cell was cooled down was controlled by a Lauda PKS thermostat, which was served from a PC where a pre-determined cooling profile could be programmed.

3.3.5 Product removal

Product is removed continuously from the 970 L crystallizer at a rate which yields a required residence time of the slurry in the crystallizer. Crystals can be removed as either a classified or an unclassified product. Under normal operating conditions, an unclassified product is removed, but it is also possible to remove a classified product using a mechanical sieve or a hydrocyclone. After removal of the product, it is sent back to the feed and dissolution vessel to dissolve with the condensed water returning from the condensers to make fresh feed for the crystallizer. In the product stream, a sample is removed at regular intervals using a variable speed pump. The sample is diluted with saturated solution and sent through a Malvern forward light scattering instrument to measure the CSD. Provided that the sample is removed isokinetically from the crystallizer, the measurement will give an accurate indication of the CSD present in the crystallizer at that time. Typical residence times in the crystallizer range from 80 to 150 minutes which corresponds to a product removal rate of 0.167 to 0.086 L/s. Also located in the product line is an Endress-Hausen density meter which measures the slurry density with a frequency of 1 measurement per 4 seconds.

The product removal system for the 22 L crystallizer is different to that of the 970 L crystallizer. This arises as to operate at the same residence times as the large crystallizer (60 to 150 minutes), the product flow rate would have to be as low as 5 ml/s. Pumping such low amounts of slurry from the crystallizer presents a number of difficulties. In the first place, very few pumps exist which can deliver this kind of flow rate for a suspension of crystals, and still guarantee that the sample is isokinetically removed. Secondly, the pressure at the base of the 22 L crystallizer is only 150 mbars so the pump would also have to provide an adequate seal between the surroundings and the crystallizer. Lastly, such low sample volumes also present problems for the CSD measurement devices, as in the current set-up, samples of this size cannot be analysed accurately on-line after the sample has been diluted. Continuous sample volumes more in the order of 200 to 400 mls are necessary to sustain accurate measurement of the CSD.

For these reasons, it was decided to use a cylinder to remove product at intermittent periods from the crystallizer, and to dilute this product with a saturated

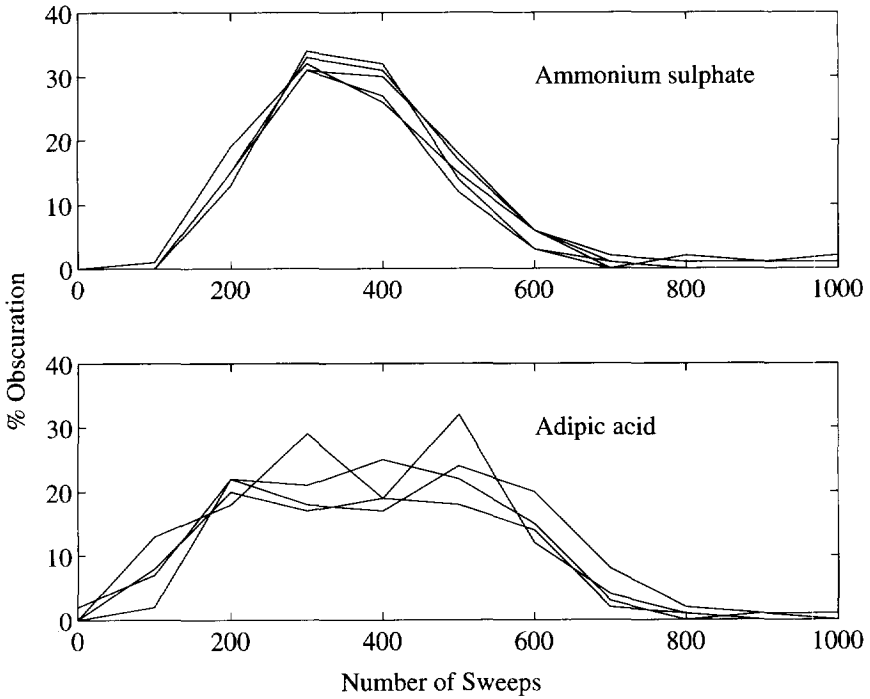


Figure 3.6 : *Obscuration trend variation in time as a function of sweep number for ammonium sulphate (upper) and adipic acid (lower).*

solution and pass the diluted product through two sensing devices located in the same line. The cylinder chosen has a volume of 300 mls and operates hydraulically. The residence time of the product is regulated by changing the frequency with which a sample is removed from the crystallizer, which is typically at time intervals of between 1.5 to 3 minutes. Control of the air operated valves at the head and base of the cylinder unit determine when a sample is taken from the crystallizer, and the speed with which a sample is removed from the crystallizer or injected into the dilution liquid line, can be changed by varying the air pressure applied to the cylinder base and head. An increase in pressure to the base of the cylinder for example will cause the cylinder to draw the sample more quickly from the crystallizer, while an increase of air pressure to the cylinder head, will increase the speed with which the sample is injected into the dilution liquid line. Regulation of these speeds is necessary for a number of reasons. Firstly, the properties of the materials, typically those materials with a high solubility in the solvent, will develop a large suspension density, and must therefore be injected slowly (300 mls in 10 seconds) into the dilution liquid line to avoid problems of multiple scattering in the Malvern. Higher crystal densities will require faster removal

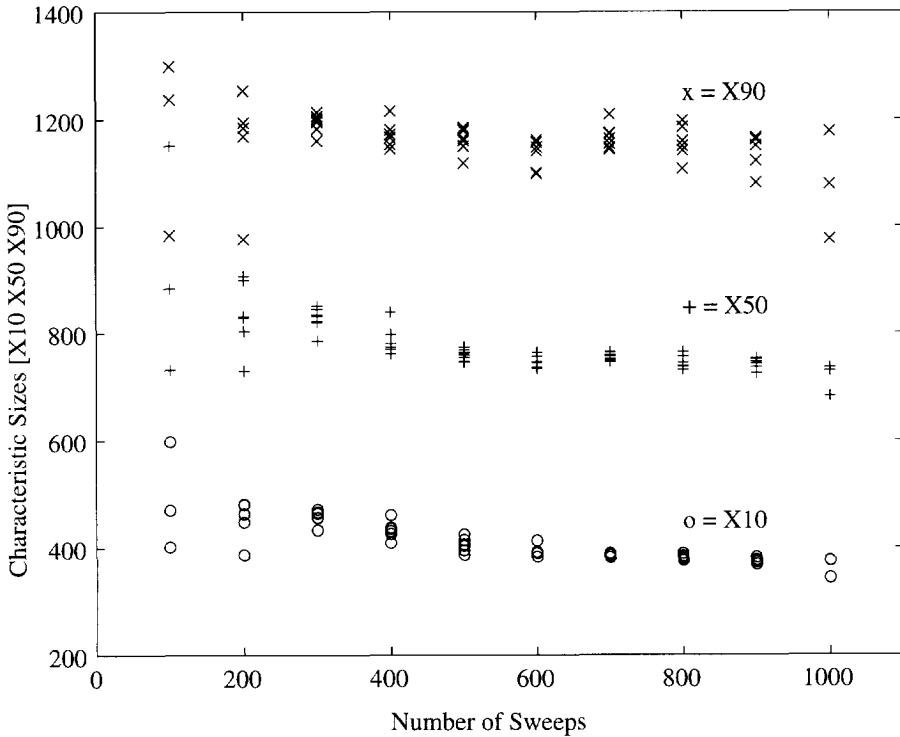


Figure 3.7 : *Effect of using a limited number of sweeps to evaluate the CSD*

speeds from the crystallizer to ensure that the largest crystals passing the exit tube are removed. Ideally, the speeds of sample withdrawal and injection into the dilution liquid line must be kept as high as possible as a too long residence time of the sample in the cylinder, and the crystals tend to classify, the larger crystals sinking to the bottom of the chamber. To remedy this, a small injection of saturated liquid is sucked into the cylinder before its' contents are injected into the dilution liquid line, to make sure that the sample is homogeneously mixed. A number of measurements with and without the injection of this liquid, showed that the problem was partially corrected but not wholly under control. The current situation is illustrated in figure 3.6 where the obscuration signal is plotted as a function of the number of sweeps taken of the sample by the Malvern (CSD measurement) for five samples at steady-state for ammonium sulphate and adipic acid. It is seen that as the sample passes through the Malvern that the obscuration first increases to a maximum value of about 30 % and then reduces to 0 %. This comes due to the classification effect in the cylinder causing the concentration of particles to vary over the time that the sweeps are measured when the

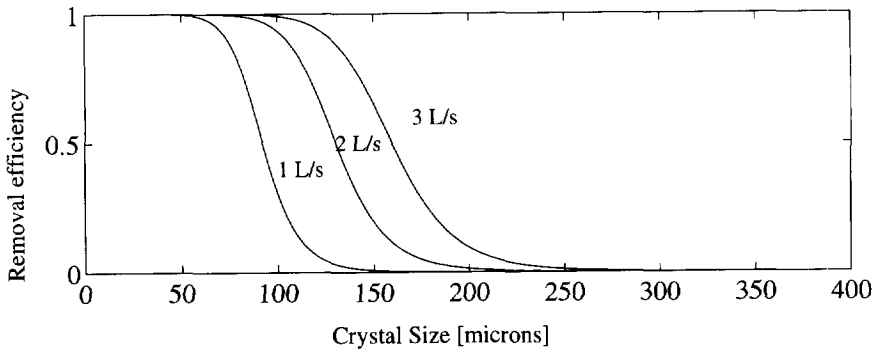


Figure 3.8 : *Fines flow rate as a function of crystal size for three fines flow rates for ammonium sulphate in the 970 L crystallizer.*

sample is injected into the dilution liquid line. To examine the effect of evaluating the CSD over a varying number of sweeps, three of these curves were taken, and the corresponding characteristic sizes evaluated by the deconvolution software and they were plotted as a function of the number of sweeps (figure 3.7) for ammonium sulphate. The figure shows that at a low number of sweeps (< 300 sweeps), the scatter in the characteristic sizes is much greater than at higher sweep numbers (< 800 sweeps). With greater than 800 sweeps, the spread in the characteristic sizes increases again. It can also be seen that there is a general decrease in the median and other characteristic sizes, with an increasing number of sweeps. This is again due to a classification effect whereby more of the large crystals are measured over the first 300 sweeps thus giving a biased estimation of the CSD towards the larger sizes. In general, it can be said that by using between 500 and 800 sweeps in a measurement, a good estimate of the CSD is made and that the noise in the results will be at a minimum.

A summary of continuous product dilution methods is given in the thesis of H. Gerla (1995).

3.3.6 Fines removal

The removal of fine particles from a crystallizer has been shown to be an effective process input in controlling the amount of crystals which grow into the CSD in crystallizers (Eek, 1995). Fines removal operates by taking advantage of the classifying behaviour of a CSD in a vertical classifying zone, in which the fluid velocity can be regulated by the withdrawal rate of the suspension. To effect fines removal from the 970 L crystallizer, an annular zone was built around the crystallizer which was connected to the crystallizer at the base of the draft-tube as is shown in

figure 3.2. A pump situated on the ground floor of the plant, removes a fines flow at a rate which is set by the operator at the operating console. After removal from the crystallizer, the fines are dissolved and pumped back to the crystallizer at a temperature of 60°C.

The classifying behaviour of the annular zone was modelled (Prins, 1992) by placing a Malvern forward light scattering instrument in the fines line and comparing the CSD in the fines line with that in the product line. By varying the flow rate through the fines line, a classification function was determined as a function of this flow rate (Q_f). The function takes the following form :

$$h_f = \frac{1}{1 + (x/x_c)^{p1}} \quad (3.1)$$

$$x_c \propto \sqrt{p2 * Q_f} . \quad (3.2)$$

Figure 3.8 shows the form this function takes as a function of crystal length for three values of the fines flow rate.

3.4 Sensing equipment

3.4.1 Light scattering devices

3.4.1.1 Forward light scattering

The main instrument used to gain results in this work is a combination of a commercially available forward light scattering instrument (a Malvern 2600C) and software (ROMA) which was developed within the UNIAK I group by A. Boxman (1992). The Malvern is located next to the product line from which samples are intermittently withdrawn and mixed with a dilution liquid to enable a measurement of the CSD to be made. A re-enforced

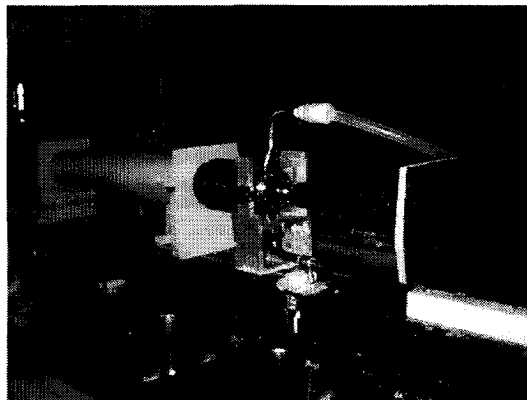


Figure 3.9 : The Malvern FLS instrument located at its' on-line location

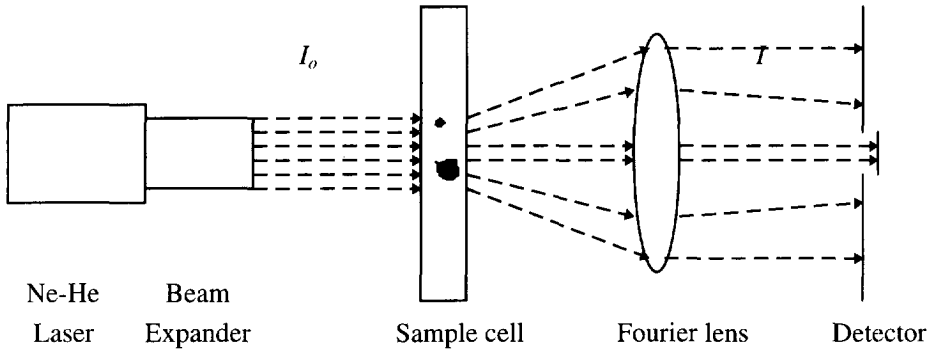


Figure 3.10 : Principle of forward light scattering

anti-reflection coated optical glass measurement cell is located in the Malvern through which the diluted slurry passes and a Ne-He laser beam which is directed onto the cell is diffracted. Figure 3.9 shows a photograph of the Malvern at its' on-line location. The diffraction pattern of the laser beam falls onto a number of narrowly spaced, semi-circular photo diodes situated in the focal plane of the measurement cell. The energy level detected on each diode, is at low concentrations linearly proportional to the number of crystals of a particular size which diffract the laser beam at that angular range. A schematic diagram of the set-up is shown in figure 3.10. Each crystal diffracts the light according to a number of its' properties, namely its' size, shape and orientation within the laser beam to give a characteristic signal on the sensor. Undiffracted light will be absorbed by a detector located behind the array sensor. In general, the smaller the crystal, the wider will be the angle of scattering. Thus, going from the inner rings to the outer rings, the sensitivity for small crystals will increase. This is demonstrated in figure 3.11 which shows the signal recorded for the outgrowth of a group of ammonium sulphate fines isolated from the 970 L crystallizer into the 2 L growth cell as measured by the Malvern. The diffraction pattern in the upper plot shows that as the initial distribution grows out, the signal moves from the outer rings to the inner rings indicating that the crystals are becoming larger. The increase in the surface area of crystals in the growth cell is represented by the increase in the obscuration signal with time which is defined by,

$$obsc(t) = 1 - \frac{I(t)}{I_o}, \quad (3.3)$$

I_o = intensity of the incident beam

$I(t)$ = intensity of refracted beam.

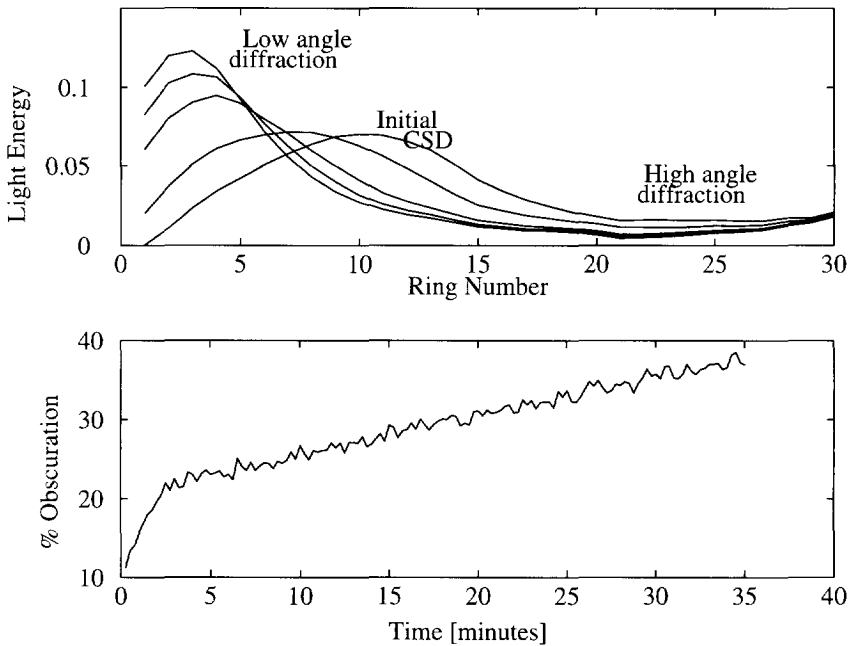


Figure 3.11 : Diffraction pattern for the outgrowth of an ammonium sulphate crystal suspension (upper) in the 2 L growth cell and the increase in the obscuration signal with time (lower)

It has been shown (Brown and Felton, 1985) that, it is possible to use the obscuration signal from the laser diffraction instrument to calculate the mass of solids (M_T) in the beam volume (V_b) and thus in the crystallizer (V_c), provided that the corresponding CSD ($\Delta V(x_i)$) is known at the same time.

$$M_T(t) = \frac{\rho_c V_b}{V_c} \frac{\ln(I(t)/I_o)}{3 \sum_{i=1}^k \Delta V(x_i, t) l/d_i} \tag{3.4}$$

This technique will be applied later in chapter 4 in evaluating results from the 2 L growth cell.

A disadvantage with using the Malvern instrument is that the sample in the product slurry is so concentrated that it must first be diluted to avoid problems of multiple scattering, thus enabling an accurate measurement of the CSD to be made. This means that the measurement cannot be done in-situ, as the concentration in the crystallizer, except for a very short time during the start-up, will always be too dense to make this possible.

3.4.1.2 Back light scattering

A commercially available instrument (Partec 100) made by Lasentec claimed to have overcome the problem of multiple scattering by measuring not the light diffracted in the forward direction but the light reflected in the backward direction. The principle is that a laser beam generated inside the instrument is brought to a focus point at a short distance (1 mm) from a window. If a crystal passes through or near this focal point, then a reflection is caused which is picked up by a detector as a pulse of light, the length of which is determined by the scanned chord of the crystal. So in fact, a chord length distribution is measured instead of a diameter distribution. This, they claimed, overcame the problem of multiple scattering and the instrument had the added advantage of being able to be fitted in-situ in a crystallizer. To test the instrument, a number of experiments were done whereby saturated solutions of pentaerythritol and adipic acid were cooled down until a primary nucleation event was reached. The crystals were allowed to grow out for some time to see the development in the CSD and how the Partec would register. A Malvern was also used to measure the results of the experiments up to a point when multiple scattering made the measurement unreliable. The results showed that the Partec consistently undersized the CSD when compared to the Malvern measurements due to the weak reflecting properties of the crystals in the liquid and also due to the sharp facets of the crystals.

3.4.2 Camera Observations

A charged coupled device (CCD) camera was placed on-line next to the Malvern to monitor a number of properties of the crystals and of the background dilution liquid. The CCD camera is useful from two aspects. Firstly, it is useful from an operational point of view as the quality of the dilution liquid can be continuously monitored on-line, for the presence of undesirable effects such as air bubbles or large impurities. Such effects are also visible with the Malvern, however, continuous attention and a well trained eye are needed to pick them up quickly. The camera is much easier to use in these respects. If a problem is detected, the operator can act quickly to correct the fault. The second aspect mentioned above, is from a research point of view, where absolute crystal properties, such as crystal morphology and habit can be recorded and also where crystallizer effects on the crystal can be seen, such as the effect of attrition on the shape of parent crystals and the effect of impurity levels on the shape of the crystals. This is demonstrated in figures 3.12 and 3.13 below where two crystallizer start-ups are shown. In figure 3.12 (a), (b), (c) and (d) the development of the CSD in a system which contained very low levels of impurities is

shown. Figure 3.12 (a) shows the CSD 1 hour 45 minutes after the primary nucleation event where a narrow CSD of small sized crystals is encountered. This represents the beginning of outgrowth of the initial population which was present after the primary nucleation step. In the next photograph, figure 3.12 (b), taken 4 hour 13 minutes after the primary nucleation, the crystals have grown out further to populate larger sizes. In figure 3.12 (c), taken after 6 hours, the CSD has widened due to the effect of attrition on the larger particles producing a population of attrition fragments which are also growing out. The effect of attrition has also acted to round off the larger crystals making them lose their original sharp character which was evident in figure 3.12 (a). In figure 3.12 (d), the small attrition fragments have grown a small amount and there are fewer large crystals present in the CSD.

Figure 3.13 (a), (b), (c) and (d) show the same trend in the development of the CSD, but this time the composition of the solution had changed as the levels of impurities in the solution had built up to a much higher level. The main impurity present in the system were chromium ions which were thought to have come from the walls of the crystallizer which is constructed from stainless steel which contains high levels of chromium. Also, sections of the ancillary piping for water and saturated feed are constructed from ordinary construction steel which also contain a high level of chromium. The incorporation of chromium ions into ammonium sulphate crystals has been shown to cause ammonium sulphate crystals to grow with another habit, which may have led to the observed elongated habit of the ammonium sulphate crystals in figure 3.13. The evolution of the CSD is, however, similar to that of the pure substance in figure 3.12.

3.4.3 Synchrotron Radiation Source

In chapter 4, the results of experiments done at the Daresbury synchrotron radiation source, near Warrington in England are presented. These experiments were designed to examine the level of strain present in a crystal to see if this could explain the observed size dependent growth rate of sub 300 μm crystals of ammonium sulphate in the 970 L crystallizer. The crystals for experimentation were removed from the crystallizer after a steady-state had been reached. They were subsequently dried by simply absorbing the excess saturated liquid onto filter paper and then dried in an oven

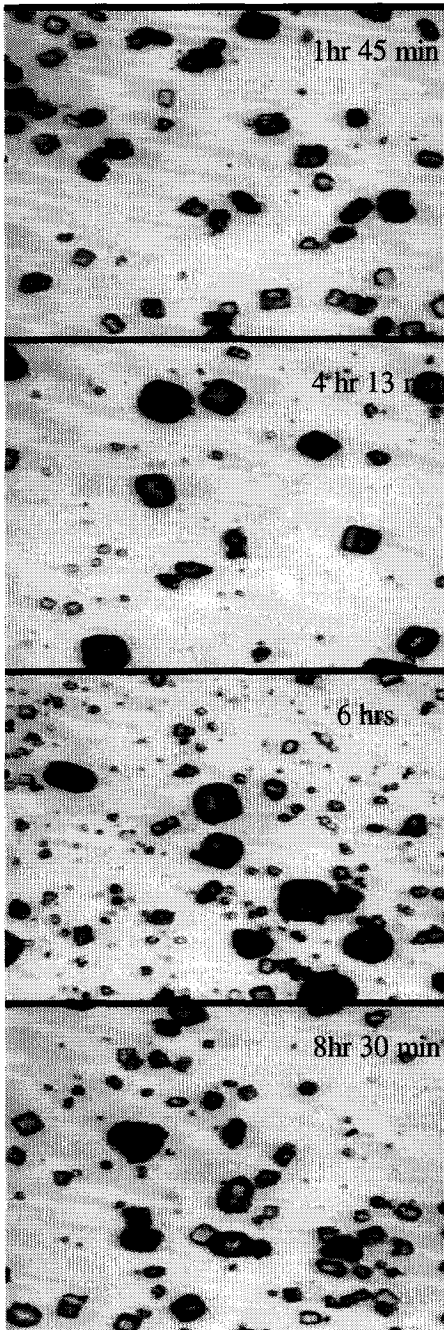


Figure 3.12 : Development of the CSD of $(\text{NH}_4)_2\text{SO}_4$ crystals grown from a pure solution in the 970 L crystallizer

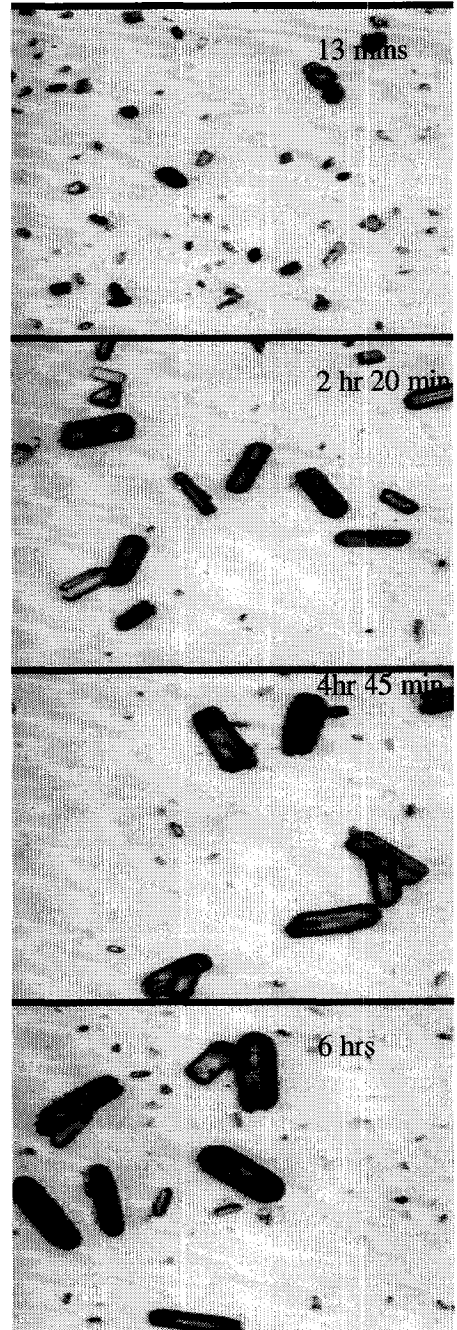


Figure 3.13 : Development of the CSD of $(\text{NH}_4)_2\text{SO}_4$ from an impure solution in the 970 L crystallizer (Cr^{3+} , Mg^{2+})

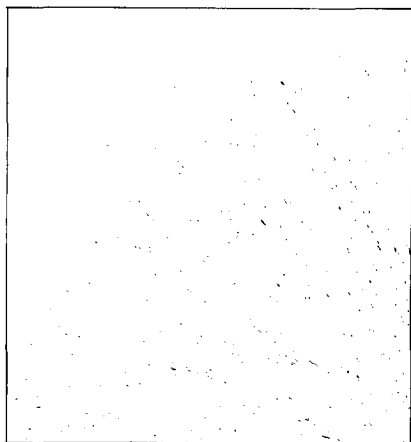


Figure 3.14 : *Upper left hand quadrant of a Laue diffraction image for a group of 124-148 micron A. S. crystals from the 970 L crystallizer*

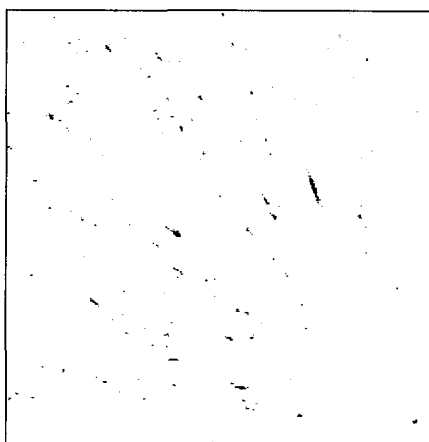


Figure 3.15 : *Digitised and filtered version of figure 3.14*

for 24 hours. The dried crystals were then sieved into ranges from 20 μm to 800 μm and placed in individual plastic containers for transport to the research facility at Daresbury.

The analysis of the internal structure of crystals was pioneered by amongst others Wood et al., (1983), Moffat et al., (1984), Andrews et al., (1987), Helliwell et al. (1989) who did experiments to analyse the internal structure of protein crystals such as pea lectin and other small molecule crystals. From their results of Laue diffraction experiments on station 9.7 at the Daresbury facility, they were able to map the internal structures of the protein. In their results they also noted that this method of analysis was very sensitive for any mosaic spread (or 'plane misorientation') within a crystal structure. Since then, other workers (Harding et al., 1992, Ristic et al., 1990) have tried to relate the growth rate of crystals in a saturated solution, to the level of internal strain in these crystals. Their research has met with varying levels of success.

Using the synchrotron Laue radiation source has several advantages over a conventional radiation source. Firstly, the current of the beam is much higher than what is normally encountered with a conventional X-ray generator. The source at the TU Delft, for example (an Enraf/Nonius 7), generates a beam of 20 mA. With this current, exposure times of up to 45 minutes are necessary to obtain a reliable Laue diffraction pattern for a 100 μm crystal. The beam source at Daresbury generates a beam with a current of over 240 mA, which enables much shorter exposure times for crystals to as low as 50 ms to be used to gain as good a result for the same crystal.

This saving in time allows much more time for the optimisation of equipment (collimator size, beam attenuation) and operation parameters (exposure time, crystal/photo-detector distance).

A second advantage to using the Daresbury facility is that the 'white' beam generated there contains a very narrow range of wavelengths from 0.3 to 2.5 Å. A narrower range of wavelengths means that more internal reflections will be produced thus yielding a much more detailed Laue diffraction pattern of the crystal structure.

The set-up of the experiment is as shown in figure 3.16. A beam with the required wave length is tapped off the central wiggler line. This beam can then be reduced to the required diameter by passing it through a collimator. The beam intensity can also be attenuated if required by placing a number of aluminium plates in front of the beam. The crystal and its' glass fibre holder are placed on a goniometer in alignment with the beam. Behind the crystal, a photographic sensor is placed which can be either a film or a CCD sensor.

Figure 3.14 shows a quarter of a typical Laue pattern for a group of crystals in the size range 124-148 μm. Normally, these films are analysed by laboriously measuring each diffraction spot. As a large number of films need to be analysed, advantage was taken of powerful image processing software currently on the market. For this purpose TIM software was used to first digitise the image (figure 3.14) and then the grey background was filtered out of the image to get the image in figure 3.15. In this form the software is easily able to trace each diffraction spot and measure its dimensions and its' distance from a given reference point. With this information, the mosaic spread, η , could be calculated using equation 3.5. D is the crystal to film distance, R is the spot elongation and θ is the Bragg angle :

$$\eta = \frac{R}{2D} \cos^2(2\theta). \quad (3.5)$$

3.5 Model Materials

The model material chosen at the beginning of the UNIAK I phase to test the development of control strategies and implementation was ammonium sulphate ((NH₄)₂SO₄). The main reason for choosing ammonium sulphate as the model material was that its' crystallization behaviour out of solution was very well

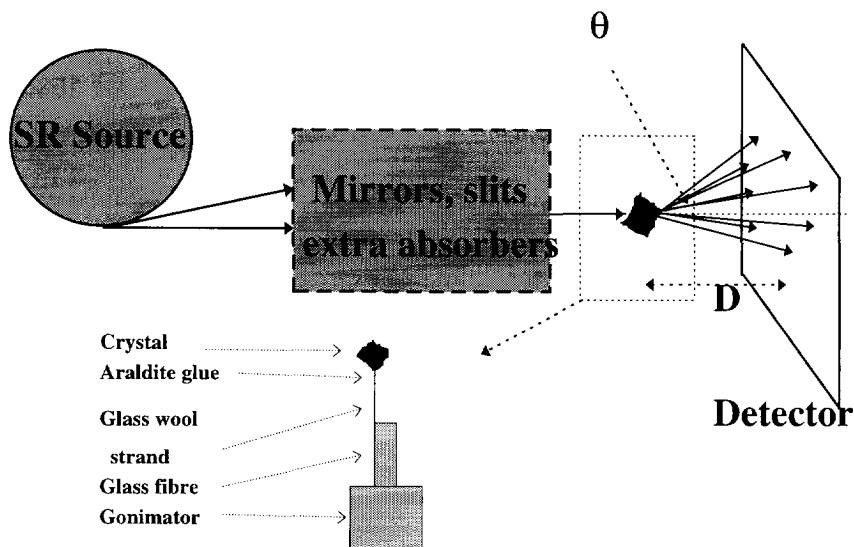


Figure 3.16 : Set-up for mosaic spread experiments at Daresbury Synchrotron radiation source

researched, and the results of this research had shown that the kinetics were quite straight forward, needing very little added research on the kinetic level, thus allowing more time to be concentrated on solving the control problem. Another reason for choosing ammonium sulphate was that its' crystallization behaviour involved few undesirable operational complications such as encrustation on crystallizer walls or in product/feed lines.

As the main objectives of the UNIAK II project did not differ from those of the UNIAK I project, work was continued with this material in developing strategies for the control of the product CSD. However, it was also thought that it was time to extend the methods and procedures developed within UNIAK to the crystallization of other types of materials and for the model materials to act as test cases for the validation of the general models for crystallization developed in this work.

To choose a suitable second model material for the large 970 L crystallizer, it was decided to first do some trials with the 22 L crystallizer with which it was thought, results could be more easily gained for new materials. In choosing a second material, a number of criteria were defined by which their compatibility and suitability could be judged. The criteria can be split up into two categories, one determining the possibility to use the material on the basis of its' material properties without consideration for the crystallization plants. These criteria can be summarised by the following points.

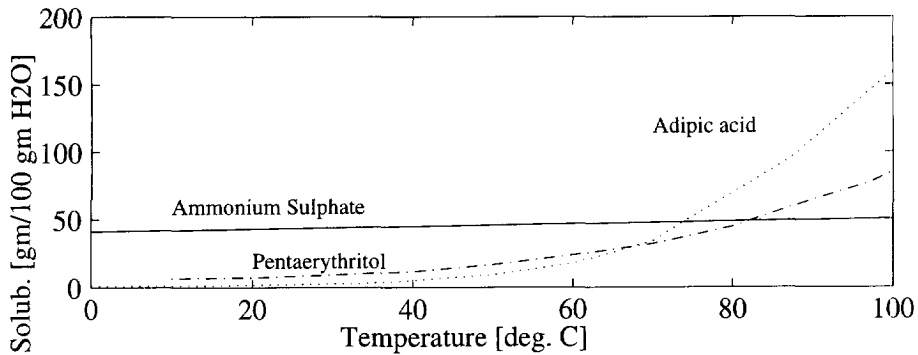


Figure 3.17 : Solubility curves for the three model materials, Ammonium Sulphate, Pentaerythritol and Adipic acid

- 1 Safety and handling.
- 2 Compatibility with materials and equipment.
- 3 Crystallizes from aqueous solution at low temperatures (below 70 to 80°C).
- 4 No undesirable physical properties such as high viscosity or an inclination to encrust.

A second set of criteria is related to the research purpose at hand which is the validation of modelling procedures developed for ammonium sulphate. These criteria can be summarised as,

- 1 Are the crystallization kinetics comparable to that of the ammonium sulphate crystallization or can the models be validated ?
- 2 Can the crystal size distribution of the process be monitored by the existing detection technique ?
- 3 Can the process dynamics be influenced by the classified fines and product removal systems ?
- 4 Is the size range and shape of the crystals comparable to that of ammonium sulphate ?
- 5 Is the material industrially relevant and is it relevant to improve the control of the crystallization process ?

On the basis of these criteria one main material was chosen for preliminary trials in the 22 L crystallizer. Pentaerythritol is a tetrahedral neopentyl alcohol which has wide application in resins, plastics and explosives. Pentaerythritol has a bi-

pyridimal morphology, a relatively low solubility up to 70°C and a wide metastable zone. The economical importance of pentaerythritol is dependent mostly on its' use in alkyl coatings for which 70 % of the total production volume is used. The use of pentaerythritol in the manufacture of adhesives and functional monomers is also expanding.

Pentaerythritol provides a good material to compliment the work done with ammonium sulphate during the UNIAK project. Its' kinetics are close enough to that of ammonium sulphate to act as a material to validate any general kinetic models developed with ammonium sulphate as a basis, while its' absolute solubility at normal operating conditions (50°C-60°C) is different enough to that of ammonium sulphate to be able to confirm the models for a broad range of inorganic and organic materials exhibiting similar kinetics to that of ammonium sulphate. Table 3.1 gives a list of physical properties of pentaerythritol, adipic acid (Kirk-Othmer) and ammonium sulphate (Daudey, 1987), while figure 3.17 gives a plot of the solubility of both materials (Kirk-Othmer, Belkin, 1990, Daudey, 1987) as a function of temperature.

The results of experiments with pentaerythritol are reported in chapter 7, where results from continuous experiments with the 22 L crystallizer are reported and modelled using the model developed in chapter 5. In chapter 7, the results of continuous experiments with adipic acid in the 22 L crystallizer are also reported. Physical properties for adipic acid are also listed in table 3.1.

Table 3.1 : *Physical properties of ammonium sulphate, pentaerythritol and adipic acid crystals*

<i>Material</i>	<i>Ammonium Sulphate</i>	<i>Pentaerythritol</i>	<i>Adipic acid</i>
Molecular Formula	$(\text{NH}_4)_2\text{SO}_4$	$\text{C}_5\text{H}_{12}\text{O}_4$	$\text{C}_6\text{H}_{10}\text{O}_4$
Molecular Weight (gr/mol)	132	136	146
Melting Point ($^{\circ}\text{C}$)	513	261	153
Boiling Point ($^{\circ}\text{C}$)	-	358	265
Density (kg/m^3)	1769	1396	1344
Morphology	Rhombic	Tetragonal, bi-pyramid	Monoclinic prisms
Refractive Index	1.523	1.554	-
Safety	Corrosive	Corrosive, flammable	Corrosive, flammable
Crystallization Mode	Evaporative/ Cooling	Evaporative/ Cooling	Cooling
Crystallizer Compatibility	yes	yes	yes
Chemistry	Anorganic	Organic	Organic
Industrial Use	Fertiliser	Surface coatings	Nylon 6,6
Heat of formation (J/kmol)	$-1.1808 \cdot 10^9$	$-7.767 \cdot 10^8$	-
Heat of melting (J/kmol)	-	$2.02 \cdot 10^7$	-
Heat of combustion (J/kmol)	$-8.33 \cdot 10^7$	$-2.4981 \cdot 10^9$	$2.8 \cdot 10^6$

Chapter 4

Growth of ammonium sulphate crystals in a crystallizer

Summary - A literature review of models used to account for the observation of an apparent size dependent growth rate (SDG) is made. Growth rate dispersion (GRD), random fluctuation growth (RF) and a fast-growers slow-growers (FGSG) manner of growth are considered. The models are discussed in terms of their relevance to the modelling of industrial crystallization processes. A number of published underlying mechanisms leading to the above growth types are considered, with special attention being paid to the effect of crystal internal strain on crystal growth rate. An empirical SDG function to describe the growth of ammonium sulphate crystals in the 970 L crystallizer is derived, by measuring the growth rate of samples of sub- 300 μm crystals in a 2 L growth cell. The results of internal strain measurements, using a synchrotron X-ray source, on these crystals are presented and it is shown that in the sub 300 μm ammonium sulphate crystals, a considerable amount of strain is present which can lead to a SDG effect.

4.0 Introduction

In early crystallization experiments, it was noticed that the measured population versus crystal size function deviated significantly from the function which was predicted by the ideal MSMPR model. The deviations occurred in the small particle size ranges, below a size of about 100 μm and in the large particle size range, above 600 μm . The deviation in the small size range was attributed to either a Growth Rate Dispersion (GRD) mechanism, the phenomena that crystals of the same size grow at different rates, or a Size Dependent Growth (SDG) mechanism, the phenomena by which crystals of a different size, growth at different rates.

Up to very recently, the upward curvature in the small particle size ranges was ignored and an effective secondary nucleation rate was determined by extending the ideal part of the logarithm of the number density distribution of crystals [$\#/m^3s$] versus the crystal size to zero size and from the point of interception with the y-axis, the effective nucleation rate was determined. A more accurate approach leading to a better description of the kinetics and a better prediction of the crystal population, is of course to include either a SDG or a GRD correlation in any system simulation to account for the upward curvature in the small crystal size ranges.

First however, a review of crystal growth experiments and modelling is given with two purposes in mind. Firstly, to review the types of growth behaviour measured in small scale experiments (50 ml growth cells) and steady-state CMSMPR experiments, and secondly to review the mechanisms put forward to explain these growth behaviours.

In this chapter, a closer look is taken at the processes which are occurring in the sub- 300 μm size range for ammonium sulphate crystals in the 970 L crystallizer.

Two approaches are taken. The first is to make a direct measurement of the growth rates of fine crystals (sub 300 μ) by placing samples from the fines line of the 970 L crystallizer, into a 2 L growth cell and measuring the growth behaviour of the crystals. The growth behaviour is modelled using a SDG function. The second, more indirect approach is to measure the internal strain in similar sized ammonium sulphate crystals from the same source (970 L) and to relate the level of strain to their growth rate via a physical model which adjusts the driving force for growth by accounting for the reduced supersaturation felt by the strained crystals.

4.1 Background

GRD is defined as the phenomenon whereby similar sized crystals under identical conditions of supersaturation, temperature and hydrodynamics grow at different rates. This phenomenon has been observed for many different crystal types and sources (Garside, 1985).

A GRD mechanism was reported as far back as 1971 by White and Wright who observed that an initial seeded narrow distribution of sucrose crystals with a median size of 500 μm and also a narrow distribution of aluminium trihydroxide crystals with an initial median size of 55 μm showed a dispersion in growth rates as the initial seeded population grew out.

Other experiments (Garside et al., 1984) with seeded potassium chloride crystals showed similar results. Even though the crystals showed a distribution in growth rates, the growth rate of each individual crystal was constant over time. This type of growth is called constant crystal growth (abbreviated CCG). Other recent measurements (Wang and Mersmann, 1992, Mitrovic 1994) have shown that there may also be a correlation between the initial crystal size and its' growth rate.

A GRD mechanism has been observed for crystals produced by primary nucleation (Davey et al., 1979, Garside and Ristic (ADP), 1983). In these references, the growth rates of individual crystals were followed over a long period of time (60 mins.) in a stagnant solution. The results showed that, each crystal possessed an individual growth rate, and the crystal maintained their initial growth rate over a long period of time. The growth rates of these individual crystals were modelled using the Burton, Cabrera, Frank (BCF, 1951) spiral growth theory by fitting the dominating dislocation group activity parameter ϵ , to the data, (see also Valcic, 1975). In this way, it was supposed that the numbers of active dislocations was the controlling factor in determining the growth rate of a particular crystal face. A more recent paper (Bhat et al., 1987) shows similar results for potash alum, whereby sections cut from a large 50 cm^3 crystal of potash alum were regrown in solution. This regrowth of the new section led to the development of lattice strain at the interface between the original seed and the new growing face, resulting in the emergence of dislocations at the new interface. (No information on the size of these new sections is given but because Lang topography is applied, it can be assumed that they have a size of greater than 1 mm.) The growth rate of the new section of the crystal was shown to be directly proportional to the numbers of dislocations. It was further shown that by directly applying strain to such a growing crystal, its' growth rate was lowered in proportion to the applied strain. Thus, it was concluded that if the internal strain in a crystal was released plastically, dislocations were formed which could contribute to the growth process. If the strain is retained, this leads to a reduction in growth rates.

This hypothesis was supported by the findings of Ristic et al. (1988) who measured the growth rates of sodium chlorate secondary nuclei and subsequently the level of 'mosaic spread' or internal strain in each nucleus by obtaining a Laue diffraction pattern using the synchrotron X-ray radiation source at Daresbury. Their measurements showed an inverse relationship between the level of internal strain and the growth rate of the particular crystal. A weak dependence of the growth rate on the initial crystal size was detected in the sense that the majority of small crystals ($< 30 \mu\text{m}$) showed a very low growth rate. This trend resembles the results of other workers who have measured a much more definite difference in growth rates between large ($> 10 \mu\text{m}$) and small ($< 10 \mu\text{m}$) secondary nuclei. Rusli et al. (1980) for example produced potash alum crystals in the size range of 2 to 25 μm by contacting a large potash alum crystal with a steel rod. Particles below 4 μm grew at a very low rate or not at all while those larger than 25 μm showed a strong dependence of size on the growth rate. In an earlier work Garside and Larson (1978) obtained similar results for potash alum. The number of particles produced with an initial size $> 10 \mu\text{m}$ was found to be dependent on the supersaturation, while the numbers of particles with an initial size smaller than 10 μm were found to be independent of the supersaturation conditions. Daudey (1987) interpreted these results by suggesting that the two types of crystals were produced from different sources. The larger crystals ($> 20 \mu\text{m}$), he envisaged as being produced by a surface breeding mechanism whereby surface growth features such as macrosteps are removed by attrition, while the smaller crystals ($< 20 \mu\text{m}$), are produced by a mechanical breeding mechanism, whereby fragments, not previously recognisable as potential secondary nuclei are removed into solution. The mechanically bred crystals may contain more strain, and thus grow with a very low growth rate. Daudey (1987) suggested that this phenomenon could be modelled by imposing two types of growth rate on the population of secondary nuclei, which he called a 'fast growers', 'slow growers' (FGSG) growth mechanism.

A final type of crystal growth suggested in the literature for large crystals is where the growth rate of a crystal fluctuates around an average constant crystal growth rate (random fluctuation growth (RF), Randolph and White, 1977). This was thought to be caused by the influence of changing surface structures with time leading to a non-random growth rate variation on a particular surface.

In the modelling of steady-state continuous MSMMPR kinetics, several workers have been successful in predicting the upward curvature of the $\ln(n)$ vs. x population density plot by using empirical relations describing a size dependent growth rate. The correlations contain only one parameter i.e. crystal length, and describe an increasing function with particle size. In Abegg et al. (1968) and White et al. (1976), good

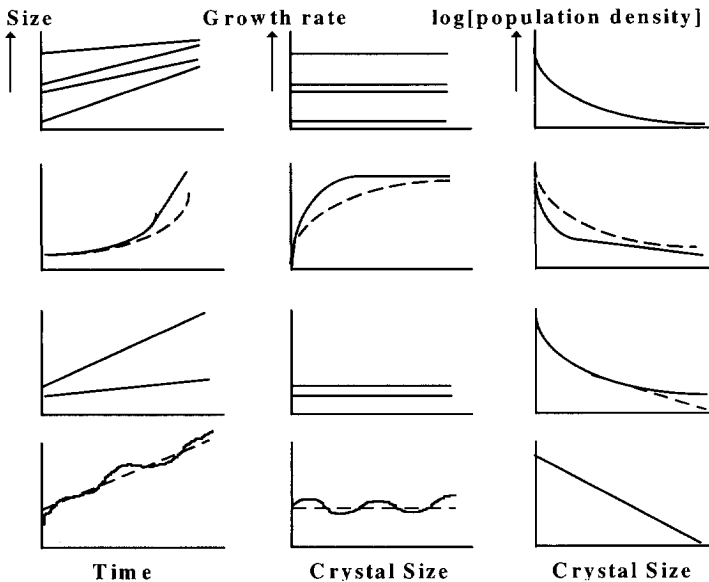


Figure 4.1 : Different types of growth mechanism reported for secondary nuclei CCG (top), SDG, FGSG and, RF (bottom)

examples are to be found of the application of SDG correlations to crystallizer CSD data.

It should be kept in mind that the SDG correlations are purely empirical relations and give no insight into the kinetic processes occurring in the small particle size range. No evidence has yet been found that an individual crystal growth rate increases its' growth rate over time under the same conditions of temperature and supersaturation, and that a unique growth rate exists for a particular size of a crystal of a specific compound.

The success of SDG correlations can be attributed to the fact that for a group of crystals exhibiting a range of growth rates, the fastest growing crystals will reach an appreciable size in a shorter time than the slower growing crystals. Thus, the larger size classes will be populated by faster growing crystals while the lower size classes will be populated by slower growing crystals which gives the impression of a SDG rate. In a crystallizer with a continuous product removal, the slower growing crystals will also be removed before they reach any appreciable size, compounding the effect. In combination with this, is the fact that in some systems, a size dependence on initial fragment size exists (Berglund et al, 1984, Wang and Mersmann, 1992) also giving rise to an apparent SDG effect.

4.2 Sources of growth rate dispersion

Figure 4.1 summarises the different types of growth of individual crystals discussed above and their effect on the average growth rate of the crystals and on the population density plot function. Three types of growth lead to the observed upward curvature in the population density versus crystal size plot in the small crystal size range, the CCG, SDG and FGSG growth behaviour. The CCG and FGSG behaviours are in fact the same type of growth in that each crystal has a constant growth rate imposed upon it. The difference is that in the FGSG behaviour, a crystal has one of two growth rates, while in the CCG behaviour, a distribution of growth rates exists. Also, for the FGSG type of growth, the observation that the growth rate of the slow growers is a factor 10 times slower than that of the fast growers means that the slow growers will only grow to a certain critical size before they are removed from the crystallizer, leaving only fast growers in the crystallizer above this size. This causes the $\log(n)$ vs. x plot to straighten above this critical size. If the ratio of growth rate between fast and slow growers is much smaller and the numbers of each species is the same, then the curvature will persist to larger sizes. If a distribution of growth rates is present in the CCG behaviour, the curvature remains in the $\log(n)$ vs. x plot. A SDG rate which expresses the average growth rate of all crystals at a particular size also leads to a similar curvature in the $\log(n)$ vs. x plot. In the RF growth behaviour, assuming that the growth rate of all crystals fluctuates around an average constant growth rate, the $\log(n)$ vs. x plot will exhibit no curvature. If each crystal grows at a different rate, and also fluctuates around different average growth rates, yielding a hybrid CCG/RF growth behaviour, then a curvature in the $\log(n)$ vs. x plot will be observed.

All of the above growth types are based on the observations of the growth rates of individual crystals in small scale set-ups where the crystals grow in a stagnant solution. As the objective of most experiments is to gain information on the growth kinetics of a certain material in a large scale crystallizer, it is important to convert the observed types of growth behaviour into mathematical formulations. These can then be combined into the kinetic growth rate expression for crystals, to yield an effective growth rate of crystals as given by equation (2.18). Before doing this however, a number of interpretation criteria have to be resolved, as it is not possible to apply the models directly to a large scale crystallizer, without accounting for changes in experimental conditions and the manner in which the crystals are produced.

The most important changes in conditions, will of course, be hydrodynamic changes. Different hydrodynamic conditions are promoted in small growth cells and in

large industrial crystallizers to achieve a desired result. In a small cell, the desired result is to examine the growth rate of the smallest possible crystals, which means that the contents of the cell must be kept still, while the measurement of the crystal sizes is continuing. This will yield a stagnant situation in the cell. In an industrial crystallizer, a well fluidised system is desired to avoid problems with internal classification and ensure an even distribution of the supersaturation created in the boiling zone. Because the hydrodynamics of both situations are different, the crossover from an integration limited growth rate to a volume diffusion limited growth rate may occur at a different crystal size. Thus, before applying the results of small scale experiments to large scale unit operations, careful account of the growth regime must be taken to make sure that the results applicable in the integration regime are not applied to the volume diffusion limited regime. Allied to this point, is the fact that the growth rate of crystals in a small cell is mostly limited to observations over a limited period of time until the crystals reach a certain size. Using the results of these measurements to represent the growth behaviour of the same type of crystals over a much broader size range in a crystallizer, can lead to inaccurate results, as there may be a change in the controlling mechanism of growth as the crystal grows above the size for which the model is relevant.

For most contact experiments reported in literature (Johnson et al., 1975, Clontz and McCabe, 1971, Wang and Mersmann, 1992, Van der Heijden, 1990), attrition can be said to be the representative source of secondary nuclei in a crystallizer. In these experiments, a single crystal is glued to a holder and it is allowed to grow before attrition fragments are produced by contacting the crystal surface with a steel rod. These crystals fall to the base of a glass cell and are grown in a stagnant situation by cooling of the surrounding solution. Similarly in a crystallizer, attrition fragments are produced by contacts between a crystal in suspension and the impeller or between two crystals.

The only other contributory factor where the growth rate of crystals in a crystallizer may differ from that in a growth cell, is that the composition of the fluid phase may be different, i.e. the presence of impurities in an industrial crystallizer may affect the growth rate and the types and number of growth features on the crystal surface (Davey, 1979, 1982). Thus other types of secondary nuclei may be produced by collision mechanisms.

4.3 Mechanisms of GRD

No completely satisfactory reason behind the phenomenon of growth rate dispersion (GRD) has been found. Several suggestions have, however, been put

forward to try and explain the observations of GRD. An early reason put forward independently by Garside et al. (1983), Davey et al. (1979) and Valcic, A.V. (1975) and more recently by Chernov (1990), was based on the BCF theory of crystal growth. It was thought that the activity (ε) of the dominating group of dislocations on a crystal surface may enhance or reduce the growth rate of a particular crystal surface. The activity is a parameter in the BCF growth model :

$$G(\sigma) = C_1 \varepsilon \left(\frac{\sigma^2}{\sigma_1} \right) \tanh \left(\frac{\sigma_1}{\varepsilon \sigma} \right). \quad (4.1)$$

The influence of ε is confined to the region where σ_1 has an influence on the growth rate, so will be more important in the linear law region ($\sigma/\sigma_1 \gg 1$). An increase in activity will cause a linear increase in the growth rate $G(\sigma)$.

It should be noted at this point, that the experiments in validating this mechanism for GRD were done on crystals produced by primary nucleation and the measurement of crystal growth rates was commenced only when the crystals had reached a size greater than 50 μm .

Another possibility to explain observed differences in growth rates between crystals is that either the mass transfer coefficient or the equilibrium concentration is size dependent. The latter effect is called the Gibbs-Thomson effect whereby a shift in phase equilibrium occurs at a curved surface:

The possibility that the mass transfer coefficient may cause a SDG behaviour was examined by Daudey (1987) for ammonium sulphate crystals. He showed that if the mass transfer coefficient were responsible for a SDG rate, then the growth rate would be influenced in the opposite direction to that shown in the $\log(n)$ versus x plot, i.e. that the growth rate would decrease with increasing sizes up to a size of about 50 to 60 μm , at which point the diffusion step would then become rate limiting. Below this size, the growth rate would be incorporation step limited.

The Gibbs-Thomson effect was put forward by Wang and Mersmann (1992) to explain a possible SDG rate. They claimed that a low radius of curvature of badly formed attrition fragments may reduce the chemical potential difference between the solid and liquid phases, thus reducing the supersaturation 'felt' by crystals, from σ_∞ to σ_r with a low radius of curvature (r) according to,

$$\sigma_r = (1 + \sigma_\infty) \exp\left(-\frac{2\tilde{M}\gamma}{RT\rho} \cdot \frac{1}{r}\right) - 1, \quad (4.2)$$

where \tilde{M} is the molar mass (kg/kmol), γ is the surface free energy (J/m^2), r is the radius of curvature and σ_∞ is the supersaturation felt as $r \rightarrow \infty$. The Gibbs-

Thomson effect cannot, however, give an explanation for the observed SDG behaviour as it is really only applicable in the sub - 1 μm region. This result was confirmed by the measurements of Van der Heijden et al. (1992) who showed that the refacetting process lasts only a very short time after the attrition fragment is formed. For a spherical particle, he calculated that the time necessary for such a particle to be transformed from a non-faceted to a faceted state, assuming a diffusion constant of $10^{-9} \text{ m}^2/\text{s}$, and an initial crystal size of 10 μm lasted between 10 and 100 ms. With times of this order, it is safe to say that the crystals will be instantaneously refaceted after they are born and that the Gibbs-Thomson effect will have no more effect on the growth behaviour or rate.

The evidence that it is the internal strain present in a crystal (as either a 0, 1, 2 or 3 dimensional lattice strain) which is responsible for GRD has been gathering some support over the past few years. The presence of strain in a crystal leads to a strain energy which must be added to the internal energy of the crystal, increasing the chemical potential of the solid phase. An increase in the chemical potential difference between solid and liquid phases will lead to a decrease in the growth rate of the crystal. Strain in a crystal will lead to some degree of misorientation between adjacent parts in a crystal during their further growth. This phenomena is called mosaic spread. This misorientation can be measured if a particular crystal is examined using X-ray diffraction. For example, a Laue diffraction pattern will yield an image where the diffraction spots, normally round symmetrical spots for perfect crystal structures, become elongated ellipses in the case that the crystal contains an amount of strain. From the spot elongation, the mosaic spread (η) can be calculated (section 3.4.3), which can be translated into the level of misorientation in the crystal. Four possible ways in which the strain was present in the crystal was reviewed by Van der Heijden (1992).

4.4 Strain mechanisms

Van der Heijden considered four ways in which strain could be introduced into the crystal. this could be either by a 0,1,2 or 3- dimensional effect (see figures 4.2 to 4.5). The amount of strain introduced into a crystal is summarised in table 4.1.

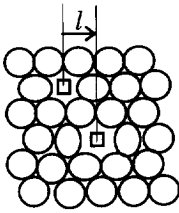


Figure 4.2 : Crystal structure showing two point defects (vacancies)

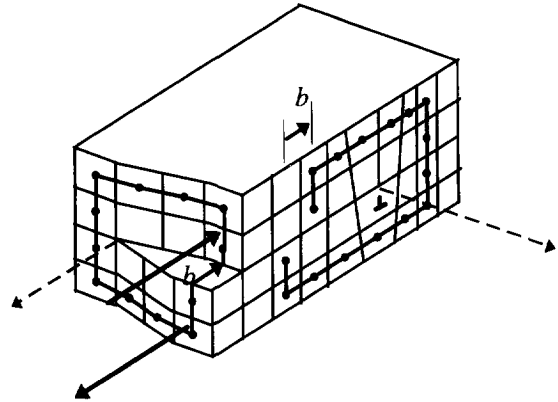


Figure 4.3 : Crystal structure showing a cube with a mixed edge/screw dislocation (line defects)

Table 4.1 : Mosaic spread and energy of a crystal of characteristic size x , subject to strain (ϵ_{ii} = strain tensor, b = Burgers' vector, θ = grain boundary angle, μ shear modulus, G = Youngs' modulus)

Mechanism	Point defects	Line defects	Grain boundaries	Volume strain
Mosaic Spread (degs. or rads.)	$\eta \approx \sqrt{\frac{x}{l}} \frac{\epsilon_{ii}}{3}$	$\eta \approx \sqrt{\frac{x}{l}} \frac{b}{l}$	$\eta \approx \sqrt{\frac{x}{l}} \theta$	$\eta \approx \sqrt{\frac{x}{l}} \frac{\Delta l}{l}$
Lattice strain (J) (W_i)	$W_0 \approx \frac{\epsilon_{ii}}{3}$	$W_1 \approx G b ^2$	$W_2 \approx G \theta ^2$	$W_3 = \frac{\mu \epsilon^2}{2}$

4.5 Identifying the strain mechanism

In his thesis, Van der Heijden (1992) derived expressions which described the amount by which the chemical potential of the solid would increase, due to the presence of strain, introduced by each of the four mechanisms in table 4.1. The relative supersaturation ($\sigma = \Delta\mu / kT$) will thus decrease by an amount given by the increase in energy per particle (W_i / kT) due to the presence of either a, ($i =$) 0, 1, 2 or 3 dimensional strain effect :

$$G(\eta, x, \sigma) = k_G \left(\sigma - \frac{W_i(\eta, x)}{kT} \right)^g. \tag{4.3}$$

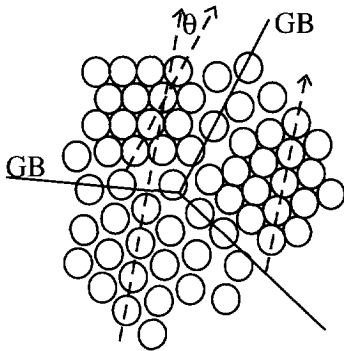


Figure 4.4 : Grain boundaries in a crystal between regions growing with different orientations causing the formation of dislocation lines

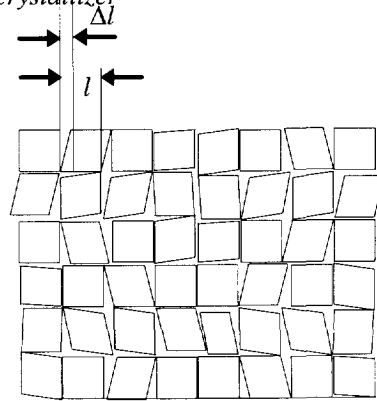


Figure 4.5 : Strained regions (volume strain) in a crystal between sub-blocks without the formation of grain boundaries or dislocations between the regions

By filling in the expressions for the energy per particle, he showed that the presence of strain in either of the above forms, leads to a GRD effect, in that at a particular crystal size, a distribution of strain is present. It also leads to a SDG effect as is clear by the inclusion of a characteristic crystal size (x) in the expressions in table 4.1. The physical interpretation of this expression is that as a damaged crystal grows, the strain originally present will gradually decrease and the crystal will be able to grow at a faster rate. This is sometimes referred to as a ‘healing’ process of the crystals.

Assuming that a maximum growth rate $G(\sigma)$ can be defined as $G = k_G \sigma$, and that the growth order is linear with respect to the supersaturation ($g = 1$), then equation (4.10) can be rearranged to give,

$$\frac{G(\eta, x, \sigma)}{G(\sigma)} = 1 - \frac{W_i(\eta, x)}{\sigma kT} \quad (4.4)$$

Thus, three pieces of information are required to identify the manner in which the strain is present in the crystals. The first is the growth rate of individual crystals, as a function of their maximum growth rate, given by the left hand side of equation (4.4). The second is the mosaic spread of these crystals measured at periodic intervals during their outgrowth, and the third is the supersaturation in the crystallizer measured at the same times as the growth rate and the mosaic spread.

Using the data of Ristic et al. (1988), who correlated the initial growth rate of sodium chlorate crystals produced by secondary nucleation to their mosaic spread, Van der Heijden (1992), was able to show that it was most likely strain in the form of grain boundary dislocations, which led to the observed reduced growth rates of highly strained crystals.

The experiments carried out to obtain these mosaic spread/ growth rate correlations were done in a small growth cell with a volume in the order of 20 ml. In such a set-up, it is relatively easy to measure these quantities, as the supersaturation is externally controlled and the crystals are stationary. The growth rate of each individual crystal can be followed relatively easily using the microscope. However, some problems are encountered when trying to do the same type of experiments in a large crystallizer. The obvious problem is that crystals are in suspension to avoid classification, making it impossible to follow the growth rate of an individual crystal in-situ. Another problem is that the supersaturation is not known. In a growth cell, this is controlled by lowering the temperature of the solution by an certain amount below its' saturation temperature, which will give an almost constant supersaturation in the cell during the time that the crystals are growing. This can be achieved as the mass of crystals in the cell is very small, almost negligible in comparison to the dissolved material present in the solution to create the supersaturation. In a crystallizer, the supersaturation depends on many factors from operating conditions, to the mass of crystals in the suspension and cannot be directly changed by altering the operating conditions.

4.6 Experimental Strategy

Due to the success of the modelling procedure of Van der Heijden, it was decided to try the same procedure with ammonium sulphate crystals grown in the 970 L crystallizer. The growth rate of small ($< 300 \mu\text{m}$) crystals, and the mosaic spread of the same crystals had to be measured.

To measure the growth rates of ammonium sulphate crystals, it was also decided to build a small 2L growth cell (section 3.3.3) into which samples from the crystallizer could be pumped. This sample would be cooled down from 50°C to 46°C to examine the growth rate of the crystals. From the results, it was intended to find out whether crystals grew with a reduced growth rate in the crystallizer, and if so, to estimate the magnitude of the growth rate as a function of crystal size. A drawback of the 2 L growth cell is that the growth rate of individual crystals cannot be measured to compare with mosaic spread measurements, but the choice of a large (2 L) was made for other reasons. They were that by using a 2 L suspension growth cell, the growth rate of enough crystals could be measured to obtain a reliable average growth function for further application in the population balance, equation (2.3). It was also thought that the conditions for growth in the crystallizer would be best represented in a growth

cell where the contents were held in suspension. Samples from the fines line where already a classified CSD was present could be used to inoculate the 2 L growth cell.

Because average growth rates as a function of crystal size are measured in the 2 L growth cell, no direct distinction can be made between a GRD and a SDG behaviour of the crystals. Rojkowski (1993) showed that even from a mathematical point of view, no distinction can be made between the two mechanisms if no direct measurements of individual growth rates are made. Given these limitations and the success of previous workers in modelling the upward curvature in the $\log(n)$ versus x plot of steady-state MSMPR data, a SDG function is chosen for modelling purposes.

Parallel to the measurements in the 2 L growth cell, crystals were also removed from the crystallizer and dried to be used later for mosaic spread measurements.

Knowledge of strain levels in the crystals, and the growth rate of similar sized crystals from the growth cell experimental results, would enable a comparison to be made between the chemical potential difference necessary to provide the driving force for growth of a crystal of a particular size, and if this chemical potential difference value corresponds to the energy levels recorded by the mosaic spread measurements. From these calculations, at least some estimate of the manner in which strain is present could be gained.

4.7 2 L Growth Cell Experiments

4.7.1 Operation

The 2 L growth cell (described in section 3.3.3) is inoculated by taking samples from the fines line of the large crystallizer. The suspension in the fines line is very convenient to use as samples for the growth cell, as the CSD has already been classified. The CSD in the crystallizer ranges typically from 1 μm to 2 mm. Operating at a fines flow rate of for example 1 L/s, a cut-size of 50 μm can be achieved. Figure 3.8 (section 3.3.6) shows the classification function of the 970 L fines line with increasing fines flow rate. The initial median size, distribution spread and initial solids concentration are determined not only by the fines removal rate, but more importantly by the CSD of the product crystals in the crystallizer. For this reason, no correlation between the fines removal rate and the initial values of these parameters can be discerned by examining the trends in figure 4.7.

The initial crystal population in the cell is grown out by cooling the suspension down from an initial 50°C to 46°C over a time period of 20 minutes. In this way, any SDG effects become apparent by examining the development in the CSD of these fines.

For the results presented in this chapter, samples were removed from the fines line of the 970 L crystallizer while experiments were being carried out to examine the influence of a variable fines flow on the behaviour of the product CSD. The fines flow ranged from 0.75 L/s to 2 L/s during the experiment.

Many 2 L growth cell experiments were carried out using this procedure. The details of three experiments are given in table 4.2, the results of which will be used to determine a SDG correlation in section 4.7.3.

Table 4.2 : *Experimental conditions for Runs 1,2 and 3 and growth cell cooling rates*

<i>Run</i>	<i>Fines flow rate</i>	<i>Cooling rate</i>
1	1 L/s	.08°C/min
2	2.13 L/s	.08°C/min
3	1.55 L/s	.04°C/min

During the sampling of the fines line for the 2 L growth cell, some crystals were separately removed, filtered and dried, for examination of the surface structure with an optical microscope to see if the growth type could be identified.

4.7.2 Modelling of the 2 L growth cell CSD results

Population balance

To model the development of the CSD in the 2 L growth cell, the population balance approach of Randolph & Larson (1988) is also used for this case of a batch reactor, where the driving force for growth is generated by cooling the contents of the growth cell. An initial population is assumed to exist in the cell and no primary or secondary nucleation occurs during the course of the experiment because the size of the crystals is too small for attrition and the supersaturation is too low to provoke primary nucleation. The vessel is assumed to be well mixed and the sample for measurement is isokinetically removed and returned to the growth cell. Under these assumptions the population balance assumes the following form :

$$V \frac{\partial n(x,t)}{\partial t} + V \frac{\partial G(x,t)n(x,t)}{\partial x} = 0, \quad (4.5)$$

with the boundary condition that,

$$n(x_0,t) = \frac{B(t)}{G(x_0,t)} = 0. \quad (4.6)$$

Growth rates

By expressing the growth rate term $G(x, t)$ in equation (4.5) as the product of two separate terms, the dependency of the growth rate on the time and on crystal size can be treated separately :

$$G(x, t) = G(x)G(t). \quad (4.7)$$

The first term in this expression $G(x)$, expresses the dependence of the growth rate on crystal length, while the second term expresses the maximum growth rate at a point in time, which only depends on σ can be calculated by the crystal mass balance. Three functions (equations (4.8) , (4.9) and (4.10)) describing a size dependent growth rate ($G(x)$) were used to simulate the data. These functions from literature, successfully described the growth behaviour of a particular crystallizing system in a suspension crystallizer. These correlations are purely empirical and only indicate the average growth rates found in a particular size class. The trend in average growth rate may have arisen via a GRD mechanism of growth or a pure SDG mechanism or a combination of both,

$$G(x) = x^n \quad \text{Bransom (1960)} \quad (4.8)$$

$$G(x) = (1 + \gamma x)^n \quad \text{Abegg et al. (1968)} \quad (4.9)$$

$$G(x) = 1 - \exp\left(-\left(\frac{x}{x_g}\right)^n\right) \quad \text{Wang et al. (1992).} \quad (4.10)$$

Note : The parameters n, γ, x_g in the above equations are denoted SDG_{PAR} in the rest of the chapter.

Crystal mass balance

By multiplying each term of the population balance (equation (4.5)) with $k_v x^3$, where k_v is the volumetric shape factor, and integrating with respect to crystal length, the following expression is obtained :

$$\frac{d\varepsilon(t)}{dt} = -3k_v \int_0^{\infty} G(x)G(t)n(x, t)x^2 dx, \quad (4.11)$$

where

$$\varepsilon(t) = 1 - k_v m_3(t),$$

$\varepsilon(t)$ is the volumetric void fraction or the fraction of the total volume in the crystallizer which is not occupied by solid crystal mass. By multiplying equation (4.11) with ρ_c , the crystal density, and integrating with respect to time, it is possible to calculate the total crystal mass of crystals $M_T(t)$ in the system after a time t i.e. -

$$M_T(t) = \rho_c(1 - \varepsilon(t)) = \rho_c \left(1 - \int_0^t (-3k_v \int_0^\infty G(x)G(t)n(x,t)x^2 dx) dt\right). \quad (4.12)$$

By rearranging equation (4.12), an expression for the kinetic growth rate is obtained,

$$G(t) = \frac{d\varepsilon(t)}{dt} \bigg/ -3k_v \int_0^\infty G(x)n(x,t)x^2 dx. \quad (4.13)$$

Population number

It has been shown (Brown & Felton, 1985) that it is possible to use the obscuration signal from the laser diffraction instrument to calculate the mass of solids in the beam, provided that the corresponding CSD ($\Delta V(x_i, t)$) at the same time is known,

$$M_T(t) = \frac{\rho_c V_b}{V_c} \frac{\ln(I(t)/I_0)}{3 \sum \Delta V(x_i, t) l / d_i}. \quad (4.14)$$

V_b is the beam volume, V_c is the cell volume, l is the path length of the beam and d_i is the median diameter in class i . From the solid mass ($M_T(t)$) the void fraction can be calculated and the relative volume distribution can be converted to a number distribution basis,

$$\varepsilon(t) = 1 - \frac{M_T(t)}{\rho_c}, \quad (4.15)$$

$$n(x_i, t) = \frac{\Delta V(x_i, t) M_T(t)}{\rho_c k_v x_i^3 \Delta x_i}. \quad (4.16)$$

Initial distribution

It was found that a log-normal distribution (equation 4.17) adequately approximated the shape of the initial distribution removed from the fines line. A fit procedure was carried out to optimise the parameters in the log-normal distribution equation to obtain a best fit for the initial distribution. Three parameters fully describe the distribution i.e. the position (x_m), width (σ) and height (a) of the distribution :

$$n(L, t_0) = a \exp\left(-\frac{[\log(L_m) - \log(L)]^2}{2\sigma^2}\right) \tag{4.17}$$

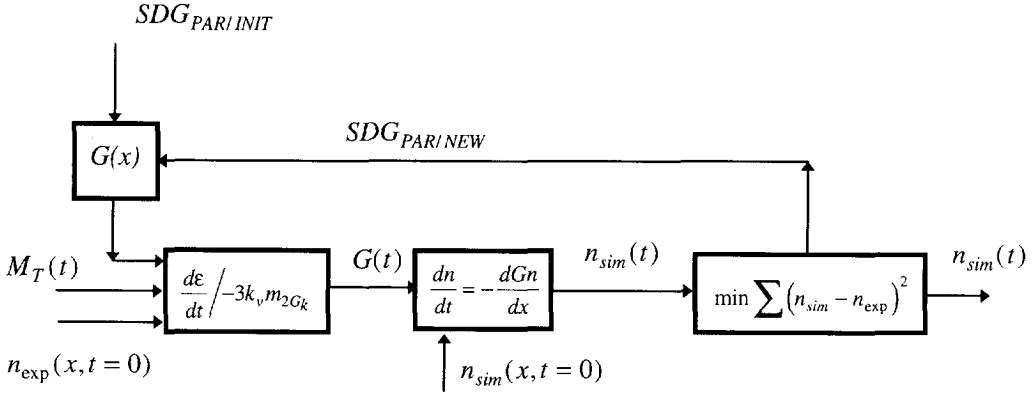


Figure 4.6 : Flowsheet for the optimisation of the parameters SDG_{PAR} rate function parameters

4.7.3 Simulation

The equations developed in the above section were combined in a simulation procedure to simulate the outgrowth behaviour of the CSD. An optimisation routine was also used to estimate the values of the unknown fit parameters (SDG_{PAR}) in the SDG rate equations (4.8), (4.9) and (4.10). A quadratic condition based on the difference between the simulated and measured distributions was used as a criterion to estimate the best fit. The flow diagram in figure 4.6 shows the procedure followed in the optimisation.

In the following section, the results of the optimisation are shown for Runs 1,2 and 3. A simulation of the entire CSD as it develops with time is also shown in figure 4.11. These simulations are repeats of sim1 described in section 2.4.3 (figure 2.4) but here the growth rates of crystals are also made size dependent.

4.7.4 Results and Discussion

Figures 4.7 show the trends of the median, the distribution spread (X75-X25) and the obscuration over a time of 30 minutes, after inoculation of the 2 L cell with a

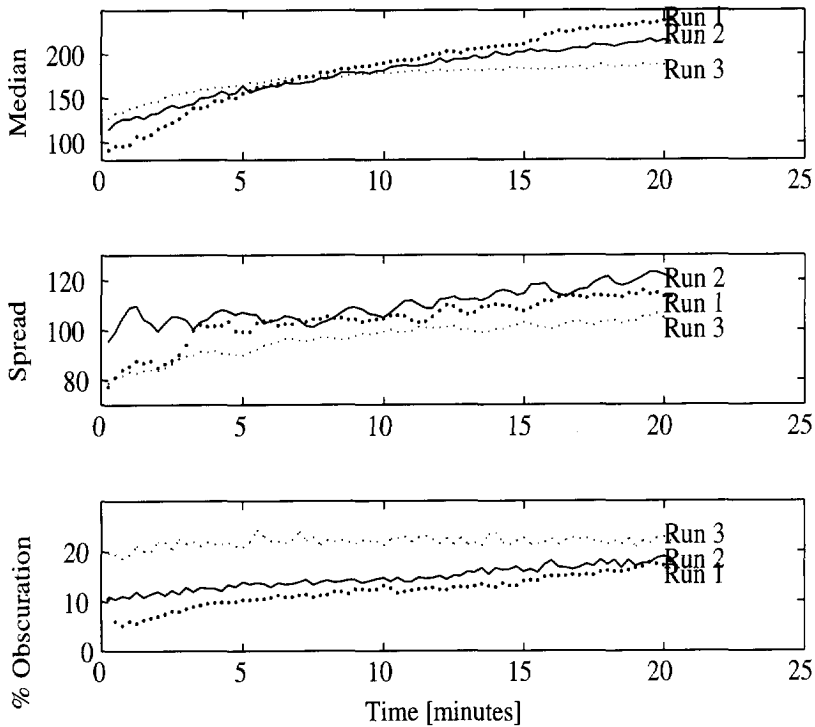


Figure 4.7 : *Runs 1, 2 and 3 : Measured trends in the distribution median size (top), distribution spread (centre) and obscuration (bottom) with time after sample was taken from fines line.*

sample from the 970 L fines removal line. The fines are taken at different fines removal rates as is given in table 4.2.

As the contents of the growth cell are cooled, the obscuration signal increases, which indicates an increase in the crystal mass in the growth cell consistent with a conversion of dissolved material into solid mass.

Figure 4.8 shows the results of the optimisations for Runs 1,2 and 3. The exponential model (equation (4.10)), was found to best describe the experimental data. The other two correlations, equations (4.8) and (4.9), were found not to be able to predict the behaviour of the crystal size distributions for two reasons. Firstly, because the functions cannot express a low, almost zero growth rate for small particle sizes, and secondly because these are always increasing functions of length and do not reach a maximum value. The exponential function, on the other hand predicts a low growth rate for particles smaller than 40 μm and the growth rate reaches a maximum above

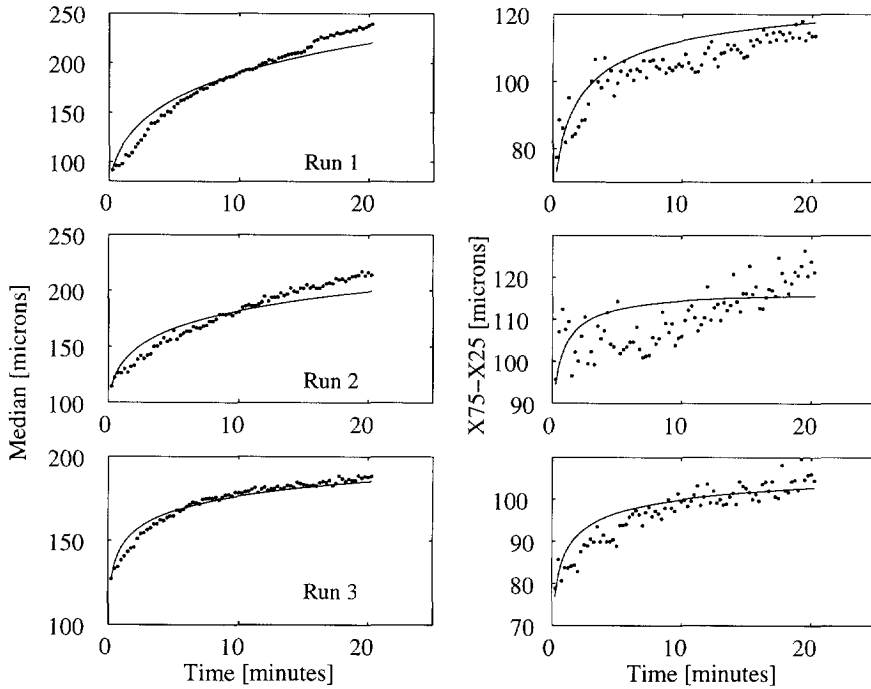


Figure 4.8 : Measured and simulated trends in the distribution median sizes (X_{50}) and spread ($X_{75}-X_{25}$) for Runs 1, 2 and 3 in the 2 L growth cell.

200 - 250 μm . The optimised exponential growth curves resulting from the optimisations are shown in figure 4.9 (a) and the parameter values for each run are listed in table 4.3. An initial slow growth of crystals below 40 μm is consistent with the slow growth rates recorded for initial fragments produced by contact nucleation by other workers. The maximum growth rate reached by the crystals is determined by the supersaturation in the growth cell at a particular time. The supersaturation in all three experiments is not constant throughout the entire 20 minute duration of the experiment but decreases from an initial value of 1.5 % to 0.5 % at the end of the experiment. This change in supersaturation will doubtlessly change the location and form of the SDG function accordingly, however, no account is taken of this in the current modelling procedure and cannot be attempted without the availability of more fundamental information on how the supersaturation level effects the crystal growth regime (reaction or diffusion limited). The SDG function calculated here is thus an averaged function independent of supersaturation over the entire experimental duration. Figure 4.9 (b) shows the fit of an optimised log-normal distribution to the initial

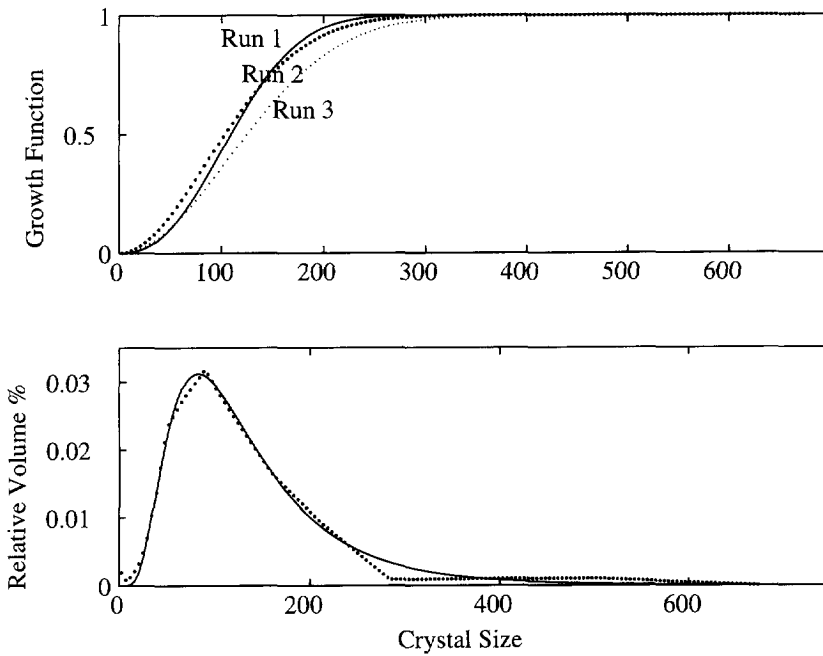


Figure 4.9 (a) and (b) : Growth rate function curves calculated from the fit procedure for Runs 1, 2 and 3 (upper) and the fit of a log-normal distribution to the first distribution measured in the 2 L growth cell for Run 3 (lower)

distribution of fine crystals in the growth cell. This distribution along with successive experimental and simulated distributions for Run 1 are shown in figures 4.10 (a & b).

Table 4.3 : Optimised parameter values for the exponential growth model

Run	Parameter (n) [-]	Parameter (x_g) [m]
1	1.8511	1.3535e-04 m
2	2.3934	1.2731e-04 m
3	2.4041	1.5174e-04 m

Figure 4.11 shows the experimentally determined start-up behaviour of the CSD in the 970 L crystallizer starting at a point directly after the primary nucleation took place, and up to a time of 15 hours thereafter. Details of the experiment are shown in table 2.1. Figure 4.11 (a) shows the median size trend and figure 4.11 (b) shows the distribution quartile ratio. For the first 4 hours of the experiment, the

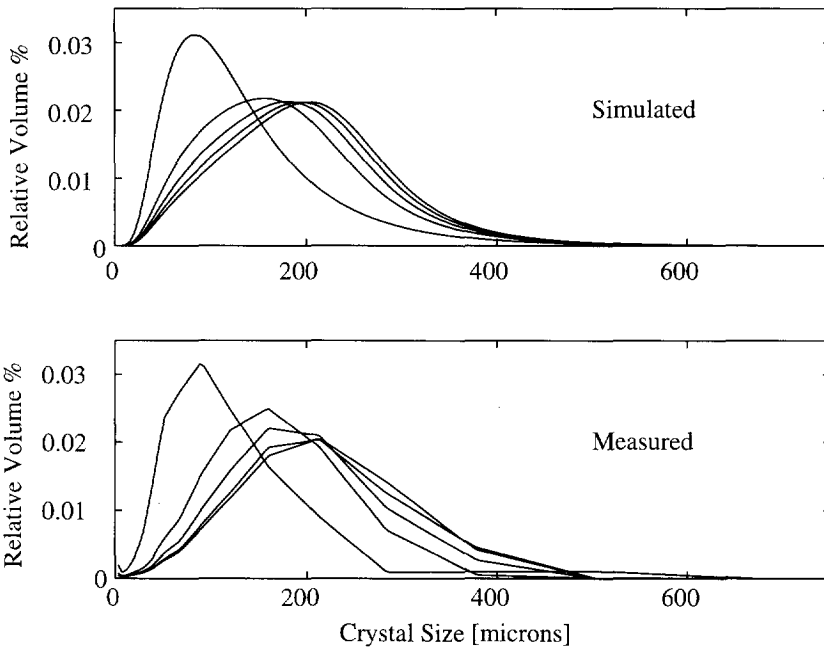


Figure 4.10 (a) and (b) : Measured and simulated distributions for Run 1 in relative volume %

population grows out to a maximum median size of 800 μm . After the median has reached its' maximum value, it begins to decrease due to a combination of product removal, attrition of the larger particles and outgrowth of secondary nuclei. The distribution spread, expressed by the quartile ratio ($\log(X75/X25)$), becomes broader over the same period.

The parameters resulting from the optimisation of the exponential growth rate function of Runs 1, 2 and 3 were averaged and these parameters were used for the simulation where a SDG correlation was included. Equation (4.10) was amended to set a lower limit on the growth rate as a function of the maximum growth rate ($1 - m$),

$$G(x) = 1 - m \exp\left(-\left(\frac{x}{x_g}\right)^n\right). \quad (4.18)$$

The function estimated to model the results of the 2 L growth cell results has a sharp slope towards the small sizes which eventually reaches a zero growth rate below about 30 μm . Non-growers in the system below this size may be responsible for the

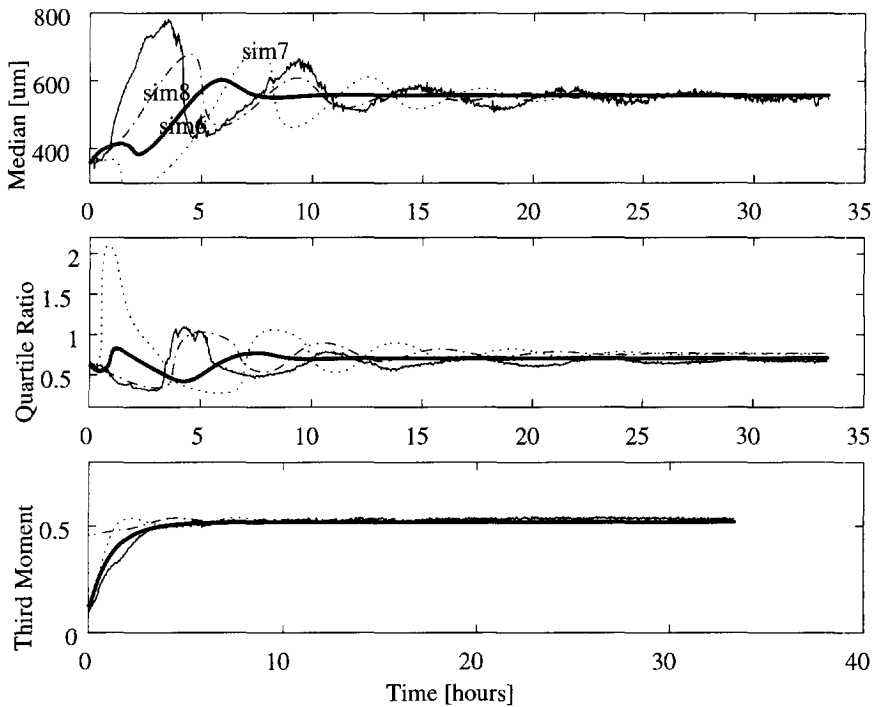


Figure 4.11 : Start-up behaviour of the 970 L crystallizer. Models used for the simulations are described in table 4.4.

very low growth rate below these sizes, and the good resolution of the Malvern is able to detect this population. Equation (4.10) is however amended to equation (4.18) for use in the 970 L crystallizer, as the non-growers in the continuous model are already accounted for by assuming a survival efficiency factor. This factor assumes that a fraction of the crystals do not grow and simply leave the crystallizer via the product line or are dissolved in the fines line, while the remainder grow with an average growth rate as given by equation (4.18).

The same kinetic expressions are used as were used in table 2.2 for sim1, the only difference being that the growth rate is made size dependent in simulations sim7 and sim8. Attrition was not modelled and equation (2.6) was used to describe the nucleation rate. The data used are the same as those used to show the effect of different secondary nucleation models on the dynamic behaviour in chapter 2 (figure 2.4). Simulation sim6 shows how using the power law and a supersaturation dependent growth rate, the median size oscillates out of phase with the measured data and reaches a steady-state very quickly. Simulation sim7 is the same as sim6 except that

the SDG function is implemented. For the lower limit of the growth rate, a value of $(I-m) = 0.20$ was taken for the underlimit in the growth function (equation (4.18)), which from later work (chapter 5) was found to give a proper fit. The inflection point ' x_g ' was $140 \mu\text{m}$ and the power ' n ' was 2.30. The simulation (sim7) shows that by including a SDG function, that the CSD oscillates much more. This happens for two reasons. Firstly, a SDG rate introduces a curvature in the sub $250 \mu\text{m}$ region of the $\ln(n)$ vs. x plot and means that the nucleation rate is much higher. The nuclei grow out much more slowly due to the SDG effect, and as the numbers of large crystals in the crystallizer reduce due to attrition and product removal, the presence of the large number of slow growing crystals will be seen in the low median size. The same effect occurs several times to give rise to the observed oscillating behaviour. To show that the oscillations are in phase with the measured data, the boundary condition was changed in simulation sim8 and it is seen that the simulation oscillations correspond to the measured oscillations.

Figure 4.12 (a) and (b) shows photographs of the surfaces of two ammonium sulphate crystals removed from the fines line. On the surfaces of both crystals, a series of concentric rings can be seen emanating from the centre of the crystal faces and propagating to the edges of the crystals. This type of growth is probably caused by spiral activity where a number of dislocations at the centre of the crystal faces act as the source of the spiral steps. It can also be seen that as the steps reach the edges of the crystals, they increase in size due to the bunching of individual steps to form macrosteps. At some points along the wavefronts, local curvatures are introduced into the step. These curvatures are probably caused by growth instabilities.

Table 4.4 : Kinetic models used for simulations in figure 4.11

Tag	sim6	sim7	sim8
Growth	$\sim \sigma$	$\sim \sigma \cdot f(x)$	$\sim \sigma \cdot f(x)$
Attrition	-	-	-
Nucleation	$\sim m3\sigma^2$	$\sim m3\sigma^2$	$\sim m3\sigma^2$

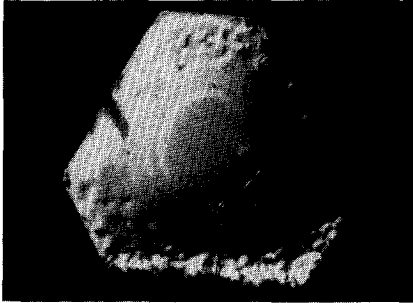


Figure 4.12 (a) : *Surface structure of ammonium sulphate crystal. Width of crystal 200 microns*

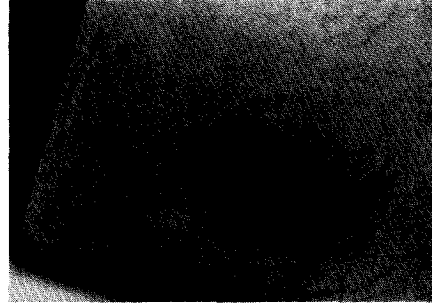


Figure 4.12 (b) : *Ammonium sulphate crystal. Face width 300 microns*

4.7.5 Conclusions : 2 L Growth Cell Experiments

The growth rate of sub 250 μm particles can be described using an exponential SDG rate correlation. Such a model can be incorporated into the population balance to simulate the entire crystallization behaviour. It is then possible to obtain a better fit to the experimental data.

Even though a SDG function is successful in describing the average growth behaviour of the crystals as a function of crystal size, the actual growth of individual crystals may not be size dependent. Small 30 ml growth cells into which samples from the fines line can be diverted, to measure the growth rate of individual crystals would give an insight into the actual growth mechanism.

4.8 Mosaic Spread Measurements

4.8.1 Experimental

For the Laue diffraction experiments, ammonium sulphate crystals were removed from the product line of the 970L crystallizer. The crystals were filtered out of suspension, were dried and sieved (for a short time) into several classes (table 4.5). For the analysis, the measurements were done on single crystals and also on groups of crystals from each sieve range, to get a more dependable estimate of the range and average mosaic spreads present in each class. Previous measurements, also of sieved groups of ammonium sulphate crystals, using a normal X-ray source (Enraf/Nonius 7,

45 kV, 20 mA), showed that a high degree of strain existed in the crystals for the lower size classes $< 100 \mu\text{m}$, as evidenced by the elongated spots in the Laue diffraction pattern (not shown here). Due to the very low intensity of the X-ray beam, exposure times of up to 45 minutes were required. Such long exposure times made it very difficult to optimise experimental settings such as the film to sample distance, the number of crystals used in the sample and the collimator size. The experimental results shown here were carried out at the Daresbury synchrotron radiation source (SRS) in England.

Table 4.5 : Details of crystal sieve fractions and the measurements.

Ammonium Sulphate Class	Beam intensity mA	Exposure Time ms	Film/Sample distance mm
22 - 44	256.5	500	62
52 - 60	253.1	400	62
60 - 88	224.9	100	62
88 - 124	227.2	50	60
124 - 148	222.2	60	62
148 - 176	220.0	60	62
176 - 228	228.2	50	62

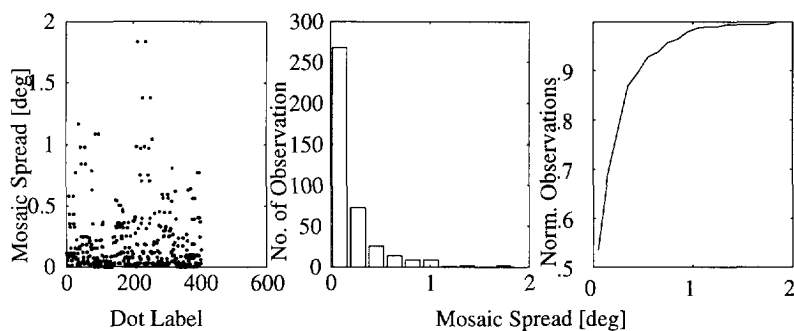


Figure 4.13 a,b,c : (a) Dot label no. versus mosaic spread (b) Ordered number of observations versus mosaic spread and (c) Normalised and cumulative no. of observations vs. mosaic spread

The high beam intensity (0.3 - 2.5 Å) using the Laue diffraction beamline (station 9.7) means that much shorter exposure times are necessary to obtain good Laue diffraction images. The crystals were prepared and mounted in the same way as described in Harding et al. (1992), using a glass fibre rod on which a short length (1 cm) of glass wool is glued (araldite epoxy glue). The crystal(s) is (are) glued to the end of the glass wool fibre.

4.8.2 Analysis

To analyse the results, a CCD camera was used to first digitise the diffraction images and the accompanying software was used to measure the spot extensions automatically.

The mosaic spread, η , of a crystal is a measure of the amount of strain present in a crystal. The mosaic spread is calculated from Laue diffraction patterns. The effect of high mosaic spreads is to produce Laue patterns whose spots are radially elongated ellipses. The degree of elongation provides a measure of η . By measuring the elongation (R), the distance of the centre of the film negative from the centre of the examined crystal and by calculating the Bragg angle (θ) (see section 3.4.3, chapter 3), the mosaic spread can be calculated with equation (4.19), (Helliwell et al., 1989) :

$$\eta = \frac{R}{2D} \cos^2(2\theta). \quad (4.19)$$

Harding et al. (1992) report that a crystal of good quality will have a mosaic spread of about 0.1° or less. For a mosaic spread greater than about 0.5° , internal strain is evident and the spot extension is then linearly related to η . Therefore they chose 0.5° as the limit above which mosaic spread is a measure for the internal strain. This approach was also used in the work of Ristic et al. (1988), and is also used here.

Figure 3.15 (chapter 3) shows a digitised image of a quarter of the diffraction pattern for a group of crystals in the 124-148 μm sieve range. The dark background has been filtered out of the original negative image (figure 3.14) and each diffraction spot has been given a number. The length of each spot was measured and its' distance from the centre of the image to calculate the Bragg angle. Using equation 4.19, the mosaic spread represented by each spot (observation) was calculated. Figure 4.13 (a) shows a plot of the extent of mosaic spread in each observation (spot) while figure 4.13 (b) is the same as figure 4.13 (a) except that the mosaic spread observations are ordered into 20 classes between 0 and 2° of mosaic spread. It was found difficult however, to compare the results of samples from different crystal size classes when represented by a histogram (as in figure 4.13 (b)) as the total number of observations

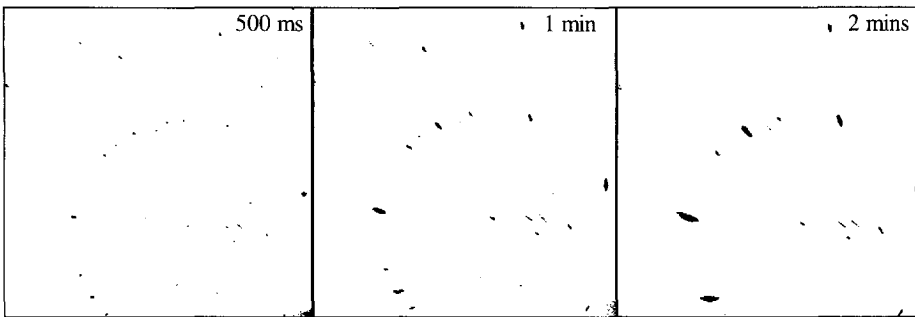
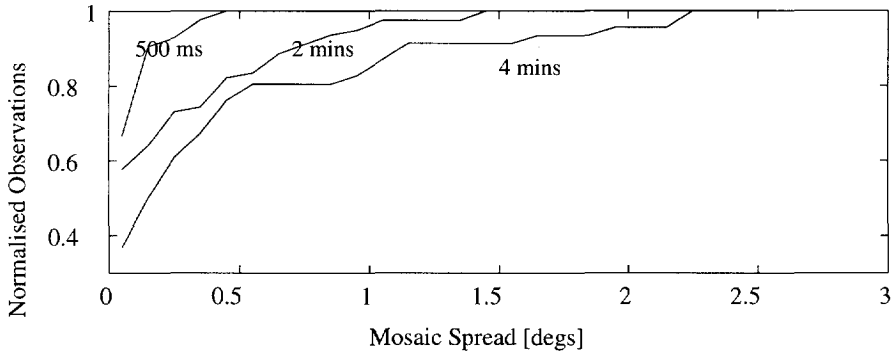


Figure 4.14 (a) to (d): Effect of overexposure on the extent of mosaic spread in a single crystal 150/150/100 microns, 500 ms (a), 1 min (b) and 2 mins (c). Upper diagram (4.14 (d)) shows the normalised and cumulative mosaic spread.

varied from one sample to the next. To enable comparison of the various crystal size classes, the results were represented as cumulative curves of the numbers of observations vs. the mosaic spread, and the curve was further normalised by dividing the number of observations in each mosaic spread class by the total number of observations over all classes in one sample to give the curve as in figure 4.13 (c).

4.8.3 Results and discussion

Diffraction experiments

Both sets of diffraction experiments with a single and a group of crystals were successfully carried out. The single crystal experiments revealed that not every crystal in a particular class contained the same level of strain but it varied from crystal to

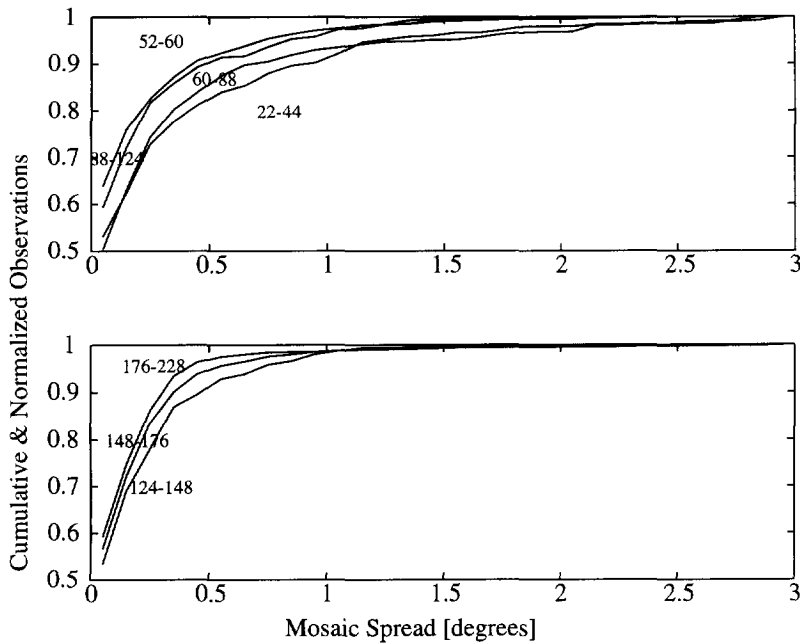


Figure 4.15 (a) and (b) : *Change in mosaic spread in each class of crystals*

crystal. Very little information could be gathered from the diffraction image of one crystal especially from the smallest crystals (22 μm) as the Laue pattern had only a few spots. A better representation of the average strain level in a particular sieve class was found by analysing the Laue diffraction pattern for a group of crystals glued to the holder. Figure 4.13 results from the analysis of the Laue diffraction pattern recorded after exposure of a group of crystals from the 124-148 μm class to the SRS. A quarter of this pattern is shown in figure 3.15. Each point in figure 4.13 (c) represents the relative cumulative fraction of spots having a mosaic spread up to that particular amount. About 53% of the spots have a mosaic spread between 0 and 0.1°. This indicates the presence of large unstrained areas of the crystal (or unstrained crystals). If a lower limit of 0.5° is chosen as the limit above which the presence of mosaic spread can lead to a SDG/GRD effect, almost 80% of the observations will lie below this point. The presence of mosaic spread above 0.3° indicates that at sizes between 124-148 μm , there will be a GRD/SDG effect present. The maximum extent of mosaic spread in this sample is about 1.3° above which only about 2 observations are present as can be seen from figure 4.13 (a).

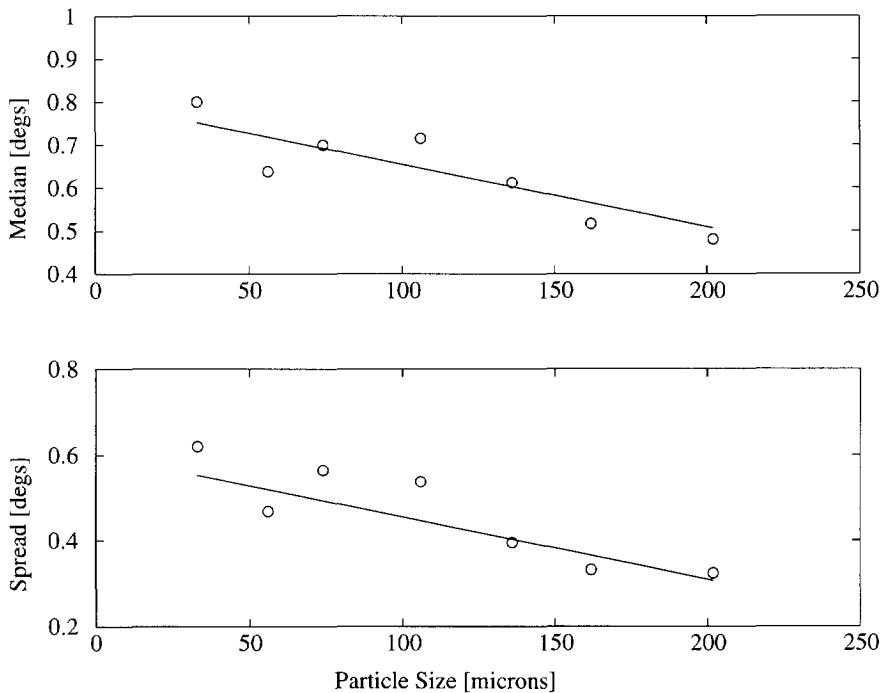


Figure 4.16 : Median and spread in mosaic spread as a function of crystal size

Figures 4.14 shows the effects of overexposing a single crystal of dimensions 150/150/100 μm to too much radiation. The initial exposure of 500 ms is shown in figure 4.14 (a). The crystal was further subjected to a 2 minute exposure of the X-ray beam (figure 4.14 (b)). The diffraction pattern remains the same but the diffraction spots have become elongated indicating the introduction of mosaic spread into the crystal structure associated with radiation damage. After 4 minutes (figure 4.14 (c)), the crystal was further damaged as can be seen by the increase in spot size. Also some spots present in figure 4.14 (a) and (b) have begun to disappear. The resulting cumulative plots of the mosaic spread from these measurements are displayed in figure 4.14 (d). The first measurement (figure 4.14 (a)) shows no mosaic spread above 0.3° , but as the crystal is further exposed to radiation, more mosaic spread is introduced into its' structure. In general, the ammonium sulphate crystals over the entire range from 20 to 800 μm proved to be very robust, showing consistently no damage below an exposure time of 30 secs. With exposure times varying from 100 to 500 ms as in normal experiments, the results shown here are well outside of the danger zone. Exposure times for all the samples shown here are given in table 4.5.

Figure 4.15 (a) and (b) shows the curves obtained for each of the classes shown in table 4.5. Once again, these curves show the cumulative and normalised number of observations in every class. In each case, the number of observations in the first mosaic class exceeds 50% of the total number. With increasing sieve sample size, the maximum extent of mosaic spread decreases. The curve representing the sample in the 176 to 228 μm size class reaches its' maximum unity value much quicker than the 22 to 44 μm sample. Figure 4.16 shows a plot of the median and standard deviation in the mosaic spread with increasing sample size. A lower limit of 0.5° was set to the data in accordance with Harding et al. (1992) to obtain these data. Figure 4.16 shows in general that there is a decrease in the median and standard deviation of the mosaic spread with increasing sample size. In terms of the average growth rate in relation to equation (4.4), this indicates that the growth rate increases with increasing crystal size but that the spread in growth rate decreases.

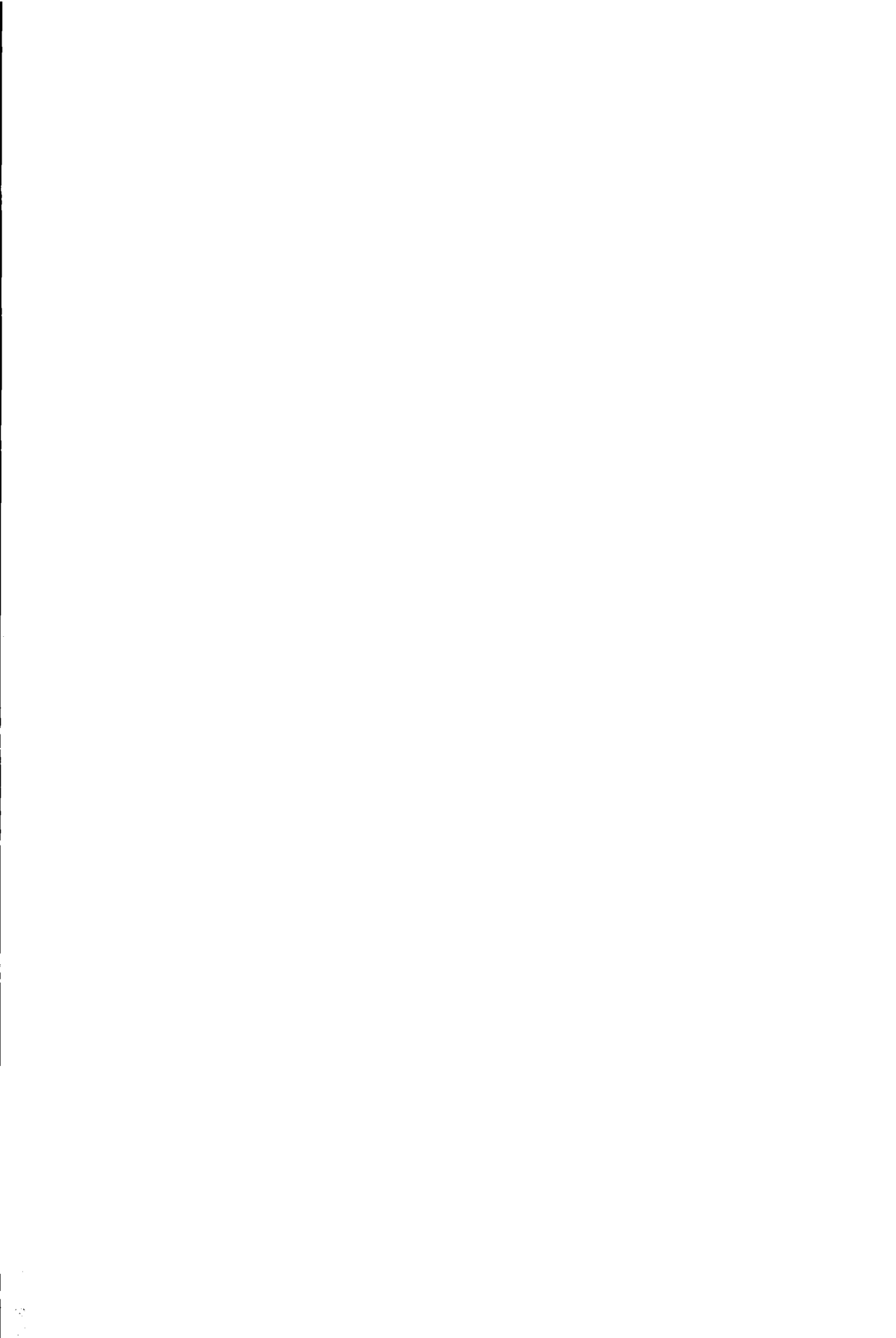
4.8.4 Conclusions

From the results presented above, several conclusions can be drawn.

- Crystals of ammonium sulphate produced in the 970 L crystallizer exhibit a SDG behaviour (below 250 μm) which can be characterised by an exponential SDG model.
- In general, the average level of mosaic spread decreases with increasing crystal size, while the standard deviation in the mosaic spread also decreases. These trends are consistent with a combination SDG and a GRD mechanism, and confirm the expected trend in mosaic spread as is predicted by equation (4.3).
- Above a size of about 200 μm , there exists very little mosaic spread in the crystals above 0.5° . If mosaic spread above 0.5° is an indication of the existence of SDG/GRD, then these crystals should grow with a maximum growth rate.

The results of the Laue diffraction experiments show a surprisingly good agreement with the growth rate experiments. Figure 4.9 (a) shows that the SDG effect leaves the crystals when they reach a size of between 180 to 250 μm . At these sizes, the mosaic spread should have a value of about 0.5° indicating that the effects of SDG/GRD are no longer appreciable. From figure 4.16 (a), one sees that this is indeed

the case with the mosaic spread in the 176-228 μm size class having a median of 0.3° . This result goes a significant way to confirming that increased levels of internal strain in nuclei produced by an attrition process leads to a reduced growth rate of crystals.



Chapter 5

A Model for Secondary Nucleation in a Suspension Crystallizer

Summary - A model is presented with which it is possible to evaluate the secondary nucleation rate in a pilot scale industrial crystallizer. This is done by relating the secondary nucleation rate directly to the volume rate of attrition of large parent crystals. Two other terms are included in the equality, one which expresses the distribution formed by the attrition fragments and the other expressing a survival efficiency accounting for the percentage of attrition fragments which grow out after the attrition step. The model is further tested on a 970 L draft-tube-baffled evaporative crystallizer with ammonium sulphate as the model material used for crystallization and having an on-line crystal size distribution measuring device.

Three types of experiments on the 970 L crystallizer have been done to validate the model. The first are continuous start-up experiments where an initial distribution is formed by primary nucleation and the system is operated under constant operating conditions until a steady-state is reached. Secondly, a series of short semi-batch start-up experiments have been carried out also under constant external operating conditions. Lastly, an identification experiment is carried out where the crystallizer was operated until a steady-state was reached, and then step changes in the fines flow rate, the heat input and the residence time were programmed.

The model was satisfactorily able to simulate the three types of responses, validating the proposed model.

5.1 Introduction

The task of modelling secondary nucleation, has, in the past, been made difficult by the fact that very little experimental data was available over sustained periods of time with which quantitative relationships could be derived between the rate of secondary nucleation and the rate of attrition of the parent crystals.

Because of this, the rate of secondary nucleation was modelled as an 'effective' nucleation rate and was related empirically to parameters describing the energy input to the crystallizer, the growth rate of crystals and a parameter representing the crystal size distribution (CSD), such as the second or third moment of the distribution. These correlations do not perform accurately (see section 2.4.3), when modelling the dynamics of crystallising systems, and also the fact that these correlations are empirical in nature, means that they give little insight into the mechanism of secondary nucleation. Moreover, they miss the vital link with the process of attrition from which the nuclei originate. Further, they also use the 'effective' nucleation rate as a boundary condition depositing the total number of secondary nuclei at one point along the crystal length axis, ignoring the fact that a distribution of fragments is produced.

Much experimental work has been done in evaluating the rate of production of attrition fragments for several different materials under non-growing conditions. To allow an accurate measurement of the attrition rate to be made, sharp crystal fractions were suspended in either saturated solutions or inert liquids and mixed using any one of a number of suspension impellers (Mazarotta, 1992, Jager, 1990). Using this method, a length dependent attrition function could be built, including parameters accounting for the effects of impeller type and power input to the crystallizer. This approach assumes that the rate and source of attrition fragment production, as well as the distribution formed by the fragments under conditions of non-growth, will satisfactorily reflect the same quantities under conditions of growth in a suspension crystallizer. This is highly unlikely as the crystals lose their sharp edges and corners under non-growing conditions.

The main objective of this chapter is to show that it is in essence possible, to model secondary nucleation in a suspension crystallizer using only CSD data obtained from a continuous crystallisation of ammonium sulphate. This is done by assuming a length dependent attrition function and by directly relating the volume of attrited particles to the secondary nucleation function via a survival efficiency. Two parameters are also incorporated to describe the position and spread of the attrition particle distribution.

The growth rate of crystals in the small size ranges is accounted for by implementing the SDG function developed in chapter 4.

The model is validated for the case of ammonium sulphate crystallization in this chapter by fitting the model to the results of three types of experiments, i.e. continuous start-ups, semi-batch start-ups and a steady-state identification experiment.

5.2 Theory of Secondary Nucleation models

5.2.1 The empirical power law

The notion of modelling the CSD in a crystallizer using the model assumptions associated with the **Mixed-Suspension-Mixed-Product-Removal** (MSMPR) concept has been used by many workers to simulate the CSD present at steady-state in a crystallizer (O'Dell and Rousseau, 1978, Rojkowski, 1993). This concept results in a straight line function by plotting the logarithm of the population density function ($n(x)$ ($\#/m^4$)) against the crystal size (x (m)). The slope of this line is determined by the growth rate of the crystals (G_{kin}) and the residence time (τ) of the suspension in the crystallizer, according to the MSMPR equation (section 2.3.3) :

$$\ln(n(x)) = \ln(n_o) - \frac{x}{G_{kin}\tau}, \quad (5.1)$$

where n_o is the population density in the first size class formed by a secondary nucleation process. When comparing the function predicted by the MSMPR theory with the real distribution measured in a crystallizer at steady-state, several deviations are apparent. In the large particle size ranges (figure 5.1), a downward curvature is seen which indicates that, assuming a well mixed system, there is a reduction in growth rate at these sizes. This reduction in growth rate has been attributed to crystal attrition and has been modelled as a negative growth rate ($G_{attr}(x)$) (Jager, 1991). In the small particle size ranges, an upward curvature is observed in the $\ln(n(x))$ vs. x plot. This deviation has been attributed to the observation that in reality, crystals are born over a distribution of sizes, and exhibit size dependent growth (SDG) and growth rate dispersion (GRD) up to sizes of 80 to 100 μm giving rise to this upward curvature (Rusli et al., 1980, Rojkowski, 1993) . To account for these phenomena, accurate knowledge of such a birth function and also of the initial growth rates of secondary nuclei is required. As this information is, in most instances not available, the problem is addressed by assuming that all particles grow at the same rate and an 'effective'

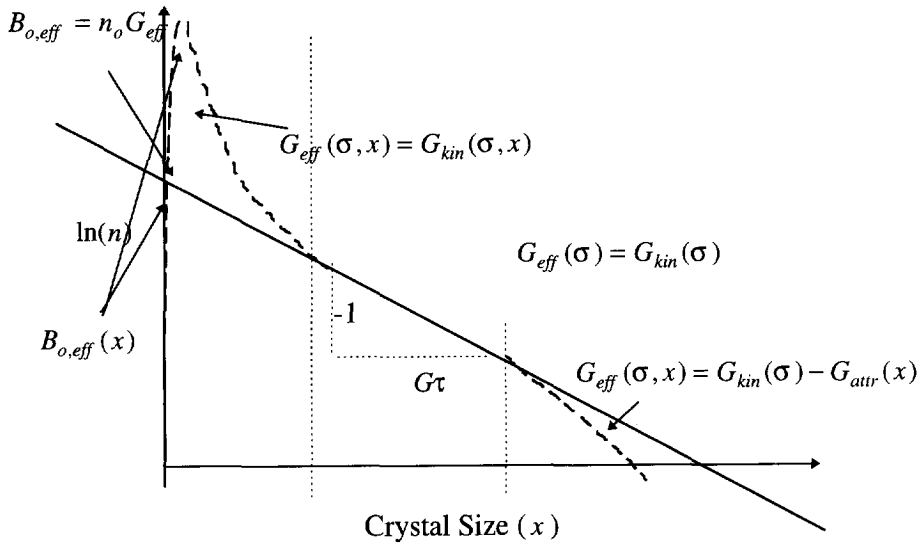


Figure 5.1 : Plot of $\ln(\text{population density})$ vs. Crystal length, MSMPR and deviations

nucleation rate is used ($B_{o,eff}$ ($\#/m^3 s$)) whereby crystals are born at a size close to zero as in the MSMPR concept. Over the years, many correlations have been proposed for the 'effective' rate of secondary nucleation, which are related to properties of the crystallising solution such as the supersaturation or growth rate ($\sigma, G_{kin}(\sigma)$), the mechanical agitation in the crystallizer (impeller speed or power input, N, ϵ) and a property representing the crystal size distribution (CSD), such as the mass hold-up (M_p):

$$B_o \sim \sigma^b N^h M_p^j \sim G_{kin}^i \epsilon^k M_p^j \tag{5.2}$$

Empirical in nature, these correlations give poor descriptions of the dynamics of the systems (see section 2.4.3) on which they are modelled. The power law has also been used as a scale-up criteria, but judging from the volume of published data on the subject (see for example, Grootcholten et al., 1982, Garside and Jancic, 1979, Bourne and Hungerbuehler, 1980), no rigorous method has yet been developed to use the equation, to predict the secondary nucleation rate of different materials on different scales based on information regarding vessel geometry and properties of the material. Also, being empirical, the power law gives little insight into the mechanism behind secondary nucleation.

5.2.2 Mechanistic models

In early descriptions of secondary nucleation, Ottens et al. (1972) and Botsaris (1976), proposed that the secondary nucleation rate per crystal could be related to three factors,

$$B_o = \dot{E}_t F_1 F_2 \quad (5.3)$$

where (\dot{E}_t) represents the rate of energy transfer to the crystal, F_1 is the number of attrition entities produced per unit of collision energy, and F_2 is the fraction of entities which survive to become nuclei.

Later, Mersmann et al. (1988), attempted to make a more precise estimate of the volume of material attrited from a parent crystal by introducing material parameters into the modelling procedure. To do this, the theory of Herz-Huber (Landau and Lifshitz, 1986) for the elastic interactions between two bodies was used, thus enabling the attrited volume to be calculated. Another notion introduced in this work was the idea of target efficiencies, whereby the probability of a collision between a crystal and the impeller could be calculated based on considerations of particle size and impeller geometry and rotational speed. By evaluating all these factors, the volume rate of attrition (\dot{V}_{attr}) could be calculated which could then be related to the 'effective' nucleation rate ($B_{o,eff}$), by the following expression :

$$B_{o,eff} \approx \frac{m_{a,eff}}{m_{a,tot}} \frac{\dot{V}_{attr}}{k_v x_{attr}^3} \quad (5.4)$$

The second group of terms in this expression represents the number of all loose fragments produced by attrition (\dot{E}, F_1), while the first represents the fraction of the total mass of produced particles which act as effective secondary nuclei (F_2).

In reality then, this work also consists of a two step process similar to those proposed by Ottens et al. and Botsaris.

In 1990, Daudey et al. proposed a more detailed three step model to describe secondary nucleation, which was consistent with experimental observations of the growth behaviour of secondary nuclei and also attempted to account for the formation of surface growth structures of crystals in suspension. They defined two sources of nuclei, the first leading to the production of nuclei by attrition of macrosteps or other growth formations (F) on the crystal surface, a mechanism which they termed '**surface breeding**' and the second related to the attrition of portions of the crystal lattice which could not previously have been identified as possible sources of nuclei.

This manner of production, they termed '**mechanical breeding**' and would be the category into which previous modelling of secondary nucleation would fall. Further, they suggested that the surface relief related nuclei and the mechanical fragments would exhibit different (*survival* and) *outgrowth* ($\eta_{survival}$) kinetics as mechanical fragments may be more stressed than surface relief fragments (Garside and Larson, 1978). In equation form then, the effective nucleation rate is given by :

$$B_{o,eff} = \eta_{survival} \eta_{removal} F \quad (5.5)$$

In this equation again, the last two terms ($\eta_{removal} F$) can be lumped together to express the total number of attrition particles released by the parent crystals, while the first term ($\eta_{survival}$) expresses the fraction of these particles which grow out to larger sizes.

Working within the same framework, Van der Heijden et al. (1994), assuming a spiral growth mechanism, refined this theory by introducing parameters accounting for the height and the number density of steps on the crystal surface. They also pointed out that the amount of impurities present in the suspension are of great importance in determining the rate of production of secondary nuclei. The adsorption of such impurities would lead to weak points in the crystal lattice between successive layers of macrosteps, making them more susceptible to attrition processes. Also, the level and type of impurities in the suspension, effects the number and height of steps on the crystal surface. Both of these effects support the notion of a surface breeding mechanism suggested by Daudey et al. (1990). It has already been shown that such growth entities are responsible for the formation of secondary nuclei (Van der Heijden et al., 1990). In a separate paper (Van der Heijden et al., 1989), they showed that a distribution of fragments was produced by contacting a steel rod with a stationary crystal surface. The distribution of fragments took the form of a log-normal distribution with a median size of about 9 μm . Nienow et al. (1978) detected distributions having a lower limit of 1 μm and a mean size of 5 μm in abrasion experiments using copper sulphate crystals. Other workers (Youngquist and Randolph, 1972) have shown that by suspending samples of crystals in a crystallizer, secondary nuclei in the size range $< 3 \mu\text{m}$ were produced. A lower limit to the size of secondary nuclei produced could not be detected due to restrictions in the range of the CSD measuring instrument. Similar measurements for potash alum contact nuclei (Rusli et al., 1980) have shown similar results, where a large number of nuclei smaller in size than 4 μm were detected. These crystals were further shown to grow very slowly or not at all.

Assuming that attrition fragments are distributed over a range of sizes ($H(x)$), equation (5.5) becomes :

$$B_{o,eff}(x) = \eta_{survival} \eta_{removal} H(x) F \quad (5.6)$$

Note that the secondary nucleation function is given in terms of number density ($\#/m^4 s$), being a length dependent function, unlike in the literature references above, where it is given as the total number of attrition particles ($\#/m^3 s$), and used as a boundary condition.

5.3 New Model

Keeping the framework described in the above section in mind, an example of how to determine the secondary nucleation rate is given below, for the specific case of ammonium sulphate crystallization for which much kinetic information regarding attrition is available.

Many correlations for the attrition rate ($G_{attr}(x)$) exist which are normally taken as functions of particle length only. It has been shown that the following expression satisfactorily describes the attrition rate in the draft tube crystallizer under study in this work (Eek et al., 1995), for ammonium sulphate crystallization,

$$G_{attr}(x) = p6 \left(1 - \left(\frac{1}{1 + \left(\frac{x}{p7} \right)^{p8}} \right) \right) \quad (5.7)$$

The length term 'x' in this equation could also be expressed as the surface area ($\propto x^2$) or the volume of the crystal ($\propto x^3$), thus reducing the power in the attrition function appropriately.

The deviation in the MSMPR $\ln(n(x))$ vs. x line due to attrition of large particles is shown in figure 5.1.

The correlation in equation (5.7) contains three unknown parameters ($p6, p7, p8$), which must be evaluated from experimental CSD curves obtained under growing conditions. The term $p6$ is the product of two terms. For the case of ammonium sulphate crystals, the value of $\eta_{removal}$ is unity, therefore it is lumped together with the attrition rate constant $p6$. Evidence for making the assumption of $\eta_{removal} = 1$ was gathered by examining the surfaces of ammonium sulphate crystals which were sampled in the product line from the crystallizer under study in this work. The photographs showed that no loose or partially loose attrition

fragments were located on the crystal surfaces, even though there was clear evidence of attrition on the crystal corners and edges (see section 5.5). Very often, these parameters are determined independently of the crystallizing system by suspending a pre specified distribution of crystals in either a saturated or inert solution. According to the models discussed above (Van der Heijden, Daudey), using this method, it would only be possible to gain information about the mechanical breeding mechanism of nuclei production as under normal crystallising circumstances, the renewable growth structures on the crystal surfaces, would yield more attrition fragments. There is also a possibility that the distribution resulting from such experiments would be different. On top of this, little account is also taken of the properties of the suspending liquid and its' possible effect on the attrition rate.

Analogous to equation (5.5), the volume rate of production of attrition fragments is given by the product of the formation and removal terms ($\dot{V}_{attr} = \eta_{removal} F$). In equation (5.5), this was calculated from first principle considerations of the mechanics of particle collisions. Here, it is suggested that from the method of moments, the production rate of attrition fragments can be calculated by equation (5.8), from knowledge of the attrition rate function (G_{attr}) of parent crystals and the second moment of the CSD as follows.

$$\dot{V}_{attr} = \int_0^{\infty} G_{attr}(x)n(x)x^2 dx \quad (5.8).$$

The growth rate of all crystals is then expressed as the kinetic growth rate ($G_{kin}(x, \sigma)$) less the growth rate caused by particle attrition,

$$G_{eff}(x, \sigma) = G_{kin}(x, \sigma) - G_{attr}(x). \quad (5.9)$$

A constraint must also be included at this point :

$$\forall x > 0 \Rightarrow G_{eff}(x) > 0.$$

Little information exists on the form and location of the distribution assumed by the attrition fragments. This is, in the most part, due to reasons of practical difficulty. The presence of a very wide distribution of sizes in a suspension crystallizer (1 - 2000 μm) makes it difficult to focus in on a particular size range with conventional on-line measuring devices. The accuracy of sieving techniques are sensitive to errors introduced during the sampling and drying steps. As mentioned in the previous section, experiments carried out under a microscope have shown that by contacting a growing crystal surface with a steel rod, a log-normal distribution of particles is produced (van der Heijden et al., 1989). There are indications that for the

970 L crystallizer, a distribution of attrition fragments is produced which has an average size around 10 μm (see results section 5.5).

During the attrition process, stress will enter the crystal lattice (Bhat et al., 1987). Because of this, and subject to the supersaturation level in the crystallizer, some of these particles will tend to grow out while some will not, and the particles which do grow out will show a distribution in growth rates (Rusli et al., 1980). Many literature references report this phenomena from small scale suspended single crystal experiments to larger scale experiments where the nuclei are produced in suspension. In the model presented here account is taken of a size dependent growth (SDG) rate by using the exponential growth curve used in the simulations in chapter 4. The equation used takes the form (see section 4.7.4),

$$G_{kin}(x, \sigma) = p1\sigma^{p2} (1 - (1 - p3) \exp(-(\frac{x}{p4})^{p5})). \quad (5.10)$$

An efficiency factor is defined, $\eta_{survival}$, which is defined as the ratio of the volume of attrition fragments which grow out to the total volume of attrition fragments produced:

$$\eta_{survival} = \frac{\text{Volume of fragments which grow out}}{\text{Total volume of attrition fragments produced}} \quad (5.11)$$

$\eta_{survival}$ is a function of the supersaturation as a high supersaturation will encourage crystals with a higher stress to grow out, thus,

$$\eta_{survival} = k_{survival} \sigma \quad (5.12)$$

(Note : $k_{outgrowth}$ is labelled $p9$ in the rest of this chapter.)

By assuming $\eta_{survival}$ is constant instead of a function of the supersaturation, a certain size dependent growth rate would be imposed on a fraction of the crystals (equation (5.10)), while the remaining crystals would be assumed not to grow at all.

At this point, it is now possible to derive an expression for the rate of secondary nucleation based on the above considerations. Such an expression is as follows :

$$B_{o,eff} = \eta_{survival} H(x) \dot{V}_{attr}. \quad (5.13)$$

This is subject to a condition of mass conservation :

$$\int_0^{\infty} H(x)x^3 dx = 1.$$

Assuming a log-normal distribution for the attrition fragments, two parameters have to be specified i.e. the position and spread of the distribution.

5.4 Experimental

The experimental procedure for the three types of experiments which will be used to validate the model described above will be outlined in this section.

5.4.1 Effect of attrition on the start-up behaviour

The objective of this series of experiments was to examine the effect of increased attrition levels on the dynamic behaviour in the crystallizer.

Two series of experiments were carried out. A preliminary series on an 800 ml bench scale was carried out with a suspension of sieved ammonium sulphate crystals suspended in a number of organic fluids. Each suspension (800 ml volume) was pumped around in a closed loop containing a Malvern forward light scattering instrument to measure the CSD. This was done to see if a mono type pump could cause attrition of ammonium sulphate crystals and to examine if the properties of the suspending liquid had any effect on the attrition rate. Each experiment lasted 30 mins., after which the cell was emptied, cleaned and refilled with a new suspension. A list of the organic fluids, ammonium sulphate sieve fractions and fluid properties are given in table 5.1. The same starting fraction was used in each case, i.e. 300-400 μm sieve size class and the concentration was also held constant at 1 volume %. A schematic representation of the set-up is given in figure 5.2.

Table 5.1 : *Experimental details and suspension properties*

Run	Run Time	Suspension		Operating conditions		
		Medium		P	η	ρ
	min	Type	Volume	mbar	cp	kg/m ³
1	30	methanol	800	1	.57	.79
2	30	isopropanol	800	1	1.77	.79
3	30	ASsaturated solution	800	1	2.4	1.25
4	30	glycol	800	1	11.1	1.11

The second series of experiments was carried out in a draft-tube baffled crystallizer with a volume of 970 L (see section 3.3.1). Evaporative experiments were carried out under near vacuum (85 mbars) and 50°C. Ammonium sulphate was the

model material for crystallization. For all experiments, the same nominal operating conditions were used (75 mins residence time, 120 kW heat input, 1 L/s fines flow). A variable speed internal impeller was used to fluidise the suspension. Its' speed was held constant throughout all the experiments. An on-line Malvern 2600C was used to measure the change in the CSD with time.

Two types of experiment were carried out. The first type was under crystallizing conditions (supersaturated solution, Run 6 and 19) and the second type mainly under non-crystallizing conditions (Run 26). The operating conditions are shown in table 5.2.

Table 5.2 : *Operating conditions for Run 6 and 19 in the 970 L crystallizer*

<i>Experiment</i>	<i>Heat input (kW)</i>	<i>Fines flow rate (L/s)</i>	<i>Residence time (minutes)</i>	<i>Pump flow rate (L/s)</i>
Run 6	120	1	75	0
Run 19	120	1	75	1

In Run 19, an external (mono) pump was switched on at the beginning of the experiment before the primary nucleation event took place to recirculate the slurry in an external loop, and kept running at a constant speed of 1 L/s until a steady-state was reached after 22 hours. A blank experiment was also carried out where the pump was not in operation (Run 6), but all other operating conditions remained the same. Run 6 was also continued until a steady-state was reached after 30 hours. The details of these experiments are summarised in table 5.2.

The second type of experiment with the 970 L crystallizer was mainly under non-crystallizing conditions (saturated solution, Run 26). The start-up conditions were identical to those of the blank experiment (Run 6), except that 3 hours 20 minutes after the primary nucleation event, the heat of evaporation was switched out and the system changed from a continuous to a batch mode to conserve the crystal mass in the crystallizer. If the crystallizer had been kept in continuous mode, the crystal mass in the crystallizer would gradually have been pumped out of the crystallizer and not been replaced as the heat of evaporation which produces the supersaturation was switched off. The crystallizer was held stationary for 1 hr. 25 mins. This means that no streams were leaving the crystallizer and no streams were entering. This enabled one to observe what the effect of any inherent attrition sources (crystal/impeller interactions) on the CSD was. After 4 hrs. 45 mins., the external pump was switched on at a rate of

2 L/s until the end of the experiment at 8 hrs. 30 mins.. By switching the heat out, the driving force for growth was reduced to zero, and the effect of mechanical stirring and pumping action on the CSD could be observed.

Parameters used to characterise the position and form of the distribution are the volume based median size and the quartile ratio (or the logarithmic ratio of the 75 % to 25 % sizes).

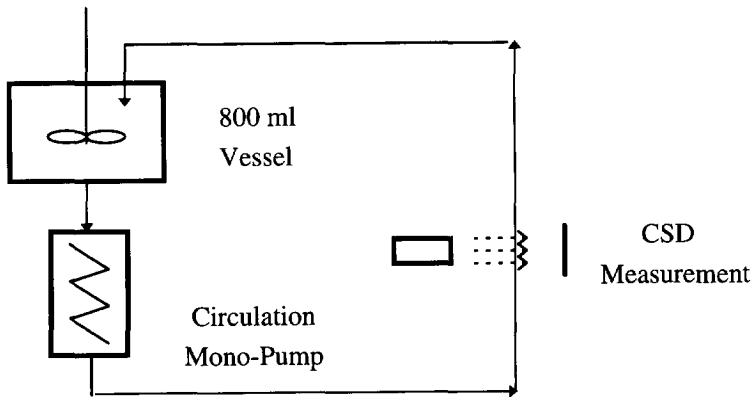


Figure 5.2 : Schematic drawing of small 800 ml recirculation loop

5.4.2 Semi-batch Start-ups

These experiments were also carried out in the 970 l crystallizer. The procedure was basically the same as for the continuous experiments except that no product was removed from the crystallizer. The volume of the suspension was held constant by allowing feed to enter the vessel, to compensate for the water leaving the suspension due to evaporation. A set of three start-ups were carried out under the exact same conditions with no fines removal, to examine the repeatability of the primary nucleation and initial CSD growth phases. The heat input was set at 120 kW. Each experiment lasted about 1.5 hours before water was added to dissolve the crystals and a new run was started.

5.4.3 Continuous identification experiments

In this experiment (Run 56), the crystallizer was started-up as usual from a primary nucleation event until a steady-state had been reached by using a single input

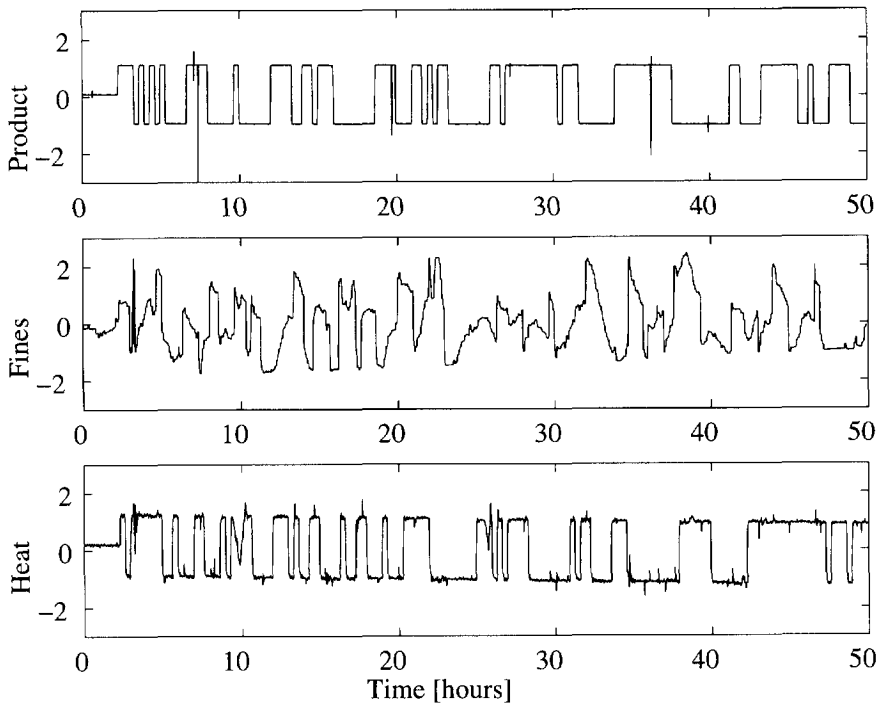


Figure 5.3 : Trend in the product removal rate (upper, (a)), the fines removal (middle, (b)) and the rate of heat input (bottom, (c)) for the continuous identification experiment Run 56

single output (SISO) PI-control loop, which uses a signal related to the amount of sub-30 μm and constructed from Malvern light energy signals as its' input and the fines removal rate as its' output (Eek, 1995). After the steady-state had been reached, three process inputs - fines removal rate (Q_f), residence time (τ) and heat input (P_{hc}) were varied around nominal set points according to a pre-programmed oscillating sequence. The set-points followed by the three process inputs are shown in figure 5.3. The set-points are shown to oscillate around nominal values with fixed maximum amplitudes. The details are shown in table 5.3.

The idea behind this experiment is that when an industrial crystallizer is being operated, the process disturbances which will effect the CSD will be those which will disturb the steady-state situation of the crystallizer. Start-up oscillations will only be encountered when the crystallizer is being put back into operation after a shut-down. These process disturbances will act by changing the process operating conditions in some way, which may be simulated by directly changing the operating conditions as is

done in this experiment. This procedure can only be done when the CSD is at a steady-state, because if it is started before this time, the response of the CSD to the change in operating conditions will be lost in the much stronger start-up oscillatory behaviour of the CSD.

Table 5.3 : *Input values for the crystallizer operating conditions (Run 56)*

<i>Process Input</i>	<i>Nominal Value</i>	<i>Maximum Amplitude</i>
Fines (L/s)	1.5	1
Product (L/s)	.215	.035
Heat (kW)	120	30

5.5 Results and Discussion

5.5.1 Attrition experiments

5.5.1.1 Bench Scale

The median size (X_{50}) and the 25 % size are plotted in figure 5.4. The starting point of the distributions in each experiment is the same which is to be expected as the same crystal fraction is used in all four experiments. During the 30 minute period of the experiments, the median and X_{25} decreases for all the samples at rates which are approximately indirectly proportional to the viscosity of the suspending liquid. Glycol which has the highest viscosity shows the slowest decrease in the median and X_{25} values and methanol which has the lowest viscosity shows the sharpest decrease. Clearly, the evaluation of any kind of attrition function for ammonium sulphate crystals based on these experiments would incur serious errors if no account was taken of the properties of the suspending liquids.

The results of these experiments shows that the action of a mono pump on a crystal suspension causes size reduction of a distribution of crystals. The concentration of crystals was so low (1 volume %) that interactions between crystals leading to this behaviour are discounted. The dependence of the rate of attrition fragment production on the viscosity arises as any force imparted to crystals by the rotor will be absorbed to some extent by the fluid viscous forces. The number and energy of collisions between crystals and the rotor and stator varies according to the viscosity of the suspending liquid. Less energetic collisions will result in the production of fewer attrition fragments.

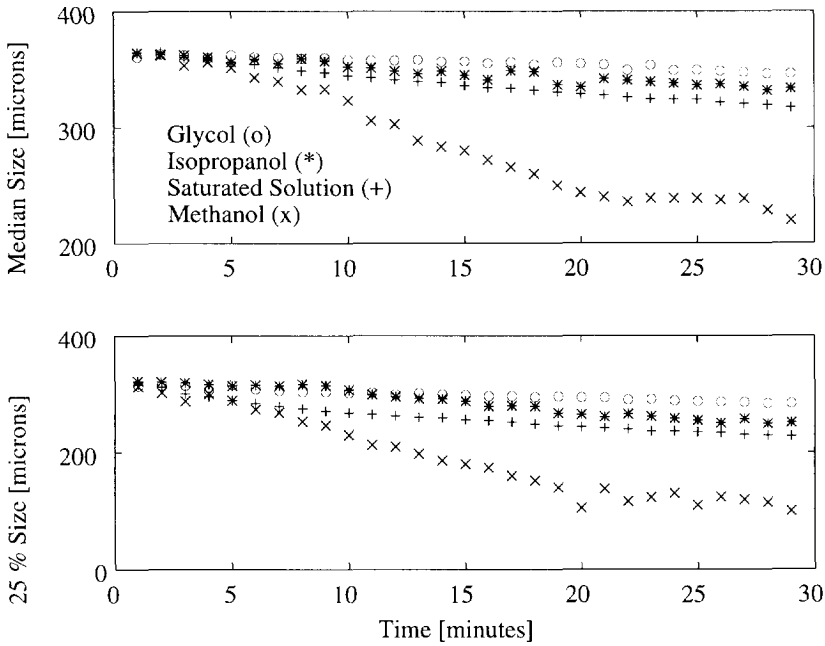


Figure 5.4 : Change in the 50 and 25 % sizes of an initial ammonium sulphate sample due to the action of a mono pump when the crystals are suspended in liquids of varying properties

5.5.1.2 Pilot Scale experiments

In this section, the results of Runs 6, 19 and Run 26 will be discussed.

Having shown by the 800 ml experiments (section 5.5.1.1) that a mono pump causes attrition of crystals, it was decided to use a much larger mono pump which can pump a larger volume, to effect attrition of the crystals in the 970 L crystallizer.

Non-crystallizing conditions

The results of Run 26 will be discussed first, as these give an insight into the mechanism of pump attrition and the difference between the attrition mechanism in an 'inert' solution (supersaturation = 0) and in a solution where a driving force for crystal growth exists, which are all relevant when discussing the series of experiments under crystallizing conditions.

Figure 5.5 shows the results of Run 26. Three classes (15th, 19th and 20th) with respective class median sizes of 480, 951 and 1197 μm of a twenty class grid (ranging from 20 to 1400 μm) are shown.

The heat of evaporation was switched off 3 hours 20 minutes after the primary nucleation event. It was known that under normal operating conditions, between 3 to 4 hours after the nucleation, the CSD median size was at a maximum (see figure 5.8) and that here, a considerable amount of large crystals were present. This occurs as the original distribution present in the crystallizer has grown to larger sizes and this is confirmed in figure 5.5, by the decrease in the signal in class 14 over time, and the increase in the signal in the higher two classes, as the initial distribution grows to the sizes represented by these classes. Based on the assumption that the larger crystals would be more susceptible to attrition, it was important to have a large number of these crystals in the crystallizer as any attrition instigated by the pump would be more noticeable.

After the heat of evaporation was switched out, the crystallizer was changed from continuous operation to a batch mode. The system was held stationary for 1 hr. 25 mins. (see experimental section 5.4.1) to see if the inherent crystallizer attrition sources (crystal/crystal and crystal/crystallizer interactions) had a significant effect on the CSD. The results show that the signal in all three classes remained quite stationary indicating that inherent crystallizer attrition effects were not very strong.

After the pump was switched on after 4 hours 45 minutes (marked in figure 5.5) to a speed of 2 L/s, the signal of the largest class (20th) began to decrease over a period of 30 minutes, while that of the 19th increased slightly over the same period. No change in the contribution of the classes below the 19th could be seen, although this is not to say that these classes are not effected. It could simply be that the resolution of the measuring instrument cannot resolve the change in the contribution in these classes due to attrition or that the magnitude of the response was not great enough to be seen above the experimental noise. The decrease of the signal in the 20th class is caused by size reduction of the crystals due to an attrition effect. The corresponding rise in the 19th class is a consequence of the attrited crystals from class 20 entering this class. After a time of 5 hrs. 15 mins., the signal in classes 19 and 20 stop decreasing and remain constant until the end of the experiment. A SEM examination of crystals (not shown here) before the pump was switched on and after the signal in class 20 had stopped decreasing, revealed that the crystals had lost their sharp edges and corners and had become rounded. This effect is caused by the action of the pump on the crystals in the same way as in the 800 ml experiments. Over time, the pump action rounds the crystal off by removing the areas more susceptible to attrition (corners and

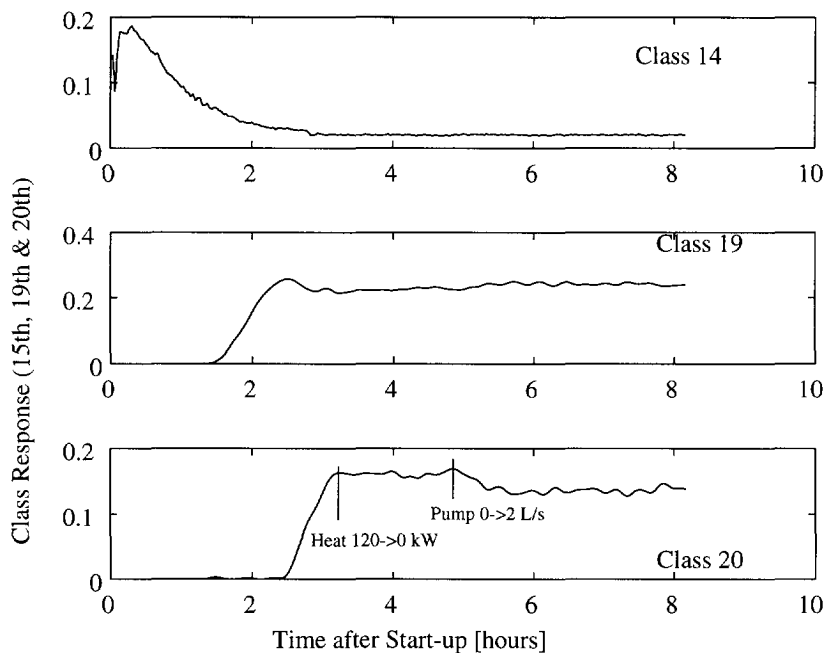


Figure 5.5 : Results of Run 26 where the heat was switched off after 3 hours 20 minutes and the external mono pump was switched on to a speed of 2 L/s after a time of 5 hours

edges). Thereafter, the pump has little effect on the crystal shape. A conclusion which can be drawn from this observation, is that the pump will have an appreciable effect on the attrition rate in a crystallizer, above that of the inherent crystallizer attrition sources, if the crystal has sharp features. The crystals are more likely to be sharp if the supersaturation is positive as opposed to zero, as it is in this experiment.

Crystallizing conditions

The above conclusion was tested in Run 6 and 19. Figure 5.6 shows a photograph taken of a crystal internal structure using an optical microscope projected onto the (100) face taken from Run 6 when the CSD had reached a steady-state. The black areas between the growth sectors are inclusions, which have formed due to the overgrowth of damaged corners and edges. In the photographs, blunt edges and

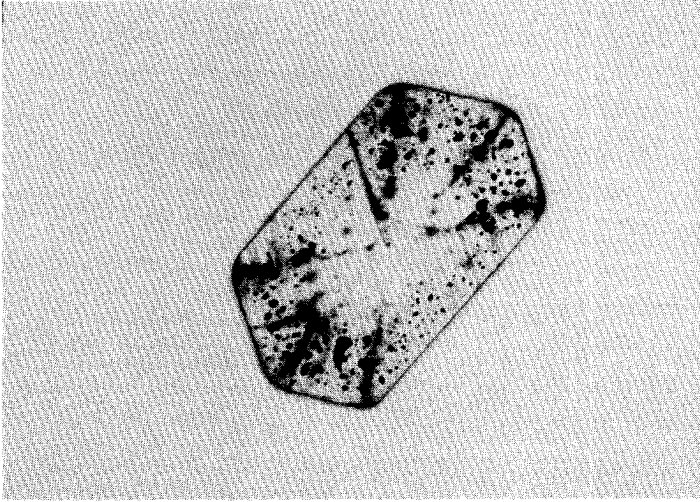


Figure 5.6 : *Optical micrograph of the internal structure of an ammonium sulphate crystal removed from the crystallizer towards the end of Run 6. Projection is of the (110) face (\longleftrightarrow =500 μ m)*

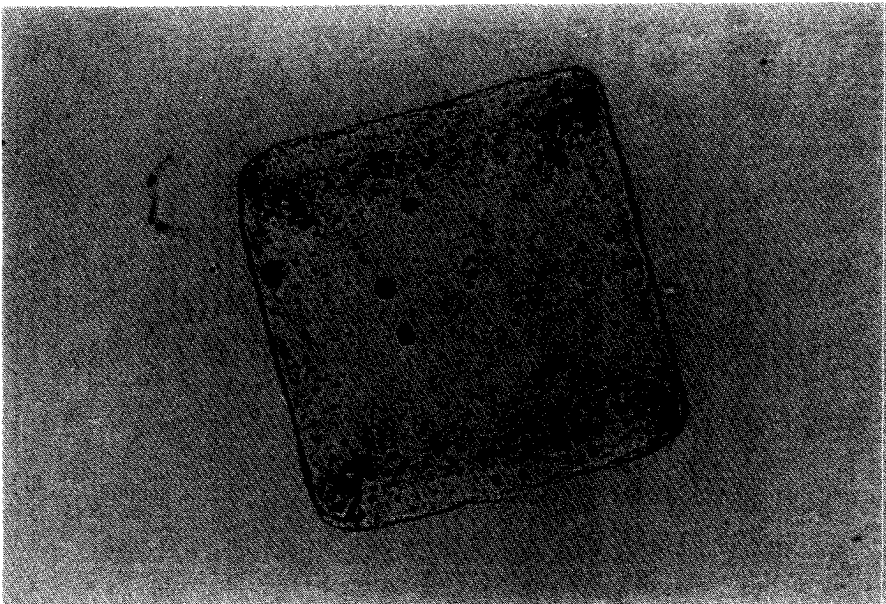


Figure 5.7 : *Optical micrograph of the internal structure of a crystal taken near the end of Run 6. Projection shows the (101) face (\longleftrightarrow 600 μ m)*

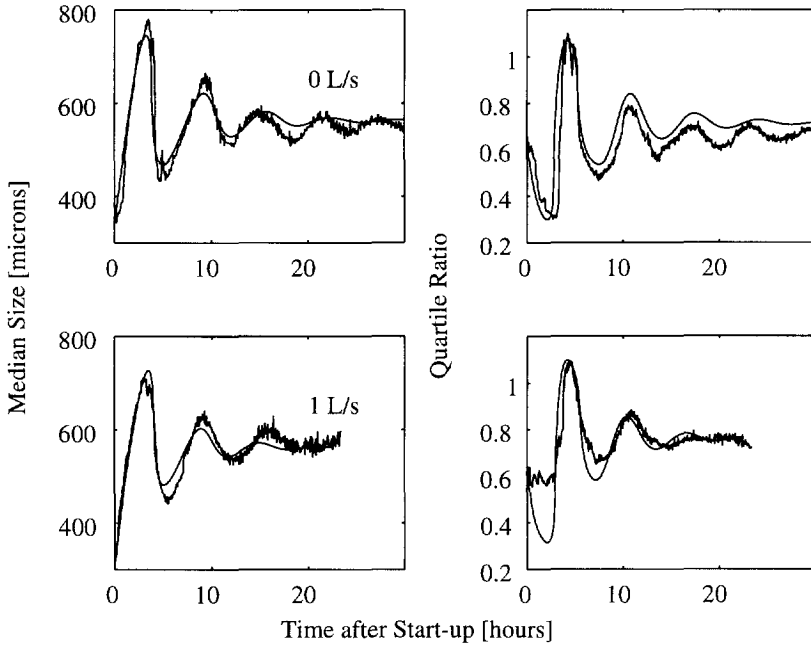


Figure 5.8 : Measured and simulated start-up median and quartile ratio trends for Runs 6 (upper left and right) and 19 (bottom left and right).

Table 5.3 : Parameters Values

Parameters	$p1$	$p2$	$p3$	$p4$	$p5$	$p6$	$p7$	$p8$	$p9$
Units	m/s	-	-	μm	-	m/s	μm	-	-
Run 6	5e-06	1	0.35	100	1	3.3e-09	750	13	68.5
Run 19	5e-06	1	0.2	175	2	2.5e-08	750	3.5	133

corners are seen which have obviously been chipped away by an attrition process. Inside a diameter of about 500 μm in figure 5.6, there are no inclusions present which leads one to the conclusion that attrition was not prominent below this size. Figure 5.7 shows another crystal, but this time the photograph is taken of the (010) face. The same features can be made out, the inclusions between the growth sectors as well as other inclusions in each sector.

Figure 5.8 shows the median size and quartile ratio oscillations of two runs (6 with and 19 without the attrition pump turned on). There is little difference between the eventual steady-state median values of the two experiments (550 μm) although

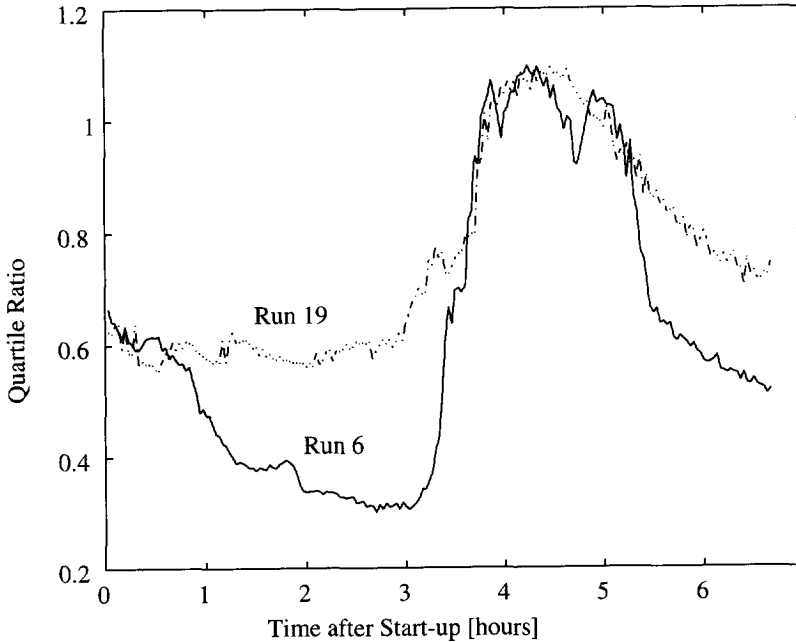


Figure 5.9 : *Quartile ratio trend over the first 6 hours after the primary nucleation step in Runs 6 and 19*

the time taken to reach a steady-state differs. For Run 6, it is reached after about 34 hours and for Run 19, after 18 hours. The quartile ratio, on the other hand expressing the width of the distribution is greater throughout the experiment and at steady-state for Run 19 at a value of 0.75, than for Run 6 at 0.65. This is due to the greater number of attrition particles present in Run 19 in the lower classes making the observed distribution broader.

Using the model outlined previously, the responses of the experiments (6 & 19) to the various process conditions were modelled, to gain an insight into the effect of added attrition on the crystallization kinetics. The modelled responses are also shown in figure 5.8, and the resulting simulation fit parameters are listed in table 5.4. The parameters in the secondary nucleation distribution ($H(x)$) in equation (5.13) for both runs were the same. For Run 6 and Run 19, the median size was $12 \mu\text{m}$. The standard deviation for both was the same at 0.20. In figure 5.8, the measured and simulated dynamic responses of the system are shown.

In general, it can be said that the model is well able to simulate the system dynamic response in terms of the wave period and amplitude, for the case where there

is no attrition pump present (Run 6) and when there is an attrition pump present (Run 19). Given the different parameter set, the simulation is also able to predict the point at which the CSD reaches a steady-state for both experiments. The accuracy of the model is however unsatisfactory in figure 5.8 with respect to the quartile ratio where the simulated value is consistently higher (Run 6) than the measured value.

Very noticeable is the difference in the start-up behaviour between both experiments as expressed by the quartile ratio up to a time of three hours after the initial primary nucleation. In figure 5.9, the distribution spread (quartile ratio) is plotted which highlights the deviation up to this time. The CSD in the case of Run 19 broadens much more quickly than that of Run 6, where the quartile ratio of the distribution remains quite constant over the first three hours, before it increases between 3 and 4 hours due to the combined effects of attrition and secondary nucleation. The model is not able to simulate the combined, inherent crystallizer attrition effects and the pump attrition effect during this period using one attrition function (equation (5.7)). A second attrition function to describe the pump attrition effect might lead to a better fit of Run 19. Introducing such a function would create three new parameters, increasing the amount of fit parameters to eleven. This is too many parameters to evaluate from on-line data, without more a priori information regarding the action of pump attrition.

In subsequent simulations, it was seen that a secondary nucleation distribution ($H(x)$) having a median size between 2 and 20 μm did not have a significant effect on the dynamic behaviour. The only difference in having different values is that at lower values, the nucleation rate increases significantly. The reason for this is that due to the low growth rate of these crystals, the fines removal system will dissolve a larger proportion of them if they have a lower initial size. At higher sizes, the crystals are safer as the fines function which is very sharp (see figure 3.8) will dissolve less crystals.

A significant difference between the parameters is in the power predicted for the attrition function (equation (5.7), p8). For Run 6, this is 13, while for Run 19, it is only 2. This is a consequence of trying to describe two attrition effects (internal/external) with only one attrition function which as mentioned above, is not entirely capable of describing the system dynamics. The lower power in the attrition function for Run 19 means that the function is not as sharp as the function for Run 6. This indicates that the pump attrition effect has a lot more uniform effect on the entire CSD and not just on the larger sizes as in the Run 6 attrition function (inherent crystallizer sources). At steady-state, the survival efficiency for Run 6 was 0.50 and for Run 19, it was 0.70.

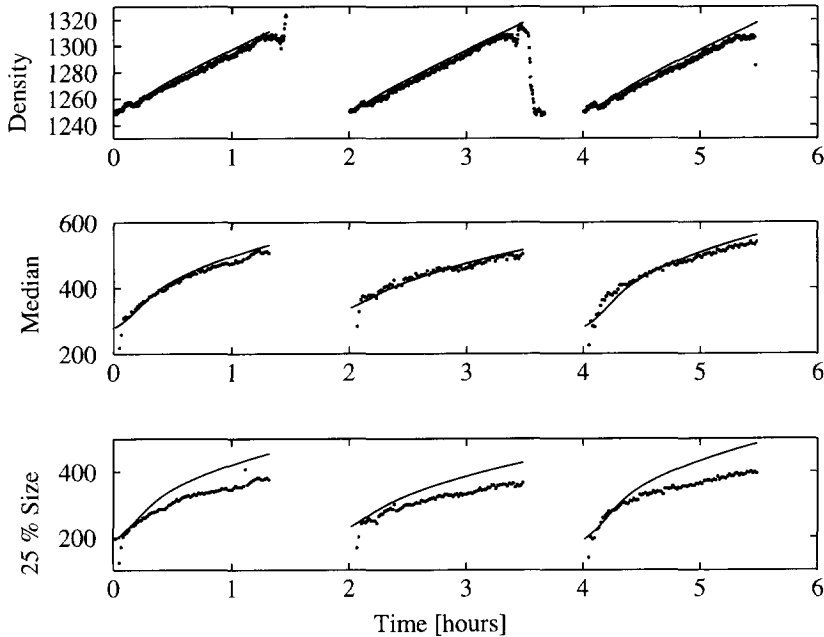


Figure 5.10 : *Three consecutive batch start-ups in the 970 L crystallizer under the same operating conditions (120 kW heat input and no fines removal). Trends in the product density (top), median size (middle) and 25 % sizes are shown.*

An analogy of the effect of a difference in the attrition function between Runs 6 and 19 can be seen in the simulations in figure 2.4 (compare sim3 to sim5). Here the nucleation power law, in which the nucleation rate is related to the entire third moment of the distribution yields an almost non-oscillating start-up behaviour and reaches a steady-state very quickly. The nucleation rate given by equation (2.9) on the other hand, which correlates the nucleation rate to a part of a moment of the CSD using target efficiencies, gives a start-up which oscillates to a greater extent (see sim5, figure 2.4). In the nucleation model presented here, the attrition function in effect, acts as a size dependent target efficiency describing the combined probability of a crystal/impeller collision, and the probability that the collision will produce an attrition fragment. In other words, the nucleation function is correlated to that part of the CSD, i.e. the larger crystals, which have a higher collision probability with the impeller and a higher probability that an attrition fragment will be produced from that collision. The attrition function does therefore have a physical background, and the availability of

more complicated models describing crystal/impeller interactions could be incorporated into the secondary nucleation model.

The simulation fits in figure 5.8 shows that the proposed secondary nucleation model is very effective in predicting the start-up dynamic behaviour of an ammonium sulphate crystallizer. In the next two sections, the model will be tested on other types of crystallization modes.

5.5.2 Batch Start-ups

Table 5.5 : Parameter values for the batch start-up experiments

Parameters	$p1$	$p2$	$p3$	$p4$	$p5$	$p6$	$p7$	$p8$	$p9$
Units	m/s	-	-	μm	-	m/s	μm	-	-
Batch	5e-06	1	0.2	120	2.3	2e-09	750	10	50

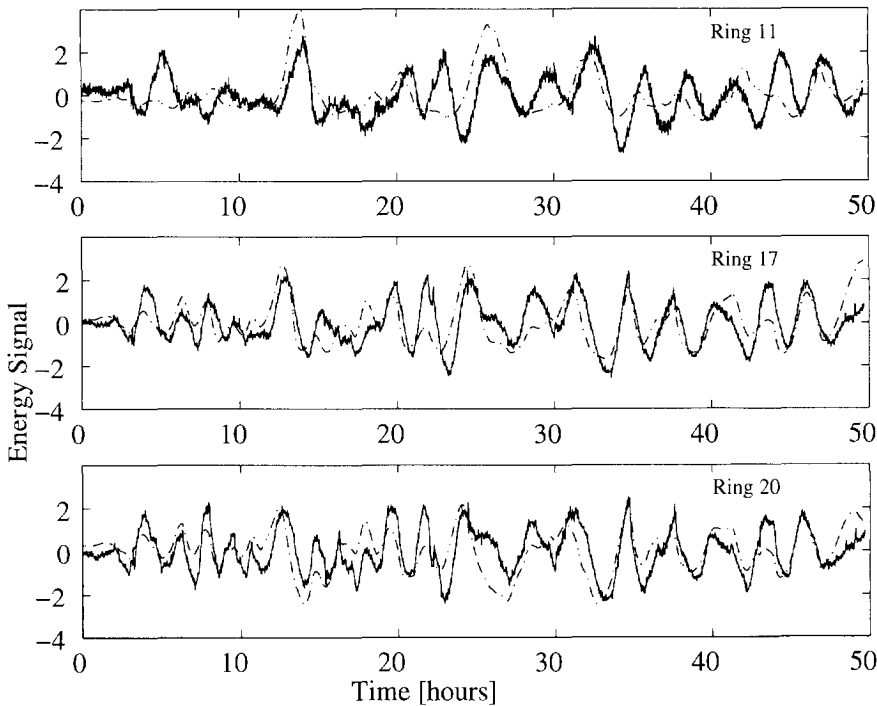


Figure 5.11 : Results of Run 56 continuous identification experiment. The energy signal on three of the Malvern rings (Ring 11, 17 and 20) are shown here. The energy signals have been detrended and scaled.

Figure 5.10 shows the measured and simulated results for the batch runs. The simulated curves are also included and the parameter values resulting from the simulations of Run 6 were used as the first approximation to model the results of the batch experiments. The optimised parameter values are listed in table 5.5.

The fit of the distribution median size corresponds very well to the measured trend. The slurry density profile predicted by the simulation also follows the measured trend very accurately. As would be expected with a batch experiment, the density of the suspension increases linearly at a constant heat input. The trend in the simulated 25 % size does not correspond to the measured value as accurately as the median size measured and simulated trends. In a batch experiment, the form and location of the initial distribution will have a strong bearing on how the final distribution after a given period of crystallization will appear. For a continuous experiment, the effect of the initial distribution will not be as significant, as the crystals leave the crystallizer in the product stream and their effect on the CSD will lessen gradually. Even though a reasonably good fit to the initial distribution was found in these experiments by using a combination of two log normal distributions having median sizes of 100 μm and 145 μm , the outgrowth behaviour in the small size ranges is difficult to model. The secondary nucleation rate at the start of the experiment will be very high due to the high supersaturation. Large numbers of crystals in the sub 20 μm size range which are outside of the reliable measurement range of the Malvern may later have a strong effect on the development of the CSD as they grow to larger sizes. Another complication is that during the start-up of the 970 L crystallizer, an agglomeration step occurs, provided that the heat input is above 100 kW (see Eek et al., 1995). This agglomeration step produces poor quality crystals (inclusions and irregular morphology) which may have different nucleation characteristics. The combination of two log-normal distributions was used to describe the CSD after the agglomeration step occurred and was not intended to describe a bi-modal distribution.

The simulation results are for the moment however, quite satisfactory. The fact that the kinetic parameter fitted here (table 5.5) are quite similar to those predicted for Run 6 (table 5.3) in the previous section, shows how kinetic parameters determined for a particular mode of operation can be used to obtain an estimate of how the CSD quality and quantity will appear in another mode of operation.

5.5.3 Continuous identification experiments

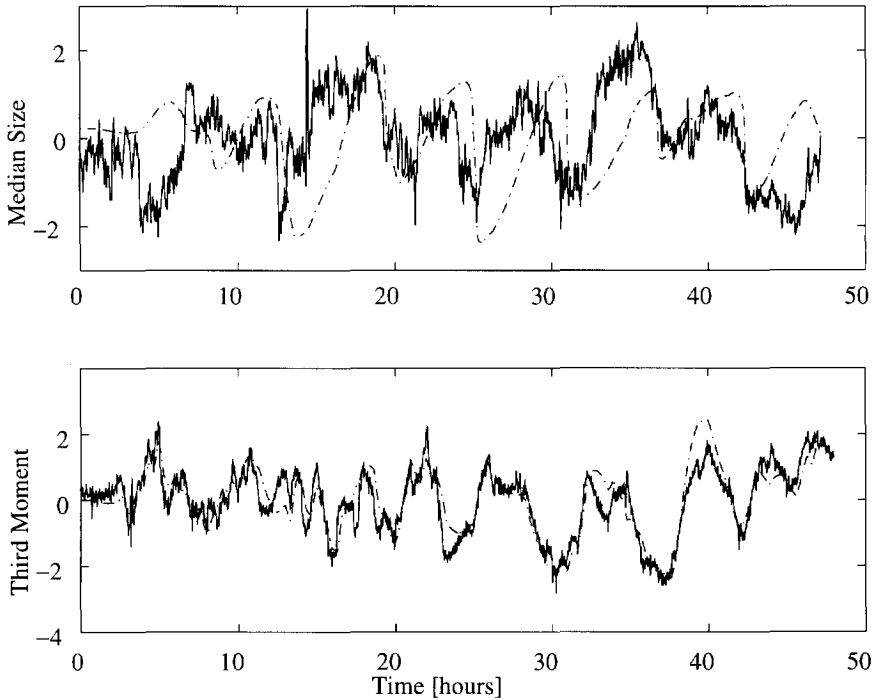


Figure 5.12 : Resulting measured and simulated responses in the median size and the product density for Run 56.

Figure 5.3 (a), (b) and (c) show the signals which were used to vary the operating conditions in the crystallizer once it had reached a steady-state with respect to the CSD.

The raw sensor data resulting from the identification experiment (Run 56) are processed according to the procedure outlined in Eek (1995). As a result of this processing, all the inputs (figure 5.3) and outputs are detrended and scaled. The response of the CSD in terms of the detrended energy signal recorded by three of the 31 rings are displayed in figure 5.11. The detrended distribution median size and the product density are shown in figure 5.12 along with the simulated behaviour.

The parameters used for the model are those which were evaluated from the fit procedure of Run 6.

The fit of the simulated to the measured light energies is quite accurate for the set of ring signals shown here over the entire length of the experiment. The fit of the measured median size (reconstructed from the energy signals) is compared with the simulated value in 5.12. The measured and simulated slurry density are also shown in this figure.

The fit of the simulated median size can be said to follow globally the same trend as the measured value. Clearly, a certain “lag” exists in the simulation with respect to the position of the CSD. The increase in the simulated median size after the distribution has reached a local minimum occurs much more slowly than in the real system. This may be due to there being more secondary nuclei growing out in the crystallizer than is predicted by the simulation, as a result of there being more attrition fragments produced than is predicted by the simulation. This can be concluded from the extent to which the median “drops” after it has reached a local maximum in the simulation. In the real system, the median drops more slowly and not to such an extent as in the simulation. Clearly, inaccuracies still exist in describing the events occurring in the large and small particle size ranges which must be looked at more closely. A major contribution to modelling the system more accurately, would be to take a closer look at the effects of internal classification on the CSD, especially in the larger size ranges. The impeller speed used for these experiments was 317 RPM, which, as will be shown in chapter 6, is below the limit at which the crystallizer can be said to be well mixed. As will be discussed in chapter 6, the hold-up of a large number of crystals inside the draft tube may lead to the production of fewer attrition fragments than would be expected, as these crystals are not located in a zone where the crystals are growing.

The simulations show that in the case of steady-state operating condition step changes, which approaches closest to the industrial situation, the proposed model is able to simulate the global changes in the CSD and the product density but it is not very satisfactory. The kinetic parameters used for the fits are those which were estimated for Run 6 and it may not be entirely justified in simply applying the parameters to this experiment. Possible reasons for the inadequate fit may have to do with the survival efficiency function assumed in equation (5.12), which can express a survival efficiency which is greater than unity, if the supersaturation increases to a high enough value. A better physical relation between crystal size, supersaturation and internal strain will have to be found for future simulations. Internal classification may also have an influence as discussed above.

It is worthwhile to try and improve the model as other system disturbances encountered in industry such as varying feed concentrations, varying steam supply pressure or an injection of water to clear a blockage could also be simulated using this model, because these disturbances will alter the CSD by changing the supersaturation analogous to the way which was done in Run 56.

5.6 Conclusions

By coupling the secondary nucleation rate to the attrition rate, via a (survival and) outgrowth efficiency term, it is possible to obtain a good representation of the CSD dynamic behaviour in a crystallizer. The new model presented here, performs much better than traditional power law correlations for the secondary nucleation rate as demonstrated in chapter 2. The model has been shown to be applicable to a range of operating modes, from batch to continuous start-up situations. By exciting the operating conditions of the crystallizer with a pre-programmed series of steps, a data set rich in variation of CSD and product density was obtained which could be modelled using the new secondary nucleation model presented in this chapter. The fit even though adequate to describe the global changes in the CSD, was not very accurate. Improvements in the model are still possible.

A set of kinetic parameters determined for the crystallizer in one mode of operation can also be applied to the same system but operated in a different mode.

From the results of the parameter estimation procedures, and from the evidence of crystal internal and external structure, it is shown that the onset of attrition occurs quite suddenly above a certain minimum size, and can be described satisfactorily by an attrition rate function having crystal length as the only parameter.

From kinetic parameter estimation, it is clear that a large population of non-growing attrition fragments are present in the crystallizer, which may cause blockage problems in downstream processes such as in filter units or centrifuges. The need for an effective fines removal system is justified if the amount of fine crystals in the product stream from the crystallizer can be reduced.

By recirculating the contents of the crystallizer through a mono pump situated in an external loop to the crystallizer, a greater number of attrition fragments were produced which caused the crystallizer product CSD to reach a steady-state quicker. The shape of the attrition function has an important bearing on the oscillating behaviour of the CSD.

Internal classification due to inadequate suspension of the crystal slurry, may introduce a bias into the measurement of the CSD towards smaller sizes. A classification function should be estimated for the crystallizer to account for this effect in the simulation model.



Chapter 6

Kinetics and the Scale of Crystallizers

Summary - In this chapter, the model developed in the previous chapters for crystal growth, attrition and secondary nucleation and validated on results from the 970 L crystallizer, is shown to be able to predict the correct dynamic behaviour of the same material on a 22 L scale also using the same kinetic relations.

The model developed so far has been based on the assumption that the 970 L crystallizer is a well-mixed vessel. In the first section of this chapter, this assumption is tested. This is done by making steps in the impeller speed when the system has reached a steady-state. The impeller steps cause a dynamic response in the crystal size distribution which takes up to 12 hours to dampen out. It is argued that the dynamic response resulting from the steps does not arise due to a pure kinetic effect, but that it is induced by the effect which the impeller speed has on the hold-up of crystals in the draft-tube. A high impeller speed is recommended to avoid internal classification.

To examine the effect of scale on the kinetics of crystallization, a number of experiments are carried out on a 22 L scale to compare with experiments on the 970 L scale. The results show that the start-up dynamic behaviour of the CSD in the two vessels is very similar in terms of wave amplitude and period. The model developed in the previous chapters is tested on the 22 L crystallizer results. The model is shown to be able to fit the data accurately, although different kinetic parameters are obtained for the 970 and 22 L crystallizers.

6.1 Introduction

One of the goals of developing a secondary nucleation model is to be able to predict the rate of secondary nucleation on an industrial scale, in the absence of direct measurements of the product CSD and density, by extrapolating the results for a small scale experiment up to a large scale by applying suitable scale-up rules.

Scale-up studies of crystallizers, where a particular material was crystallized in different sized crystallizers, either geometrically or not geometrically similar, were aimed at developing scale-up rules for secondary nucleation. Some studies have also examined the change in growth behaviour of the crystals of similar materials on different scales. No references were found regarding changes in attrition behaviour of crystals with a change in scale.

All of the secondary nucleation models reported in literature are based on CSD data at steady-state operation of crystallizers. As has been shown in the previous chapters, a steady-state situation is very difficult to obtain, and requires operating the crystallizer for up to 15 to 20 times the residence time after a primary nucleation event for well-soluble materials. For seeded experiments, the time to reach a steady-state may be much shorter, but information regarding the CSD is still necessary, to ensure that a steady state has been reached, and that process disturbances have a minimal effect on the stationary state of the CSD. Further, it was shown in chapter 2, that models developed for secondary nucleation based on steady-state CSD data were inaccurate when applied to the dynamic phase of operation.

In chapter 5, a new model for secondary nucleation was developed which took account of the attrition phenomena of large crystals and the observed size dependent growth rate of attrition fragments up to sizes of about 250 μm . This model has been validated only for the crystallization of ammonium sulphate in the 970 L crystallizer. In this chapter, the model will be examined to see if it can also be used to describe the crystallization of ammonium sulphate on a 22 L scale. Traditional secondary nucleation models (section 2.2.3) claimed to have this property, by including a term for the impeller speed or the specific power input via the impeller.

In this chapter, the starting point for a model for the 22 L crystallizer will be the parameters for growth, attrition and secondary nucleation of ammonium sulphate estimated for the 970 L scale experiments.

To be able to compare the models for the two crystallizers, it must first be ensured that both crystallizers comply with the well-mixed assumption. A section of this chapter deals with the subject of the effect of impeller speed on internal classification effects in the 970 L crystallizers.

6.2 Scale-up review

Secondary nucleation model as scale-up criterion

The secondary nucleation power law approach to secondary nucleation has already been treated in chapter 2. It was shown to be inaccurate in simulating the dynamic phase of operation but could be used to determine steady-state properties of the system. By adding an impeller speed or power input term to the expressions for secondary nucleation in chapter 2, several workers (table 6.1) have also been able to use the correlation to predict the nucleation rate in a geometrically similar crystallizer of a different volume.

Table 6.1 : Summary of nucleation and growth models for scale-up purposes based on the results of CMSMPR experiments

Authors	Secondary Nucleation $B_{o,eff}$	Scales of operation	Material	Growth kinetics
Ploß & Mersmann (1988) Experimental	$\sim \epsilon^{0.60} \mu_3^{0.75} G^2$	6 & 60 L	KCl/H ₂ O	-
Ploß & Mersmann (1989) Model	$\sim N^{2.2} \mu_3$	1.3, 5, 30 L	KCl/H ₂ O	-
Garside & Jancic (1979) Effective Nucleation	$\sim N^{1.8} \mu_3 \Delta c^{2.52}$	1.3, 5, 30 L	KAl.(SO ₄) ₂ 12H ₂ O	$G_{eff} \sim \Delta c^{1.33}$ & ASL
Garside & Jancic (1979) Total Nucleation	$\sim N^4 \mu_3 \Delta c^{2.52}$		KAl.(SO ₄) ₂ 12H ₂ O	$G_{eff} \sim \Delta c^{1.33}$ & ASL
Bourne (1980)	$\sim N^3 \mu_3 \Delta c^{2.5}$	1.67, 42 L	KAl.(SO ₄) ₂ 12H ₂ O	$G_{eff} \sim d^{0.4} \Delta c^{1.4}$ & ASL
Pohlisch (1988)		5.7, 63 L	KNO ₃ /H ₂ O	-
Grootscholten (1982)	$\sim N^2 \mu_3 G^2$	5, 10, 55 91 L	NaCl	-
Ottens (1973)	$\sim \epsilon \mu_3 \Delta c$	10, 40	KAl.(SO ₄) ₂ 12H ₂ O	-

Table 6.1 gives a summary of the models developed to describe the change in kinetics on scale-up of the crystallization process to either a geometrically similar or dissimilar crystallizer.

In the work of Ottens et al. (1973), Bourne et al. (1980), Garside and Jancic (1979) and Ploß and Mersmann (1989), geometrically similar crystallizers of different volumes were used. In the work of Grootscholten (1982), crystallizers of different geometries and sizes were used. All of the above results are obtained for DTB crystallizers equipped with a three bladed marine type impeller. Three types of material have been used with water in each case as the solvent. The crystallizers vary in volume from 1.3 up to 91 L.

The effective secondary nucleation rate ($B_{o,eff}$) has been calculated for each series of experiments. Garside and Jancic (1979) have also derived an expression for the total nucleation rate. The secondary nucleation rate correlation for all cases can be summarised by the following equation,

$$B_{o,eff} = k_B \epsilon^{1.8 \rightarrow 4} M_T^{75 \rightarrow 1.0} G^{1.8 \rightarrow 2} \quad (6.1)$$

However, large differences exist between the ranges of the powers and especially in the magnitude of the secondary nucleation rate constant (k_B), which means that experimental results are always necessary to determine scale-up criteria.

Most workers consider only differences between the rates of secondary nucleation at differing scales. It may also be important to consider differences in other kinetic phenomena such as the attrition and growth behaviours at differing scales. Garside and Jancic (1979) and Bourne et al. (1980) account for the effect of a size dependent growth rate of the potash alum crystals in their crystallizer by using the ASL (after Abegg, Stevens, Larson, 1968) model which has the crystal length only as a parameter. With the ASL model for growth, Garside and Jancic use a total nucleation rate as opposed to the effective nucleation rate.

Most workers report no change in the overall growth kinetics between scales, as given by equation (2.13). Only Bourne et al. (1980), who detected a dependence of the growth rate constant on the impeller diameter, found a difference between the growth rate constant on different scales. It is clear from the plots of $\log(n)$ vs. x that account should be taken of size dependent growth effects especially in the cases for Ottens et al. (1972) and Grootscholten et al. (1982) where it is clear from the $\log(n)$ vs. x plots that a size dependent growth effect is present. Whether a change of scale will have any effect on the size dependent growth behaviour of secondary nuclei is not possible to say from the results presented in literature.

Other work in the area of scale-up by Scrutton et al. (1982) reported that impeller/ draft-tube clearance is an important consideration in secondary nucleation rates. In previous work on the crystallization of NaCl in a 10 and 55 litre MSMR crystallizer (Scrutton, 1978, Asselbergs, C.J., 1978), the median size was lower than that obtained in a 5 litre crystallizer in the work of (Scrutton et al., 1982), when the experiments were done at the same conditions of temperature, impeller speed and crystal residence time for NaCl. This result is not in line with the generally observed trend that at smaller scales, the median product CSD size reduces due to a higher secondary nucleation rate, as expressed by the constant k_B in equation (6.1) (Bourne et al., 1980). They were able to show that by reducing the clearance between the impeller tip and crystallizer wall, the nucleation rate increased. It was concluded that the production of attrition fragments occurs due to the crushing of larger crystals between the impeller tip and the crystallizer wall.

Few references are available on batch experiments. The results of one series of batch scale-up experiments (Budz et al., 1987), have shown that the nucleation rate decreases with increasing crystallizer volume with no change in the kinetics of growth, similar to the results obtained for continuous experiments.

As has been shown in previous chapters, the form and position of the steady-state CSD is not only determined by the secondary nucleation rate, but also by the growth and attrition of crystals.

On scale-up of a system to a geometrically similar crystallizer, all possible changes to the processes of crystal growth, attrition and secondary nucleation must be considered.

On increase in the size of the crystallizer, several criteria can be chosen with respect to the impeller speed. Commonly, scale-up is done with either a constant impeller speed, a constant power input, or at an impeller speed which will give a well-mixed suspension criterion. For the constant power input criteria, assuming a similar type of suspension propeller, the impeller speed is normally lower with an increase in scale. This is the criterion which is most commonly used, and results in the collisions between individual crystals and the impeller to occur less frequently. This causes a shift away from crystal/impeller interactions and towards crystal/crystal interactions in the crystallizer. This may cause a change in the shape and magnitude of the attrition function as well as its' dependence on some variables such as the total crystal mass.

The attrition fragments of a particular material produced on several different scales may exhibit different outgrowth behaviours, as the amount of stress in the crystal may vary depending on the way in which they were bred. The higher velocity interactions between impeller and crystal on a small scale for example, may introduce

a greater amount of stress into the crystals and this may effect the rate at which they 'heal'.

By the same token, varying amounts of strain in attrition fragments from scale to scale may alter the survival efficiency of the particles. A higher stress in a particle may require a higher level of supersaturation to promote outgrowth of the attrition fragments.

Effect of internal classification on crystallization kinetics

As well as having to account for a possible change in process kinetics on scale-up of a crystallizer, changes in hydrodynamics may also lead to problems as the well mixed assumption on which the kinetic models are based may no longer be valid.

Internal classification is said to be occurring in a crystallizer if the product being removed from the crystallizer differs in either magma density or CSD from that in the crystallizer. In some crystallizers, this is seen as a positive effect, as in a crystallizer elutriation leg (as in a forced circulation crystallizer) where the ability of the largest particles to settle out of suspension is used to remove a coarse product from a calandria. In most crystallizers however, where an isokinetic product is expected, internal classification is a detrimental effect signifying a poorly mixed suspension. A well mixed suspension on the other hand not only reduce the effect of internal classification but also ensure that the supersaturation generated in the boiling zone is distributed throughout the crystallizer, making sure that all crystals come into contact with a positive supersaturation and that no locally high supersaturations can lead to a primary nucleation event.

Making sure that the content of the crystallizer is well-mixed is dependent on the design of the crystallizer vessel itself, but much more importantly on the type, position, geometry and operation of the impeller. The impeller provides the driving force for mixing and suspension in the crystallizer. The effect of a too low impeller speed has not only a direct effect on product removal by internal classification but also has an indirect effect on the product CSD by altering the kinetics of crystal growth and secondary nucleation. Large particles which have a long residence time in the draft tube can experience a lower driving force for growth as they do not have enough momentum to penetrate the boiling zone area, but short circuit to the outside of the draft-tube.

In terms of the MSMPR theory at steady-state, a lower growth rate of larger particles caused by internal classification would be expressed as a deviation in the large particle size ranges similar to the deviation which is caused by a length

dependent attrition effect. This makes it difficult to determine an attrition function for a particular system from on-line CSD data. In terms of the secondary nucleation mechanism developed by Daudey et al. (1987) and later by Van der Heijden et al. (1994), a reduced growth rate of large particles would cause a shift in the mechanism of secondary nucleation away from a surface breeding mechanism, where the numbers of attrition fragments produced is dependent on the numbers of macrosteps present on a crystal surface which in turn is dependent on the supersaturation encountered by a particular crystal surface. With less macrosteps present on a crystal surface to act as potential nuclei, it is expected that the secondary nucleation rate in the crystallizer will decrease. An increase or a decrease in the impeller speed will thus not only have an immediate effect on magma density and the position and shape of the CSD, it also has an indirect effect on the kinetics.

Due to the lack of experimental facilities and opportunity, very little information regarding the effect of crystallizer design and operation on internal classification exists. What does exist is mostly relevant on a small scale (Kuijvenhoven, 1982, Molerus and Latzel, 1987). Other more general papers give broad based rules of thumb which should be followed during the initial design of crystallizers to avoid internal classification and ensure a good suspension in the crystallizer (Bourne, 1979, Musil et al., 1979, Shaw, 1982).

6.3 Experimental

6.3.1 Equipment

Two crystallizers are under study in this work, the 970 L (section 3.3.1) and 22 L (section 3.3.2) DTB crystallizers. Distinguishing features of the 970 L crystallizer is that it has an internal heat exchanger (shell and tube) located inside the draft-tube just above the impeller and is used to effect evaporation of the ammonium sulphate - water solution. The slurry is tube side and the hot water is shell side. The heat exchanger in the 22 L crystallizer is located inside the draft tube walls and hot water is again used to effect evaporation. Both crystallizers are operated at a constant temperature of 50°C and a pressure of 80 mbars. Product is continuously removed from the 970 L crystallizer via a line situated at the base of the draft-tube and on the outside. In the 22 L crystallizer, product is removed at intervals of two minutes through a line connected to the mid-section of the crystallizer. The impeller used in both crystallizers is a three blade marine type impeller. In the 970 L crystallizer, it is coated with rubber to reduce attrition and breakage of crystals in the crystallizer. Both crystallizers are fed with a

crystal free saturated solution of the ammonium sulphate - water mixture at the same temperature as the operating temperature of the crystallizer.

6.3.2 Experiments

To examine the validity of the well-mixed assumption in the 970 L crystallizer, an experiment was carried out (Run 62) which lasted 50 hours where the impeller speed was alternately increased and decreased at intervals of about 15 hours, to examine its' effect on the crystallizer dynamic behaviour. An initial steady-state was reached 15 hours after the initial primary nucleation by using the proportional controller described in Eek (1995). At the end of this experiment, a series of short steps at intervals of 10 minutes were done to see what was the instantaneous effect of an impeller speed step change on the CSD and slurry density leaving the crystallizer in the product stream.

From these experiments, an impeller speed was chosen for the 970 L crystallizer which gave the contents as close a state as possible to a well-mixed situation. At this impeller speed (370 rpm), another start-up experiment (Run 64), similar to Run 6 and Run 19 in chapter 5 was done. No fines removal was applied as it was the intention to compare the response of this experiment to similar experiments in the 22 L crystallizer, where it is not yet possible to remove a fines stream.

Two types of experiments were carried out in the 22 L crystallizer. Firstly, a number of short (2 minute duration) start-ups (B205a,b,c, B206a,b,c) were done to examine what happens during the primary nucleation step and directly thereafter. In similar experiments carried out in the 970 L plant, it was seen that directly after the primary nucleation step, and provided that the heat input was greater than 100 kW/m^3 , an agglomeration step occurred (Eek, 1995), in which the primary nuclei combined to form larger crystals having sizes of about $300 \mu\text{m}$. Similar experiments to these were carried out in the 22 L crystallizer. As well as the heat input being varied, the impeller speed was also varied as it was thought that the hydrodynamic conditions would influence the formation of the agglomerates (David et al., 1991).

The second type of experiments carried out were also start-up experiments but the behaviour of the CSD was observed up to a time of 30 hours after the primary nucleation. Three such experiments were carried out, the first lasted 24 hours (Run 201) and Runs 202 and 203 lasted 30 and 32 hours.

The experimental conditions of all the experiments described above are shown in tables 6.2 and 6.3.

To obtain the results shown in figure 6.3 (short 2 minute start-ups), a Malvern was attached directly to the crystallizer in a short loop containing a centrifugal pump. The experiments were carried out under the same conditions as a normal continuous experiment on this scale i.e. under a vacuum of 80 mbars and a temperature of 50°C, the only difference being that they are carried out in batch mode and that only the primary nucleation step and the first two minutes of outgrowth of the initial population were followed.

The CSD for the longer experiments with the 22 L crystallizer was measured using the procedure outlined in section 3.3.5.

Table 6.2 : *Experimental details of the classification experiment carried out in the 970 L crystallizer*

<i>Experiment</i>	<i>Heat (kW)</i>	<i>Residence Time (min.)</i>	<i>Fines Flow (L/s)</i>	<i>Impeller Speed (rpm)</i>	<i>Impeller Steps (rpm)</i>	<i>Time of Steps (hrs.)</i>
Run 62	107	75	1.35	315	315-345	16
					345-290	28
					290-315	47.5

Table 6.3 : *Details of batch and continuous experiments in the 22 L crystallizer and supplementary experiment in the 970 L crystallizer (Run 64)*

<i>Run</i>	<i>Plant</i>	<i>Duration</i>	<i>Heat Input</i>	<i>Residence Time</i>	<i>Impeller Speed</i>
	L	HR	kW/m³	Minutes	RPM
B205a,205b,205c	22	2.5	4.3	Batch	750
B206a,206b,206c	22	2.5	3.3	"	750,600,400
Run201	22	23	118	204	750
Run202	22	30	118	204	750
Run203	22	32	118	160	750
Run 64	970	16	120	95	370

6.4 Results and discussion

Impeller speed step changes

Figure 6.1 shows the responses of the median size, the product density and the 10 % (X_{10}) value to changes in the impeller speed for Run 62.

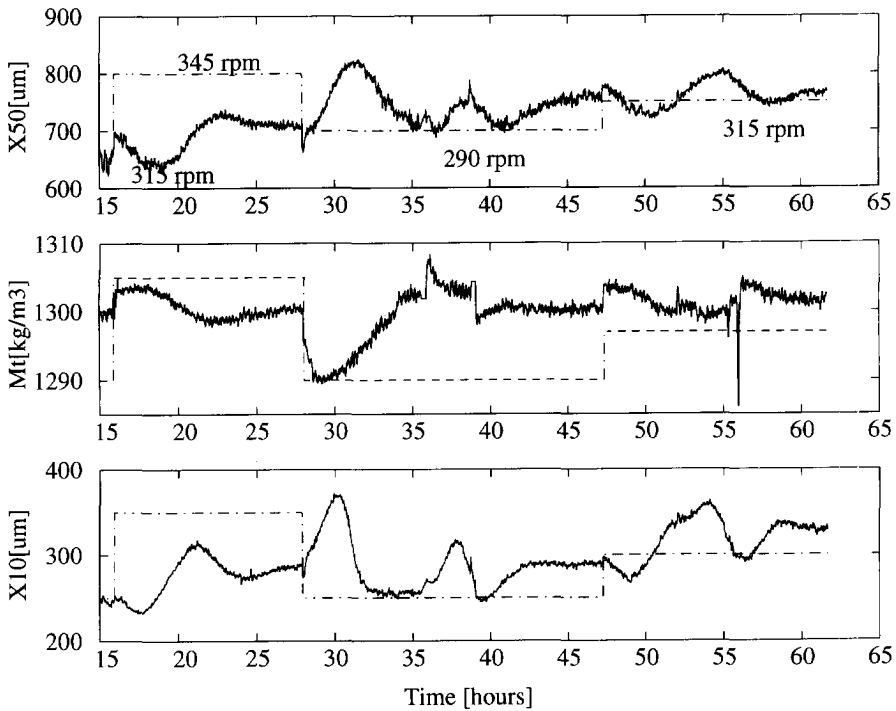


Figure 6.1 : *Dynamic response of the CSD to a series of changes in the impeller speed*

315 → 345 RPM

The initial response of the CSD median and the product density (crystal suspension in product stream (M_t)) to a change in the impeller speed can be seen after 16 hours. The median size increased instantaneously on a step increase in the impeller speed from a value of $665 \mu\text{m}$ to $700 \mu\text{m}$. The density also increased at precisely the same time from 1300 to 1303 kg/m^3 . Given that 1248 kg/m^3 is the saturation concentration, this increase in mass represents about 5 % of the total solid mass in the crystallizer. After this step response, the CSD and product density enter an oscillation

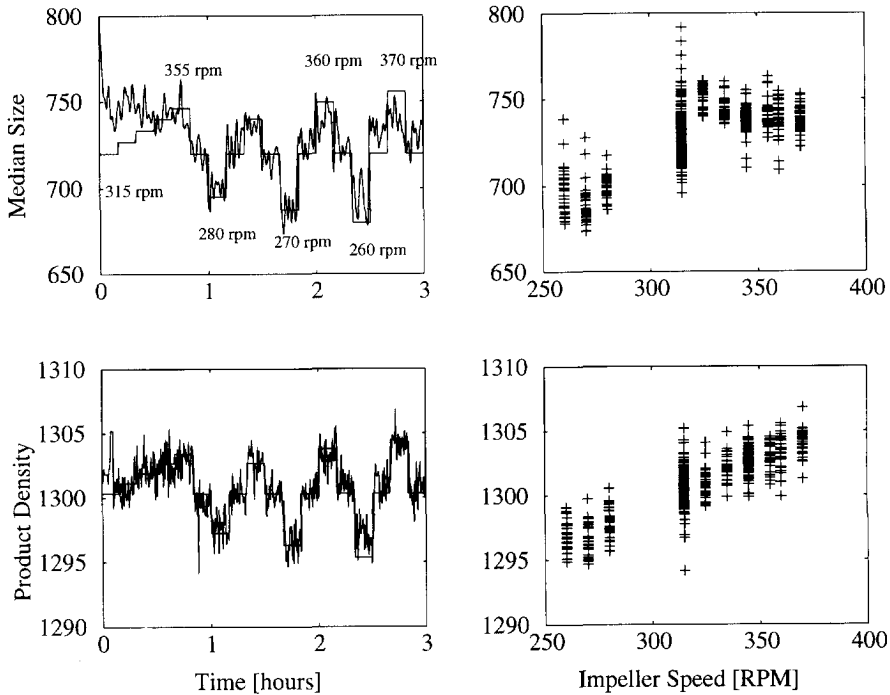


Figure 6.2 : Response of the system to a series of steps in the impeller speed. Figures show the change in median size and product density plotted as a function of time (left) and impeller speed (right)

and both eventually reach another steady-state, 10 hours after the original step was programmed. The new steady-state is different to the original steady-state before the step was made. The distribution has shifted to larger sizes as is evidenced by the larger X10 and X50 values. The product density, also having completed an oscillation has returned to its' pre-step value of 1300 kg / m^3 , as should be the case.

Intuitively, it would be expected that if the impeller speed was increased, the CSD would move to the left on volume % versus crystal size basis, resulting in a lower median size, because a higher impeller speed yields a greater probability of collision with crystals, and more attrition fragments are produced. A higher nucleation rate should result, giving a lower median size for the same operating conditions. It would not be expected that the product density should vary, as in a well mixed crystallizer, the operating conditions of residence time and heat input are the only two factors which effect the product density. This leads to the idea that the crystallizer is not well-mixed but that internal classification is occurring whereby excess mass is being held

up inside the draft tube. This hold up results as the vertical velocity imparted to the suspension by the impeller is equal to the settling velocity of the larger crystals in the suspension. These crystals have a lower growth rate than crystals which are not held up inside the draft tube, because the supersaturation generated in the boiling zone will be at a minimum when the supersaturated solution generated in the boiling zone reaches the inside of the draft tube. Due to their size, the larger crystals will also have a lower chance of penetrating the boiling zone thus also experiencing a lower supersaturation. On an increase in impeller speed in this case, the extra mass held up inside the draft tube re-enters the circulating suspension and begins to grow again. Evidence of this mechanism is seen in the step change in the product density value which occurs when the impeller step is programmed. The re-introduction of this material into the circulating suspension causes the CSD to enter the observed oscillation. The final higher values of the X10 and X50 values provide more evidence that internal classification is occurring as at a higher impeller speed, more larger crystals are circulating in the suspension and will be measured more frequently as product is removed from the outside of the draft tube and measured in the product line.

345 → 290 RPM

In the next step from 345 to 290 rpm at 28 hours, the median size and the product density again change abruptly, this time decreasing instead of increasing because the step is in the opposite direction. After 8 hours the system was approaching its' steady-state value as can be seen from the trend of the X10 value which is stable at this point. The product density is still a bit high though at 1302 kg / m^3 . The X50 value had also stabilised at this point, assuming a lower value than before the speed of the impeller was changed. At this point (36 hours), an external disturbance caused a process computer malfunction which left the crystallizer without control or monitoring facilities for 10 minutes. During this time the pressure in the crystallizer built-up and the temperature increased to a value of 52°C . Some of the crystals were dissolved and after process monitoring was restored, it was seen that the CSD had entered an oscillation which took 10 hours to restore a steady-state situation.

290 → 315 RPM

At this point (47.5 hours) the final step was carried out in the series of steps and was an increase in the impeller speed back to its' original starting value of 315 rpm. Once again, an initial sudden change in the median size and product density were followed by a much longer dynamic response.

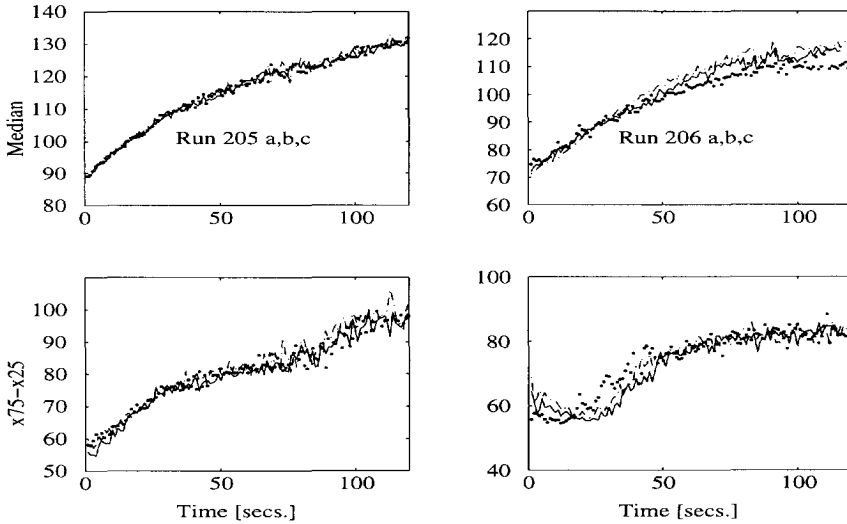


Figure 6.3 : Start-up trend of the CSD over the first 2 minutes of an experiment. Results of series Run 205 (left) and Run 206 (right) are shown.

In appendix D, it is demonstrated that if a extra population of crystals is introduced or removed form the crystallizer, after the CSD has reached a steady-state situation, a response similar to those observed in figure 6.1 results.

To get a better idea of the measured dependency of the median size and product density on the impeller speed, a series of impeller steps were performed in close succession to each other at the end of Run 62. The results are shown in figure 6.2. Figure 6.2 (left) shows the median size and product density changes with time, while figure 6.2 (right) shows a plot of median and product density versus impeller speed. In appendix C, a model is proposed which proves that this type of response results from internal classification.

Figure 6.2 shows a marked dependency of the product characteristics on the impeller speed. The product density increases linearly with impeller speed while the median size also increases up to an impeller speed of about 330 rpm.

From the results presented in figure 6.2, it is clear that to approach a well-mixed situation in the crystallizer, the impeller speed has to be operated at its' maximum allowable speed, which in this case is 370 rpm.

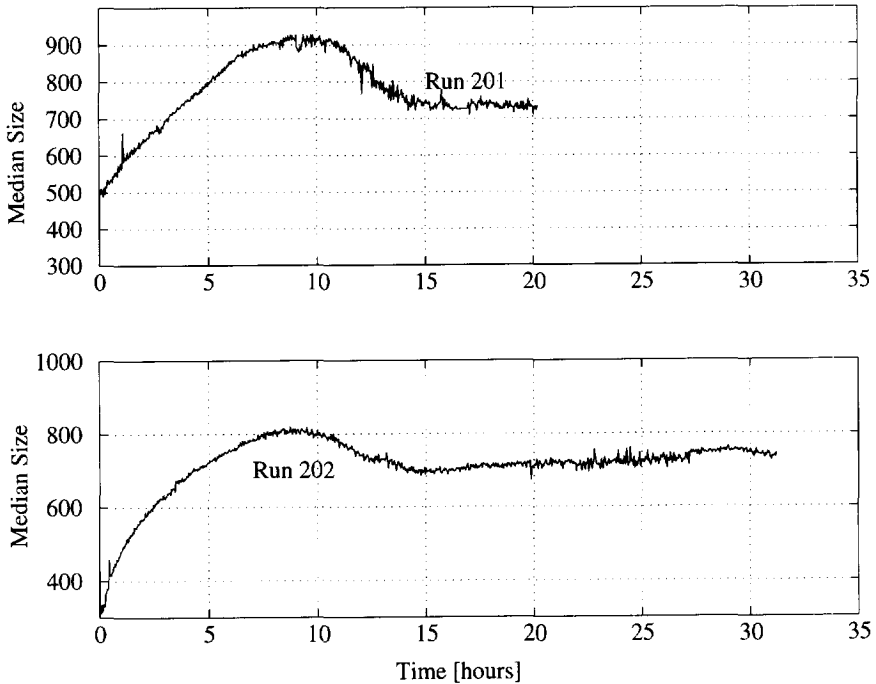


Figure 6.4 : Start-up trends for Runs 201 and 202 in the 22 L crystallizer. Conditions are given in table 6.3

Scale-up experiments

Batch Start-ups (B205 and 206 a,b and c)

The reproducibility of the start-up behaviour of the 22 L crystallizer over the first 120 seconds is shown in figure 6.3 for Run 205 and 206. The trends in figure 6.3 are very close, almost identical in behaviour. The same can be said for the Run B206 a,b,c experiments (despite the different impeller speeds), while although some deviations are present over the first minute, the trends converge thereafter until the measurements are stopped after 120 seconds.

In comparison to the results of the start-up experiments with the 970 L crystallizer, there is a significant difference in that the minimum detectable size after nucleation in the 22 L crystallizer is about 75 μm , while for the 970 L crystallizer this is above about 120 μm (see Eek, 1995, chapter 5). This could be due to the sampling system which in the case of the 22 L crystallizer is much closer to the actual crystallizer vessel, while with the 970 L crystallizer, the sampling system is situated at

a distance from the vessel, therefore there is a longer time elapsed before crystals from the 970 L crystallizer reach the sampling system, giving more time for particle growth.

The most important result from these experiments is that there seems to be no agglomeration step occurring in the 22 L crystallizer. Even at higher heat input values of 4.3 kW from the RunB205 a,b,c experiments, which is equivalent to 190 kW/m^3 , there is still no agglomeration step occurring. At heat input values above 100 kW/m^3 in the large crystallizer, an agglomeration step was already present. This difference in behaviour is probably due to the different hydrodynamic conditions present in both crystallizers. In a more turbulent and well-mixed 22 L crystallizer, the contact time between crystals is reduced, thus giving less time for a bridge to form between colliding particles. This contact time is critical in determining whether an agglomerate is formed or not.

Continuous Start-ups (Run 201,202,203 and 64)

Figure 6.4 shows the trend in the median size during a start-up and operation of the 22 L crystallizer to a steady-state distribution. The plot shows the median size trend for Run 201 and for Run 202.

The behaviour of the median size for both experiments is very similar (Runs 201 and 202, figure 6.4) whereby an initial population produced by primary nucleation grows out to a maximum size and then as the influence of secondary nucleation becomes stronger, the median size decreases to a steady-state value of $730 \mu\text{m}$. The steady-state value obtained for both experiments is similar but the initial median size and maximum median size through which the median passes after 9 hours have an offset of about $100 \mu\text{m}$ in the case of Run 201 in comparison to that of Run 202. In the previous section, it was shown that the starting distribution is very reproducible during consecutive start-ups (figure 6.3), which is surprising result as primary nucleation is a statistical event. The reason that the same start-up behaviour for Runs 201 and 202 does not give an identical CSD has to do with the way in which the crystallizer is operated. In the previous batch start-up experiments, the contents of the crystallizer for every start-up are identical and as the system is run in batch mode, no feed enters and no product is removed from the crystallizer. For the continuous runs, small changes in the suspension level arise due to the intermittent removal of product from the crystallizer and the intermittent addition of feed. For this reason, the hydrodynamics at the point of nucleation between two successive experiments is never exactly the same.

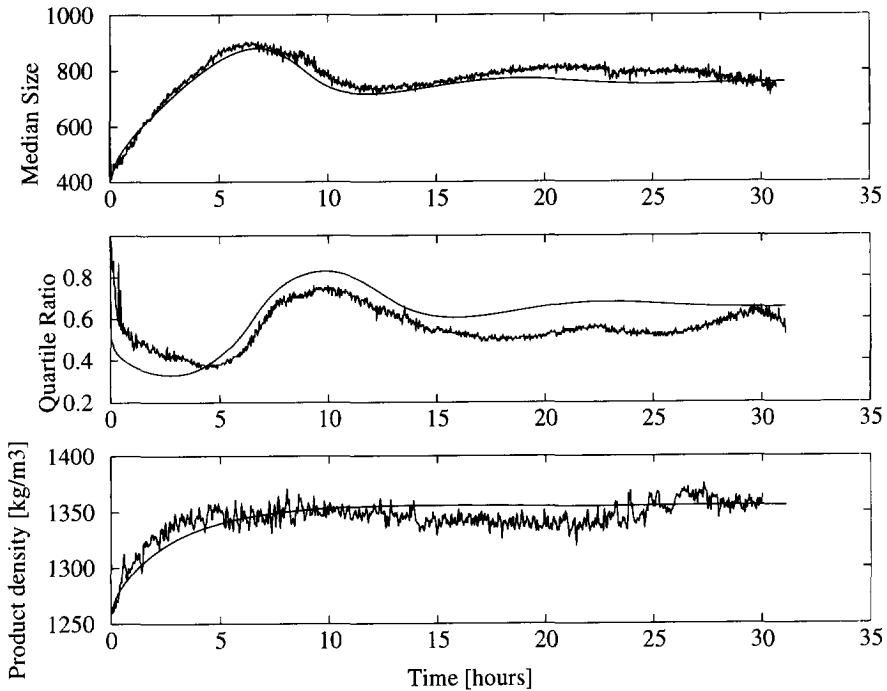


Figure 6.5 : Measured and simulated start-up response for Run 203 in the 22 L crystallizer

Therefore, the CSD of primary nuclei may differ slightly from experiment to experiment and a difference at this point, leads to a different start-up trend. But because all other operating conditions are equal, the same steady-state value is eventually reached by both experiments. The product density signal for the 22 L crystallizer is derived from the obscuration signal. The work of Eek (1995) showed that the obscuration signal is directly proportional to the product density of ammonium sulphate for values of the obscuration below 30 %. The obscuration signal was scaled by measuring the real product density at 5 hour intervals during the experiment, and then applying a multiplication factor to the obscuration signal. The dilution ratio was increased after 14 hours to reduce the obscuration signal which was exceeding 30 %. This change is reflected in a decrease in the obscuration value at this point.

The current result shows that the behaviour of the CSD on both scales is very similar contradicting the results obtained by Jager (1992) who did similar experiments with the same two crystallizers. Figure 6.5 shows plots of the measured and simulated median size and quartile ratio of Run 203 which had a shorter residence time than the previous two experiments. The measured and simulated median size for Run 203 is

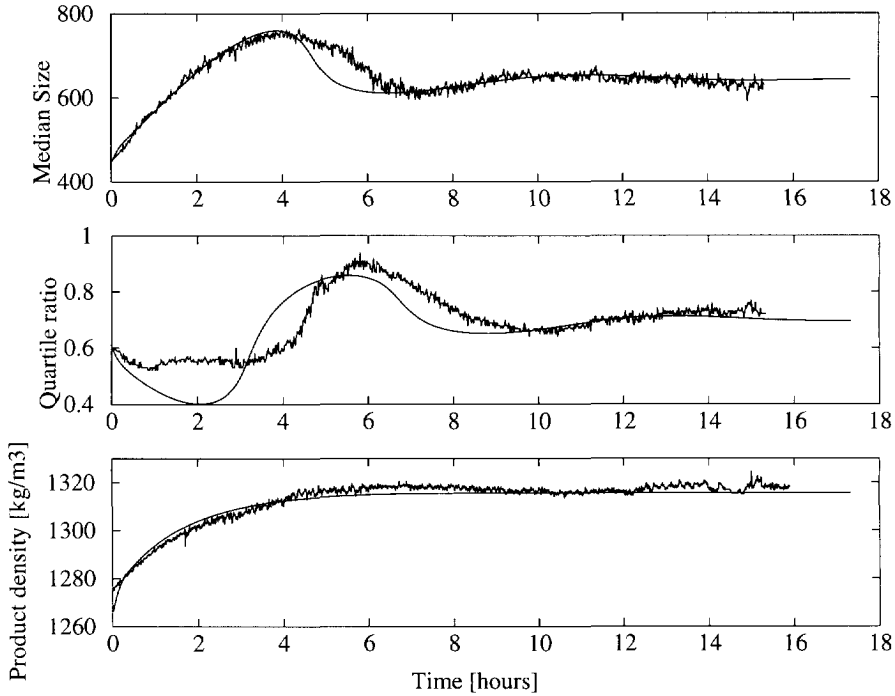


Figure 6.6 : Start-up trend for Run 64 in the 970 L crystallizer.

drawn in figure 6.5. For this experiment as well, the same trend can be seen with respect to the CSD median size. At the shorter residence time of 160 minutes than Runs 201 and 202, the response seems to be more dynamic with the CSD entering a second oscillation 10 hours after the primary nucleation step.

Figure 6.6 shows a plot of the response of the 970 L crystallizer in the absence of fines removal, with a heat input of 120 kW and a residence time of 95 minutes. Although the residence time for the 22 L crystallizer is more than 1.5 times that of the 970 L crystallizer, the behaviour of the median size (compare figures 6.6 and 6.5) is not dissimilar. The steady-state median value reached by the 22 L crystallizer is larger at 720 μm than the median size obtained in the 970 L crystallizer which is about 630 μm . This results because of the difference in residence times.

For all the experimental results discussed above, the existence of a steady-state for any one experiment cannot be said to exist, although it is clear that after operation of the crystallizers for up to 30 hours, the major CSD oscillations have left the systems. For the 22 L crystallizer, slight periodic disturbances related to operational

difficulties on a smaller scale make it difficult to maintain a steady-state for any period of time.

6.5 Model Simulations

The model framework developed in chapters 2, 4 and 5 will be applied here for the crystallization of ammonium sulphate in the 22 L crystallizer. Several assumptions are made with regard to the kinetics of ammonium sulphate on this scale. This is related to the choice of kinetic relations used for the processes of crystal growth, attrition and secondary nucleation which are taken as the same as those used for the 970 L crystallizer. A brief recap of the equations used for the simulations is given in the following paragraphs.

The effective growth rate of crystals is defined by the sum of the kinetic growth rate and the attrition rate of crystals by,

$$G_{eff}(x, \sigma) = G_{kin}(x, \sigma) - G_{attr}(x) \quad (6.2)$$

A length dependent growth rate of ammonium sulphate crystals is defined by the growth equation first introduced in section 4.7.2. That crystals grow with a length dependency in this crystallizer was shown by Daudey in his thesis (1987).

$$G_{kin}(x, \sigma) = p1\sigma^{p2} (1 - (1 - p3)\exp(-(\frac{x}{p4})^{p5})) \quad (6.3)$$

$p1$ and $p2$ are taken as the same as the values for the 970 L crystallizer. $p3$ to $p5$ are estimated from the measured CSD data.

The attrition rate is given by,

$$G_{attr}(x) = p6(1 - \frac{1}{1 + (\frac{x}{p7})^{p8}}) \quad (6.4)$$

The secondary nucleation rate is given by (parameter $p9 = k_{survival}$),

$$B(x) = \eta_{survival} \dot{V}_{attr} H(x) \quad (6.5)$$

$$\eta_{survival} = k_{survival}(\Delta c)$$

The initial distribution is fitted with the sum of two exponential distributions (on a number density basis). These distributions are shown in figure 6.7 which have been converted to volume percentage based distributions. The median size of these distributions can be compared to the starting median size values in figures 6.5 and 6.6.

The model parameters were optimised by fitting the parameters to the results of Run 203. A similar procedure was done for Run 64. For this simulation, a set of parameters from the experiments in chapter 5 (Run 6) were used as an initial guess.

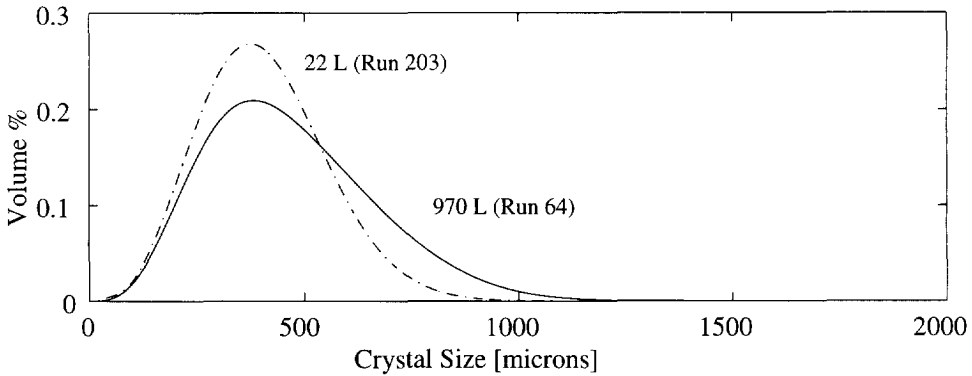


Figure 6.7 : Initial distributions for the 970 L (Run 64) and the 22 L (Run203) crystallizers. The distributions in each case show the sum of two exponential distributions on a number basis having been converted to a volume % basis.

The same initial distribution was also used but was changed from two log-normal distributions to two exponential distributions as a better fit was obtained with this combination.

Table 6.4 lists the optimised parameters calculated for both crystallizers. Figure 6.8 shows the form of the growth and attrition functions for both crystallizers as well as the trend in the nucleation rate and the supersaturation.

Table 6.4 : Parameters estimated for experiments with ammonium sulphate on two scales

Parameter	$p1$	$p2$	$p3$	$p4$	$p5$	$p6$	$p7$	$p8$	$p9$
Units	-	-	-	μm	-	m/s	μm	-	-
Run									
64	5.10^{-6}	1	0.30	120	2.3	$1.2.10^{-9}$	750	3	4.36
203	5.10^{-6}	1	0.20	120	2.3	$2.8.10^{-9}$	600	5	2.74

Figure 6.9 shows plots of the steady-state distributions in both crystallizers as calculated using equation (2.33). For both systems, the same deviations from the ideal

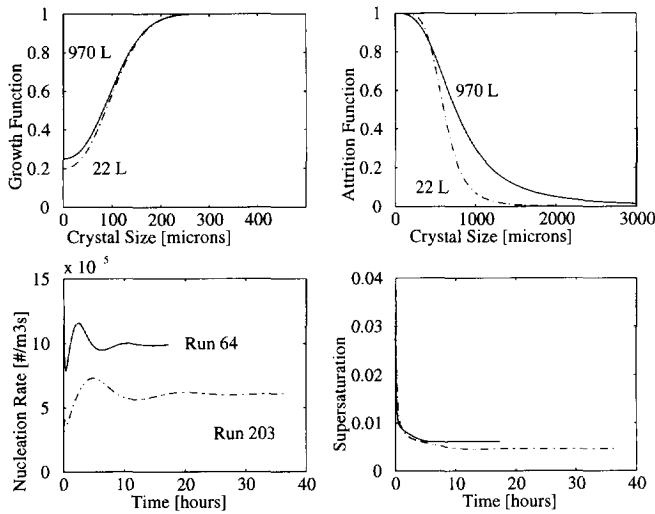


Figure 6.8 : Upper two plots show the growth (left) and attrition (right) functions from the fit procedure of Runs 203 (22 L) and Run 64 (970 L). Lower two plots show the nucleation rates and supersaturation levels in both crystallizers during the experiments.

MSMPR can be seen. In the small particle size range, below a size of 250 μm , an upward curvature can be seen while in the larger sizes, above about 500 to 700 μm , a downward curvature is evident. These deviations are indicative of a length dependent growth rate in these two zones probably caused by internal stress and an attrition effect respectively. The functions necessary to model this behaviour are shown in figure 6.8. The SDG rate function is practically the same for both systems, except that for the smallest crystals, the secondary nuclei in the 22 L crystallizer grow slower. The attrition function predicted for the 22 L crystallizer is also sharper than that predicted for the 970 L crystallizer. This indicates that attrition in the 22 L crystallizer is stronger at lower sizes. This result is expected as the circulation time in the small crystallizer is much lower than the large crystallizer, thus impeller/crystal contacts are more frequent. For both systems, the fit of the simulated distribution to the measured data is inaccurate in the sub 30 μm region where the quality of the measurement is very low. The bad fit of the simulation to experimental data for Run 64 (figure 6.8) in the large particle size ranges (above 800 μm) is caused by the fact that the measured CSD has not entirely reached a steady-state situation 15 hours after the primary nucleation event and as such the comparison is not completely valid. However, it does

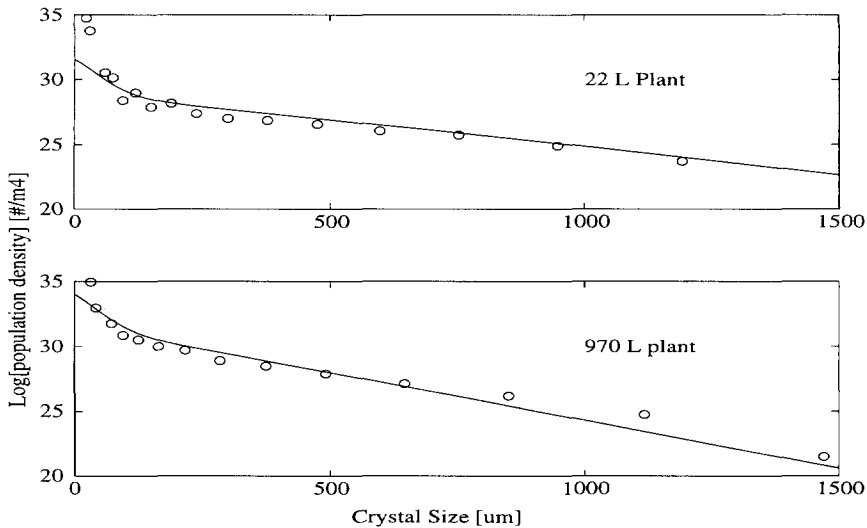


Figure 6.9 : Plot of the steady-state in the 22 L crystallizer (upper) and the 970 L crystallizer (lower)

show that the magnitude of the effect of a SDG and attrition as given by the slope of the simulation is of the right order.

The fit of the dynamic simulations to the measured data are shown in figures 6.5 and 6.6. The CSD trend predicted by the simulation for both crystallizers is always accurate, although at some points the magnitude of the signal (median size or quartile ratio) is different. The fit during the first five hours of the experiments is not very accurate for Run 64. As explained in chapter 5, the initial fit as shown in figure 6.7, although giving a good fit to the initial distribution parameters (median and quartile ratio values) may not entirely be able to account for the numbers and type of crystals present in the crystallizer. As the effect of the initial distribution becomes less important after about 5 hours, the fit improves for Run 64. The simulated distribution spread (quartile ratio) for Run 203 has a constant offset with respect to the measured spread after 15 hours even though the trend followed by the spread is accurate. The difference between the steady-state quartile ratio values corresponds to about a 50 μm difference between the widths of the measured and simulated distributions. There is no obvious reason for this difference.

Although the parameters obtained from the optimisations of Runs 203 and 64 were done separately to obtain the values listed in table 6.4, the original assumptions in applying kinetic equations developed for Run 64 directly to Run 203, may have to

be revised. Perhaps a different attrition or growth function may better be able to describe the dynamic behaviour.

Attrition fragments for both crystallizers are assumed to be born at $10\ \mu\text{m}$. In figure 6.8, the birth rates and the supersaturation in both crystallizers are plotted. The birth rate of crystals in the 970 L crystallizer is much higher. Although the attrition rate parameter p_6 for the 970 L plant is smaller than for the 22 L crystallizer, the supersaturation during the experiment is higher and therefore the dependence of the nucleation rate (equation (6.5)) on the supersaturation yields a higher secondary nucleation rate in the 970 L crystallizer.

6.6 Conclusions

The 970 L crystallizer does not entirely comply with the well-mixed assumption below an impeller speed of 370 rpm. The larger crystals are held up for a longer time inside the draft tube and may even become trapped if the crystals are large enough. Operation of the crystallizer at its' maximum speed is recommended to avoid such problems.

The dynamic behaviour of a crystallizer in terms of oscillating period and amplitude does not vary significantly with scale. It seems that the operating conditions, i.e. residence time and heat input are much more important.

The same model used to simulate the crystallization behaviour of ammonium sulphate on the 970 L scale was also able to simulate the 22 L crystallizer behaviour. The model is based on a system of mass and energy balances and kinetic relations of a length dependent growth rate, an attrition rate function and a secondary nucleation correlation.

Although the same functions were used, the parameters in the equations were different for both scales. The attrition function reveals that the onset of attrition in the 22 L crystallizer occurs at lower sizes, and that the maximum attrition rate in the 22 L crystallizer is more than twice what it is in the 970 L crystallizer. This is probably due to the more frequent collisions in the 22 L crystallizer between the crystals and the impeller. This is also due to the fact that the impeller in the 970 L crystallizer is coated with rubber and is not in the 22 L. Although the attrition rate in the 22 L crystallizer is greater, the survival efficiency is lower and the growth rate of the secondary nuclei is lower (relative to the maximum growth rate at the time). Both of these may be caused by the existence of more stress in the nuclei in the 22 L crystallizer.

A true steady-state situation in a crystallizer is difficult to achieve. Minor disturbances in the operating conditions can lead to a dynamic response of the CSD lasting several times the residence time.



Chapter 7

Crystallization of Pentaerythritol and Adipic acid

Summary - The model developed in chapters 4, 5 and 6 is extended to test on the crystallization behaviour of two other materials, namely pentaerythritol and adipic acid. They are crystallized in the 22 L crystallizer in continuous mode.

For pentaerythritol, a number of short (10 hours) start-up experiments are carried out in which the heat input and residence times are varied, but held constant for a particular experiment. At higher heat inputs, the CSD reacted more dynamically. No definite effect of residence time variation could be seen on the CSD. Only one oscillation in the CSD could be observed before the system reached a steady-state. The model was able to describe the CSD trends very accurately.

Two start-up experiments were carried out with adipic acid. The growth of the primary nuclei distribution was very rapid and the median reached a maximum within 2 hours after the primary nucleation step. Hereafter, the median size decayed until it reached a steady-state after 8 hours. At this point, steps in the impeller speed were made. The system responded very rapidly, the median size decreasing at an increase in impeller speed, and increasing at an decrease in impeller speed. By varying a parameter in the attrition rate function, a similar trend could be modelled.

7.1 Introduction

Much information regarding the dependencies of the kinetic processes of crystal growth, attrition and secondary nucleation on quantities relating to the crystal size distribution (CSD), the supersaturation and the operating conditions have been developed in the previous chapters. In this chapter, the expressions for ammonium sulphate are tested on a set of experimental data for pentaerythritol and adipic acid obtained from the 22 L crystallizer operated under continuous evaporative conditions. The population balance approach is used as the framework with which the relations are tested.

The objective of this chapter is to show that by choosing realistic kinetic relations, an accurate determination of the behaviour of the CSD in a suspension crystallizer for badly soluble materials for the above kinetic processes can be made.

7.2 Literature

Pentaerythritol

Information regarding the crystallization of pentaerythritol is very scarce. The most recent publication regarding the kinetics of pentaerythritol is by Hedstrom et al. (1993) where the distribution of nuclei produced by contact nucleation with an impeller was determined, and also the growth rate of these nuclei in the size range 1 to 150 μm was measured. The nuclei were produced in an saturated solution of pentaerythritol by secondary nucleation and allowed to grow out in another vessel having a positive supersaturation. From their work, they drew two conclusions, (a) nuclei were born in the form of a distribution having an upper limit of 50 μm , with the bulk of the nuclei located under 1 μm , this being the lower detection limit of their measuring apparatus. (b) Significant numbers of these crystals grow at very low growth rates indicating the presence of a size dependent growth (SDG) rate or a growth rate dispersion (GRD) effect.

In a much earlier, but not dissimilar work, Bujac (1976) studied the attrition and nucleation behaviour of pentaerythritol in a 1 L vessel. In this work, the distribution of nuclei produced by attrition was determined in a saturated solution of pentaerythritol (labelled in the reference as - Exp1) and also in a separate experiment in a vessel with a supersaturation (Exp2). The nuclei distribution produced from both experiments were then compared. Particles produced in the crystallizer with a

supersaturation were allowed to grow out to larger sizes. The distribution of nuclei produced from both experiments were similar at the beginning. Later on, (after 70 mins.), the distribution of nuclei from Exp1 changed with less small particles ($< 4 \mu\text{m}$) being produced and the distribution showing a general shift to larger sizes. The form of the distribution produced during the early stages is however very similar to that determined by Hedstrom et al. (1993), with an upper limit at about $50 \mu\text{m}$ and the majority of particles lying in the sub-micron zone.

Another paper by Zipp et al. (1987) reports on the effectiveness of fines destruction in a batch crystallizer producing pentaerythritol. In this work, they show that the use of selective fines destruction using a classifying leg can significantly reduce the numbers of 'fine' crystals in the crystallizer and increase the median size making the product easier to handle and filter.

Adipic acid

Very few references with regard to the kinetics of continuous or batch crystallization of adipic acid exist.

Adipic acid is the most important component in the production of Nylon 6,6. High quality and purity of adipic acid is essential to ensure that the finished Nylon product has the required physical properties. For example, the incorporation of mono- and di-basic carboxylic acid impurities has been reported to cause termination in the subsequent polymerization process. This has a significant effect on the strength of the resulting fibre (Narang et al., 1978). For this reason, it is essential that as little as possible impurities or inclusions are incorporated into the crystal structure during the crystallization phase of adipic acid. Studies into the avoidance of incorporation of additives or impurities into the crystal structure have been directed towards altering of the morphology of the crystal to reduce the surface area of the face onto which such impurities are adsorbed (U.S. Patent, 1994). Incorporation of impurities can also effect the physical properties of crystals e.g. the dissolution rate (Grant et al., 1991), which leads to certain differences in product quality and quantity between successive batch crystallizations.

The relation between the kinetics of adipic acid crystallization and the CSD from a semi-batch crystallizer forms the topic of other work (Marchal et al., 1991). The approach is similar to the approach taken here as they combine expressions for the heat, mass, population and concentration balances to the kinetics of growth and primary and secondary nucleation. An extra component included in the modelling are equations describing the agglomeration of adipic acid, a problem often reported for

this material. The authors claim a successful modelling of the crystallizer start-up behaviour starting at a point before the primary nucleation step. They claim that it is possible to extent the modelling procedure and the kinetic models of growth, nucleation and agglomeration to other modes of operation such as a continuous MSMPR operated type crystallizer.

7.3 Kinetic Relations

The same relations as were used to model the behaviour of ammonium sulphate crystallization in the 22 L crystallizer are used here. The same parameter labels are used, i.e. p1 to p9 describing growth, attrition and secondary nucleation as were used in chapter 6. Literature evidence described in the previous section supports the use of these models.

7.4 Equipment and Sensors

The crystallizer to obtain the results in this work is the 22 L DTB evaporative crystallizer described in section 3.3.2. The first material used for crystallization was pentaerythritol ($C_5H_{12}O_4$). A series of five experiments were carried out in which the evaporative heat input and the residence time were changed. The experiments were started from a crystal free saturated solution and evaporated until a primary nucleation event occurred after which continued evaporation caused the CSD to develop in time. For all the experiments, the temperature was constant at 50°C (80 mbars) and the impeller speed was constant at 750 rpm. The remaining operating conditions for each experiment are shown in table 7.1.

Table 7.1 : *Operating conditions for Pent1 to 5 in the 22 L crystallizer with pentaerythritol as the model material for crystallization.*

<i>Experiment</i>	<i>Pent 1</i>	<i>Pent 2</i>	<i>Pent 3</i>	<i>Pent 4</i>	<i>Pent 5</i>
Heat Input (kW)	3.2	2.9	2.5	2.5	2.5
Residence Time (mins)	110	110	110	70	150

The second material crystallized was adipic acid ($C_6H_{10}O_4$). Again, start-up experiments were carried out, but the duration of the experiments was much longer than for pentaerythritol (up to 28 hours, adip2). After steady-state was reached in the

experiments with adipic acid, steps in operating conditions were carried out (heat input and impeller speed). Details of the step types and the time when the steps were programmed are given in table 7.2

Table 7.2 : *Operating conditions for Adip1 and 2 in the 22 L crystallizer with adipic acid as the model material for crystallization.*

<i>Experiment</i>	<i>Adip 1</i>	<i>Adip 2</i>	<i>Time of step after start-up (hrs)</i>
Heat Input (kW)	3.0→2.25	3.0	10
Residence Time (mins)	150	150	
Impeller speed (rpm)	900	900→1150→750	16.8, 23.2

For both materials, the Malvern 2600 C was used to measure the changes in the CSD with time, and an on-line CCD camera was also used to follow the changes in the crystal shape and morphology.

7.5 Results and Discussion

7.5.1 Crystallization of Pentaerythritol

Figure 7.1 shows the measured median size trends versus time of the experiments listed in table 7.1 from the point where crystals appear in the crystallizer solution and up to 11 hours thereafter. At increasing heat inputs, the start-up behaviour over the first 12 hours of the experiment is more dynamic with the median size for the highest heat input (3.2 kW) showing the greatest variation. With a change in residence time, from 70 to 150 minutes, no obvious trend in the dynamic behaviour can be discerned. There is however, a difference in the median size of the initial distributions between the experiments (Pent 3, 4 and 5). A similar difference was observed in the 22 L crystallizer for ammonium sulphate experiments (figure 6.4). For these experiments (Run 201 and 202), the operating conditions were the same but the position of the initial CSD median size differs by about 150 μm . The maximum difference for pentaerythritol in figure 7.1 is about 100 μm (Pent 3 and Pent 5), but the difference is

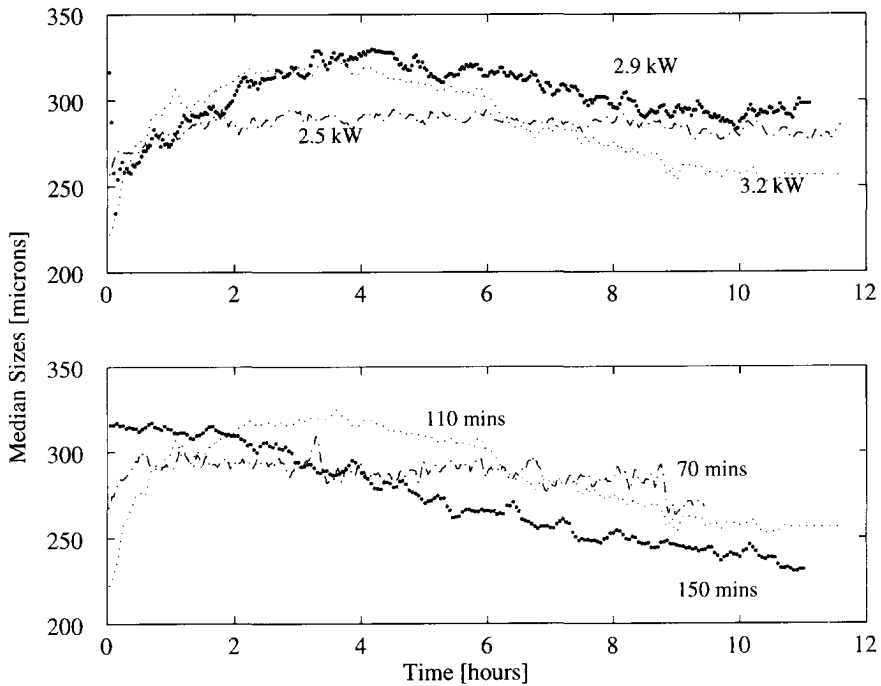


Figure 7.1 : Start-up responses for Pent 1, 2 and 3 (upper) and Pent 1, 4 and 5 (lower) in terms of the distribution median size

much more striking than for ammonium sulphate. This is because the much lower growth rates of pentaerythritol in comparison to ammonium sulphate at similar operating conditions means that the maximum median size reached by the CSD during the start-up phase will be lower than that of ammonium sulphate.

For the case of Pent 5, a maximum value is already reached by the median size at the start of the experiment, and therefore decreases throughout the rest of the experiment. In the 22 L crystallizer, the location of the primary CSD seems to be a statistical event probably influenced by small differences in the height of the suspension in the vessel, the rate of product removal and feed rate to the vessel. After the CSD reaches its' maximum median size in figure 7.1, it is subjected to attrition leading to the emergence of a second crystal population of secondary nuclei causing the median size to decrease.

In figures 7.2 and 7.3, the trends of two of these experiments (Pent 1 and 2) are also shown, in terms of three characteristic sizes, the 25, 50 and 75 % sizes as a function of time. Also, a number of fits to the data are shown using the model described in chapter 5. The initial distribution was fitted using a single log-normal

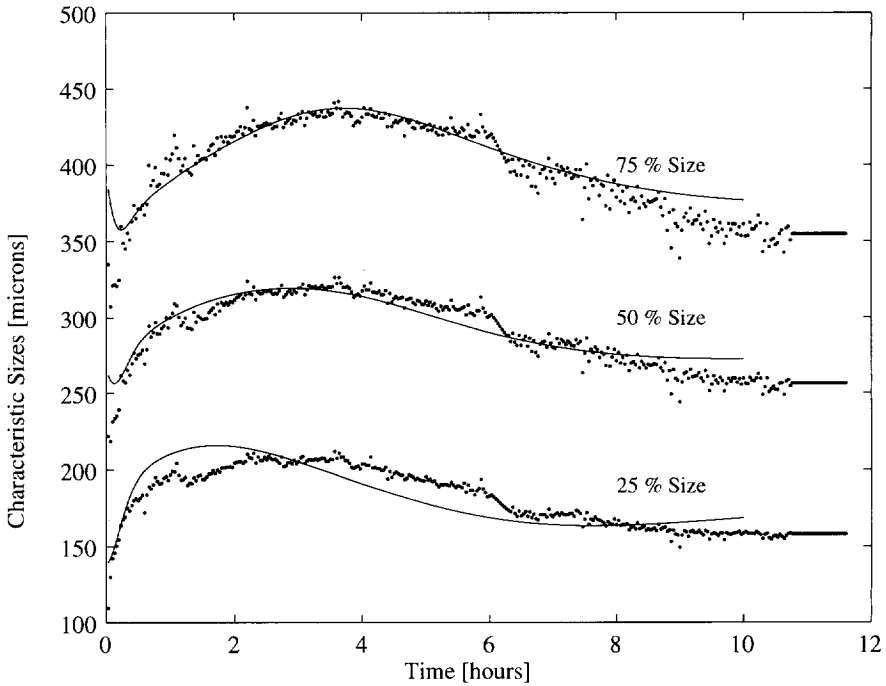


Figure 7.2 : Change in characteristic sizes (75, 50 and 25 % sizes) in time of the distribution for Pent 1

distribution. No physical or kinetic reason why a log-normal distribution should give such a good fit was found.

For the experiments simulated in figure 7.2, the following parameter values (table(7.3)) in the kinetic relations were obtained for growth, attrition and secondary nucleation.

Table 7.3 : Parameter values for the kinetic relations in chapter 6 for growth, attrition and secondary nucleation.

Parameter	$p1$	$p2$	$p3$	$p4$	$p5$	$p6$	$p7$	$p8$	$p9$
Units	m/s	-	-	μm	-	m/s	μm	-	-
Value	1e-06	1	.20	120	1.5	2.3e-09	305	5	100

To characterise the crystallization of pentaerythritol with a model, seven parameters had to be estimated from the on-line data (not including $p1$ and $p2$). This

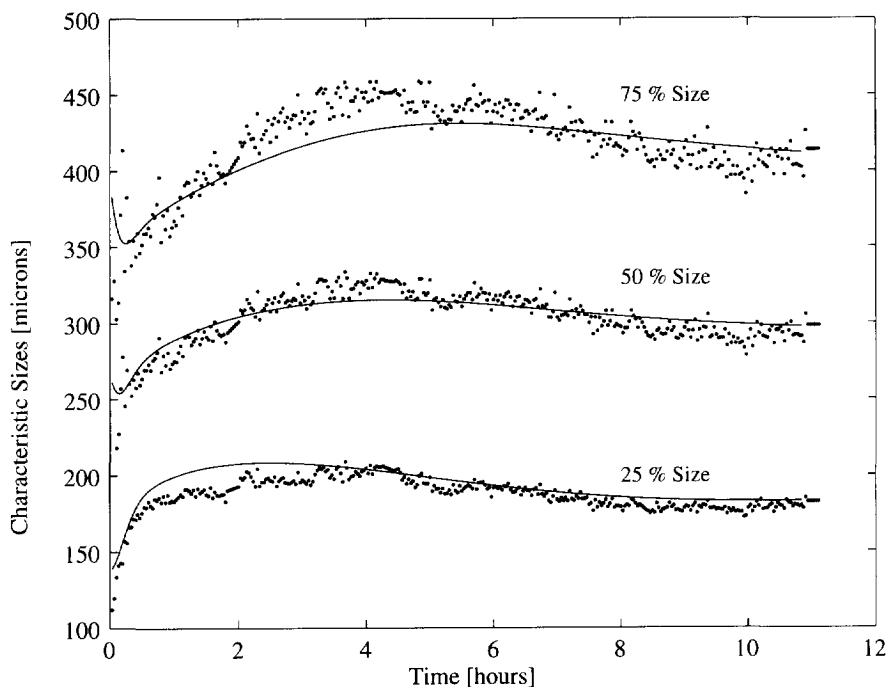


Figure 7.3 : Change in characteristic sizes (75, 50 and 25 % sizes) in time of the distribution for Pent 2

may seem like an excessive number of parameters to determine from just one data set. It was found however that the parameters determined for one experiment could also be applied to all other experiments carried out with the same material and in the same crystallizer (see e.g. the simulations in figure 7.3). With these nine parameters from the relations for growth, attrition and secondary nucleation, it is possible to accurately describe the dynamic behaviour during the first twelve hours of operation after the primary nucleation event, which justifies the application of a seven parameter set.

Figures 7.4, 7.5 and 7.6 show images recorded with the CCD camera at the beginning (2.5 hrs.), later on (6 hrs.) and towards the end (10 hrs.) of Pent1. In figure 7.4, the tetragonal morphology of the pentaerythritol crystals is evident, especially for the large crystals. A wide distribution of crystal sizes exists at this time. Figure 7.5 shows a similar distribution but what is evident this time, is that the edges and corners of the larger crystals in the image are no longer as sharp as they were in the previous photograph. The last photograph in the series, figure 7.6, shows that the large crystals have now completely lost their original shape. The decreasing amount of flat reflecting

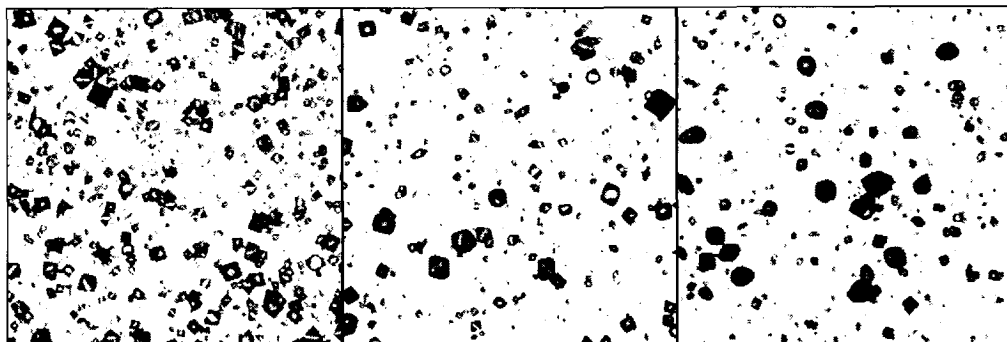


Figure 7.4, 7.5, 7.6 : *On-line CCD images of crystal suspension 2.5, 6 and 10 hours after the primary nucleation event.*

surfaces present in the successive images is also evident by examining all three images, also indicating less well defined crystal facets. In all three images, the shape of the crystal below a size of about $300\ \mu\text{m}$ remains intact. Figures 7.7 and 7.8 are SEM images of samples taken at the same time as the CCD images in figures 7.4 and 7.5. From these images, the same trend can be made out as was mentioned above with respect to the crystal shape. The process by which the crystals lose their characteristic shape is doubtlessly caused by attrition. These support the use of the attrition rate function. The SEM images also show that a large number of agglomerates are present. Not accounting for these agglomerates in the model was justified by examining the structure of the agglomerates more closely. No clear evidence of bridge formation could be seen between individual crystals and the fact that the faces of individual crystal units in the agglomerates are parallel leads one to the conclusion that the agglomerates occur because of a twinning effect, a form of agglomeration which will not have an effect on the population balance or the heat and mass balances.

Figure 7.9 shows a face of a crystal taken after 5 hours of operation, using an optical phase contrast microscope. The presence of a large number of steps on the surface can be seen, having the morphological directions as the crystal itself and apparently follows from growth instabilities.

Separate Laue diffraction measurements of pentaerythritol crystals from the crystallizer, not shown here, revealed that sub $200\ \mu\text{m}$ crystals contained a high level of stress indicating that a SDG/GRD effect was to be expected.

7.5.2 Crystallization of Adipic acid



Figure 7.7 : SEM image after 2.5 hours

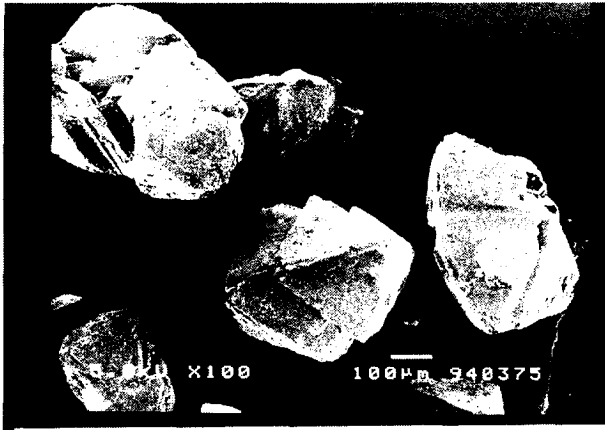


Figure 7.8 : SEM image, sample after 6 hours, notice rounded edges and corners

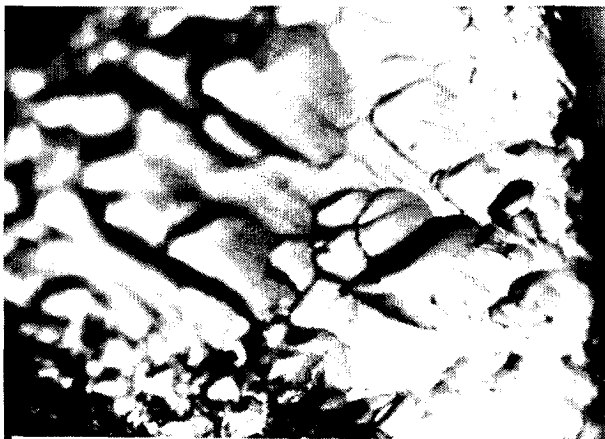


Figure7.9 : Enlargement of a crystal surface covered by a layer of gold ions. The optical photograph was taken 5 hours after nucleation, notice step patterns on surface originating from dislocations. Step height is about 20 nm.

Figure 7.10 shows the median size start-up behaviour of the two experiments listed in table 7.2. The points at which steps in the heat input and impeller speed are implemented are shown by the hatched lines. Figure 7.11 shows a comparison of the start-up trends of three experiments, in terms of the CSD median size, in the 22 L crystallizer with different materials. The operating conditions for two of these experiments are given in tables 7.1 (Pent 1) and 7.2 (Adip 2). The conditions for the experiment with ammonium sulphate are 3 kW (118 kW/m^3) of heat input and a residence time of 160 mins (Run 203, chapter 6).

Some general observations can be made with regard to the start-up behaviour of the adipic acid experiment (Adip2) in comparison to the other two materials. All three experiments were started from a primary nucleation event. The initial distribution formed in the crystallizer first goes through an outgrowth phase in which the population of primary nuclei increases in size due to growth. A maximum is reached by the CSD after a period of outgrowth after which the median size decreases again and enters a second oscillation to eventually reach an apparent steady-state. In the case of pentaerythritol, the experiment was not carried on long enough to see if the CSD enters a second oscillation, and for ammonium sulphate the second oscillation is complete as it also is for adipic acid.

In figure 7.10, the start-up behaviours of Adip 1 and 2 are shown. The start-up behaviours seem different at a first glance, but actually the initial median size differs by only $25 \mu\text{m}$ (350 and $325 \mu\text{m}$). This difference is, as mentioned for pentaerythritol due to slight differences in the operating conditions, leading to initial CSD's which have different positions and total numbers of crystals. It seems as though a much greater number of crystals are formed during the primary nucleation event of Adip1, which results in a much lower specific growth rate of the crystals and as such the CSD does not grow out at a rapid rate. In Adip 2, a low number density of crystals was formed in the primary nucleation step and resulted in a high specific growth rate of crystals, and because of this, the CSD median size grows out to larger sizes very rapidly over the first hour of the experiment. In both experiments, the behaviour after the CSD has reached a maximum is similar, with the median size decreasing and entering a second oscillation before gradually reaching a steady-state situation. A steady-state for Adip 1 is reached after 10 hours and for Adip 2 after 17 hours. The steady-state medians have approximate similar values of 315 and $325 \mu\text{m}$. After a steady-state had been reached by Adip 1, a step in the heat input was made from 3 to 2.25 kW. This change in operating condition had no effect on the CSD. In Adip 2, two steps in the impeller speed were made after 16.8 hours (900 to 1150 rpm) and 23.2 hours (1150 to 750 rpm). The median responded by decreasing in size with an increase

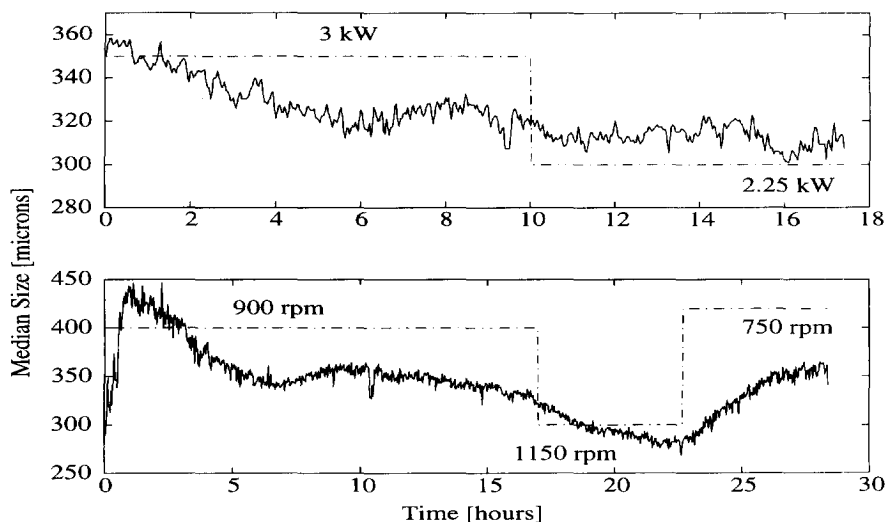


Figure 7.10 : Start-up in the 22 L crystallizer with adipic acid as the model material. Adip 1 (upper) contains a step in the heat input and Adip 2 (bottom) contains steps in the impeller speed.

in impeller speed and increasing in size with a decrease in the impeller speed. The effect of the impeller speed recorded here on the CSD can arise due to two possible effects. In the presence of agglomerates, a higher impeller speed would tend to break the looser connections between individual crystals, thus reducing the median size. This effect would be almost instantaneous and lead to a rapid decrease in the median size and an increase in the total numbers of crystals. Another possible effect leading to this behaviour could be an increased attrition rate of the large crystals due to an increased collision probability. This effect would be seen over a much longer period of time, as the reduction in median crystal size would occur much more slowly.

To examine if agglomeration was occurring during the adipic acid experiments, CCD images of the CSD were examined. Three CCD images recorded during Adip 1 are shown in figure 7.12, 7.13 and 7.14. The images show the CSD after times of 30 mins, 1 hour and 5 hours. The plate like form of the adipic acid crystals can be seen in each of the images. On visual comparison of the CCD images, the CSD does not show any significant differences as the experiment continues. This is consistent with the measured trend in figure 7.10 where the median size only varies between 360 and 300 μm over the first five hours. Very little evidence of agglomeration was seen in these images as well as subsequent SEM photographs of crystal samples from the crystallizer.

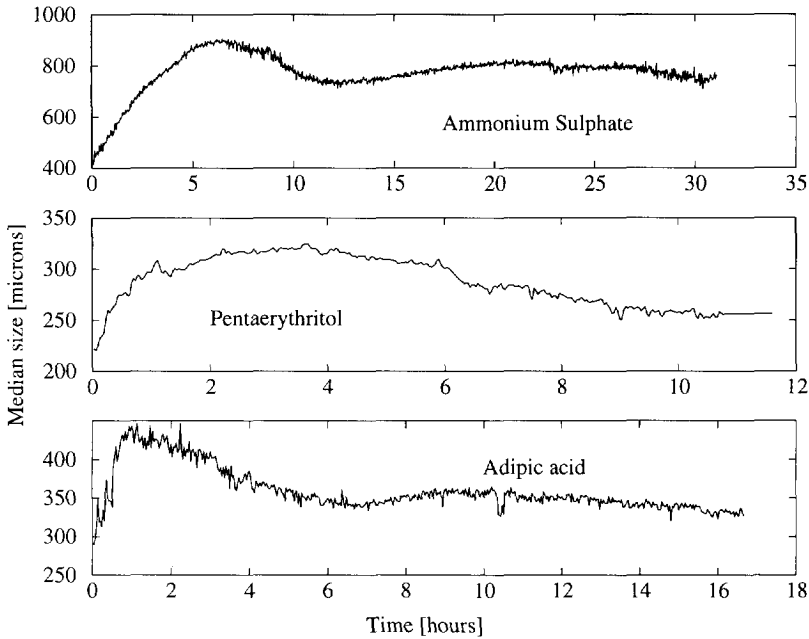
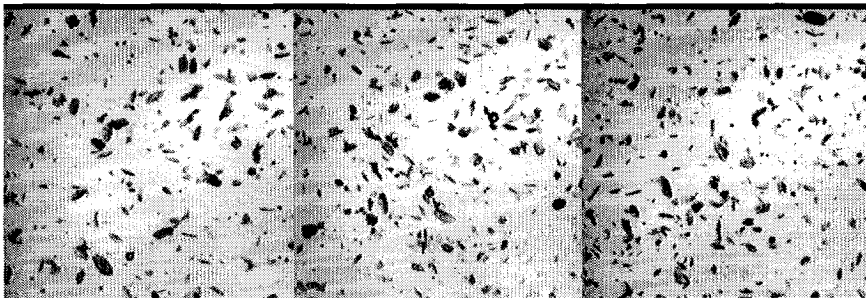


Figure 7.11 : Comparison of start-up trends for three different materials in the 22 L crystallizer.

From the modelling of the start-up behaviours of ammonium sulphate and pentaerythritol, it was seen that with the model outlined in chapter 5, it was possible to describe the crystallization behaviours of these materials. This model considered the kinetic processes of growth, attrition and secondary nucleation. From the broad similarities between the start-up behaviours of adipic acid with the other materials,



Figures 7.12,7.13,7.14 : CCD images of adipic acid crystals in the product line from the 22 L crystallizer : Experiment Adip 1 after 30 minutes, 1 hour and 5 hours

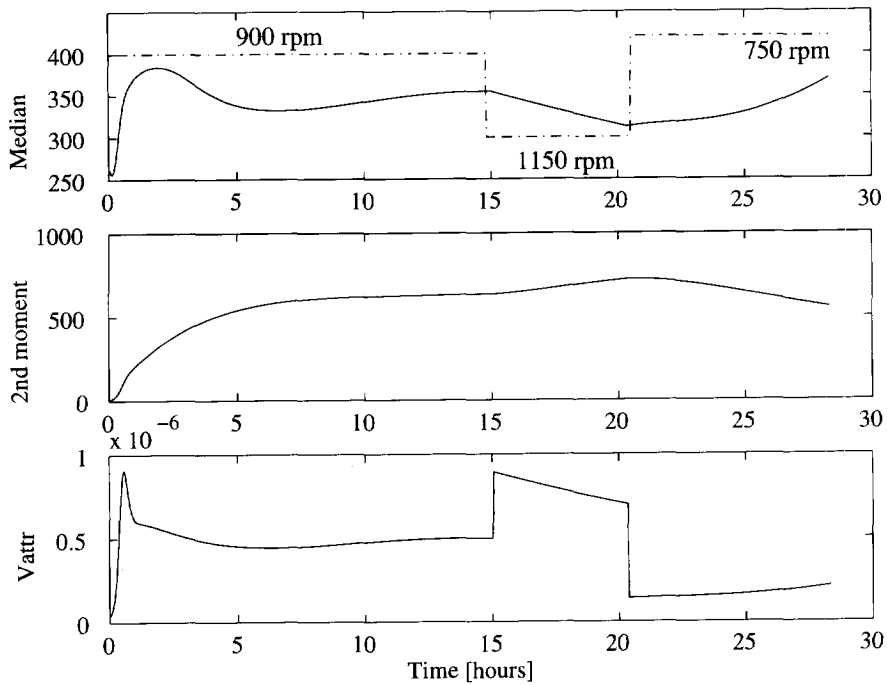


Figure 7.15 : Results of the simulation of an adipic acid experiment with the parameters given in table 7.4. Figure shows the median size (top, in microns), the second moment and the volume rate of production of attrition particles (bottom, in $m^3/m^3.s$)

and as agglomeration seems not to play a role in the process leading to the shape and position of the product CSD, the same model was applied to the results of Adip 2. Figure 7.15 shows the results of such a simulation. A better fit of the initial distribution in the crystallizer could be achieved with an exponential distribution as opposed to a log-normal distribution, but even this fit was not entirely satisfactory, and for this reason, the kinetic parameters cannot be estimated with great certainty. Table 7.4 shows the parameters recorded from the simulation fit procedure. Additionally, to get a first impression of the effect of an increased impeller speed on the CSD, the attrition rate constant p_8 was changed at the points where the impeller speed was either increased (value of p_8 up by 80% from its' value at the original steady-state) or decreased (value of p_8 down by 50% from its' value at the original steady-state). Figure 7.15 shows the median size, the second moment of the distribution and the volume rate of attrition fragment production in the crystallizer over time. These output parameters were chosen as they are quantities which show the effect of an increased

attrition rate on the existing CSD (median and second moment) and the attrition fragment production rate.

By increasing the impeller speed, the collision probability between crystals and the impeller increases. The increased probability must be reflected in the parameter chosen in the attrition function to simulate a step in the impeller speed. For this reason p_8 was chosen as it will increase the collision probability of all crystals by a fixed amount. By changing another parameter in the attrition function, it may also have been possible to obtain the same effect.

Table 7.4 : *Parameter values for the kinetic relations in chapter 6 for growth, attrition and secondary nucleation of adipic acid crystallization.*

Parameter	p_1	p_2	p_3	p_4	p_5	p_6	p_7	p_8	p_9
Units	<i>m/s</i>	-	-	μm	-	<i>m/s</i>	μm	-	-
Value	2.5e-06	1	.25	150	2.5	1.6e-09	350	9	37.5

The simulation shows that the observed dynamic behaviour of adipic acid start-up in the crystallizer can be described with the same model framework as was used for pentaerythritol. Some important points to note are that again a SDG function and a supersaturation dependent outgrowth term were critical to reach a satisfactory modelling of adipic acid crystallization.

7.6 Model choice effect on simulation

To demonstrate how important all the elements in the model used for the simulations in figures 7.2, 7.3 and 7.15 are, a number of simulations are carried out where an element is missing or the power law for secondary nucleation (equation 1.2) is used to simulate the dynamic behaviours. For these simulations, the sample results of Pent1 and Adip2 are used. Details of the equations for the kinetic processes are given in table 7.5. In simPE1 and simAA1, the power law relation for secondary nucleation is used together with the standard attrition rate function (equation (5.7)) and a size independent growth rate (equation (2.13)). In simPE2 (simAA2), the power law model is replaced by the secondary nucleation model developed in chapter 5 but the survival efficiency is held constant throughout the experiment instead of having it as a function of the supersaturation. SimPE3 (simAA3), is the same as simPE2 but the survival is assumed to be a linear function of the supersaturation. The parameter

values assumed for the kinetic equations are those which resulted from the optimisations for Pent1 (table 7.1) and Adip2 (table 7.2). Where the kinetic parameters have not previously been given in any of these tables, they are included in table 7.4.

Table 7.5 : Kinetic relations and parameter values used for the simulations in figures 7.16 and 7.17 for pentaerythritol and adipic acid.

Tag	simPE1/simAA1	simPE2/simAA2	simPE3/simAA3
Growth	$G_{kin} \sim \sigma$	$G_{kin} \sim \sigma$	$G_{kin} \sim \sigma$
Attrition	$G_{attr} \sim f(x)$	$G_{attr} \sim f(x)$	$G_{attr} \sim f(x)$
Survival	-	$\eta_{survival} = k_{survival}$	$\eta_{survival} = k_{survival}\sigma$
PE value		$\eta_{survival} = 0.70$	
AA value		$\eta_{survival} = 0.33$	
Nucleation	$B_o = k_n m_3 G_{kin}^2$	$B(x) = \eta_{surv} H(x) V_{attr}$	$B(x) = \eta_{surv} H(x) V_{attr}$
PE value	$B_o = 1.5 \cdot 10^{13} m_3 G_{kin}^2$		
AA value	$B_o = 4 \cdot 10^{13} m_3 G_{kin}^2$		

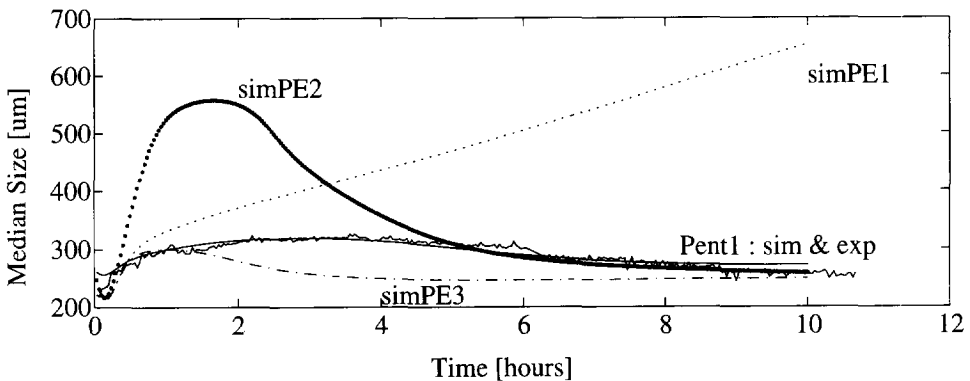


Figure 7.16 : Demonstration of four different combinations of relations to simulate the results of experiment Pent1. Models used are listed in table 7.5.

The results of the simulations are plotted in figures 7.16 and 7.17 for pentaerythritol and adipic acid respectively. The simulation fits from figure 7.1 and 7.15 are also included as well as the measured start-up trend for pentaerythritol in figure 7.16. SimPE1 where the power law is used shows an increasing median size throughout the entire experiment. This occurs as the attrition function constant ($p8$) is too low to prevent the median size from increasing at an almost linear rate. An

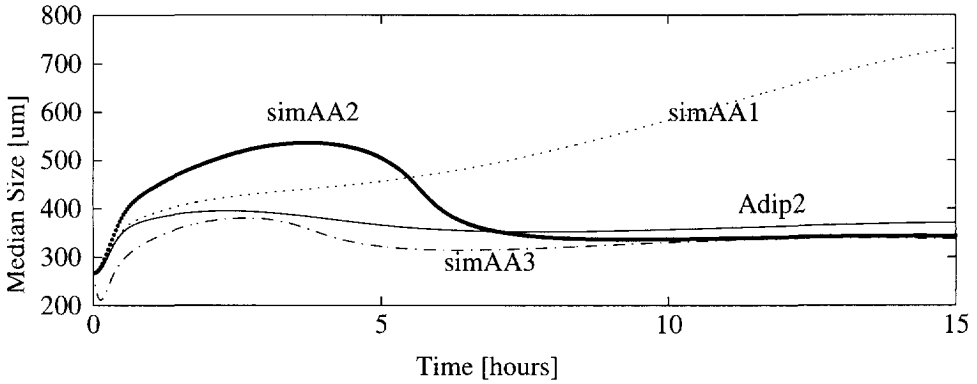


Figure 7.16 : Demonstration of four different combinations of relations to simulate the results of experiment Adip2. Models used are listed in table 7.5.

increase in the value of parameter p_8 will lower the trajectory of simPE1 but the fit will not improve. The other three simulations show the importance of including a supersaturation dependent survival efficiency (simPE2 and simPE3) and of including a SDG rate of crystals (Pent 1). A SDG rate function has a much stronger effect on these materials than on ammonium sulphate, because the distribution in the case of pentaerythritol and adipic acid lie much more in the area where a SDG rate effects the growth rate of crystals ($<250 \mu\text{m}$), whereas for ammonium sulphate the bulk of the distribution on a volume basis lies well outside this area. The importance of a supersaturation dependent survival efficiency is also seen, as a high supersaturation at the beginning of these experiments means that a lot of secondary nuclei are produced. If it is a constant, much less are produced and the lower total surface area of crystals allows the initial distribution to grow out to much greater sizes.

7.7 Concluding Comments

From this work, it can be concluded that the original assumptions made in choosing kinetic models to describe the processes of growth, attrition and secondary nucleation for ammonium sulphate, can be successfully extended to describe the crystallization behaviour of other materials which have very different solubility characteristics.

Further, the choice made as to which kinetic relations to include or omit from the dynamic simulations is critical to gain an accurate simulation of the CSD. This

choice can be aided by gathering information regarding crystal shape change during the experiment.

Chapter 8

Conclusions and suggestions for future work

8.1 Conclusions

The three most important conclusions resulting from the work presented in this thesis are that :

- A new mechanistic approach to describing the formation of attrition particles and their survival to become secondary nuclei has been suggested and validated.
- The introduction of a size dependent growth (SDG) function to describe the growth rate of secondary nuclei has shown to be crucial when modelling the CSD dynamic behaviour of badly soluble materials.
- The suggested models for growth, attrition and secondary nucleation have shown to be applicable to the crystallization of a material on different scales and materials with large differences in solubility characteristics.

From evaluating the kinetics of a number of different materials, namely, ammonium sulphate, pentaerythritol and adipic acid, some guidelines can be stated

when choosing kinetic relations for the modelling of the dynamic behaviours of well and badly soluble materials.

- Use of the 'traditional' power law model for secondary nucleation yields a poor description of the CSD dynamic behaviour for all the materials tested. This occurs, as in the power law, the nucleation rate is correlated to the entire mass of crystals in the crystallizer, whereas in fact, only the large crystal fraction contribute to the nucleation production rate.
- A model where the secondary nucleation rate is related to only the fraction of crystals from which secondary nuclei are formed gives much better results for the dynamic behaviour of the CSD. The production rate of attrition fragments is obtained from an attrition function which describes the downward curvature in the large particle size ranges in a $\log(n)$ versus x type plot of a steady-state distribution.
- Inclusion of a supersaturation dependent survival efficiency function for the attrition fragments is crucial to accurate modelling of the nucleation rate. This is especially true for the materials which have a low solubility in the solvent. The physical explanation for the inclusion of such a survival efficiency term is because the level of internal strain in the crystals introduced during the attrition step and/or during the outgrowth step, causes the crystal to 'feel' a lower driving force for growth than if the crystal was free of internal strain. The survival efficiency can have a maximum value of unity.
- The use of a length dependent nucleation function can account for the observation that crystals are born over a range of sizes and not just at a finite size. Suitable functions describing the shape of the produced attrition fragments can be incorporated into the simulation framework.
- For materials with a low solubility, the inclusion of a size dependent growth function is very important to the correct modelling of the dynamic behaviour. The inclusion of a SDG/GRD function does not have such a large effect on the dynamics of a well soluble material (ammonium sulphate). This can be explained

by the fact that for low soluble materials, the median size lies between 300 and 400 μm . If a SDG/GRD effect is present in crystals up to sizes of 250 μm , then the majority of crystals will be under the influence of a SDG/GRD effect. For well soluble materials with a median size which is much greater, the effect of SDG/GRD will not be felt so strongly. For all material types, the inclusion of a SDG/GRD rate will increase the secondary nucleation rate predicted for the system by the simulation package, by a significant amount.

By comparing the crystallization behaviour of three materials (ammonium sulphate, pentaerythritol and adipic acid), several conclusions can be drawn with respect to the behaviour of different materials crystallized in a continuous operating mode.

- All of these materials exhibit a dynamic behaviour during the start-up phase of operation which persists for up to 13 times the length of one residence time, before the system comes to a steady-state. The dynamic behaviour is initiated by the fact that the initial condition in the crystallizer, directly after the primary nucleation step, is not the same as the steady-state condition.
- The processes of crystal growth, attrition and secondary nucleation determine the shape of the start-up CSD response, between the time the first distribution appears in the crystallizer and the time that a steady-state condition is reached.

With respect to the scale of operation of crystallizers, results were obtained which contradict the work of other workers who have studied the crystallization behaviour in the 970 and 22 L crystallizers. Ammonium sulphate was crystallized on both scales and the results showed that the dynamic behaviour in both crystallizers was very similar and could be described using the same model which was originally developed for the 970 L crystallizer. The median size obtained in the 22 L crystallizer was also greater than that produced in the 970 L crystallizer. This was probably due to the longer residence times of the experiment in the 22 L crystallizer. The influence of the different geometries of both crystallizers on the CSD has to be examined by doing experiments with similar residence times.

From the work done on the more fundamental aspects of crystal kinetics, conclusions can be drawn about the mechanism of growth of secondary nuclei in the crystallizer.

- Crystals grow with an apparent size dependent growth rate for all of the materials tested up to sizes of between 200 and 300 μm . This type of growth behaviour could also be caused by a growth rate dispersion mechanism, but the way in which the growth function was determined i.e. for a suspension sample withdrawn from the fines loop in the crystallizer and inoculated in a 2 L growth cell, the difference between the two types of growth could not be discerned.
- The presence of crystal internal strain in ammonium sulphate crystals removed from the 970 L crystallizer is most likely responsible for the observation of the SDG or GRD phenomena effect in the crystallizer. The internal strain measured, using Laue synchrotron radiation, showed that the level of strain in crystals is significant ($> 0.5^\circ$) up to sizes of 200 μm .
- The necessity of a supersaturation dependent survival efficiency of secondary nuclei agrees with the previously observed growth behaviour of secondary nuclei reported in literature. It was observed that contact nuclei with an initial size $< 4 \mu\text{m}$ grew very slowly or not at all in a supersaturated medium. No division according to size between growers and non-growers could be made in this work.

8.1 Suggestions for future work

To obtain a more complete picture of the kinetics of crystallization and to reduce the uncertainty in the parameters used for growth, attrition and secondary nucleation, attention to the following topics should be paid.

Theoretical :

Many of the kinetic relations used in this thesis are more empirical in nature than kinetic. Further efforts at clarifying the dynamics of suspension crystallization should be made by examining the driving forces behind the processes. Theoretical relationships for the following points should be derived :

- The relationship between the internal strain of crystals, the survival efficiency of secondary nuclei and the level of supersaturation.
- The relationship between crystal internal strain and the growth rate of secondary nuclei.
- The effect which crystal internal strain has on the rate limiting step during the growth process.
- The relationship between crystal properties (morphology, inclusion structure) and their attrition rate.
- The possibility of primary nucleation occurring in some parts of the crystallizer where a very high supersaturation exists may lead to a limit cycle. Thus, it may be wise to prepare a model describing this phenomena to fit into a compartmental approach to the modelling of the dynamics. A compartmental model of a crystallizer is constructed by considering the crystallizer as being made up of a series of compartments. The choice of compartments is made by isolating the major processes (kinetical, physical) occurring in the crystallizer. Two obvious compartments are the boiling zone and the impeller zone.

From an experimental point of view :

- A lot of information on the crystallization kinetics of different materials can still be gained by doing experiments on the 22 L scale. Up to now, the main type of experiments have been start-up experiments from a crystal free environment. More steady-state operating condition step changes should be done as they are much more time efficient and the disturbances encountered in industry will be closer to these kind of disturbances. The results of such experiments can act as data to validate the above theoretical models.
- A sampling system to remove product from different points in the 22 L crystallizer as a first step to obtaining data for validation of a compartmental

model approach for the crystallizer. Measurement of a supersaturation profile in the crystallizer is also very important for validation of a compartmental model.

- To gain information on the real growth behaviour of secondary nuclei, a small (20 to 100 ml) growth cell could be placed in parallel with the fines removal line to isolate samples of crystals and to follow their growth behaviour using a microscope. With such a device, it could be seen if the growth mechanism leading to the SDG function measured in chapter 4, results from a true SDG behaviour or if it is a GRD mechanism which is occurring.
- From the evidence in the literature, there are a number of important design factors which have an influence on the shape and position of the distribution of the CSD. These factors are for example, the top of the draft tube to boiling zone clearance, the impeller tip to draft-tube clearance and the position of product removal and feed entry to the crystallizer. It may be worthwhile to redesign parts of the crystallizer to evaluate these parameters as CSD actuators and optimum design criteria.

Appendix A

Mass and energy balances

A well mixed crystallizer is considered and the assumptions given in section 2.2 of chapter 2 are relevant.

Four balances are considered, the crystal population balance, the dissolved and crystalline salt balance, the energy balance and an overall mass balance. General equations for the system described in chapter 2 are first formulated, and they are then subjected to several simplifications to yield three equations with three unknowns. The equations are then solved for the cases of a class one and a class two system.

Population balance

$$\frac{\partial n(x,t)V}{\partial t} = -V \frac{\partial n(x,t)G(x,t)}{\partial x} - (Q_p h_p + Q_F h_F)n(x,t) + B(x)V \quad (\text{A1})$$

By multiplication each term in this equation times $k_v x^3$, the following is obtained,

$$k_v \frac{\partial V}{\partial t} \int_0^{\infty} n x^3 dx + k_v V \int_0^{\infty} \frac{\partial n}{\partial t} x^3 dx = -k_v V \int_0^{\infty} \frac{\partial n G}{\partial x} x^3 dx - k_v Q_p \int_0^{\infty} h_p n x^3 dx - k_v Q_F \int_0^{\infty} h_F n x^3 dx - k_v Q_i \int_0^{\infty} n_i x^3 dx - k_v V \int_0^{\infty} B(x) x^3 dx \quad (\text{A2})$$

Defining the voidage fraction in the crystallizer as $\varepsilon = 1 - k_v m_3$, and substituting for the third moment wherever it occurs, the crystal mass balance over the crystallizer results, giving,

$$\frac{\partial V}{\partial t}(1-\varepsilon) - V \frac{\partial \varepsilon}{\partial t} = +3k_v V \int_0^{\infty} G n x^3 dx - Q_p(1-\varepsilon_p) - Q_F(1-\varepsilon_F) + Q_i(1-\varepsilon_i) + k_v V \int_0^{\infty} B(x)x^3 dx \quad (\text{A3})$$

Salt balance

$$\begin{aligned} \frac{\partial}{\partial t} [\varepsilon V C + (1-\varepsilon)V \rho_c] = & Q_i [\varepsilon_i C + (1-\varepsilon_i)\rho_c] + Q_d C_d - Q_p [\varepsilon_p C + (1-\varepsilon_p)\rho_c] \\ & - Q_F [\varepsilon_F C + (1-\varepsilon_F)\rho_c] \end{aligned} \quad (\text{A4})$$

Partial differentiation of the left hand side of equation yields,

$$\frac{d}{dt} [\varepsilon V C + (1-\varepsilon)V \rho_c] = \varepsilon V \frac{dC}{dt} + (\rho_c - C) \left[(1-\varepsilon) \frac{dV}{dt} - V \frac{d\varepsilon}{dt} \right] + C \frac{dV}{dt} \quad (\text{A5})$$

By substitution of A3 into A5, the following is derived,

$$\begin{aligned} \varepsilon V \frac{dC}{dt} = & Q_d C_d - C \frac{dV}{dt} - Q_p C - Q_F C + Q_i C + Q_i \varepsilon_i [C_i - C] \\ & - (\rho_c - C) \left[3k_v V \int_0^{\infty} G n x^2 dx + k_v V \int_0^{\infty} B(x)x^3 dx \right] \end{aligned} \quad (\text{A6})$$

Energy balance

$$\begin{aligned} \frac{d}{dt} T [\varepsilon V \rho c_p + (1-\varepsilon)V \rho_c c_{pc}] = & Q_i [\varepsilon_i \rho_i c_{pi} + (1-\varepsilon_i)\rho_c c_{pc}] T_i + Q_d \rho_d c_{pd} T_d + P_{imp} + P_{hc} - P_{loss} \\ & - Q_p [\varepsilon_p \rho c_p + (1-\varepsilon_p)\rho_c c_{pc}] T - Q_F [\varepsilon_F \rho c_p + (1-\varepsilon_F)\rho_c c_{pc}] T - Q_v [\rho_v R_v + \rho_v c_{pv} T] \end{aligned} \quad (\text{A7})$$

Partial differentiation of the left hand side of equation A7 yields,

$$\begin{aligned} \frac{d}{dt} T [\varepsilon V \rho c_p + (1-\varepsilon)V \rho_c c_{pc}] = & [\varepsilon V \rho c_p + (1-\varepsilon)V \rho_c c_{pc}] \frac{dT}{dt} + T [\rho c_p - \rho_c c_{pc}] \frac{d\varepsilon}{dt} \\ & T [\varepsilon \rho c_p + (1-\varepsilon)\rho_c c_{pc}] \frac{dV}{dt} + T \varepsilon V c_p \frac{d\rho}{dt} + T \varepsilon V \rho \frac{dc_p}{dt} \end{aligned} \quad (\text{A8})$$

By substituting for the last two terms by the following equalities,

$$\frac{d\rho}{dt} = \frac{d\rho}{dT} \frac{dT}{dt} \quad \frac{dc_p}{dt} = \frac{dc_p}{dT} \frac{dT}{dt}$$

a new form of equation A8 is obtained

$$\begin{aligned} \frac{d}{dt} T [\varepsilon V \rho c_p + (1-\varepsilon)V \rho_c c_{pc}] = & [\varepsilon V \rho c_p + (1-\varepsilon)V \rho_c c_{pc} + T \varepsilon V c_p \frac{d\rho}{dT} + T \varepsilon V \rho \frac{dc_p}{dT}] \frac{dT}{dt} \\ & + [T \rho_c c_{pc} - T \rho c_p] \left[(1-\varepsilon) \frac{dV}{dt} - V \frac{d\varepsilon}{dt} \right] + T \rho c_p \frac{dV}{dt} \end{aligned} \quad (\text{A9})$$

By substitution of A3 into A9, and by making the assumption that $\epsilon_F \cong 1$ and $\epsilon_p \cong 1$, the following is derived,

$$\begin{aligned}
 V[\epsilon\rho c_p + (1-\epsilon)\rho_c c_{pc} + T\epsilon[c_p \frac{d\rho}{dt} + \rho \frac{dc_p}{dt}]] \frac{dT}{dt} &= -T\rho c_p \frac{dV}{dt} + Q_d \rho_d c_{pd} T_d \\
 + Q_i [T_i \epsilon_i \rho_i c_{pi} + T\rho c_p (1-\epsilon_i)] + Q_i [\rho_c c_{pc} (1-\epsilon_i)(T_i - T)] - Q_p \rho c_p T - Q_F \rho c_p T \\
 - Q_v [\rho_v R_v + \rho_v c_{pv} T] - [T\rho_c c_{pc} - T\rho c_p] [3k_v V \int_0^\infty G n x^2 dx + k_v V \int_0^\infty B(x) x^3 dx] \quad (A10)
 \end{aligned}$$

Total mass balance

$$\begin{aligned}
 \frac{d}{dt} [V(\epsilon\rho + (1-\epsilon)\rho_c)] &= Q_i [\epsilon_i \rho_i + (1-\epsilon_i)\rho_c] + Q_d \rho_d - Q_p [\epsilon\rho + (1-\epsilon)\rho_c] \\
 - Q_F [\epsilon_F \rho + (1-\epsilon_F)\rho_c] - Q_v \rho_v \quad (A11)
 \end{aligned}$$

Once again, by expanding and rearranging the left hand side of A11 gives,

$$\frac{d}{dt} [V(\epsilon\rho + (1-\epsilon)\rho_c)] = (\rho_c - \rho) [(1-\epsilon) \frac{dV}{dt} - V \frac{d\epsilon}{dt}] + \rho \frac{dV}{dt} + V\epsilon \frac{d\rho}{dt} \quad (A12)$$

Substituting A3 into A12 and assuming that $\epsilon_F \cong 1$ and $\epsilon_p \cong 1$, yields,

$$\begin{aligned}
 \rho \frac{dV}{dt} + V\epsilon \frac{d\rho}{dt} &= Q_d \rho_d + Q_i [\rho + \epsilon_i (\rho_i - \rho)] + Q_d \rho_d - Q_p \rho - Q_F \rho - Q_v \rho_v \\
 - (\rho_c - \rho) k_v [3V \int_0^\infty G n x^2 dx + V \int_0^\infty B(x) x^3 dx] \quad (A13)
 \end{aligned}$$

Under the following assumptions, the salt concentration (A6), energy (A10) and total mass (A13) balances can be simplified.

- 1 The feed is crystal free : $\epsilon_i = 1$
- 2 The nucleation rate term is negligible in comparison to the growth rate term or

$$3V \int_0^\infty G n x^2 dx \gg V \int_0^\infty B(x) x^3 dx$$
- 3 The temperature of the system remains constant : $\frac{dT}{dt} = 0$
- 4 The variation in suspension density is negligible : $\frac{d\rho}{dt} = 0$
- 5 The volume of the crystallizer is constant : $\frac{dV}{dt} = 0$

Salt balance

$$\epsilon V \frac{dC}{dt} = Q_d C_d - Q_p C - Q_F C + Q_i C - (\rho_c - C) [3k_v V \int_0^{\infty} G n x^2 dx] \quad (\text{A14})$$

Energy balance

$$Q_d \rho_d c_{pd} T_d + Q_i T_i \rho_i c_{pi} - Q_p \rho_p c_p T - Q_F T \rho c_p - Q_v [\rho_v R_v + \rho_v c_{pv} T] \\ P_{imp} + P_{hc} - P_{loss} - [T \rho_c c_{pc} - T \rho c_p] [3k_v V \int_0^{\infty} G n x^2 dx] = 0 \quad (\text{A15})$$

Total mass balance

$$Q_d \rho_d - Q_p \rho - Q_F \rho + Q_i \rho_i - Q_v \rho_v - (\rho_c - \rho) [3k_v V \int_0^{\infty} G n x^2 dx] = 0 \quad (\text{A16})$$

A14, 15 and 16 form a system of three linear equations, which completely define the system in terms of in- and outgoing flows and quantities. The equations must be solved to give expressions for the three unknowns, i.e. the growth rate (G), the feed flow rate (Q_i) and the vapour flow rate (Q_v).

Derivation of the growth rate function for a Class II system.

A Class I material, according to the definition given by Randolph and Larson (1988), normally refers to a well soluble material. In this case, it is assumed that the variation in the supersaturation with time in the crystallizer is negligible, or in other words that mass transfer from the liquid to the solid crystalline phase is instantaneous.

Under these circumstances, the concentration term on the left hand side of equation A14 is set to zero, $\frac{dC}{dt} = 0$. Equation A14 is then rearranged to give an expression for the feed flow rate (Q_i) in terms of the growth rate (G).

$$Q_i = \frac{(\rho_c - \rho) 3k_v V \int_0^{\infty} G n x^2 dx + Q_p C + Q_F C - Q_d C_d}{C} \quad (\text{A17})$$

Q_i is eliminated from the mass balance by substitution of A15 into A14. The further assumption that the concentration difference between the feed stream and the vessel contents is negligible, i.e. $C = C_i$. An expression for the vapour flow rate in terms of the growth rate is obtained.

$$Q_v = \frac{1}{\rho_v} [\rho_c (\frac{\rho_i}{C} - \rho_i + \rho - 1) 3k_v V \int_0^\infty Gnx^2 dx + (Q_p + Q_f) (\frac{\rho_i - \rho}{\rho_v}) + Q_d [\frac{1}{\rho_v} (\rho_d - C_d \frac{\rho_i}{C})]] \tag{A18}$$

Another expression for Q_v can be obtained by substituting for Q_i from A17 into the energy balance A15. A further assumption applied at this point is that the heat loss to the environment is equal to the heat input due to the impeller action ($P_{loss} = P_{imp}$) the following expression is obtained.

$$Q_v = \frac{1}{(\rho_v R_v + \rho_v c_{pv} T)} [((\rho_c - C) \frac{T_i \rho_i c_{pi}}{C} - (T \rho_c c_{pc} - T \rho c_p)) 3k_v V \int_0^\infty Gnx^2 dx + Q_p (T_i \rho_i c_{pi} - T \rho c_p) + Q_f (T_i \rho_i c_{pi} - T \rho c_p) + Q_d (T_d \rho_d c_{pd} - T_i \rho_i c_{pi} (\frac{C_d}{C})) + P_{hc}] \tag{A19}$$

To derive an expression for the growth rate, the two expressions for Q_v A18 and A19 are set equal to each other and an expression for the growth rate is obtained. Firstly a few terms in the expressions are gathered together to make the next calculations easier to perform.

$$K1 = (Q_p + Q_f) (\frac{\rho_i - \rho}{\rho_v}) + Q_d [\frac{1}{\rho_v} (\rho_d - C_d \frac{\rho_i}{C})]$$

$$K2 = \rho_c (\frac{\rho_i}{C} - \rho_i + \rho - 1)$$

$$K3 = Q_p (T_i \rho_i c_{pi} - T \rho c_p) + Q_f (T_i \rho_i c_{pi} - T \rho c_p) + Q_d (T_d \rho_d c_{pd} - T_i \rho_i c_{pi} (\frac{C_d}{C})) + P_{hc}$$

$$K4 = (\rho_c - C) \frac{T_i \rho_i c_{pi}}{C} - (T \rho_c c_{pc} - T \rho c_p)$$

$$K5 = \frac{1}{(\rho_v R_v + \rho_v c_{pv} T)}$$

Equating A18 and A19 then becomes,

$$\frac{1}{\rho_v} [K2 * 3k_v V \int_0^\infty Gnx^2 dx + K1] = \frac{1}{k5} [K4 * 3k_v V \int_0^\infty Gnx^2 dx + K3] \tag{A20}$$

From A20, The growth rate is taken outside of the integral sign as it is a constant and the terms of G are collected to lead to the final form for the growth rate.

$$G = \frac{1}{3k_v V \int_0^\infty nx^2 dx} [(\frac{K3}{K5} - K1) / (K2 - \rho_v \frac{K4}{K5})] \tag{A21}$$

Once the growth rate is known the values for Q_i and Q_v can be calculated from A17 and A18.

Derivation of the growth rate function for a Class I system.

For a class I system, the variation in the concentration with time is not negligible and is not eliminated from equation A14 ($\frac{dC}{dt} \neq 0$). For a class I system, an extra expression can be introduced into the system of equations for the growth rate as a function of the supersaturation.

$$G = k\Delta C^n = k' \left(\frac{\Delta C}{C^*} \right)^n \quad (\text{A22})$$

Using A14, A15 and A16 as a starting point, the following terms are gathered together to derive an expressions for the growth rate.

$$K6 = \rho_v c_{pv} T + \rho_v R_v$$

$$K7 = \rho_i c_{pi} T$$

$$K8 = Q_p (T_i \rho_i c_{pi} - T \rho c_p) + Q_f (T_i \rho_i c_{pi} - T \rho c_p) + Q_d (T_d \rho_d c_{pd} - T_i \rho_i c_{pi} \left(\frac{C_d}{C} \right)) + P_{nc} \\ + (\rho c_p - \rho_c c_{pc}) T 3k_v V \int_0^{\infty} G n x^2 dx$$

$$K9 = \rho_i$$

$$K10 = \rho_v$$

$$K11 = -Q_d \rho_d + Q_p \rho + Q_f \rho - (\rho - \rho_c) 3k_v V \int_0^{\infty} G n x^2 dx$$

The following relations can be established by substitution in the basic expressions for the mass, energy and total mass balances,

$$Q_v = \frac{K7 * K11 + K8 * K9}{K6 * K9 - K10 * K7} \quad (\text{A23})$$

$$Q_i = \frac{K10 * K8 + K11 * K6}{K6 * K9 - K10 * K7} \quad (\text{A24})$$

Description of the fines removal system

$$Q_d C_d = Q_F [\epsilon_F C + (1 - \epsilon_F) \rho_c]$$

$$Q_d \rho_d = Q_F [\varepsilon_F \rho + (1 - \varepsilon_F) \rho_c]$$

Other definitions

$$\varepsilon_i = 1 - k_v m_{3,i}$$

$$m_{j,i} = \int n_i(x) x^j dx$$

(i=finest/product/crystallizer contents)

$$n_p(x) = h_p n(x)$$

$$n_F(x) = h_F n(x)$$



Appendix B

Material physical properties

Solubility

The solubility of the materials in water (*kg material/m³ of solution*) follows the relation,

$$w = C_{sat,1} + C_{sat,2} * T$$

Density

The density of the solid materials (*kg material/m³ of material*) is given by,

$$\rho_c = \rho_{c,1} + \rho_{c,2} * T \quad (B1)$$

and of a saturated solution at temperature T ,

$$\rho_l = \rho_{l,1} + \rho_{l,2} * T + \rho_{l,3} * w \quad (B2)$$

Specific heat capacity

The specific heat capacity of the saturated solution is given by,

$$Cp_l = Cp_{l,1} + Cp_{l,2} * w + Cp_{l,3} * T + Cp_{l,4} * T^2 \quad (B3)$$

and of the solid crystalline substance by,

$$Cp_c = Cp_{c,1} + Cp_{c,2} * T \quad (B4)$$

The constants in equations (B1) to (B4) for the materials ammonium sulphate, pentaerythritol and adipic acid are given in table B1 below.

<i>Material</i>	<i>Ammonium Sulphate</i>	<i>Pentaerythritol</i>	<i>Adipic acid</i>	<i>Units</i>
Parameter				
$C_{sat,1}$.4118	-.088	.08458	-
$C_{sat,2}$.0009121	.00756	-	C^{-1}
$\rho_{l,1}$	1008	1030	1010	kg/m^3
$\rho_{l,2}$	-.384	-.8684	-	$kg/m^3 \text{ } ^\circ C$
$\rho_{l,3}$	568.9	223.9	-	kg/m^3
$\rho_{c,1}$	1778	1397	1344	kg/m^3
$\rho_{c,2}$	-.1969	0	-	$kg/m^3 \text{ } ^\circ C$
$Cp_{l,1}$	4.259	4	4.022	$kJ/kg \text{ } ^\circ C$
$Cp_{l,2}$	-3.032	-.7159	-	$kJ/kg \text{ } ^\circ C$
$Cp_{l,3}$	-.001767	0.003612	-	$kJ/kg \text{ } ^\circ C^2$
$Cp_{l,4}$	4.287e-06	-0.00007	-	$kJ/kg \text{ } ^\circ C^3$
$Cp_{c,1}$	1.376	1.208	1.59	$kJ/kg \text{ } ^\circ C$
$Cp_{c,2}$.0213	.00618	-	$kJ/kg \text{ } ^\circ C^2$
ρ_v	1000	1000	1000	kg/m^3
R_v	2.494e-06	2.494e-06	2.494e-06	kJ/kg
Cp_v	4000	4000	4000	$kJ/kg \text{ } ^\circ C$

Table B1 : *Material constants*

Appendix C

Simple Classification Model

The internal classification occurring the draft-tube can be represented as shown in figure C1.

To construct a simple model of the situation, three equations are used. The first refers to the terminal settling velocity of particles (U_{settle}) in a fluid given by Stokes' law (Perry, 1984).

$$U_{settle} = k_1 \frac{g x^2 (\rho_c - \rho_f)}{18\mu} \quad (C1)$$

where k_1 is a constant and is a function of the sphericity ψ (surface area of a sphere having the same volume as the particle divided by the surface area of the particle), given by,

$$k_1 = 0.843 \log(\psi/0.065) \quad (C2)$$

The second equation refers to the velocity of a particle due to the action of the impeller ($V_{impeller}$).

$$V_{impeller} = p_1 \sqrt{N} \quad (C3)$$

Finally, to account for the effect of a high concentration of particles on the apparent viscosity and density of the solution, the Richardson-Zaki relation is used, which relates the actual settling velocity of a crystal in a suspension (U_{is}) to its' settling velocity (U_{settle}) in a clear liquid,

$$U_{is} = U_{settle} \epsilon^n \quad (C4)$$

where ϵ is the volume void fraction and n is a constant which is 4.65 for the Stokes law' region ($N_{RE} < 0.30$) and 2.33 for the Newton's law regime ($N_{RE} > 1000$).

This set of equations contains only one unknown (p_1) which must be estimated from the data given in figure C2. Ideally, it should be estimated by measuring the pumping capacity of the impeller as a function of its' speed, but in the current configuration this has never been done.

To model the internal classification in the crystallizer, the CSD present at two points is chosen, these are at the top of the draft tube and at the base of the draft tube as indicated in figure C1. The base of the draft-tube is chosen as this is the point at which the product is removed from the crystallizer. In this simulation, only the classification effect in the crystallizer is considered. The effect of kinetic phenomena such as growth, attrition and secondary nucleation are not considered. This assumption is justified by assuming that the time needed to make the steps in the impeller speed (2 hours) was short in comparison to the time needed to cause a significant dynamic response in the CSD. The greatest effect on the CSD was expected to come from the instantaneous effect on the position and spread of the CSD and the density of the slurry due to a change in impeller speed. The model is initiated by introducing a log-normal distribution into the crystallizer at the top of the draft-tube. The way that this CSD distributes itself in the crystallizer is modelled using the following equation.

$$\frac{dn(x,t)}{dt} = -\frac{dn(x,t)U(N,x)}{dh} \quad (C5)$$

h represents the height of the draft-tube, and $U(N,x)$ is the velocity of the particles in either the inside or outside of the draft-tube. Given that the CSD is evaluated at only two points in the crystallizer, equation C5 can be rewritten to express the CSD at these locations.

$$\frac{\Delta n_{base}}{\Delta t} = \frac{n_{top}U_{down} - n_{bot}U_{up}}{h} \quad (C6)$$

$$\frac{\Delta n_{top}}{\Delta t} = \frac{n_{base}U_{up} - n_{top}U_{down}}{h} \quad (C7)$$

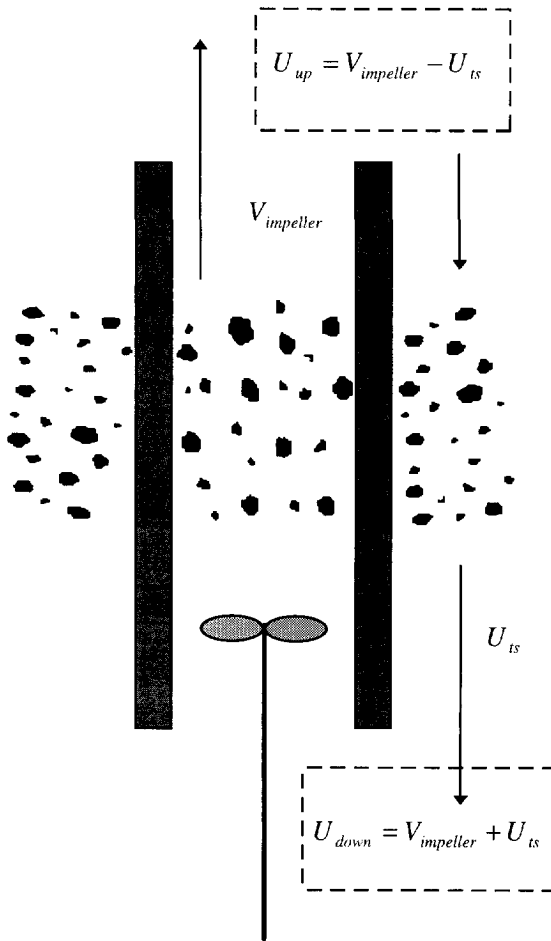


Figure C1 : Schematic drawing of the draft-tube and impeller

Figure C3 (top) shows a plot of the classification functions calculated by dividing the distributions at the top and base of the draft tube by the original distribution put into the crystallizer. Figure C3 (bottom) shows the effect of such a classification function on a typical steady-state $\log(n)$ vs. x plot under the assumptions of no attrition, fines removal or other size dependent growth functions.

The deviations from the MSMPR plot are similar to the deviations which occur due to attrition in the crystallizer.

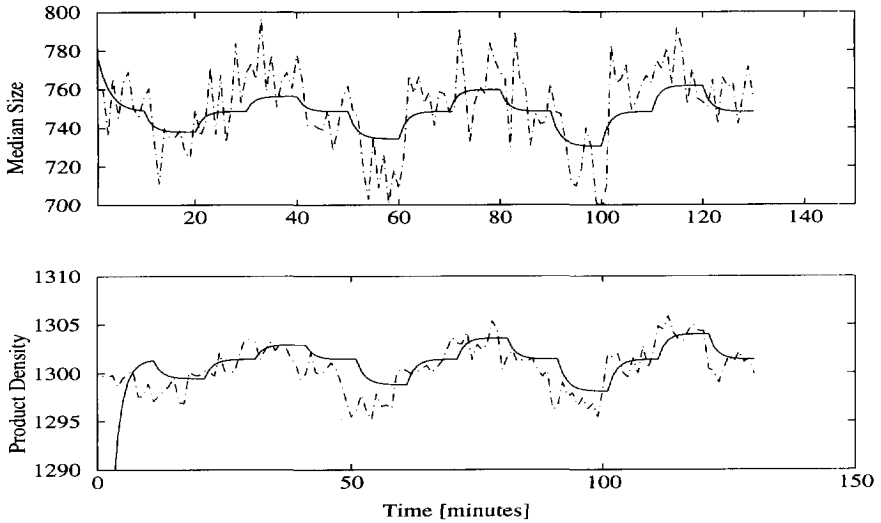


Figure C2 : Modelled response to change in impeller speed using simplified model. Measured data (hatched line) and simulation (solid line)

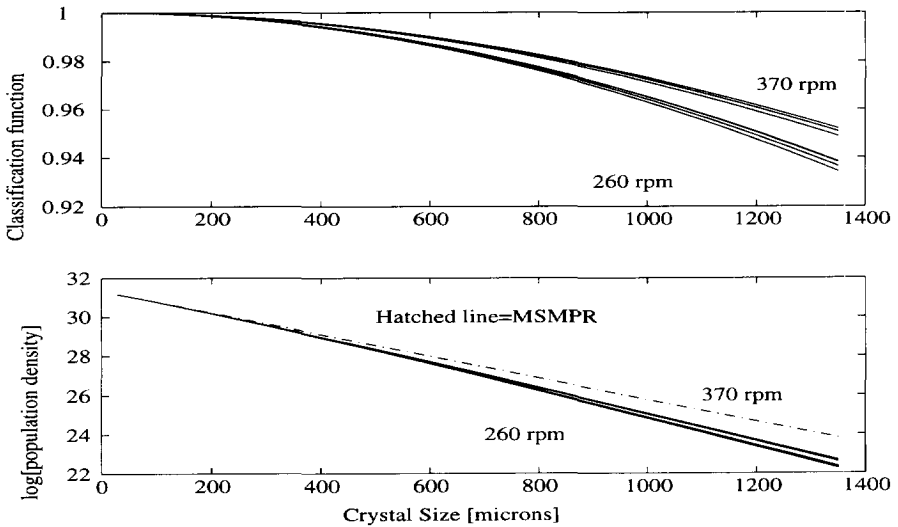


Figure C3 (a) and (b) : Effect of classification on the steady-state distribution (upper) and the classification function calculated from figure C2

Appendix D

Impeller step change response in a non-ideally mixed crystallizer

To examine if internal classification can give rise to the longer term dynamic behaviours observed in figure 6.1, a simulation was carried out, in which account of the kinetics of the system was made. For this simulation, the dynamic model first introduced in chapter 3 was used. A steady-state for a standard set of kinetic parameters (Run 6) and nominal operating conditions (Run 6 : 120 kW, 75 mins., 1 L/s fines removal) was calculated. To simulate the effect of internal classification, a log-normal distribution of crystals was introduced in the feed stream to the crystallizer and its' effect on the dynamic behaviour of the CSD observed. This approach is justified by looking at what happens when internal classification occurs in a crystallizer. The longer residence time of the crystals inside the draft-tube reduces their growth rate as the supersaturation generated in the boiling zone will be at a minimum once it has reached the inside of the draft-tube. The larger particles will also short-circuit the boiling zone in going from the inside to the outside of the draft-tube (Gerla, 1995), thus encountering a lower supersaturation than smaller particles which do penetrate the boiling zone. Lastly, the longer residence time of the larger particles inside the draft-tube will also contribute to the lower growth rate of larger particles. If the impeller speed is increased, these effects reducing the growth rate of the largest crystals will become less pronounced. Also, the very largest crystals which could not escape from the inside of the draft-tube due to their large mass may be re-introduced into the supersaturated environment. For these reasons, it was thought that the effect of increasing the impeller speed could be simulated by introducing a distribution of large crystals into the crystallizer in the feed stream. Conversely a reduction in

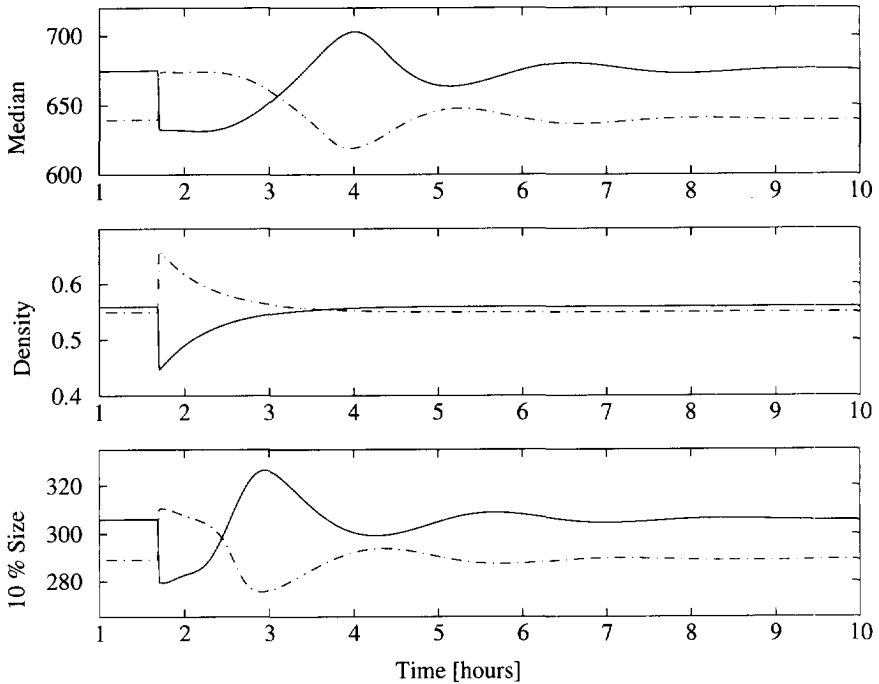


Figure D1 : *Response of CSD dynamics to the introduction of a log-normal population in the feed to the crystalliser (hatched line), and the response of product CSD to the removal of a log-normal population of large particles (solid line).*

impeller speed was simulated by removing the same distribution instantaneously in the product stream.

Figure D1 shows the responses of the CSD to a step input in the CSD of a log-normal distribution. These figures can be compared to figure 6.1 which show the experimental responses. The step was programmed 1.5 hours after the system had reached a steady-state. The two test cases, where a distribution is introduced and removed from the crystallizer show that the system responds by entering a dynamic phase which lasts for up to 10 hours. This type of response is similar to that measured in figure 6.1 where an introduction or removal of crystals from the 'active' circulating suspension causes the CSD to enter an oscillation.

To simulate the effect of internal classification on the start-up dynamic behaviour in the crystallizer is not attempted here, as the interactions between the supersaturated fluid and the crystal population cannot be accounted for under the assumption of a well mixed crystallizer. Because internal classification acts on the

CSD in the same way as an attrition function would, it is expected that the effect would be to lower the median size and make the distribution narrower throughout the experiment. As the attrition function compensates for the presence of internal classification, but does not increase the amount of attrition fragments in the crystallizer, it is expected that a simulation will give a lower survival efficiency of attrition fragments than is actually the case.



References

- Abegg, C.F., Stevens, J.D., Larson, M.A., Crystal size distributions in continuous crystallizers when growth rate is size dependent, *AIChE J.* **14** (1):118-122, 1968
- Andrews, S.J., Hails, J.E., Harding, M., The mosaic spread of very small crystals deduced from Laue diffraction patterns, *Acta Cryst.* **A43**, 70-73, 1987
- Asselbergs, C.J., Ph.D. Thesis, Delft University of Technology, The Netherlands, 1978
- Bauer, L.G., Rousseau, R.W., McCabe, W.L., Influence of crystal size on the rate of contact nucleation in stirred-tank crystallizer, *AIChE J.*, 20 p 653-659, 1974
- Belkin, D.I., *Zhurnal Prikladnoi Khimii*, **63** (11):2542-2548, Nov. 1990
- Bennema, P., Industrial Crystallization 1976, J.W. Mullin ed., North Holland Publishing Company, 91-112, 1976
- Bennett, R.A., Fiedelman, H., Randolph, A.D., Crystallizer influenced nucleation, *Chem. Eng. Prog.*, **69** (7): 86-93, 1973
- Bennett, R.C., Crystallizer selection and design, in *Handbook of industrial crystallization*, ed. Myerson, A.S., Chapter 5 p103-130, 1992
- Berglund, K.A., Larson, M.A., Modeling of growth rate dispersion of citric acid monohydrate in continuous crystallizers, *AIChE J.* **30** (2): 280-287, 1983
- Bhat, H.L., Sherwood, J.N. and Shripathi, T.S., The influence of stress, strain and fracture of crystals on the crystal growth process, *Chem. Eng. Sci.* **42** 609-618, 1987
- Botsaris, G.D., Secondary Nucleation - a review, *Industrial crystallization '75*, Plenum Press, 1976
- Bourne, L.J., Hydrodynamics of crystallizers with special reference to classification, *Industrial Crystallization '78*, eds. E.J. de Jong and S.J. Jancic, 1979

- Bourne, J.R., Hungerbuehler, K., An experimental study of the scale-up of a well-mixed crystallizer, *Trans IChemE* **58**, 1980
- Boxman, A., *Particle Size Measurement for the Control of Industrial Crystallizers*, PhD Thesis, Delft University of Technology, The Netherlands, 1992
- Bransom, S.H., Factors in the design of continuous crystallizers, *Br. Chem. Engng.*, **5** 838, 1960
- Bransom, S.H., Brown, D.E., Heeley, G.P., *J. Chem. E. Symp. Ind. Cryst.*, 45-57, 1969
- Brown, D.J., Felton, P.G., Direct measurement of concentration and size for particles of different shapes using laser light diffraction, *Chem. Eng. Res. Des.* **63** 125-132, 1985
- Budz, J. Jones, A.G., Chianese, A., and Mazarotta, B., Effect of Scale on crystallization kinetics of potassium sulphate in batch and continuous crystallizers, *Proc. Techn. Proc.* **6**, *Ind. Cryst.* '87, 315-318, 1987
- Bujac, P.B.B., *Indus. Cryst.* '75, ed. Mullin, J.W., Plenum Press, N.Y. - London, 23-31, 1976
- Burton, W.K., Cabrera, N., Frank, F.C., (1951); *Phil. Trans. Roy. Soc. London*, **A243** 299-358, 1951
- Chambliss, C.W., *Nucleation and growth kinetics in a cooling crystallizer*, Ph.D. Thesis, Iowa State Univ., Ames, Iowa, Univ. Microfilms Inc., Ann Arbor, Michigan no. 67-2025, 1966
- Chernov, A.A., in: *Industrial Crystallization '90*, ed. Mersmann, A., p343, 1990
- Chianese, A., Di Cave, S. and Mazzarotta, B., Secondary nucleation by abrasion of potassium sulphate, *World congress III of chemical engineering*, Tokyo, 937-940, 1986
- Clontz, N.A., McCabe, W.L., *Chem. Eng. Progr. Symp. Ser.* **67** (110): 6, 1971
- Daudey, P.J., *Secondary nucleation kinetics of ammonium sulphate*, Chapter 7, Ph.D. Thesis, Delft University of Technology, The Netherlands, 1987.
- Daudey, P.J., van Rosmalen, G.M. and De Jong, E.I., Secondary nucleation kinetics of ammonium sulphate in a CMSMPR crystallizer, *J. Crystal Growth* **99** 1076-1081, 1990
- Davey, R.J., Ristic, R.I., Zizic, B., The role of dislocations in the growth of ammonium dihydrogen phosphate crystals from aqueous solutions, *J. Crystal Growth*, 47 1-4, 1979

- Davey, R.J., The control of crystal habit, *Industrial Crystallization '78*, eds. E.J. de Jong and S.J. Jancic, p169, North Holland, Amsterdam, 1979
- Davey, R.J., Role of additives in precipitation processes, *Industrial crystallization '81*, eds. S.J. Jancic and E.J. de Jong, p123, North Holland, Amsterdam, 1982
- Davey, R.J., 1982, Role of additives in precipitation processes, *Industrial Crystallization '81*, eds. S.J. Jancic and E.J. de Jong, p123, North Holland, Amsterdam, 1982
- David, R., Marchal, J., Klein, J., Villermaux, J., Crystallization and precipitation engineering-III : A discrete formulation of the agglomeration rate of crystals in a crystal process, *Chem. Eng. Sci.* **46**:(1) 205-213, 1991
- De Wolf, S., *Modelling, System identification and control of an evaporative continuous crystallizer*, Ph.D. Thesis, Delft University of Technology, The Netherlands, 1990
- Dirksen, J.A. & Ring, T.A. : Fundamentals of crystallization: kinetic effects on particle size distribution and morphology, : Review article number 34, *Chem. Eng. Sci.* **46** (10): 2389-2427, 1991
- Eek, R.A., Modelling and observation of CSD dynamics in a continuous crystallizer Proceedings first separations divisions topical conference on separations technologies : new developments and opportunities, 653-659, *AIChE annual meeting*, Miami beach, November, 1992
- Eek, R.A., Dijkstra, S.J., and van Rosmalen, G.M., Dynamic modelling of suspension crystallizers, using experimental data, *AIChE J.*, 41 (3): 1-14, 1995
- Eek, R.A., Rusticus, S.J., Dijkstra, S.J., Design of robust stabilizing feedback controllers for a continuous crystallization process, *Submitted to Chem. Eng. Sci.*, November, 1994
- Eek, R.A., *Control and Dynamic Modelling of Industrial Suspension Crystallizers*, Ph.D. Thesis, TU Delft, 1995
- Garside, J., Larson, M.A., Direct observation of secondary nuclei production, *J. Crystal Growth*, **43**, 694-704, 1978
- Garside, J., Jancic, S.J., Measurement and scale-up of secondary nucleation kinetics for the potash alum-water system, *AIChE J.* **25** (6): 948-958 (1979)
- Garside, J., Ristic, R.I., Growth rate dispersion among ADP crystals formed by primary nucleation, *J. Cryst. Growth* **61**, 215-220, 1983

- Garside, J., Webster, G., Davey, R.J., Ruddick, A.J., The relation between growth rate dispersion and the mechanical properties of crystals, *Industrial Crystallization '84*, ed. S.J. Jancic & E.J. de Jong, 459-462, Amsterdam 1984
- Garside, J., *Industrial Crystallization from Solution - Review Article No. 15*, *Chem. Eng. Sci.*, **40** (1):3-26, 1985
- Gerigk, M.A., *Effektive keimbildung in zwangumlauf kristallisatoren*, Ph.D. Thesis, Technische Hochschule Aachen, 1991
- Gerla, J.H., *Control of Industrial Crystallizers-The Physical Aspects*, Ph.D. Thesis, TU Delft, 1995
- Gerla, J.H., Kramer, H.J.M., Van Rosmalen, G.M., Scarlett, B., First approach of the implementation of hydrodynamics in the modelling of industrial crystallizers, *12th Symposium on Industrial Crystallization*, 5-133 ed. Z. Rojkowski, Warsaw, Poland, Sept. 21-23, 1993
- Grant, D.J.W., Chow, K.Y., Chan, H.K., Modification of the physical properties of adipic acid by crystallization in the presence of alkanolic acids, *AIChE. Symp. Ser.* **87**, 38-43, 1991
- Grootscholten, P.A.M., Leer, B.G.M., de Jong, E.J., Asselbergs, C.J., Factors affecting secondary nucleation rate of sodium chloride in an evaporative crystallizer, *AIChE J.* **28** (5): 728-737, 1982
- Harding, M.M., Rule, R.J., Oldman, R.J. and Davey, R.J., Growth rate dispersion in small crystals and its' relation to mosaic spread, *J. Crystal Growth* **123**, 373-384, 1992
- Hedstrom, L., Rasmusen, A.C., Kinetics of secondary nuclei of pentaerythritol, *12th Symposium on Industrial Crystallization*, 4-149, ed. Z. Rojkowski, Warsaw, Poland, Sept. 21-23, 1993
- Helliwell, J.R., Habash, J., Cruikshank, D.W.J., Harding, M.M., Greenhough, T.J., Campbell, J.W., Clifton, S.S., Elder, M., Machin, P.A., Papiz, M.Z., Zurek, S., The mosaic spread of very small crystals deduced from Laue diffraction patterns, *J. Appl. Cryst.* **22** 483-497, 1989
- Hull, D., and Bacon, D.J., *Introduction to dislocations*, 3rd ed., Pergamon Press, Oxford, pp. 71-81, 1984
- Hurle, D.T.J., *Handbook of crystal growth*, North -Holland, Amsterdam, 1994
- Jager, J., *Control of Crystallizers : The physical aspects*, Ph.D. Thesis, Delft University of Technology, 1990

- Jager, J., Wolf, S. de, Kramer, H.J.M., Jong, E.J. de, Estimation of Nucleation Kinetics from CSD transients for a Continuous Crystallizer, *Chem. Eng. Sci.*, **46** (3): 807-818, 1991
- Jager, J., De Wolf, S., Kramer, H.J.M. and de Jong, E.J., 1991, Estimation of nucleation and attrition kinetics from csd-transients in a continuous crystallizer, *Trans IChemE* 69A 53
- Johnson, R.T., Rousseau, R.W. and McCabe, W.L., Factors effecting Contact Nucleation, *AIChE Symp. Series* **68** (121): 31-41, 1972
- Jones, A.G., Budz, J., Mullin, J.W., Crystallization kinetics of potassium sulfate in an MSMPR agitated vessel, *AIChE J.* **32** (12): 2002-2009, 1986
- Juzaszek, P. and Kawecki, W., Effect of crystal attrition on crystal size distribution in continuous crystallizers, *5th Symp. Ind. Cryst.*, Chisa, Czechoslovakia, 1973
- Kirk-Othmer, *Encyclopedia of chemical technology*, Vol. 7, 243, J. Wiley & sons., inc. USA
- Klug, D.L., The influence of impurities and solvents on crystallization, in *Handbook of industrial crystallization*, ed. Myerson, A.S., Chapter 3, p75, 1992
- Kramer, H.J.M., Ó Meadhra, R., Van der Heijden, A.E.D.M. and Van Rosmalen, G.M., Modeling of the attrition kinetics in industrial crystallizers, *12th Symp. on Ind. Cryst.*, Z.H. Rojkowski ed., Warsaw, 1993
- Kuijvenhoven, L.J., *Aspects of continuous sucrose crystallization*, Ph.D. thesis, Delft University of Technology, The Netherlands, 1983
- Lal, D.P., Mason, R.E.A and Strickland-Constable, R.F., Collision breeding of crystal nuclei, *J. Crystal Growth* **5**, 1-8, 1969
- Landau, L.D. and Lifshitz, E.M., in : *Theory of Elasticity*, Pergamon Press, Oxford, 1986
- Larson, M.A., Klekar, S.A., In-situ measurement of supersaturation in crystallization from solution, *presented at the 66th annual AIChE meeting*, Philadelphia, 1973
- Larson, M.A., Mullin, J.W., Crystallization kinetics of ammonium sulphate, *J. Crystal Growth*, **20** 183-191, 1973
- Levich, V.G., *Physicochemical Hydrodynamics*. Prentice-Hall, New York, 1962
- Marchal, P., David, R., Klein, J.P., Villiermaux, J., Crystallization and precipitation engineering - IV. Kinetic model of adipic acid crystallization, *Chem. Eng. Sci.* **46**, pp 1129-1136, 1991

- Mazarotta, B., Abrasion and breakage phenomena in agitated crystal suspensions, *Chem. Eng. Sci.* **47** (12): 3105-3111, 1992
- Mersmann, A., Sangl, R., Kind, M. and Pohlisch, J., Attrition and secondary Nucleation in Crystallizers, *Chem. Eng. Technol.* **11**, 80-88, 1988
- Mitrovic, M.M., Influence of initial crystal size on growth rate of crystals from solution, *J. Crystal Growth* **139**, 332-335, 1994
- Moffat, K., Szebenyi, D., Bildarback, D., *Science*, 223, 1423-1425, 1984
- Molerus, O., Latzel, W., Suspension of solid particles in agitated vessels-II. Archimedes numbers >40 , reliable prediction of minimum stirrer angular velocities, *Chem. Eng. Sci.* **42** (6):1431-1437, 1987
- Mullin, J.W., Chakraborty, H., Mehta, K., *J. Appl. Chem.* **20**, p367, 1970
- Musil, L., Vlk, J., Role of the geometry in the hydrodynamics of circulating slurries in a stirred crystallizer, *Ind. Cryst.* '78, eds. E.J. de Jong and S.J. Jancic, 229-240, 1979
- Narang, R.E., Sherwood, J.N., Cliff, M.J., Jones, A.G., Crystallization and impurity incorporation in adipic acid, *Inst. Chem. Eng. Symp. Ser.* **54**, 267-277, 1978
- Nienow, A.W., Bujac, P.D.B., Mullin, J.W., Slip velocities in agitated vessel crystallizers, *J. Crystal Growth*, **13/14** 488-492, 1972
- Nienow, A.W., *Chem. Eng. J.*, 9, (1975), 153-160, 1975
- Nienow, A.W., Conti, R., Particle Abrasion at high Solids Concentration in Stirred Vessels, *Chem. Eng. Sci.* **33** 1077-1086, 1978
- O'Dell, F.P., Rousseau, R.W., Magma density and dominant size for size dependent growth, *AIChE J.*, **24**, 738, 1978
- Ó Meadhra, R., Van Rosmalen, G.M., A new model for secondary nucleation, *AIChE J.*, Manuscript accepted, May 1995
- Ó Meadhra, R., Peutz, M.M.V., Kramer, H.J.M., Van der Heijden, A.E.D.M., Van Rosmalen, G.M., The Role of Attrition in the Crystallization of Ammonium Sulphate, *12th Symp. on Ind. Cryst.*, ed. Z.B. Rojkowski, Warsaw, 1993
- Ohara, M., and Reid, R.C., *Modelling Crystal Growth rates from Solution*, Prentice-Hall, Englewood Cliffs, NJ., 1973
- Ohashi, H.T., Sugawara, T., Kikuchi, T., Henmi, T., Mass transfer between particles and liquid in a solid-liquid two phase upflow in vertical pipes, *J. Chem. Eng. Japan*, **12** 190-195, 1979
- Ottens, E.P.K., Janse, A.H. and De Jong, E.J., Secondary nucleation in a stirred vessel cooling crystallizer, *J. Crystal Growth* **13/14**, 500-505, 1972

- Ottens, E.P.K., De Jong, E.J., A model for secondary nucleation in a stirred vessel cooling crystallizer, *Ind. Engng Chem Fundls* **12**, 179-184, 1973
- Perry's Chemical Engineers' Handbook*, International edition, Mc-Graw-Hill, ed. R.H. Perry, D. Green, 5-66, 1984
- Ploß, R., Tengler, T., Mersmann, A., *Chem. Eng. Tech.*, synopsis 1364 in *Chem. Ing. Tech.*, **57**, 536, 1985
- Pohlisch, J., Mersmann, A., The influence of stress and attrition on the crystal size distribution, *Chem. Eng. Technol.*, **11** 40-49, 1988
- Ploß, R. and Mersmann, A., A new model of the effect of stirring intensity on the rate of secondary nucleation, *Chem. Eng. Technol.* **12** 137-146, 1989
- Pohlisch, J., Ph.D. Thesis TU Munchen 1987, p2
- Powers, H.E.C., *Ind. Chemist* **39** 351, 1963
- Prins, Graduate report thesis, *Fines removal in a 970 L DTB crystallizer*, TU Delft, 1992
- Ramshaw, C, Secondary nucleation in mechanically agitated Crystallizers : Crystal motion in the impeller region, *The Chem. Eng.*, July/August, p 446-449, 1974
- Randolph, A.D., Larson, M.A., A population balance for countable entities, *Canadian Journal of Chem. Engng.*, **42**, 280-281, 1964
- Randolph, A.D., White, E.T., Modeling size dispersion in the prediction of crystalsize distribution, *Chem. Eng. Sci.*, **32**, 1067-1078, 1977
- Randolph, A.D., Larson, M.A., *Theory of particulate processes*, Chapter 3, Academic Press inc., 2nd edition, 1988
- Randolph, A.D., Larson, M.A., *Theory of particulate Processes*, Academic Press, New York, 1983
- Randolph, A.D., Larson, M.A., *Theory of particulate processes*, Chapter 5, Academic Press inc., 2nd edition, 1988
- Randolph, A.D. and Larson, M.A., *Theory of Particulate Processes*, 2nd ed., Academic Press, New York, 1988
- Rojkowski, Z.H., Crystal growth rate models and similarity of population balances for size dependent growth rate and for constant growth rate dispersion, *Chem. Eng. Sci.* **48** (8): 1475-1485, 1993
- Ristic, R.I., Sherwood, J.N., Wojciechowski, K., Assessment of the strain in small sodium chlorate crystals and its' relation to growth rate dispersion, *J. Crys. Growth* **91** 163-168, 1988

- Ristic, R.I., Sherwood, J.N. and Shripathi, T., Strain variation in the {100} growth sectors of potash alum single crystals and its' relationship to growth rate dispersion, *J. Crystal Growth* **102** 245, 1990
- Rosenberg, H.M., *The Solid State*, Oxford physics series, 1985, 2nd edition
- Rojkowski, Z.H., 'Crystal growth rate models and similarity of population balances for size- dependent growth rate and for constant growth rate dispersion', *Chem. Eng. Sci.* **48** (8): 1475-1485, 1993
- Rusli, I.T., Larson, M.A., Garside, J., Initial growth of secondary nuclei produced by contact nucleation, *Design, control and analysis of crystallization processes - AIChE Symp. Series J.* **76** (193):52-58, 1980
- Scrutton, A., 5th Int. Symp on Salt, Hamburg, 2:383 (*Northern Ohio Geological Soc Inc*), 1978
- Scrutton, A., Grootcholten, P.A.M., de Jong, E.J., Effect of Impeller Draft Tube Clearance on the Crystallisation kinetics of Sodium Chloride, *Trans IChemE* **60**, 345-351, 1982
- Shaw, J.A., The design of draft tube circulators, *Proc. Australas. Inst. Min. Metall.* No. 283, 47-58, September 1982
- Shimizu, K., Kubota, N., Tsukamoto, K., Sunagawa, I., Yonemoto, T. and Tadaki, T., The effect of surface treatments on initial breeding of potassium alum, *J. Crystal Growth* **69**, 115-119, 1984
- Shimizu, K., Kubota, N., Sunagawa, I., Evaluation of the contribution of different mechanisms to the secondary nucleation of potassium alum, *J. Crystal Growth* **69**, 119-124, 1984
- Shimizu, K., Tsukamoto, K., Horita, J. and Tadaki, T., Origin of secondary nuclei as revealed by isotopic labelling, *J. Crystal Growth* **69**, 623-626, 1984
- Sung, C.Y., Estrin, J. and Youngquist, G.R., Secondary nucleation of magnesium sulfate by fluid shear, *AIChE J.* **19**, 957-962, 1973
- U.S. Patent No. 5,296,639, Adipic acid purification, March, 1994
- Valcic, A.V., The influence of dislocations on the growth rate of saccharose crystals, *J. Crystal Growth* **30** 129-136, 1975
- Van der Heijden, A.E.D.M., Elwenspoek, M., Van der Eerden, J.P., "Size Distribution of Embryos produced by Crystal-Rod contacts", *J. Crystal Growth* **98**, 398 1989
- Van der Heijden, A.E.D.M., Elwenspoek, M., Contact nucleation : in-situ and ex-situ observations of surface breeding, *J. crystal Growth* **99** 1087, 1990

- Van der Heijden, A.E.D.M., Van der Eerden, J.P., Chapter 11, Ph.D. Thesis, University of Nijmegen, The Netherlands, 1992
- Van der Heijden, A.E.D.M., Van der Eerden, J.P., Growth rate dispersion : The role of lattice strain, *J. Crystal Growth* **118**, 14-26, 1992
- Van der Heijden, A.E.D.M., Van der Eerden, J.P. and van Rosmalen, G.M., The secondary nucleation rate : A physical model, *Chem. Eng. Sci.*, **49** (18), 3103-3113, 1994
- Vermuri, V., Karplus, W.J., *Digital computer treatment of partial differential equations*, Chapter 4, Prentice-Hall Inc., 1981
- Wang, S., Mersmann, A., Initial size dependent growth rate dispersion of attrition fragments and secondary nuclei, *Chem. Eng. Sci.* **47** (6) 1365-1371, 1992
- White, E.T., Bendig, L.L., Larson, M.A., *AIChE Sym. Ser.* **72** 41, 1976
- White, E.T., Wright, P.G., Magnitude of size dispersion effects in crystallization, *Chemical engineering progress symposium series*, **67** (110): 81-87, 1971
- Wissing, R., Elwenspoek, M. and Degens, B., In-situ observation of secondary nuclei, *J. Crystal Growth* **79**, 614-619, 1986
- Wood, I.G., Thompson, P., Mathewman, J.C., *Acta Cryst* **B39**, 543-547, 1983
- Youngquist, G.R., Randolph, A.D., Secondary nucleation in a class II system : Ammonium sulphate-water, *AIChE J.* **18** (2): 421, 1972
- Zipp, G.L., Randolph, A.D., Selective fines destruction in batch crystallization, *Proc. Tech. Proc. (Ind. Crys. '87)*, 469-473, 1987
- Zumstein, R.C. and Rousseau, R.W., Utilization of industrial data in the development of a model for crystallizer simulation, *AIChE Symp. Series* **83** (253): 130-138, 1987



List of Symbols

Symbols

b	=	Burgers' vector	m
B_o	=	Birth rate at size $x=0 \mu\text{m}$	$\#/m^3 s$
$B(x)$	=	Length dependent birth rate	$\#/m^4 s$
c_p	=	Specific heat	$KJ/kg K$
C	=	Constant (equation 2.22)	
C	=	Fluid phase concentration	kg/m^3
$B_{o,eff}$	=	Effective birth rate at finite size	$\#/m^3 s$
C_1	=	Constant (BCF model)	
D	=	Distance of crystal to negative	m
$D(x)$	=	Length dependent death rate	$\#/m^4 s$
\dot{E}_l	=	Energy transfer rate to crystals	$KJ/m^3 s$
F	=	Formation rate	$\#/m^3 s$
F_1	=	Number of collisions/ unit of collision energy	$\#/KJ$
F_2	=	Survival factor of attrition fragments	
g	=	Gravity constant	m/s^2
g	=	Growth rate constant (power)	
G	=	Shear modulus	N/m^2
$G(x)$	=	Length dependent growth rate	m/s
G_{eff}	=	Effective growth rate	m/s
G_{kin}	=	Kinetic growth rate	m/s
G_{attr}	=	Attrition rate	m/s
h	=	Height	m

h_f	=	Fines classification function	
h_p	=	Product classification function	
$H(x)$	=	Secondary nuclei distribution	$\#/m^4 s$
I	=	Laser beam intensity (after cell)	eV
I_0	=	Laser beam intensity (before cell)	eV
k	=	Boltzmanns constant	J/K
k	=	Growth rate constant	m/s
k'	=	Growth rate constant	m/s
k_G	=	Growth constant	m/s
k_n	=	Nucleation constant	
$k_{survival}$	=	Survival efficiency	
k_v	=	Shape factor	
k_1	=	Stokes' law constant	
K_{attr}	=	Attrition rate constant	m/s
K'_{attr}	=	Attrition rate constant	m/s
K_B	=	Nucleation constant	
l	=	Malvern cell width	m
l	=	Period of strain oscillations	m
L	=	Crystal size	m
\tilde{M}	=	Molar mass	$kg/kmol$
M_p	=	Product density	kg/m^3
M_T	=	Mass of solids	kg/m^3
$m_{attr,eff}$	=	Mass of attrition fragments which grow out	kg
m_j	=	j^{th} moment of the distribution	m^{j+1}/m^4
$m_{attr,tot}$	=	Total mass of attrition fragments produced	kg
n_{base}, n_{top}	=	Population number density at the top and the base of the draft-tube	$\#/m^4$
$n(x, t)$	=	Population number density	$\#/m^4$
n_0	=	Population number density at $x=0 \mu m$	$\#/m^4$
N	=	Impeller speed	RPM
N_{cum}	=	Cumulative number density distribution	$\#/m^3$

N_{RE}	=	Reynolds' number	$\#/m^3$
p_1, \dots, p_9	=	Kinetic parameters	
P_{hc}	=	Heat input	kW
P_{imp}	=	Power input via impeller	kW
P_{loss}	=	Heat loss to the environment	kW
Q	=	Volumetric flow rate	m^3/s
r	=	Radius of curvature	m
R	=	Universal gas constant	$KJ/molK$
R	=	Laue diffraction spot elongation	m
R_v	=	Enthalpy of evaporation	KJ/kg
t	=	Time	sec
T	=	Temperature	$^{\circ}C$
U	=	Velocity	m/s
U_{settle}	=	Settling velocity	m/s
U_{settle}	=	Settling velocity	m/s
U_{ts}	=	Corrected settling velocity	m/s
V	=	Vessel volume	m^3
\dot{V}_{attr}	=	Volume production rate of attrition fragments	m^3/s
V_b	=	Beam volume	m^3
V_c	=	Crystallizer volume	m^3
$V_{impeller}$	=	Particle velocity due to impeller	m/s
W_i	=	Stress energy per particle ($i = 0, \dots, 3$)	$J/par.$
x	=	Crystal size	m
x_{attr}	=	Average size of attrition particles	m
x_c	=	Fines fraction parameter	m
x_{d1}, x_{d2}	=	Locations of log-normal distributions at time $t=0$	m
x_g	=	Attrition function size parameter	m

Greek letters

ϵ	=	Power input	kW/kg
ϵ	=	Void fraction	
ϵ	=	Activity co-efficient (BCF model)	

γ	=	Surface free energy	J/m^2
γ_∞	=	Surface free energy felt by a particle of infinite size	J/m^2
η	=	Efficiency	
η	=	Mosaic spread	deg or rad
μ	=	Chemical potential	$J/mole$
μ	=	Shear modulus	N/m^2
μ	=	Viscosity	kg/s^2
ρ	=	Density	kg/m^3
θ	=	Angle of mismatch	deg or rad
θ	=	X-ray diffraction angle	deg or rad
σ	=	Supersaturation	
σ_1	=	Parameter (BCF model)	
σ_∞	=	Supersaturation felt by a crystal of infinite size	
σ_{d1}, σ_{d2}	=	Spread of log-normal distributions at time $t=0$	
ψ	=	Sphericity (equation 6.1)	
Ψ	=	Stokes' number	

Superscripts

b, h, j

i, k = Exponents in the power law

Subscripts

attr = attrition

c = crystal

d = dissolved fines stream

eff = effective

F, f = fines stream

i = feed stream

kin = kinetic

outgrowth = outgrowth

p = product

removal = removal

v = vapour stream

min, max minimum, maximum

t = target

Abbreviations

CCD = Charged coupled device

CSD = Crystal size distribution

UNIAK Universal Instrumentation and Automation of Crystallizers

Samenvatting

Modellering van de Kinetiek van Suspensiekristallisatoren

Het modelleren van de kristalgrootteverdeling (KGV) van industriële suspensiekristallisatoren brengt nog steeds veel problemen met zich mee. Inadequate modellering van de produktkwaliteit is het gevolg van het feit dat de combinatie van kinetische processen resulterend in de produktie van de KGV niet goed geïdentificeerd kan worden. Verder ontbreekt het aan betrouwbare mechanische modellen die toegepast kunnen worden voor een grote verscheidenheid van materialen, om de KGV van een ideaal geroerde kristallisator te simuleren.

In dit proefschrift worden de bovenstaande problemen onderzocht. De belangrijkste eis is om mechanische modellen te ontwikkelen voor de kinetische processen van de kristalgroei, attritie en secundaire nucleatie, waarmee het mogelijk is om het oscillerende KGV-gedrag in de produktstroom van de kristallisator te beschrijven.

De eerste stap is om een "first principles"-methode toe te passen voor de modellering van een kristallisatorsysteem. Een reeks van massa- en energiebalansen, samen met een kristal-populatie balans is gebruikt om de veranderingen te definiëren in de concentratie in de vloeistoffase en in de veranderingen in de toestand van de KGV. De populatiebalans geeft een raamwerk waarmee de invloed van de kinetische processen van de kristalgroei, attritie en secundaire nucleatie op de KGV beschreven wordt. Een numeriek schema om de populatiebalans op te lossen wordt geïntroduceerd.

Met dit simulatie-raamwerk wordt een aantal bestaande modellen uit de literatuur getest. Er wordt aangetoond dat de empirische energiewet voor secundaire nucleatie - welke in de literatuur vaak toegepast wordt om de evenwichts toestand te voorspellen voor de nucleatie-snelheden van een bekend systeem - kan niet gebruikt worden om het oscillerende opstartgedrag te simuleren van de KGV. Een aangepaste versie van de energiewet, waar efficiëntie-doelen zijn toegepast om de kristallen te identificeren die

met de roerder botsen en daarmee attritiefragmenten creëren, geeft een veel beter gedrag tijdens simulatie van de opstartfase.

Er wordt dieper ingegaan op de groei van de secundaire nucleï in hoofdstuk 4. In de literatuur kunnen veel referenties gevonden worden over mechanismen voor groeisnelheidsverspreiding (GSV) voor de groei van verschillende materialen. In een suspensie-kristallisator, kunnen mechanismen voor een GSV-type voor de groei en een lengte-afhankelijke groei (LAG) niet van elkaar onderscheiden worden. Dit is ook niet mogelijk vanuit een mathematisch oogpunt. Door dit laatste en omdat een LAG-correlatie makkelijker hanteerbaar is in de populatiebalans, is een LAG-mechanisme functie bepaald voor ammoniumsulfaat. Dit is on-line gedaan door de groei-snelheid te meten van een suspensie van sub-250µm kristallen, in een 2l. groeicel geïsoleerd, waarbij gebruik gemaakt is van een Malvern voorwaarts lichtverstrooiings-instrument. De resultaten laten zien dat de groeisnelheid van ammoniumsulfaat beschreven kan worden door gebruik te maken van een LAG-snelheid. Dit laat zien dat de gemiddelde kristalgroeisnelheid van ammoniumsulfaat toeneemt tot aan een grootte van 250µm. In hetzelfde hoofdstuk worden recente modellen getest die claimen dat de interne kristalspanning tot een GSV/LAV-mechanisme leidt. Gelijksoortige kristallen zijn geanalyseerd met gebruik van een Laue diffractie-techniek. Resultaten laten zien dat verwacht mag worden dat een GSV/LAV-mechanisme voor ammoniumsulfaat geldig tot aan 300µm, in overeenkomst met de 2l. groeicel experimenten.

In hoofdstuk 5 is een nieuw secundair nucleatie-model ontwikkeld. Een drie-stappen model is gebruikt. De eerste stap is de informatie van attritie-fragmenten. Dit is beschreven door een empirische attritie-functie die een toenemende attritie-snelheid beschrijft met een toenemende kristallengte, waarmee het mogelijk is om de formatiesnelheid van attritie-fragmenten te berekenen. De verwijdering van attritie-fragmenten, de tweede stap, beschrijft de kans dat attritie-fragmenten worden verwijderd van het kristaloppervlak en vervolgens terecht komen in de suspensie. Voor de meeste materialen is de waarde van deze factor een.

De laatste stap is de overleving en uitgroei van attritie-fragmenten. Uit de resultaten van de "mosaic"-verdeelde metingen in chapter 4 bleek, dat sub-60 micron kristallen een hoge mate van rek hebben, hetgeen kristallen ervan kan weerhouden uit te groeien tenzij zij aan een hoge graad van oververzadiging onderhevig zijn. Om deze reden is een oververzadigingsafhankelijke overlevingsefficiëntie gedefinieerd. Het model is gevalideerd met een data set van de 970-liter kristallisator. Drie soorten experimenten zijn voor de validatie gebruikt: start-up experimenten met constante bedrijfstoestand, semi-batch start-up experimenten en continue steady state identificatie-experimenten.

In hoofdstuk 6 en 7 worden de modellen, ontwikkeld in hoofdstuk 2, 4 en 5, getest door kristallisatie van drie verschillende stoffen op een 22-liter schaal volgens het principe van continue verdamping.

De stoffen waren ammoniumsulfaat, pentaerythritol en adipine zuur. De laatste twee stoffen hebben een veel lagere oplosbaarheid dan ammoniumsulfaat. De resultaten van de ammoniumsulfaat experimenten tonen aan dat het opstartgedrag niet wezenlijk verschilt van het opstartgedrag van ammoniumsulfaat kristallisatie op de 970-liter schaal en dat voor de beschrijving hetzelfde model kan worden gebruikt met praktisch dezelfde kinetiekparameters.

Het bleek dat de modellen ook toepasbaar waren voor de kristallisatie van de andere twee materialen. Bovendien werd aangetoond dat het meenemen van een SDG snelheid en een oververzadigingsafhankelijke overlevingsefficiëntie van belang was voor een nauwkeurige simulatie van het opstartgedrag.

Publications

Ó Meadhra, R., Kramer, H.J.M., Scarlett, B., Sub-micron Particle Sizing using the Coulter LS 130, *Partec Conference Proceedings* p133-143, 1992

Ó Meadhra, R., Peutz, M.M.V., Kramer, H.J.M., Van der Heijden, A.E.D.M., Van Rosmalen, G.M., The Role of Attrition in the Crystallization of Ammonium Sulphate, *Proceedings : 12th Symp. Ind. Crys.* 2:4-029, 1993

Kramer, H.J.M., Ó Meadhra, R., Van der Heijden, A.E.D.M., Van Rosmalen, G.M., Modelling of Attrition kinetics in Industrial Crystallizers, *Proceedings: 12th Symp. Ind. Crys.* 2:5-115, 1993

Ó Meadhra, R., Kramer, H.J.M., Van Rosmalen, G.M., Size dependent Growth behaviour related to the Mosaic Spread in Ammonium Sulphate Crystals, *J. Crystal Growth* 152:314-320, 1995

Ó Meadhra, R., Kramer, H.J.M., Van Rosmalen, G.M., 'A Model for Secondary Nucleation in a Suspension Crystallizer', *AIChE J* 1996, in press

Ó Meadhra, R., Kramer, H.J.M., Van Rosmalen, G.M., A mechanistic approach to simulating the dynamic behaviour in a suspension DTBE crystallizer, *Proceedings : ICCG Conference*, 1995

Curriculum Vitae

Ruairí Ó Meadhra was born on the 13th of April 1966 in Cork, Ireland.

1982→1984 Árd teistiméireacht, Scoil Mhúire, An Mainistir Thuaidh, Corcaigh.

1984→1988 Studied Chemical Technology at Cork Regional Technical College.

1988→1990 Worked at Henkel KGaA in Düsseldorf at their research facilities.

1990→1991 Worked at Henkel (Ireland) Ltd. as a process engineer.

1991→1995 Worked as a Ph.D. student in the UNIAK II project at the Delft University of Technology, at the Laboratory for Process Equipment in the Department of Mechanical and Marine engineering.

1995→... Working as a process research and development engineer for Eastman Chemical Company in the area of crystallization/ solid liquid separation techniques at Kingsport, Tennessee, U.S.A.